



Universidad  
Politécnica  
de Cartagena

PROGRAMA DE DOCTORADO EN TECNOLOGÍAS DE LA  
INFORMACIÓN Y LAS COMUNICACIONES

**Thesis in**

**Analysis and Synthesis of Leaky-Wave  
Devices in Planar Technology**

written by

Alejandro Javier Martínez Ros

supervised by

Dr. José Luis Gómez Tornero

Cartagena, July 2014



*To my parents,  
Alejandro and Juani*





**CONFORMIDAD DE SOLICITUD DE AUTORIZACIÓN DE DEPÓSITO DE  
TESIS DOCTORAL POR EL DIRECTOR DE LA TESIS**

D. José Luis Gómez Tornero Director de la Tesis doctoral "Analysis and Synthesis of Leaky-Wave Devices in Planar Technology"

**INFORMA:**

Que la referida Tesis Doctoral, ha sido realizada por D. Alejandro Javier Martínez Ros, dentro del programa de doctorado Tecnologías de la Información y Comunicaciones, dando mi conformidad para que sea presentada ante la Comisión de Doctorado para ser autorizado su depósito.

La rama de conocimiento en la que esta tesis ha sido desarrollada es:

- ☐ Ciencias
- ☐ Ciencias Sociales y Jurídicas
- ☒ Ingeniería y Arquitectura

En Cartagena, a 5 de junio de 2014

EL DIRECTOR DE LA TESIS



Fdo.: José Luis Gómez Tornero

**COMISIÓN DE DOCTORADO**





**CONFORMIDAD DE DEPÓSITO DE TESIS DOCTORAL  
POR LA COMISIÓN ACADÉMICA DEL PROGRAMA**

D. Fernando Daniel Quesada Pereira, Presidente de la Comisión Académica del Programa “Tecnologías de la Información y las Comunicaciones”.

**INFORMA:**

Que la Tesis Doctoral titulada, “Analysis and Synthesis of Leaky-Wave Devices in Planar Technology”, ha sido realizada, dentro del mencionado programa de doctorado, por D. Alejandro Javier Martínez Ros,

bajo la dirección y supervisión del Dr. José Luis Gómez Tornero.

En reunión de la Comisión Académica de fecha 06/06/2014, visto que en la misma se acreditan los indicios de calidad correspondientes y la autorización del Director de la misma, se acordó dar la conformidad, con la finalidad de que sea autorizado su depósito por la Comisión de Doctorado.

La Rama de conocimiento por la que esta tesis ha sido desarrollada es:

- ☐ Ciencias
- ☐ Ciencias Sociales y Jurídicas
- ☒ Ingeniería y Arquitectura

En Cartagena, a 6 de Junio de 2014

EL PRESIDENTE DE LA COMISIÓN ACADÉMICA DEL PROGRAMA



Fdo: Fernando D. Quesada Pereira

**COMISIÓN DE DOCTORADO**



*El sueño va sobre el tiempo  
flotando como un velero.  
Nadie puede abrir semillas  
en el corazón del sueño.*

*¡Ay, cómo canta el alba, cómo canta!  
¡Qué témpanos de hielo azul levanta!*

*El tiempo va sobre el sueño  
hundido hasta los cabellos.  
Ayer y mañana comen  
oscuras flores de duelo.*

*¡Ay, cómo canta la noche, cómo canta!  
¡Qué espesura de anémonas levanta!*

*Sobre la misma columna,  
abrazados sueño y tiempo,  
cruza el gemido del niño,  
la lengua rota del viejo.*

*¡Ay, cómo canta el alba, cómo canta!  
¡Qué espesura de anémonas levanta!*

*Y si el sueño finge muros  
en la llanura del tiempo,  
el tiempo le hace creer  
que nace en aquel momento.*

*¡Ay, cómo canta la noche, cómo canta!  
¡Qué témpanos de hielo azul levanta!*

*Federico García Lorca, Así que pasen cinco años, 1933.*



# Contents

<b>Introduction</b>	<b>xxix</b>
<b>1 Bases of Substrate Integrated Waveguide Technology</b>	<b>1</b>
1.1 Introduction . . . . .	1
1.2 Characteristics of the SIW . . . . .	3
1.2.1 Transitions SIW . . . . .	7
1.2.2 Applications of the SIW . . . . .	8
<b>2 1-D Leaky-Wave Line Source</b>	<b>13</b>
2.1 Introduction . . . . .	14
2.2 Analysis of a LWA in Planar Technology . . . . .	18
2.3 Designs and Measurements . . . . .	21
2.4 Conclusion . . . . .	28
<b>3 Analysis of 1-D Leaky-Wave Line Sources</b>	<b>31</b>
3.1 Introduction . . . . .	32
3.2 Development of Transverse Equivalent Network . . . . .	34
3.2.1 Accurate Modeling of Partially Reflective Inductive Posts	34
3.2.2 Development of an Accurate TEN . . . . .	37
3.3 Parametric Dispersion Curves . . . . .	41
3.3.1 Effect of Distance Between Reflective Posts $P$ . . . . .	41
3.3.2 Effect of SIW Width $W$ . . . . .	42

3.3.3	Effect of Radiating Strip Width $W_0$ . . . . .	44
3.3.4	Effect of $h$ . . . . .	48
3.4	Design Curves and Experiments . . . . .	50
3.4.1	Design Curves . . . . .	50
3.4.2	Experimental results . . . . .	52
3.5	Conclusion . . . . .	54
<b>4</b>	<b>Synthesis of Tapered Planar LW Devices</b>	<b>57</b>
4.1	Holographic Pattern Synthesis With Modulated SIW LWAs . . . . .	58
4.1.1	Introduction . . . . .	58
4.1.2	Synthesis of Modulated Holographic SIW LWA . . . . .	60
4.1.3	Design Examples . . . . .	65
4.1.4	Conclusion . . . . .	77
4.2	Conformal Tapered SIW LWA . . . . .	79
4.2.1	Introduction . . . . .	79
4.2.2	Design of Conformal Tapered LWAs . . . . .	82
4.2.3	Measured Radiation Patterns . . . . .	90
4.2.4	Conformal SIW LWA Frequency Scanning Response . . . . .	97
4.2.5	Conclusion . . . . .	101
4.3	Quasi-Elliptic Angular Bandpass Filter Using a Modulated SIW . . . . .	101
4.3.1	Introduction . . . . .	102
4.3.2	Synthesis of Quasi-Elliptic Angular Response . . . . .	104
4.3.3	Design of an Angular Bandpass Filter With Modulated SIW LWA . . . . .	108
4.3.4	Frequency Bandpass Filter Response . . . . .	114
4.3.5	Conclusion . . . . .	119
4.4	Near-Field Focusing Properties of Width-Tapered Microstrip LWAs	120
4.4.1	Introduction . . . . .	121
4.4.2	Focusing Conditions in a Microstrip LWA . . . . .	123

4.4.3	Experimental Demonstration . . . . .	128
4.4.4	Conclusion . . . . .	143
4.5	Multiplexing Using LW Near-Field Focusing Techniques in SIW Technology . . . . .	145
4.5.1	Introduction . . . . .	145
4.5.2	Uniform SIW Multiplexer . . . . .	147
4.5.3	Modulated SIW Multiplexer . . . . .	149
<b>5</b>	<b>Radial Arrays</b>	<b>153</b>
5.1	Pencil Beam Radiation Pattern From a Radial Array of SIW LWAs	154
5.1.1	Introduction . . . . .	154
5.1.2	Design of the Radial Array . . . . .	157
5.1.3	Measured Results . . . . .	160
5.1.4	Conclusion . . . . .	167
5.2	Non-Uniform Sinusoidally Modulated HM-LWL for Near-Field Focusing . . . . .	169
5.2.1	Introduction . . . . .	169
5.2.2	Analysis of the Sinusoidally Modulated HMLWA . . . . .	172
5.2.3	Design of the Radial Array Lens . . . . .	177
5.2.4	Measured Results . . . . .	181
5.2.5	Conclusion . . . . .	190
<b>6</b>	<b>Conclusions</b>	<b>191</b>
<b>A</b>	<b>Appendix</b>	<b>195</b>
	<b>Bibliography</b>	<b>197</b>
	<b>Publications</b>	<b>227</b>
	<b>Acknowledgments</b>	<b>235</b>



# List of Figures

1	Fan aerial used by Marconi at Poldhu Point in Cornwall, UK, for transmissions to Newfoundland, CA. . . . .	xxx
1.1	Configuration of a SIW structure synthesized using metallic via-hole arrays [6, Fig. 3]. . . . .	4
1.2	TE <sub>10</sub> surface currents distribution of the rectangular waveguide with slots on the narrow walls. [6, Fig. 1]. . . . .	4
1.3	Transitions between printed transmission lines and SIW [2, Fig. 5]: a) Microstrip-to-SIW transition, based on a taper. b) Coplanar-to-SIW transition, based on a current probe. c) Coplanar-to-SIW transition, based on a 90° bend. . . . .	8
1.4	Two practical SIW circuits examples: a) an SIW inductive post filter with microstrip transitions, and b) an SIW 1:16 power divider with microstrip input/output interfaces [1, Fig. 4]. . . . .	9
1.5	Two examples of SIW active circuits: a) photograph of the fabricated amplifier in [42, Fig. 5], and b) photograph of the fabricated SIW mixer in [40, Fig. 5]. . . . .	10
2.1	Planar leaky-wave antennas: a) Menzel antenna, b) Thiele half-mode LWA, c) novel PLWA proposed in this thesis and d) slotted SIW. . . . .	15

2.2	Different views of the PLWA: a) Three dimensional view and main geometrical parameters of the proposed PLWA. b) Electric field lines at the cross section of the antenna ( $E$ -plane). . . . .	17
2.3	Curves for $\alpha/k_0$ and $\theta_{\text{RAD}}$ varying the distance between posts $P$ for several values of $W$ at 15 GHz. . . . .	20
2.4	Curves for $\alpha/k_0$ and $\theta_{\text{RAD}}$ varying the width of the SIW $W$ for several values of $P$ at 15 GHz. . . . .	21
2.5	Scheme of the novel PLWA including feeding lines. . . . .	22
2.6	Photograph of the five manufactured prototypes. . . . .	23
2.7	Measured $H$ -plane radiation diagrams at 15 GHz: a) Variation of the beamwidth $\Delta\theta$ for a constant pointing angle $\theta_{\text{RAD}} = 30^\circ$ . b) Variation of the pointing angle $\theta_{\text{RAD}}$ for a constant beamwidth $\Delta\theta = 10^\circ$ . . . . .	24
2.8	Measured $E$ -plane radiation diagram at 15 GHz, including co-polarization and cross-polarization for the LWA with $\theta_{\text{RAD}} = 30^\circ$ and $\Delta\theta = 10^\circ$ . . . . .	25
2.9	Measured and simulated $H$ -plane radiation diagrams at 15 GHz for each antenna: a) $\theta_{\text{RAD}} = 30^\circ$ and $\Delta\theta = 20^\circ$ . b) $\theta_{\text{RAD}} = 10^\circ$ and $\Delta\theta = 10^\circ$ . c) $\theta_{\text{RAD}} = 30^\circ$ and $\Delta\theta = 10^\circ$ . d) $\theta_{\text{RAD}} = 30^\circ$ and $\Delta\theta = 5^\circ$ . e) $\theta_{\text{RAD}} = 50^\circ$ and $\Delta\theta = 10^\circ$ . f) Levels of co-polarization and cross-polarization for $\theta_{\text{RAD}} = 30^\circ$ and $\Delta\theta = 10^\circ$ . . . . .	26
2.10	Measured S parameters: a) Variation of the pointing angle $\theta_{\text{RAD}}$ for a constant beamwidth $\Delta\theta = 10^\circ$ . b) Variation of the beamwidth $\Delta\theta$ for a constant pointing angle $\theta_{\text{RAD}} = 30^\circ$ . . . . .	27
2.11	Measured and simulated frequency dispersion of $\theta_{\text{RAD}}$ and gain for the antenna with $\theta_{\text{RAD}} = 30^\circ$ and $\Delta\theta = 10^\circ$ at 15 GHz. . . . .	28
3.1	a) Scheme of the novel SIW LWA with its main geometrical parameters. b) Associated TEN of the cross section of the SIW LWA. . . . .	33

3.2	a) Scheme of TE plane-wave incidence on a row of periodic metallic posts. b) Equivalent T-circuit model proposed by Marcuvitz [89, pp. 285–289]. . . . .	35
3.3	Equivalent T network reactances as function of $P$ for $\theta_{\text{INC}} = 30^\circ$ . . .	36
3.4	Response of the reflexion coefficient as function of $P$ for several incident angles: a) magnitude and b) phase. . . . .	38
3.5	a) Normalized phase constant. b) Normalized leakage rate as function of frequency and different values of $P$ . . . . .	40
3.6	a) Pointing angle of the main beam. b) Normalized leakage rate as function of the separation between posts $P$ and for different widths $W$ . . . . .	42
3.7	a) Pointing angle of the main beam and b) normalized leakage rate as function of the width $W$ and for different separation between posts $P$ . . . . .	43
3.8	Dispersion curves as function of the radiating strip width $W_0$ for SIW leaky mode and higher-order channel-guide leaky modes. . .	45
3.9	Detail of coupling effect between SIW and channel leaky modes as function of the radiating strip width $W_0$ . . . . .	46
3.10	a) Pointing angle of the main beam and b) normalized leakage rate as function of the radiating strip width $W_0$ and for different separation between posts $P$ . . . . .	47
3.11	Dependence on the polarization discrimination level with $W_0$ . . .	48
3.12	Effect over the leaky mode as the thickness of the substrate is increased. . . . .	49
3.13	Dependence on the polarization discrimination level with $h$ . . . .	50
3.14	Two-dimensional dispersion chart for SIW LWA, including in circles the dimensions of the five manufactured antennas in [91]. . .	51

3.15	Measured and simulated $H$ -plane radiation diagrams at 15 GHz: a) Variation of the beamwidth $\Delta\theta$ for a constant pointing angle $\theta_{\text{RAD}} = 30^\circ$ . b) Variation of the pointing angle $\theta_{\text{RAD}}$ for a constant beamwidth $\Delta\theta = 10^\circ$ . . . . .	53
3.16	Measured and simulated frequency scanning responses for the three antennas designed in [91] to radiate at $\theta_{\text{RAD}} = 50^\circ, 30^\circ$ , and $10^\circ$ at the frequency of 15 GHz. . . . .	54
4.1	a) Holography concepts. b) Scheme of modulated SIW antenna. . .	59
4.2	Transverse equivalent network with its associated lumped elements for the SIW LWA. . . . .	62
4.3	Synthesis procedure for obtaining $W$ and $P$ given the rest of de- sign parameters. . . . .	64
4.4	a) Modulated LW aperture functions. b) Modulated dimensions. c) Layout and d) manufactured prototype of reduced SLL SIW antenna. . . . .	66
4.5	Measured $S$ -parameters for the SIW antenna with reduced SLL and pointing at $30^\circ$ for the design frequency of 15 GHz. . . . .	67
4.6	a) Objective and measured radiation pattern of reduced SLL SIW antenna for the design frequency of 15 GHz. b) Comparison with a measured non-modulated SIW LWA. . . . .	69
4.7	a) Modulated LW aperture functions and b) modulated dimen- sions for broadbeam SIW antenna. . . . .	70
4.8	Measured $S$ -parameters for the SIW antenna with broadbeam for the design frequency of 15 GHz. . . . .	71
4.9	Objective and measured radiation pattern of broadbeam SIW an- tenna for the design frequency of 15 GHz. . . . .	72
4.10	a) Modulated LW aperture functions and b) modulated dimen- sions for broadbeam SIW antenna with radiation null. . . . .	73

4.11 Measured $S$ -parameters for the SIW antenna combining a broad-beam pattern with a radiation null. . . . .	74
4.12 Objective and measured radiation pattern of broadbeam SIW antenna with radiation null for the design frequency of 15 GHz. . . .	74
4.13 a) Modulated LW aperture functions and b) modulated dimensions for SIW antenna with near-field focusing pattern. . . . .	76
4.14 a) Objective and b) measured near-field pattern for focused SIW antenna for the design frequency of 15 GHz. . . . .	77
4.15 Measured $S$ -parameters for the SIW antenna with near-field focusing pattern for the design frequency of 15 GHz. . . . .	78
4.16 Scheme of the conformal tapered SIW LWA and its lateral view. .	81
4.17 Geometrical variation of the main angles for a conformal LWA of length $L_A = 10\lambda_0$ over a cylindrical surface with radius $R = 15\lambda_0$ and radiating at $\theta_{RAD} = 45^\circ$ for the design frequency of 15 GHz. .	84
4.18 Conformal LWA of length $L_A = 10\lambda_0$ : a) quasi-uniform amplitude aperture illumination function, and b) tapered scanning angle and leakage rate along the antenna length. . . . .	85
4.19 Conformal tapered HMLWA: a) modulation of $W$ along the antenna length, b) corresponding layout for the tapered HMLWA, and c) synthesized and objective leaky-mode's tapering functions at 15 GHz. . . . .	87
4.20 Conformal tapered SIW LWA: a) modulation of the width $W$ and distance between posts $P$ along the antenna length, b) corresponding layout for the tapered SIW LWA, and c) synthesized and objective leaky-mode's tapering functions at the design frequency of 15 GHz. . . . .	89
4.21 Photographs of the conformal antenna over a foam panel and the set-up used for measuring its radiation pattern. . . . .	91

4.22	Theoretical, simulated and measured radiation patterns at the design frequency of 15 GHz for the conventional rectilinear HMLWA.	92
4.23	Theoretical, simulated and measured radiation patterns at the design frequency of 15 GHz for the conformal non-tapered HMLWA.	93
4.24	Theoretical, simulated and measured radiation patterns at the design frequency of 15 GHz for the conformal tapered HMLWA. . .	94
4.25	Theoretical, simulated and measured radiation patterns at the design frequency of 15 GHz for the conformal tapered SIW LWA. . .	95
4.26	Near-field radiation patterns for the designed: a) non-tapered rectilinear HMLWA, b) non-tapered conformal HMLWA, and c) tapered conformal LWA, with an antenna length of $L_A = 10\lambda_0$ at the design frequency of 15 GHz. . . . .	96
4.27	Measured radiation patterns at the design frequency of 15 GHz for the conformal designs of a non-tapered HMLWA, tapered HMLWA and tapered SIW LWA. . . . .	97
4.28	Measured radiation patterns for the conformal tapered SIW LWA for a range of frequencies from 14 GHz to 18 GHz. . . . .	98
4.29	Measured and simulated frequency scanning response of the radiation angle $\theta_{\text{RAD}}$ for the conformal tapered SIW LWA. . . . .	99
4.30	Measured and simulated frequency dispersion of the peak gain for the conformal tapered SIW LWA. . . . .	100
4.31	Measured and simulated S-parameters for the range of frequencies from 12 GHz to 18 GHz for the conformal tapered SIW LWA. . . .	100
4.32	Scheme of the single-layer filter scanning at a prescribed angular $\theta_0$ and operating at a given central frequency $f_0$ . . . . .	103
4.33	Chebyshev angular filtering response as a function of filter length $L$ .	105
4.34	Flowchart for the synthesis of a quasi-elliptic bandpass filter. . . .	106
4.35	Synthesis of radiation nulls to increase the angular rejection. . . .	107

4.36	Tapering of leaky wave a) local pointing angle and b) local leakage rate for the synthesis of Chebyshev and quasi-elliptic angular responses. . . . .	109
4.37	a) Scheme of modulated SIW filter with $L = 20\lambda_0 = 400$ mm. b) Modulation of SIW dimensions to synthesize Chebyshev and quasi-elliptic angular responses. . . . .	110
4.38	a) Manufactured modulated SIW quasi-elliptic filter. b) Simulated propagating leaky-mode electric field. c) Measured far-field angular pattern at 15 GHz. d) Measured input matching and return loss.	111
4.39	Simulated near-field patterns in the $zy$ -plane radiated by the modulated SIW filters: a) Chebyshev design. b) Quasi-elliptic design. .	113
4.40	Measured far-field patterns at 15 GHz for Chebyshev and quasi-elliptic angular responses. . . . .	114
4.41	Measured angular gain patterns at different frequencies for the quasi-elliptic SIW filter design. . . . .	115
4.42	Measured and simulated bandpass filtering responses (gain versus frequency) for the quasi-elliptic SIW filter designed at 15 GHz and $\theta_0 = 30^\circ$ . . . . .	116
4.43	Angular-frequency dispersion curve of the leaky mode propagating in the designed SIW angular bandpass filter for the three different substrate's permittivities ( $\epsilon_r = 2.2, 4.5$ and $10$ ). . . . .	117
4.44	Measured angular bandpass filtering performance for the quasi-elliptic SIW filter design. Gain is represented by an intensity colorbar, $\theta$ (degrees) is in $x$ -axis, and frequency (GHz) is in $y$ -axis. .	119
4.45	Scheme of width-tapered microstrip leaky-wave lens (MLWL). . .	122
4.46	Tapering of leaky mode to synthesize a rectilinear LWL. . . . .	124
4.47	a) Microstrip leaky-mode dispersion with strip width $W$ at 15 GHz. b) Characteristic curve $\alpha/k_0 - \theta_{\text{RAD}}(W)$ for substrate with $H = 0.254$ mm and $\epsilon_r = 2.2$ . . . . .	125

4.48	Characteristic curves for MLWA ( $f = 15$ GHz, $H = 0.254$ mm, $\epsilon_r = 2.2$ ) and different designed leaky-wave lenses (LWL1 $L = 20\lambda_0$ , $z_F = 25\lambda_0$ , $y_F = 25\lambda_0$ , LWL2 $L = 7.5\lambda_0$ , $z_F = 8.8\lambda_0$ , $y_F = 6.2\lambda_0$ , LWL3 $L = 7.5\lambda_0$ , $z_F = 9.3\lambda_0$ , $y_F = 4.3\lambda_0$ ). . . . .	127
4.49	Tapering of MLWA width $W(z)$ ( $f = 15$ GHz, $H = 0.254$ mm, $\epsilon_r = 2.2$ ) to synthesize a LWL with $L = 7.5\lambda_0$ , $z_F = 9.3\lambda_0$ , $y_F = 4.3\lambda_0$ . . . . .	128
4.50	a) MLWL embedded in parallel plates. b) Leaky-mode electric field lines. c) Field plot [186] for $S = 8$ mm, $W = 4.5$ mm, $f = 15$ GHz, $H = 0.254$ mm, $\epsilon_r = 2.2$ . . . . .	130
4.51	Photograph of fabricated width-modulated MLWL and parallel plates near-field measurement set-up. . . . .	131
4.52	a) Theoretical, b) simulated (HFSS) and c) measured focusing pattern for the single MLWL at 15 GHz. . . . .	133
4.53	Simulated and measured matching for single lens and array of two MLWLs. . . . .	134
4.54	a) Theoretical, b) simulated (HFSS) and c) measured time-varying near fields for the single MLWL at 15 GHz. . . . .	135
4.55	Scheme of two MLWLs placed front-to-front. . . . .	136
4.56	Measurement set-up for the array configuration. . . . .	137
4.57	a) Theoretical, b) simulated (HFSS) and c) measured focusing pattern and corresponding time-varying near-fields for the array of two MLWLs at 15 GHz. . . . .	138
4.58	Comparison between theoretical focusing patterns of single and array of two MLWLs at 15 GHz, obtained from leaky-mode theory. . . . .	138
4.59	Theoretical and measured a) axial and b) transverse cuts at 15 GHz. . . . .	139
4.60	Measured frequency scanning of the focusing region around the design frequency a) single MLWL b) array of two MLWLs. . . . .	140

4.61	Measured a) axial and b) transverse cuts as frequency is varied for the array of two MLWLs. . . . .	141
4.62	Variation of focal length, depth and width with frequency for the array of two MLWLs. . . . .	142
4.63	Scheme of leaky SIW radiating inside the integrated substrate: a) Uniform SIW and b) Modulated SIW with near-field focusing. .	146
4.64	Frequency-dispersion of the leaky mode for a uniform SIW. . . . .	148
4.65	Near-field distributions in the $zy$ -plane for 11 GHz, 14 GHz and 17 GHz: a) Uniform SIW and b) Modulated SIW. . . . .	149
4.66	Scheme of the proposed TEN for the SIW multiplexer. . . . .	150
4.67	Tapered dimensions ( $W$ and $P$ ) as function of the radiating length for the modulated SIW multiplexer. . . . .	150
4.68	Near-field distributions along the $z$ -axis for $y = D = 60$ mm as frequency is varied: a) Uniform SIW and b) Modulated SIW. . . . .	151
4.69	Near-field frequency response for $y = D = 60$ mm at the sampling positions $z_0$ : a) Uniform SIW and b) Modulated SIW. . . . .	152
5.1	Scheme of a) radial array. b) SIW LWA element. . . . .	156
5.2	Leaky mode dispersion ( $\beta/k_0$ and $\alpha/k_0$ ) as function of $W$ and different values of $P$ . . . . .	159
5.3	Synthesis procedure for obtaining broadside radiation ( $\alpha/k_0 = \beta/k_0$ ), as function of $W$ and $P$ , the 1D SIW LWA length $L_A$ and its associated array directivity $D_A$ . . . . .	160
5.4	Top photographic view of the manufactured radial array for an antenna length $L_A = 3\lambda_0 = 60$ mm and a total radius $R = 73$ mm. . . . .	161
5.5	Three dimensional view of the radiation pattern formed by $N = 8$ SIW LWAs of length $L_A = 3\lambda_0$ for the design frequency of 15 GHz. . . . .	162
5.6	$\vec{E}$ field polarization arrangement for each element of the array (black arrows), and resulting array polarization (red arrow). . . . .	163

5.7	Simulated electric field vector, $E(x,y,z)$ (V/m), over the array: a) time phase = $0^\circ$ and b) time phase = $180^\circ$ . . . . .	164
5.8	Measured and simulated radiation patterns: a) co-pol component ( $E_\phi$ ) at $H$ -plane ( $\phi = 90^\circ$ ), and b) X-pol component ( $E_\theta$ ) at $H$ - plane ( $\phi = 90^\circ$ ). . . . .	164
5.9	Measured and simulated radiation patterns for the co-pol compo- nent ( $E_\theta$ ) and X-pol component ( $E_\phi$ ) at $E$ -plane ( $\phi = 0^\circ$ ). . . . .	165
5.10	Measured and simulated gain values for the frequency range from 14.5 GHz to 15.5 GHz. . . . .	166
5.11	Measured and simulated $ S_{11} $ -parameter for the radial array of SIW LWAs, radiating broadside at the design frequency of 15 GHz. . . . .	168
5.12	Scheme of the sinusoidally modulated HMLWA with a non-uniform taper performed to control in amplitude and phase the backward radiated waves. . . . .	171
5.13	Top view for two different variations of the HMLWA with their main geometrical parameters: a) conventional HMLWA, and b) si- nusoidally modulated HMLWA. . . . .	174
5.14	Two-dimensional dispersion chart at the design frequency of 15 GHz for the leakage rate $\alpha$ and the radiation angle $\theta_{\text{RAD}}$ of the $n = -1$ space harmonic of the sinusoidally modulated HMLWA. . . . .	175
5.15	Synthesis of a near-field focusing pattern at a focal distance $z_F =$ $5.5\lambda_0 = 110$ mm for a 1-D HMLWA with length $L_A = 6\lambda_0 =$ 120 mm at the design frequency of 15 GHz. a) Tapering along the antenna length of $\theta_{\text{RAD}}$ and $\alpha/k_0$ . b) Corresponding near-field pattern for the illustrated variation of the leaky mode. . . . .	176
5.16	Tapering along the antenna length of the width of the HMLWA to synthesize a near-field focusing pattern at the design frequency of 15 GHz. . . . .	177

5.17	Simulated near fields for two symmetrically fed HMLWAs with a tapered illumination function at the design frequency of 15 GHz. . . . .	178
5.18	Scheme of the 3-D near-field focusing system consisting of a radial array with 8 sinusoidally modulated HMLWAs. . . . .	179
5.19	$E$ -field polarization arrangement for each element of the array (red arrows), and resulting array polarization (black arrow). . . . .	180
5.20	Simulated near-fields for the designed radial array of 8 sinusoidally modulated HMLWAs at the design frequency of 15 GHz. . . . .	181
5.21	Detailed view of the employed coaxial feeding with some of its main geometrical parameters: $R_0 = 13$ mm, $d = 0.5$ mm, $d_0 = 1$ mm and $h = 1.57$ mm. . . . .	182
5.22	Top photographic view of the manufactured prototype of the radial array with $N = 8$ sinusoidally modulated HMLWAs. . . . .	182
5.23	Photographs of the near-field measurement setup used for the radial array. . . . .	183
5.24	Measured and simulated transverse cuts along $\rho$ for the focal height $z_F = 110$ mm at the plane $\phi = 0^\circ$ . . . . .	184
5.25	Measured and simulated transverse cuts along $\rho$ for the focal height $z_F = 110$ mm at the plane $\phi = 45^\circ$ . . . . .	185
5.26	Measured and simulated transverse cuts along $\rho$ for the focal height $z_F = 110$ mm at the plane $\phi = 90^\circ$ . . . . .	186
5.27	Measured and simulated axial cuts along $z$ -axis at the center position $\rho = 0$ . . . . .	186
5.28	Near-field plane at the focal height $z_F = 110$ mm for the design frequency of 15 GHz: a) simulated and b) measured. . . . .	187
5.29	Near-field plane at $\phi = 0^\circ$ along the $z$ -axis for the design frequency of 15 GHz: a) simulated and b) measured. . . . .	188
5.30	Measured and simulated input matching for the radial array of $N = 8$ sinusoidally modulated HMLWAs. . . . .	189



# List of Tables

2.1	Physical Dimensions for Three Planar LWAs With Different Beamwidths and a Constant Pointing Angle ( $\eta_{\text{RAD}} = 90\%$ ) . . . . .	23
2.2	Physical Dimensions for Three Planar LWAs With Different Pointing Angles and a Constant Beamwidth ( $\eta_{\text{RAD}} = 90\%$ ) . . . . .	23
4.1	Relation between angular rejection and filter length. . . . .	105



# Introduction

Wireless communication systems are based on the transfer of information without the necessity of being connected by a physical link. First transatlantic transmission was performed on the 12th December 1901 by Marconi (see Fig. 1) between Poldhu, United Kingdom, and Newfoundland, Canada, demonstrating the capability to transmit electromagnetic waves over large distances. Since then, communications systems have experienced a tremendous growth with the development of new applications and devices. In addition to all subsystems involved in a communication system, a key part of them is related to the ability to transmit the energy in a suitable manner. Therefore, it is necessary a device that allows the conversion of electric power into electromagnetic waves. The device that performs such a conversion is known as antenna, and basically works by creating time-varying magnetic and electric fields around the antenna elements that radiate away into space as a moving electromagnetic wave.

A large variety of antennas have been designed over the years attending to a wide range of applications. An example of this are the leaky-wave antennas (LWAs). This type of antennas is based on the leakage of energy along a transmission line, and due to the features of their radiation mechanism they are also known as travelling-wave antennas. Earliest examples of LWAs were proposed in conventional waveguide technology, and later their radiation principles have been extended to almost any type of transmission line.

One of the main reasons because LWAs have received much attention over the years, is their capability to combine in one single device the radiating element

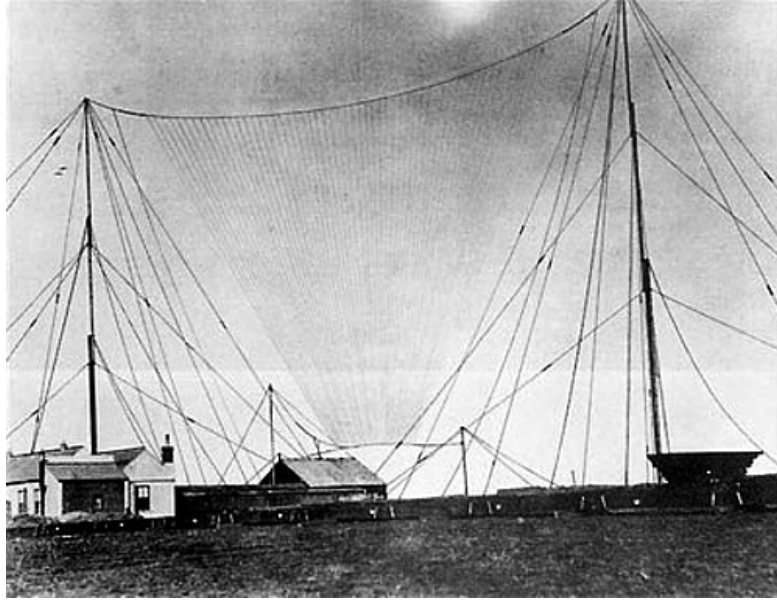


Figure 1: Fan aerial used by Marconi at Poldhu Point in Cornwall, UK, for transmissions to Newfoundland, CA.

with the transmission line. In this manner, they can be easily fed and integrated with other devices. This integration has been even more evident with the rise of the printed circuit board technology, which has allowed that most of the subsystems involved in a communication system can be integrated in a single substrate. Moreover, the development of new applications, e.g. collision avoidance systems, and their extension to consumer electronics have made possible to maintain the interest in this kind of antennas.

The radiation properties of the LWAs are mainly determined by the complex propagation constant ( $k = \beta - j\alpha$ ) of the leaky mode travelling along the antenna. For that reason, the radiation pattern provided by the antenna varies with the frequency. This property is inherent to most of LWAs, which makes them very interesting for scanning applications, such as radars. However, for point-to-point communications this dependence on the frequency is usually a drawback because the bandwidth of the antenna is limited to a range over which the beamwidth does not drop more than 3 dB respect to the maximum gain. Moreover, depending

on if the phase constant  $\beta$  is greater or smaller than the free-space wavenumber  $k_0 = 2\pi/\lambda_0$ , the leaky mode can behave as a “fast wave” ( $\beta/k_0 < 1$ ) and thus radiate or as a “slow wave” ( $\beta/k_0 > 1$ ) and be bounded inside the transmission line. Another important characteristic of the LWAs is that by suitably controlling its leakage rate  $\alpha$ , they can be designed to efficiently illuminate large radiating apertures and therefore providing high directivities. Additionally, due to the guided modes are responsible for the radiation, the analysis can be usually performed with efficient modal tools, such as transverse equivalent networks, which typically provide a better insight into the structure.

LWAs can be divided into two main categories attending to the geometry of the guiding structure. In particular, whether the geometry is uniform along its propagation length, the structure can be classified as a uniform LWA, whereas if the geometry is periodically modulated, the structure is defined as a periodic LWA. The fundamentals for both types of LWAs are similar, being the main difference between them that periodic LWAs can be analyzed as an infinite superposition of Floquet’s space harmonics,  $n = \dots, -1, -2, 0, 1, 2, \dots$ . As a result of the excitation of these space harmonics, periodic LWAs can be designed to radiate backward with a suitable choice of the structure’s period. Moreover, periodic LWAs can show a scanning range from backward to forward contrary to uniform LWAs which can only scan in the forward region. In order to obtain this backward to forward scanning capability, periodic LWAs are usually designed to operate with the  $n = -1$  space harmonic which requires to set the rest of space harmonics in the slow wave region to avoid multiple beams.

## Motivation

The main motivation to perform this doctoral thesis has been to design a new type of leaky-wave antenna in planar technology, with the capability to independently determine both the phase constant and the leakage rate of the leaky mode. Although a large variety of designs have already been proposed in different planar

technologies, such as microstrip and coplanar, no flexible control over the complex propagation constant has been reported so far. The importance of obtaining such flexible control resides in the capability to synthesize arbitrary illumination functions at the aperture of the antenna. These fields radiated at the aperture determine the radiation pattern of the antenna, and they can be directly related to the guided leaky mode. Therefore, a wide range of non-conventional radiation patterns can be synthesized by properly tapering the leaky mode along the structure.

With the purpose of solving this lack of flexibility in previous planar designs, the recently proposed technology of substrate integrated waveguide (SIW) has been used due to its main characteristics of low-profile, low losses, and high isolation. In this manner, a conventional SIW structure has been modified in order to allow the radiation of the guided mode within the SIW, moreover, by means of a flexible control over the phase constant and the leakage rate of this guided mode an effective control over the radiated fields has been obtained. Several examples have been designed to validate the theoretical concepts developed along this thesis. In particular, the synthesis of non-conventional radiation patterns both in near and far field has been obtained. Moreover, the proposed SIW LWA has been analyzed with a modal tool specifically developed to this aim, which allows the computation of the complex propagation constant as function of the main geometrical parameters of the structure.

## Outline

In order to cover the most important aspects related to the analysis and design of leaky-wave devices in planar technology. This thesis has been divided into six chapters. In particular, it has been dealt with the bases of the SIW technology, the analysis of a novel 1-D leaky-wave antenna in SIW technology, the development of a modal tool based on a transverse equivalent network of the structure, the design of several prototypes with non-conventional radiation patterns radiating both inward and outward of the substrate, and a radial array configuration to obtain

a pencil beam radiation pattern in the far-field region and a similar configuration but designed to obtain 3-D near-field focusing. Moreover, due to the modified SIW structure used in this thesis can be considered as a 1-D leaky-wave line source, its theoretical radiated fields have been included in Appendix A.

Next, a brief summary with the content of the different chapters is shown.

In Chapter 1 the bases of the technology of substrate integrated waveguide are addressed. Concretely, a brief review of the main characteristics of this technology, including equivalent width compared to conventional rectangular waveguides and computation of its material losses, has been described. Also, the most common transitions used to connect SIWs with other planar transmission lines, such as microstrip and coplanar, are outlined. Finally, some of the main applications that have already been reported for SIW devices are summarized.

Chapter 2 describes the operation principle of a new kind of leaky-wave antenna in substrate integrated waveguide technology. Particularly, the characterization of the radiation mechanism and the control of the leaky mode are described. In order to validate the proposed SIW LWA, several prototypes have been manufactured and measured. Moreover, the results have been compared with full-wave simulations of the complete structure. Also, the feeding mechanism used to connect the SIW with a conventional microstrip line is described.

In Chapter 3 a modal tool based on the transverse resonance analysis of the SIW LWA cross section is described. To this aim, the different elements that form the transverse section of the SIW have been characterized. The rows of metallic posts that delimit the width of the SIW have been modeled by an equivalent impedance obtained from an analysis of TE plane wave incidence, and the discontinuity of the dielectric filled parallel-plate waveguide with truncated upper plate has been characterized by a radiation impedance valid for electrically thin substrates. By arranging all these elements that constitute the SIW LWA cross section, a transverse equivalent network can be formed and a modal analysis can be used to compute the leaky mode as function of the main geometrical parameters

of the antenna.

Chapter 4 shows the synthesis of several designs of tapered planar leaky-wave devices radiating both in the free space and inside the substrate. With this purpose, the modal tool developed in Chapter 3 is used. In Section 4.2 the use of conformal antennas has been studied, moreover, several applications such as an angular bandpass filter in Section 4.3, near-field focusing inside a parallel-plate waveguide in Section 4.4, and a quasi-optical multiplexer in Section 4.5 have been developed, including the manufacture and measure of the prototypes.

In Chapter 5 two array designs of 1-D LWAs radially arranged around a central feeding are presented. Firstly, in Section 5.1 is shown an array of eight 1-D SIW LWAs that provides a pencil beam radiation pattern pointing at broadside thanks to the fulfillment of the splitting condition ( $\alpha = \beta$ ), and secondly, a non-uniform sinusoidally modulated half-mode microstrip structure with application to near-field focused leaky-wave radiation in the backward Fresnel zone is proposed in Section 5.2.

Finally, the main conclusions achieved along this thesis are summarized in Chapter 6, and a list with the most relevant publications that have been generated during this thesis has been added in the last section.

# **Chapter 1**

## **Bases of Substrate Integrated Waveguide Technology**

### **1.1 Introduction**

In this chapter, the main characteristics of substrate integrated waveguide (SIW) technology are addressed. Moreover, some of its main applications, which have already been reported for SIW devices, are also introduced. However, some aspects dealt along this chapter have been only briefly discussed and may be completed with other works about SIW, such as [1] and [2].

Conventional rectangular waveguide (RWG) technology has characteristics of low cost and high performance. For that reason, it is still the mainstream in the design of radio frequency systems [1], [3]. But despite being a very mature technology, is not well suited to the requirements of mass-production, because it requires great effort of assembly. Moreover, the volume and weight of the devices cannot be easily reduced to fit arbitrary requirements [1].

On the other hand, planar technologies have characteristics of low-profile and easiness of manufacture, but they typically show significant limitations such as high losses and low quality-factor. Therefore, microwave circuits frequently inte-

grate both technologies to take advantage of the best performance of each one.

With the aim of overcoming the previous drawbacks, a new generation of high-frequency circuits called as substrate integrated circuits (SICs) has been recently proposed [1]. The basis of the SICs is to integrate non-planar structures into a dielectric substrate. This new concept unifies integration of planar and non-planar circuits in the same substrate. Despite the recent apparition of the SICs, technologies based on this concept, such as the substrate integrated waveguide (SIW), have become very popular due to their similar performance to RWG counterparts.

First designs of SIW devices were known as post-wall waveguide [4] and laminated waveguide [5], and they were proposed as feeding networks in antenna arrays. Later, a large variety of applications have been developed by using this concept [2]. SIW structures mainly consist of a dielectric filled parallel-plate waveguide, which has two rows of metallic via-holes that act as the electric side-walls in RWGs. Thus, most of the components can be performed using the same standard process as in PCB technology [1]–[3]. The resulting structure shows similar electrical properties to those of the RWGs. Likewise, the design techniques used for modeling RWG devices can be successfully applied to design SIW components [2].

Although SIW devices have better loss characteristics than their counterparts in planar technologies, the use of dielectric materials, which have inherently material losses, reduces the quality-factor of the SIW compared to RWG [1]–[3]. Nonetheless, it is still better than the obtained in conventional planar technologies such as microstrip and coplanar. Therefore, it enables the design of components with high quality-factor, whereas using a manufacturing technique of low cost. In addition, the flexibility to use different substrates allows SIW devices to be integrated with other existing planar components.

## 1.2 Characteristics of the SIW

The integration of RWGs with planar circuits is often difficult and requires of a process with high precision machinery. A practical solution is to use a SIW instead of the RWG. In this manner, all the microwave components can be integrated in a single substrate, thus reducing the losses because of transitions or coupling areas. Moreover, it has the advantage that the circuits, including transitions and SIWs can be manufactured using a standard PCB process, which makes easier their manufacture. However, this integration also reduces the quality-factor compared to RWG devices, because of the higher losses of the dielectric substrate and the smaller volume of the SIW.

SIWs are usually implemented by placing two rows of metallic posts into a dielectric substrate. Fig. 1.1 shows an example for a SIW with the following main parameters:  $w$  distance between rows,  $s$  separation between posts and  $d$  diameter of the posts. The spacing  $s$  must be kept small enough to reduce losses between adjacent posts. The diameter of the posts  $d$  is also relevant to evaluate the losses of the structure, since the ratio  $s/d$  is considered more critical than the length of the spacing [6]. According to this, the following rules can be considered in order to reduce the losses in a SIW [7]:

$$d < \frac{\lambda_g}{5} \quad (1.1)$$

$$s \leq 2d \quad (1.2)$$

These conditions are sufficient but not necessary and larger diameters or separations could be used with caution. However, they ensure a minimum level of radiation, therefore, it is important to stay close to these conditions with the aim of getting optimal performance for the SIW.

SIW devices show similar modal solutions for the propagating modes than those of RWGs. In this manner, the fundamental mode in SIWs is equivalent to the  $TE_{10}$  of RWGs. However, due to the discontinuities along the propagation

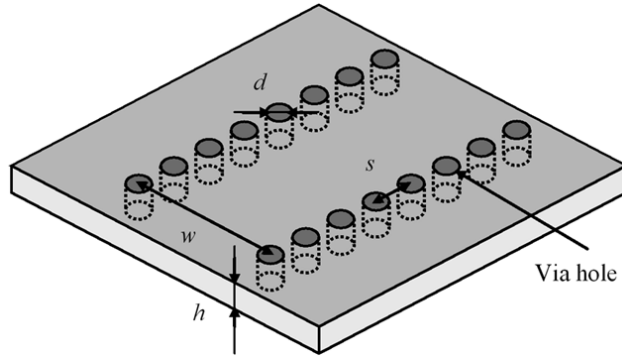


Figure 1.1: Configuration of a SIW structure synthesized using metallic via-hole arrays [6, Fig. 3].

direction only  $TE_{n0}$  modes are supported. This phenomenon is caused by the separation between posts, which interrupts the continuity of the currents for TM modes and does not allow their propagation [6]. On the other hand, the current distribution for  $TE_{n0}$  modes is not cut by the spaces between posts and thus these modes are supported by SIWs. This effect can be clearly observed by the  $TE_{10}$  surface currents distribution of the rectangular waveguide with slots on the narrow walls showed in Fig. 1.2.

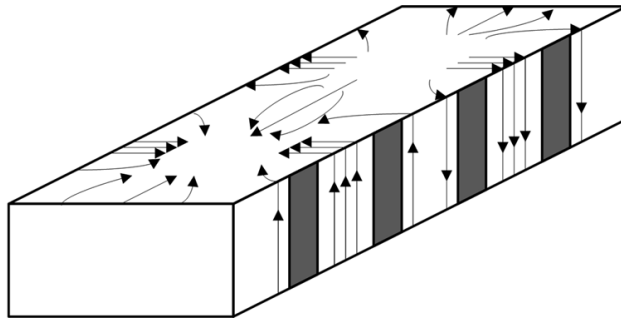


Figure 1.2:  $TE_{10}$  surface currents distribution of the rectangular waveguide with slots on the narrow walls. [6, Fig. 1].

As a result of the similar modal solutions between SIW and RWG, several empirical relations have been proposed to obtain an equivalent width for the SIW and RWG. In [8] a practical relation for obtaining the equivalent width of the SIW

was derived by using the BI-RME method:

$$w_{\text{eff}} = w - \frac{d^2}{0.95s} \quad (1.3)$$

where  $w_{\text{eff}}$  is the equivalent width for a RWG. Later, the relation in (1.3) was modified in [6]:

$$w_{\text{eff}} = w - 1.08 \frac{d^2}{s} + 0.1 \frac{d^2}{w} \quad (1.4)$$

In [9] an equivalence based on the calculation of the surface impedance at the cylinder wall was proposed and afterward refined in [10]:

$$w = \frac{2w_{\text{eff}}}{\pi} \cot^{-1} \left( \frac{s}{2w_{\text{eff}}} \ln \frac{s}{2d} \right) \quad (1.5)$$

Although these equivalences provide a good approximation for practical cases of SIW structures, they still lack the flexibility for non-standard relations of  $s/d$ . To solve this drawback a full-wave analysis of the SIW can be performed, and therefore an accurate value for the propagation constant can be obtained in a wider range of values of  $s/d$ . To this aim, some techniques based on the finite-difference time domain method or the finite-difference frequency domain [11], the boundary integral-resonant mode expansion (BI-RME) method [12], the method of lines [13] and the transverse resonance method [14], [15] have been proposed. All previous methods have the advantage of using a unit cell analysis in order to determine the propagation constant of the SIW, which significantly reduces the computational effort.

The bandwidth of conventional SIW structures is similar to that of RWGs. In this manner, the cutoff frequency of the SIW is determined by its width  $w$ . A practical bandwidth for the fundamental mode  $\text{TE}_{10}$  is given from the cutoff frequency  $f_1 = (2w_{\text{eff}}\sqrt{\mu\epsilon})^{-1}$  of the  $\text{TE}_{10}$  to the cutoff frequency  $f_2 = 2f_1$  of the  $\text{TE}_{20}$  mode.

Another important characteristic of SIW structures is related to their losses

as transmission line. There are three main losses mechanisms involved in the analysis of the performance of a SIW structure [12]: dielectric losses  $\alpha_d$  (caused by the inherent dissipation of electromagnetic energy into it), conductor losses  $\alpha_c$  (as result from Joule heating of electrical currents in the conductors) and radiation losses  $\alpha_r$  (due to the gaps between posts which do not allow the electromagnetic energy to be entirely confined in the SIW cavity). Due to the similarities between RWGs and SIWs conductor and dielectric losses can be estimated from those of a RWG. In this manner, by using the relations given in [16, pp. 340, 351] these losses expressed in Np/m are determined by:

$$\alpha_d = \frac{k^2 \tan \delta_l}{2\beta} \quad (1.6)$$

$$\alpha_c = \frac{R_s}{\eta h \sqrt{1 - \frac{k_c^2}{k^2}}} \left( 1 + \frac{2h}{w_{\text{eff}}} \frac{k_c^2}{k^2} \right) \quad (1.7)$$

where  $\tan \delta_l$  is the dielectric loss tangent,  $\beta$  the phase constant along the propagation direction,  $R_s = \sqrt{\omega\mu/2\sigma}$  the surface resistance of the conductor with  $\sigma$  conductivity,  $\eta = \sqrt{\mu/\epsilon}$  the medium impedance,  $k_c = \pi/w_{\text{eff}}$  the cutoff wavenumber for the TE<sub>10</sub> mode and  $k = \omega\sqrt{\mu\epsilon} = k_0\sqrt{\epsilon_r}$  the wavenumber of the medium. From (1.7) it can be noticed that for a given ratio  $h/w_{\text{eff}}$ , the losses due to the conductor increase as  $h$  is smaller, thus the smaller guide dimensions, the larger attenuation. On the contrary, the dielectric losses only depend on the loss tangent and therefore they can be reduced with better quality substrates. With regard to the radiation losses  $\alpha_r$ , they can be minimized by decreasing the ratio  $s/d$ . Reasonably values for the radiation losses are obtained with ratios  $s/d \leq 2$  [7]. In general, it can be stated that the dielectric losses are predominant at mm-wave frequencies, when using conventional substrates [17].

On the other hand, it is convenient to compare losses in SIW devices with other planar structures, such as microstrip and coplanar lines, in order to analyze the real performance of SIW structures. However, it is difficult to obtain an objective comparative between them since a large number of factors are involved in the

losses calculation (e.g. thickness and permittivity). Likewise, the microstrip lines can be more convenient for some kind of substrates than the SIW and the coplanar. In [18] a comparative considering the losses of the different transmission lines was performed, showing that for mm-wave frequencies the SIW has comparable or lower losses than traditional planar transmission lines.

### 1.2.1 Transitions SIW

An important part of the SIW is related to its integration with other transmission lines. To this aim, several transitions between microstrip and coplanar transmission lines and SIW have been proposed [3], [19]. Typically, microstrip and coplanar lines are broadband and cover the entire usable bandwidth of the SIW. Fig. 1.3 shows three kinds of transitions that are widely used to connect a SIW with other printed transmission lines. In particular, a microstrip-to-SIW transition is shown in Fig. 1.3a, a coplanar-to-SIW transition in Fig. 1.3b and a coplanar-to-SIW transition based on a 90° bend in Fig. 1.3c. Microstrip-to-SIW transition is the most used topology due to the wide utilization of the microstrip line. This transition is based on a tapered microstrip line, which is connected directly to the SIW as shown in Fig. 1.3a. With the purpose of obtaining a fast implementation of this type of transition, design equations for taper dimensions have been developed in [20]. It is important to note that the use of thin substrates increases the conductor losses and therefore thicker substrates are preferred to minimize this effect. However, thick substrates also have the drawback that increase the losses in the microstrip line, therefore, coplanar transmission lines can be a better solution in these cases, and as result of it, the use of coplanar-to-SIW transitions as the ones shown in Figs. 1.3b and 1.3c can be required.

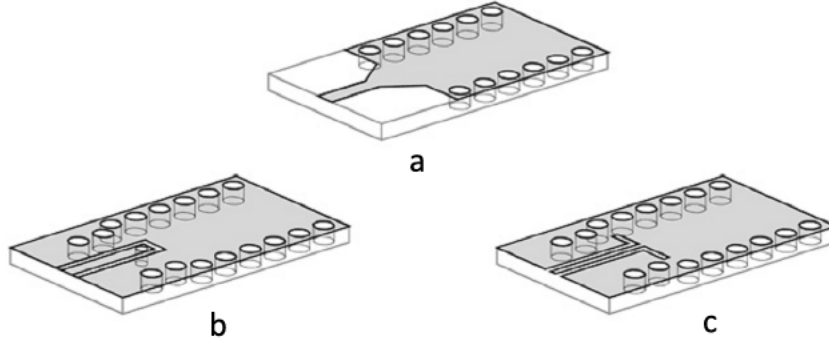


Figure 1.3: Transitions between printed transmission lines and SIW [2, Fig. 5]: a) Microstrip-to-SIW transition, based on a taper. b) Coplanar-to-SIW transition, based on a current probe. c) Coplanar-to-SIW transition, based on a 90° bend.

### 1.2.2 Applications of the SIW

Despite the recent emergence of the SIW technology [3], [4], a large number of applications have already been reported [2]. Most of them are based on their RWG counterparts, which it has allowed a fast implementation of SIW devices, such as antennas and both passive and active circuits. Some examples of SIW passive circuits are filters and couplers. In Fig. 1.4a is shown an example of SIW filter, which is formed by a conventional SIW and a row of inductive posts with different offsets [21]. The proposed filter has a bandwidth of 1 GHz for a center frequency of 28 GHz and an insertion loss of 1 dB. Another filter design was proposed in [22] for a SIW with irises operating at 60 GHz. Cavity filters with both rectangular [23] and circular [24] cavities have also been implemented in SIW. In [25] a multi-layered structure was designed to improve the performance of the filter and achieve an elliptic response in C-band. An electromagnetic band-gap structure was used in [26] to design compact super-wide-band filters.

Directional couplers are another example of passive devices that have been successfully designed in SIW technology. In [27] a design procedure to obtain different coupling rates was developed. Another design based on a cruciform structure and operating at 24 GHz was proposed in [28]. In addition to filters and

couplers, other examples such as diplexers [29], [30], magic-T [31], six-port circuits [32], [33] and circulators [34] have been also implemented in SIW. Another interesting SIW design was proposed in [35] to develop a low-cost and low-profile 1:N SIW power divider. Fig. 1.4b shows a prototype for 1:16 power divider, which provides less insertion losses than other planar alternatives. This divider can be used as power combiner for amplifier design or as feeder for antenna array.



Figure 1.4: Two practical SIW circuits examples: a) an SIW inductive post filter with microstrip transitions, and b) an SIW 1:16 power divider with microstrip input/output interfaces [1, Fig. 4].

Although SIW active circuits have received less attention than passive circuits, a large variety of designs including resonators, oscillators, mixers and amplifiers have also been implemented in SIW technology. In [36] a resonator manufactured with a conventional substrate provided a quality factor of 500. A 12.02 GHz oscillator was designed in [37] with a  $Q$  of 178. A push-push oscillator at 29.5 GHz based on a SIW resonator was presented in [38]. In [39] a tunable SIW resonator designed for X-band obtained an unloaded  $Q$  of 286 for a tuning range of 492 MHz. By combining coupling active devices with hybrid passive circuits, the capability to obtain mixers circuits in SIW technology have been demonstrated. In particular, an X-band single balanced diode mixer using a  $90^\circ$  hybrid was proposed in [40] (see Fig. 1.5b). Another design using the same topology was proposed in [41] for a 24 GHz automotive radar system-on-package front-end. An

X-band single-transistor amplifier with 9 dB gain and less than 2 dB ripple over the entire X-band was designed in [42] (see Fig. 1.5a). In [43] a Ka-band power combining amplifier based on SIW and half-mode SIW (HMSIW) technology was proposed. This device, which was designed to operate in the range from 33.5 GHz to 35.5 GHz providing a combining efficiency of 72% at 34.3 GHz, consists of an input N-way power divider, followed by N-parallel amplifier circuits and an N-way power combiner.

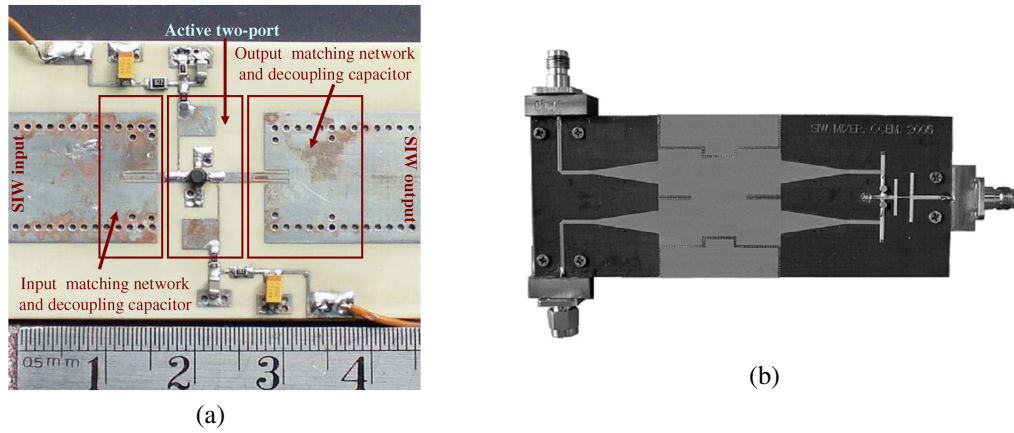


Figure 1.5: Two examples of SIW active circuits: a) photograph of the fabricated amplifier in [42, Fig. 5], and b) photograph of the fabricated SIW mixer in [40, Fig. 5].

In addition to the aforementioned SIW devices, a wide range of antennas have also been designed in SIW. As most of the other SIW components, these antennas have been based on their equivalent in other technologies. First designs were proposed from RWG antennas, e.g. a resonant array of longitudinal slots operating at X-band was designed in [44]. From the approach of travelling-wave antennas, a SIW antenna was proposed in [45]. Using the  $TE_{20}$  mode and radiating with the  $n = -1$  space harmonic a travelling-wave antenna was also designed in [46]. Based on the radiation mechanism of the microstrip first higher-order mode a leaky-wave antenna was proposed in [47]. This antenna has been developed in the course of this thesis and its performance is explained in detail along the next chapters.

Apart from the previous topologies, other antenna designs based on different radiation mechanisms have also been implemented in SIW. In [48] a modified version of the Vivaldi radiator was proposed for a center frequency of 36 GHz. Cavity-backed antennas have also been reported in several works [49]–[52] providing relatively high efficiency 70%. In [53] a dielectric loaded H-plane sectoral horn antenna was proposed. Moreover, SIW have been used to design feeding networks in multibeam applications. For example, in [54] a parabolic reflector was used to feed a multibeam array of longitudinal slots, in [55] a Rotman lens was designed to obtain a beam-forming network, a Blass matrix was proposed in [56], a leaky-wave slot array antenna fed by a dual offset Gregorian reflector system was proposed in [57], and a folded Butler matrix was used in [58].



## **Chapter 2**

### **1-D Leaky-Wave Line Source**

A novel planar leaky-wave antenna with flexible and independent control of its fundamental leaky-mode phase and leakage rate, is presented in this chapter. The proposed structure is based on a half-mode microstrip line which is loaded with an additional row of periodic metallic posts. The radiation mechanism is similar to the conventional microstrip leaky-wave antenna operating in its first higher-order mode, with the novelty that the leaky-mode leakage rate can be controlled thanks to the addition of the periodic metallic vias. In this way, it is demonstrated how the antenna pointing angle and main lobe beamwidth can be freely designed to obtain the desired high-directivity beam-scanning radiation pattern, while assuring high radiation efficiency. This total control over the leaky-mode complex propagation constant is obtained in a totally planar structure, providing a low-cost, low-profile, simple feeding, and easily integrable leaky-wave technology for high-gain beam-scanning applications. Several prototypes operating at 15 GHz have been designed, simulated, manufactured and tested, to demonstrate the operation principle and design flexibility of this leaky-wave antenna.

## 2.1 Introduction

Planar leaky-wave antennas (PLWAs) have been object of study in past decades due to their inherent capability to combine the characteristics of planar antennas (low profile, low-cost, and simplicity of integration with other planar circuits), with the performances of the LWAs (simple feeding, high directivity and frequency beam scanning capability) [59]–[81]. First attempts to achieve PLWAs were proposed in 1979 by Ermert [59] and Menzel [60] based on the radiation of the first higher order mode of the microstrip line. However, almost a decade passed until Oliner and Lee explained in detail the radiation mechanism of the PLWA based on the complex nature of the associated first higher order leaky-mode of the microstrip line [61]–[63]. Once the microstrip LWA (MLWA) could be accurately analyzed, many designs were performed [64], including more complex applications such as phased-arrays [65], [66], switch-controlled arrays [67], or active antennas [68]–[70] in MLWA technology. Fig. 2.1a shows the layout of a conventional MLWA, which is asymmetrically fed to excite the first higher order leaky mode. The electric field distribution of this mode at the microstrip cross section ( $E$ ) is plotted with continuous blue lines, and the equivalent magnetic currents radiating in the form of a space-wave from the microstrip line edges discontinuity are plotted with dotted red lines ( $M$ ).

Thiele et al. proposed a variation of the MLWA, called the half-mode MLWA (HMLWA) [71], [72] which is shown in Fig. 2.1b. As it can be seen, the width of the microstrip is reduced to half ( $W/2$  in Fig. 2.1), by using close shorting pins at one side of the microstrip line, which act as a perfect electric conductor (PEC) wall. The field lines of the operating leaky-mode and the radiating equivalent magnetic currents are also shown for this HMLWA in Fig. 2.1b. This topology has also the advantage of inherently suppressing the fundamental qTEM mode of the microstrip line, thus avoiding any undesired excitation of this nonradiating mode [61]–[63] which would result in a reduction of radiation efficiency. More-

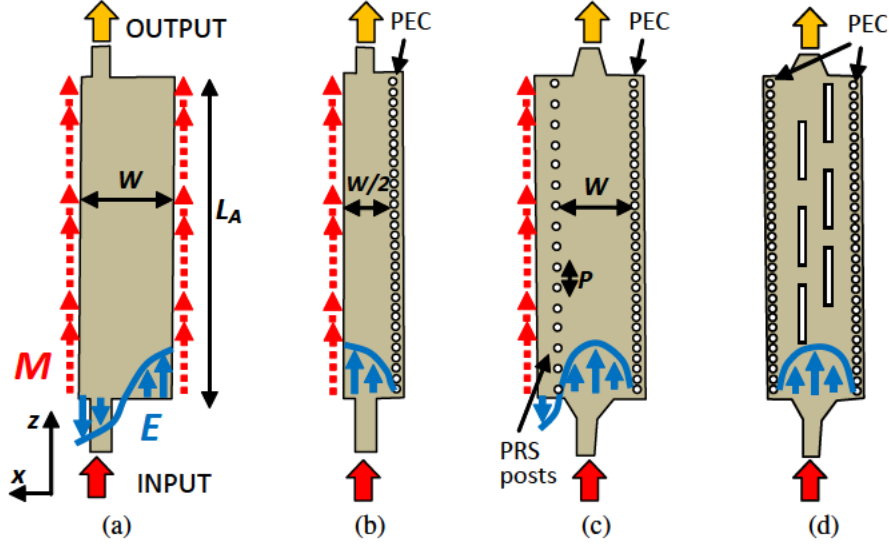


Figure 2.1: Planar leaky-wave antennas: a) Menzel antenna, b) Thiele half-mode LWA, c) novel PLWA proposed in this thesis and d) slotted SIW.

over, since the leaky mode is the fundamental mode in the HMLWA, the excitation becomes easier, and complicated feeding structures [64] are not needed anymore. Recently, some interesting designs have been proposed using this HMLWA technology [73]–[75]. Composite right-left handed microstrip lines (CRLH) have also been engineered to conceive “metamaterial” MLWAs [76]–[78]. These MLWAs are based on much more complicated periodic unit-cells to make the dominant microstrip mode become leaky, providing backward-to-forward scanning capability.

Nevertheless, the main drawback of all previous MLWAs is that the leaky-mode leakage rate  $\alpha$  and phase constant  $\beta$  cannot be independently controlled: once the substrate has been chosen, only the microstrip line width  $W$  (see Fig. 2.1) can be adjusted, resulting in a simultaneous change of the leaky-mode radiated main beam angle  $\theta_{\text{RAD}}$  and leakage rate. For this reason, the radiation efficiency  $\eta_{\text{RAD}}$  cannot be optimized for a given scanning angle and radiating length, resulting in low efficiency designs and in the generation of an unwanted reflected lobe (overall for short MLWAs). Many attempts have been made to reduce this reflected lobe in short MLWAs, such as the use of aperture coupled patches [65],

[79], [80], conducting poles [66], [67], or printed dipoles [81], located at the output end of the LWA in order to re-radiate the energy which could not be efficiently radiated by the leaky mode along the LWA length  $L_A$  (see Fig. 2.1). As it is well known, a versatile and efficient LWA is that one which allows an independent tune of the leaky-mode phase constant (which determines the scanning angle) and leakage rate (which together with the LWA length determines the radiation efficiency and the beamwidth) [82]. So far, this flexible control over the leaky-mode phase and leakage rate has only been achieved in LWAs in pure waveguide technology [82] or in hybrid topology which combines printed-circuits within a host waveguide [83]–[86].

In this chapter, a planar LWA which provides flexible control over the leaky-mode pointing angle and leakage rate is presented. In this manner, this flexible control over the leaky mode is achieved in pure planar technology, avoiding the use of bulky waveguides [82]–[86]. The scheme of the novel PLWA is shown in Fig. 2.1c. As illustrated, it is quite similar to the HMLWA (presenting a microstrip line with one row of PEC posts), with the addition of a second row of conducting vias separated a distance  $P$ , which behaves as an inductive partially reflective surface (PRS), as it will be explained in this thesis. The novel structure propagates a fundamental mode which is similar to the one propagating in substrate integrated waveguides (SIW) [3], and SIW-based slotted antennas [44], [87], [88] as the one shown in Fig. 2.1d. However, the radiation is not created by the resonant slots fed by the SIW guide as in [44], [87], [88], but it is due to the continuous radiation of the leaky mode, which leakage level can be controlled provided the PRS posts are conveniently spaced, as demonstrated in [6], [45]. The SIW LWA presented in [45], however, is different to the one presented in this chapter, since in [45] a lateral wave radiates from the open-end of the truncated substrate. Instead, the PLWA in Fig. 2.1c radiates in the form of a space leaky wave created in the microstrip lateral edge discontinuity, which is the same radiation mechanism than in conventional MLWAs [59]–[63] and HMLWAs [71]–[75].

The rest of the chapter is distributed as follows. Section 2.2 describes the working mechanism of the novel PLWA. Several designs are performed, manufactured and tested in Section 2.3 to illustrate the flexibility to control the pointing angle and the beamwidth with the proposed PLWA, while keeping high radiation efficiency and avoiding any unwanted reflected lobe. Finally, the conclusions of this chapter are summarized in Section 2.4.

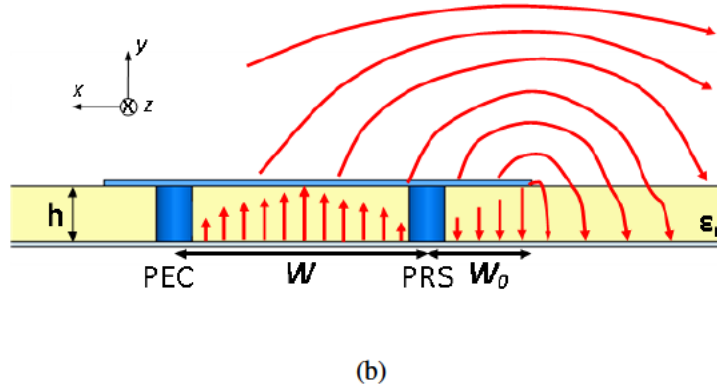
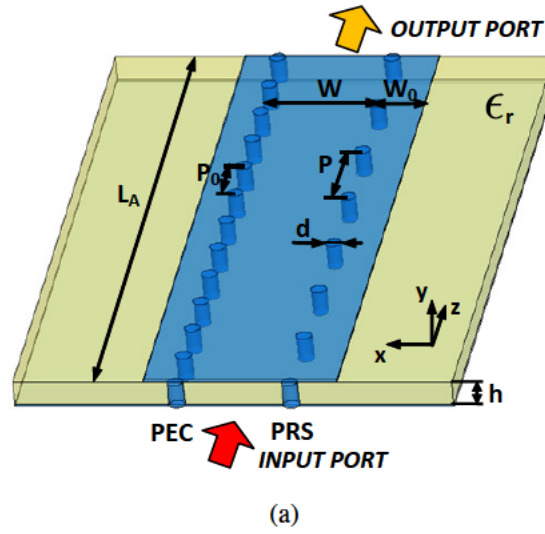


Figure 2.2: Different views of the PLWA: a) Three dimensional view and main geometrical parameters of the proposed PLWA. b) Electric field lines at the cross section of the antenna ( $E$ -plane).

## 2.2 Analysis of a LWA in Planar Technology

The PLWA proposed in this work is formed by a combination of printed circuit and via-holes, providing a completely planar structure integrated in a single substrate layer (see Fig. 2.2a). The structure has been designed to operate with the perturbed TE<sub>10</sub> leaky mode of the SIW [6] which is created between the PEC posts and the PRS posts separated a distance  $W$ . The radiation mechanism of a LWA is mainly defined by the leaky-mode complex longitudinal propagation constant [82]:

$$k_z = \beta - j\alpha \quad (2.1)$$

Concretely, the equivalent magnetic currents  $M$  created at the microstrip lateral edge, act as a line source in the  $z$ -axis (see Fig. 2.1c), and they are responsible for the high directivity in the  $H$ -plane ( $y$ - $z$  plane) while for the  $E$ -plane ( $x$ - $y$  plane) a typical fan beam is achieved [82]. This radiation mechanism is clearly observed with the distribution of the electric field lines represented in Fig. 2.2b, moreover, in this representation of the cross section of the LWA, it can also be seen the typical half-sine field pattern of the TE<sub>10</sub> mode travelling inside the SIW, and how some of the energy of the TE<sub>10</sub> mode is coupled into the parallel-plate waveguide section of length  $W_0$  which is finally responsible for the outward radiation. The amount of radiated power directly depends on the leakage rate  $\alpha$  and the LWA length  $L_A$ , and it determines the antenna radiation efficiency:

$$\eta_{\text{RAD}} = 1 - e^{-2\alpha L_A} = 1 - e^{-4\pi \frac{\alpha}{k_0} \frac{L_A}{\lambda_0}} \quad (2.2)$$

Typically  $\eta_{\text{RAD}} = 90\%$  is selected to allow a feasible control of the antenna illumination [82]. On the other hand, the efficiently illuminated LWA radiating length  $L_A$  and the pointing angle  $\theta_{\text{RAD}}$  determine the main beam width:

$$\Delta\theta \approx \frac{1}{\frac{L_A}{\lambda_0} \cos \theta_{\text{RAD}}} \quad (2.3)$$

where the scanning angle  $\theta_{\text{RAD}}$  is measured from the  $y$ -axis, and it depends on the leaky-mode phase constant  $\beta$ :

$$\sin \theta_{\text{RAD}} \approx \frac{\beta}{k_0} \quad (2.4)$$

For the proposed antenna, the control of  $\alpha$  and  $\beta$  can be easily performed by modifying the printed circuit parameters  $P$  and  $W$ , as it will be illustrated in Fig. 2.3 and Fig. 2.4. Once the substrate (thickness and permittivity) and the SIW width  $W$  have been chosen to set the leaky-wave regime in the desired frequency band, the period between posts  $P$  must be designed. For large values of  $P$ , the losses become non negligible and the transmission line suffers from radiation leakage [6]. In this case, the periodic conducting posts can be viewed as an inductive impedance [89, pp. 285–289], acting as a partially reflective surface (PRS) whose transparency can be controlled by the distance between posts  $P$ . On the contrary, the period  $P_0$  of the other row of via-holes must be chosen small enough to consider it like a perfect electric conductor (PEC) [6]. Fig. 2.3 and Fig. 2.4 shows the behavior of  $\alpha/k_0$  and  $\theta_{\text{RAD}}$  when  $P$  and  $W$  are varied. These results have been obtained for a frequency of 15 GHz in a lossless substrate with  $h = 1.57$  mm and  $\epsilon_r = 2.2$ , by using commercial full-wave simulator HFSS [90]. The rest of the printed-circuit parameters are kept constant to  $W_0 = 1.5$  mm,  $P_0 = 2$  mm and  $d = 1$  mm for all the designs. It must be highlighted that the width  $W_0$  of the edge microstrip section has to be less than  $\lambda/4$  in order to avoid the appearance of unwanted channel modes [82], which will reduce the overall performance of the antenna as it will be shown in detail in Section 3.3.3.

As it is shown in Fig. 2.3, higher values of  $P$  make the PRS more transparent independently on  $W$ , thus increasing the leakage rate  $\alpha/k_0$  from almost zero for  $P = 2$  mm to  $\alpha/k_0 = 0.04$  for  $P = 5$  mm. On the other side,  $W$  mainly controls the cutoff frequency of the perturbed  $\text{TE}_{10}$  mode of the SIW [6], therefore determining the leaky-mode phase constant  $\beta$  and the associated  $\theta_{\text{RAD}}$  (2.4) at a fixed

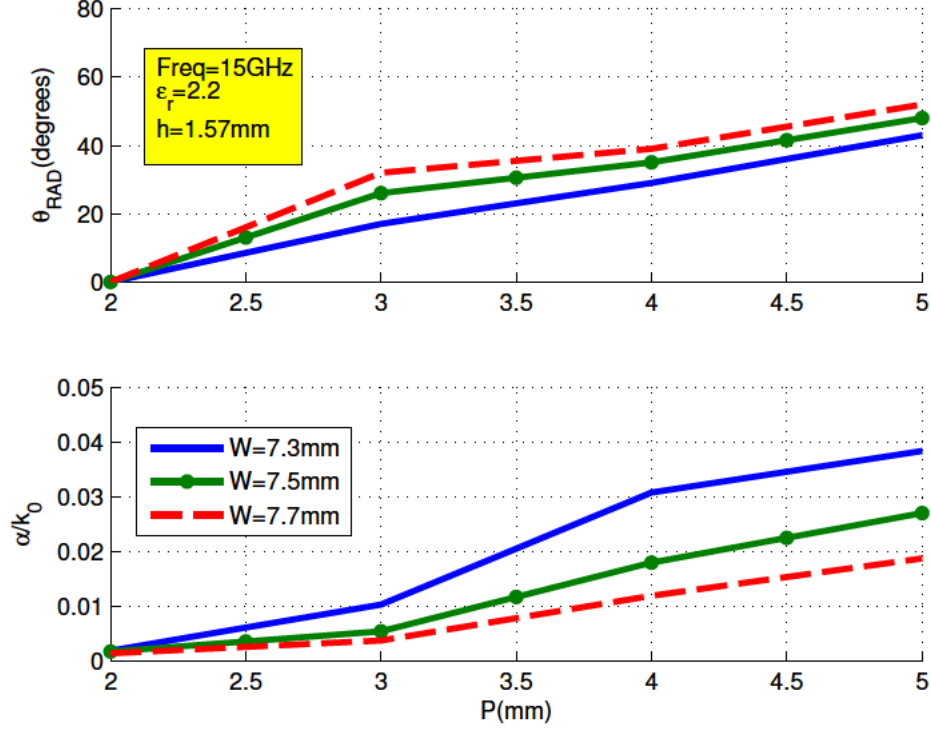


Figure 2.3: Curves for  $\alpha/k_0$  and  $\theta_{\text{RAD}}$  varying the distance between posts  $P$  for several values of  $W$  at 15 GHz.

frequency. This control mechanism of the phase constant is clearly observed in Fig. 2.4, as  $W$  is increased from  $W = 6.9\text{ mm}$  to  $W = 8.8\text{ mm}$ ,  $\theta_{\text{RAD}}$  is swept from  $0^\circ$  to  $60^\circ$  at 15 GHz. From Fig. 2.3 and Fig. 2.4 it is observed how both values of the leaky-mode propagation constant are affected mutually and therefore a simultaneous variation of  $P$  and  $W$  must be performed in order to achieve the desired values for  $\alpha$  and  $\theta_{\text{RAD}}$ . It must be highlighted that the antenna proposed in [45] shows similar flexible control, being the geometrical parameters  $l_1, l_2$  and  $p$  in [45, Fig. 2] equivalent to  $W, W_0$  and  $P$  of the antenna presented in this chapter. However, in [45] it was not demonstrated this versatility to simultaneously tailor the leaky-mode phase velocity and leakage rate, moreover, the analysis technique proposed for obtaining the complex propagation constant is only valid for large separations between posts ( $P/d > 5$ ), as it will be demonstrated in Chapter 3.

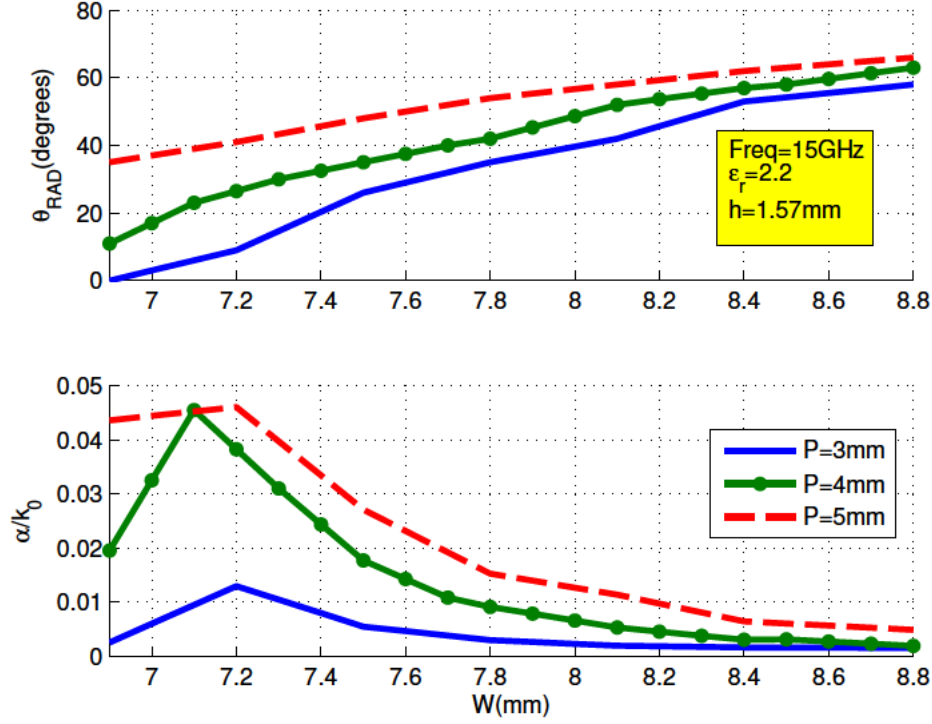


Figure 2.4: Curves for  $\alpha/k_0$  and  $\theta_{\text{RAD}}$  varying the width of the SIW  $W$  for several values of  $P$  at 15 GHz.

## 2.3 Designs and Measurements

In order to validate the theoretical concepts shown in the previous sections and to demonstrate the ability to tailor the radiation pattern, several designs have been simulated and fabricated in commercial substrate RT/Duroid 5880 ( $h = 1.57\text{ mm}$ ,  $\epsilon_r = 2.2$ ,  $\tan \delta = 0.0009$ ). A scheme of the complete structure and its main geometrical parameters is represented in Fig. 2.5. The design can be divided in three well differentiated parts:

1. Transition from a microstrip to a SIW ( $L_0$ )
2. Transition from a SIW to the LWA ( $L_1$ )
3. Radiating Leaky-Wave Antenna ( $L_A$ )

The PLWA is excited by means of a microstrip line at port 1. On the other hand, the transitions  $L_0$  and  $L_1$  compensate and reduce the mismatch between propagation constants in both microstrip and SIW transmission lines, as proposed in [3], [20]. For all prototypes the following transition lengths have been used:  $L_0 = 15$  mm and  $L_1 = 46$  mm.

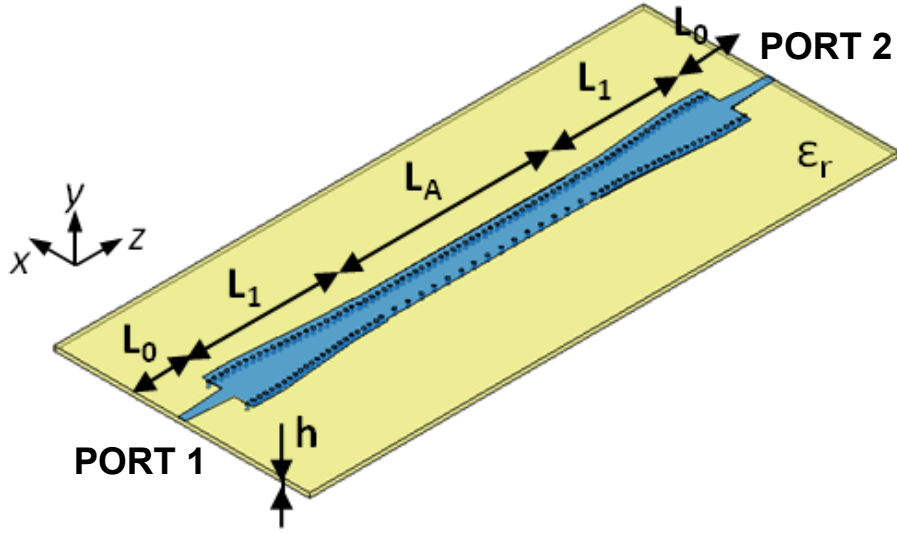


Figure 2.5: Scheme of the novel PLWA including feeding lines.

By processing dispersion curves of  $\theta_{\text{RAD}}$  and  $\alpha/k_0$  as a function of the physical parameters  $W$  and  $P$ , five LWAs have been designed. Three designs with same pointing angle (2.4)  $\theta_{\text{RAD}} = 30^\circ$  and variable beamwidth (2.3) from  $\Delta\theta = 5^\circ$  to  $\Delta\theta = 20^\circ$  were performed for the design frequency of 15 GHz, obtaining the requested values of  $L_A$ ,  $W$  and  $P$  summarized in Table 2.1. On the other hand, in Table 2.2 the physical dimensions for other three designs where the beamwidth is kept constant to  $\Delta\theta = 10^\circ$  and the pointing angle is varied from  $\theta_{\text{RAD}} = 10^\circ$  to  $\theta_{\text{RAD}} = 50^\circ$  are represented. All the LWAs of Table 2.1 and Table 2.2 are designed to provide  $\eta_{\text{RAD}} = 90\%$  (2.2) at the design frequency of 15 GHz, independently of the variation in the scanning angle and the beamwidth. The fabricated prototypes are shown in the picture of Fig. 2.6.

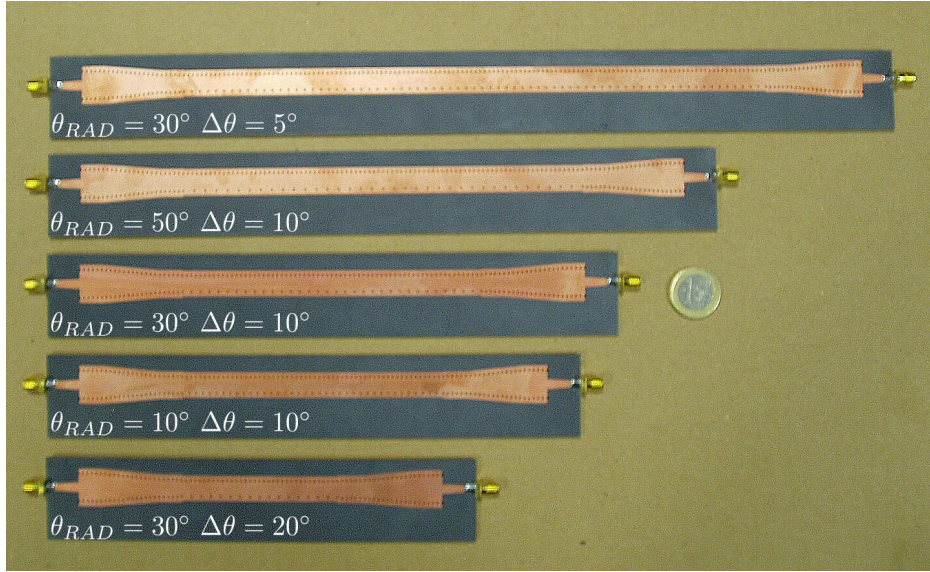


Figure 2.6: Photograph of the five manufactured prototypes.

Table 2.1: Physical Dimensions for Three Planar LWAs With Different Beamwidths and a Constant Pointing Angle ( $\eta_{RAD} = 90\%$ )

$\theta_{RAD}$	$\Delta\theta$	$L_A(mm)$	$W(mm)$	$P(mm)$
$30^\circ$	$20^\circ$	68.8	7.15	4.3
$30^\circ$	$10^\circ$	132	7.3	4
$30^\circ$	$5^\circ$	262.8	7.43	3.6

Table 2.2: Physical Dimensions for Three Planar LWAs With Different Pointing Angles and a Constant Beamwidth ( $\eta_{RAD} = 90\%$ )

$\theta_{RAD}$	$\Delta\theta$	$L_A(mm)$	$W(mm)$	$P(mm)$
$10^\circ$	$10^\circ$	115.14	7.2	3.03
$30^\circ$	$10^\circ$	132	7.3	4
$50^\circ$	$10^\circ$	177.48	7.6	4.93

The measured  $H$ -plane radiation patterns at 15 GHz for the prototype designs of Table 2.1 and Table 2.2 are plotted in Fig. 2.7a and Fig. 2.7b, respectively. As it can be seen, the desired variation in  $\theta_{RAD}$  and  $\Delta\theta$  are successfully obtained, experimentally confirming the proposed design flexibility. On the other hand, the

$E$ -plane radiation pattern is characterized by a typical fan beam [82], as it can be seen in Fig. 2.8 for the case of the antenna with  $\theta_{\text{RAD}} = 30^\circ$  and  $\Delta\theta = 10^\circ$ . As commented in the Section 2.1, a one dimensional array of LWAs might be used to increase the directivity in the  $E$ -plane [82]. The measured cross-polarization fields are also shown in Fig. 2.8, observing a maximum cross-polarization level of  $-8$  dB.

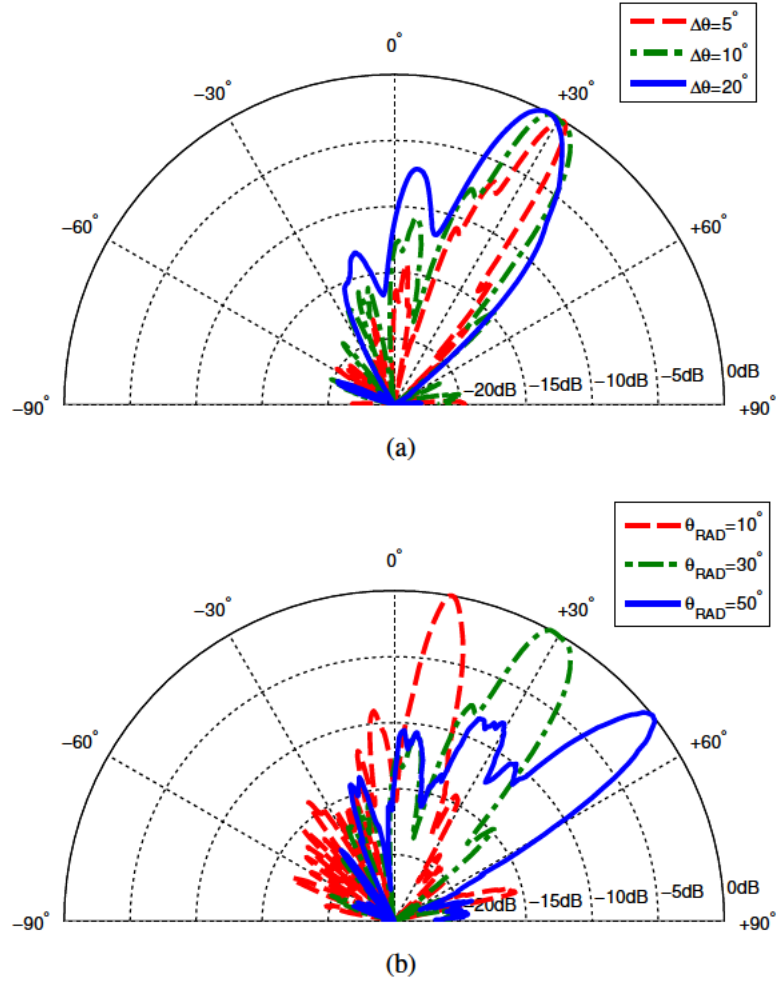


Figure 2.7: Measured  $H$ -plane radiation diagrams at 15 GHz: a) Variation of the beamwidth  $\Delta\theta$  for a constant pointing angle  $\theta_{\text{RAD}} = 30^\circ$ . b) Variation of the pointing angle  $\theta_{\text{RAD}}$  for a constant beamwidth  $\Delta\theta = 10^\circ$ .

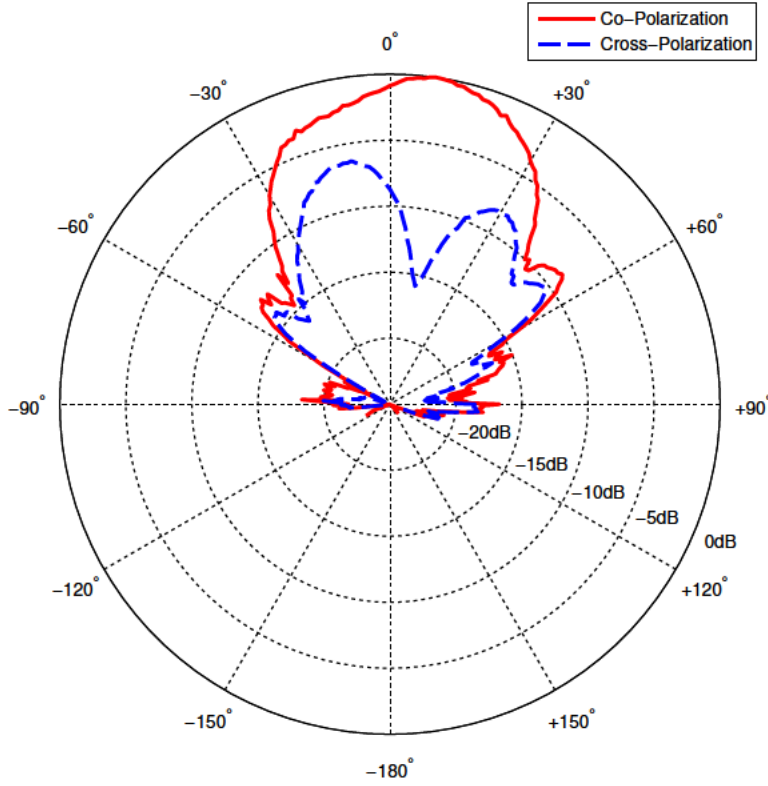


Figure 2.8: Measured  $E$ -plane radiation diagram at 15 GHz, including co-polarization and cross-polarization for the LWA with  $\theta_{\text{RAD}} = 30^\circ$  and  $\Delta\theta = 10^\circ$ .

A comparative showing very good agreement between measured and simulated  $H$ -plane radiation diagrams is depicted for all the designed antennas in Fig. 2.9. As it can be seen, the  $H$ -plane scanning angle and main beamwidth can be flexible tailored as theoretically predicted. Moreover, the measured values of gain ( $G$ ) and directivity ( $D$ ) are reported for each prototype in the insets of Fig. 2.9, together with the deduced radiation efficiency ( $\eta_{\text{RAD}} = G/D$ ). It is shown how the expected high efficiency ( $\eta_{\text{RAD}} \approx 90\%$ ) has been obtained for all tailored designs, in spite of the pointing angle and beamwidth selected. Also, Fig. 2.9f represents the measured levels of co-polarization ( $\phi$  polarization) and cross-polarization ( $\theta$  polarization) at the  $H$ -plane for the case of the antenna radiating at  $\theta_{\text{RAD}} = 30^\circ$  with  $\Delta\theta = 10^\circ$ . The rest of designs showed similar levels of cross-polarization.

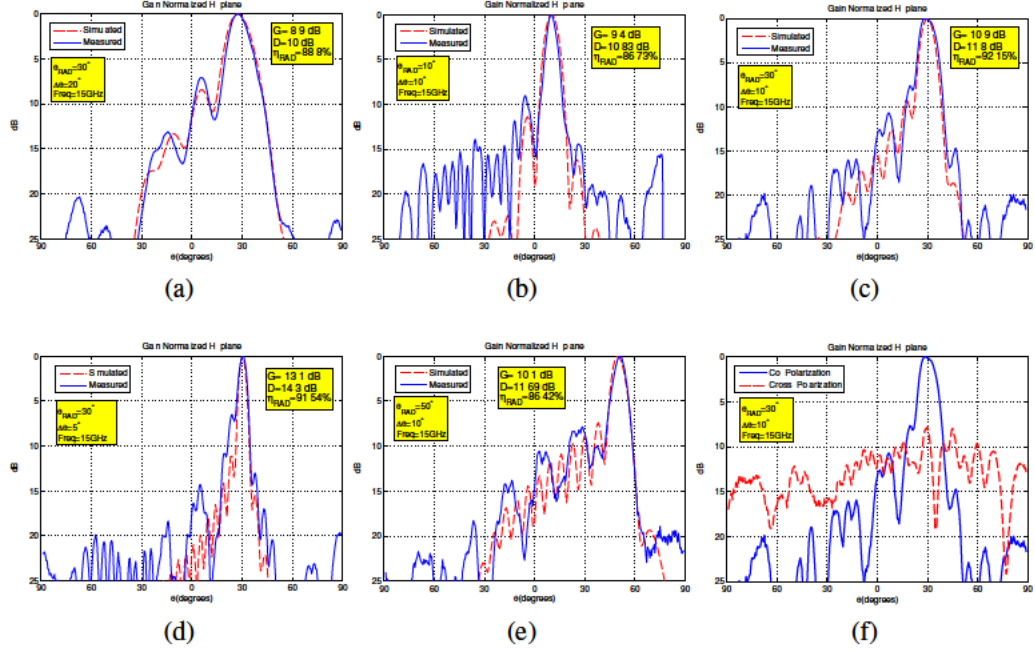


Figure 2.9: Measured and simulated  $H$ -plane radiation diagrams at 15 GHz for each antenna: a)  $\theta_{\text{RAD}} = 30^\circ$  and  $\Delta\theta = 20^\circ$ . b)  $\theta_{\text{RAD}} = 10^\circ$  and  $\Delta\theta = 10^\circ$ . c)  $\theta_{\text{RAD}} = 30^\circ$  and  $\Delta\theta = 10^\circ$ . d)  $\theta_{\text{RAD}} = 30^\circ$  and  $\Delta\theta = 5^\circ$ . e)  $\theta_{\text{RAD}} = 50^\circ$  and  $\Delta\theta = 10^\circ$ . f) Levels of co-polarization and cross-polarization for  $\theta_{\text{RAD}} = 30^\circ$  and  $\Delta\theta = 10^\circ$ .

Fig. 2.10 depicts the measured  $S_{11}$  and  $S_{21}$  parameters for the antennas with a fixed beamwidth (Fig. 2.10a), and with fixed pointing angle (Fig. 2.10b) at the center frequency. Good matching is obtained for all prototypes at the design frequency of 15 GHz ( $S_{11}$  parameter around  $-17$  dB). Moreover, it can be observed how both  $S_{11} \approx -17$  dB and  $S_{21} \approx -13$  dB remain constant for all antennas at 15 GHz. As a consequence, the radiation efficiency extracted from the measured S parameters ( $\eta_{\text{RAD}} = 1 - |S_{11}|^2 - |S_{21}|^2$ ) results in  $\eta_{\text{RAD}} \approx 90\%$  for all the designs (independently on the values of  $\theta_{\text{RAD}}$  and  $\Delta\theta$ ), in coherence with the efficiency estimated from the measured gain. By using simulations for the antenna with and without material losses, and comparing them with the measured S parameters, a difference in  $S_{21}$  parameter at 15 GHz from  $-11.5$  dB (without losses) to  $-13$  dB

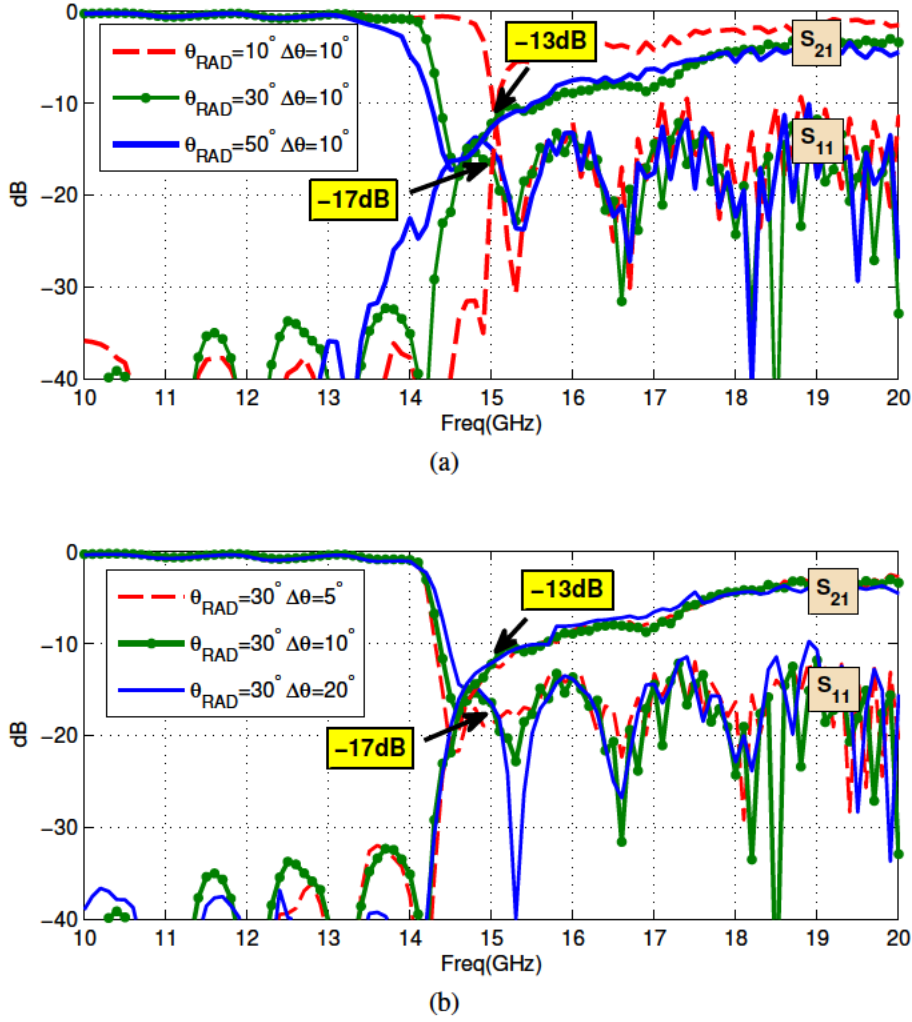


Figure 2.10: Measured S parameters: a) Variation of the pointing angle  $\theta_{\text{RAD}}$  for a constant beamwidth  $\Delta\theta = 10^\circ$ . b) Variation of the beamwidth  $\Delta\theta$  for a constant pointing angle  $\theta_{\text{RAD}} = 30^\circ$ .

(with losses, in agreement with the measured results) was obtained. Thus, it can be claimed that the 1.5 dB increase in the insertion losses is due to ohmic losses, resulting in less than 3% reduction of the radiation efficiency.

Finally, the frequency dispersion of  $\theta_{\text{RAD}}$  and peak gain for the antenna with  $\theta_{\text{RAD}} = 30^\circ$  and  $\Delta\theta = 10^\circ$  is represented in Fig. 2.11. Very good agreement between simulations (circles) and measurements (continuous line) is observed,

achieving a measured peak gain of 10.9 dB at  $\theta_{\text{RAD}} = 30^\circ$  for the design frequency of 15 GHz. Moreover, it can be observed the typical frequency beam scanning capability inherent to LWAs, that makes them useful for scanning applications, such as frequency modulated continuous-wave (FMCW) radars [82].

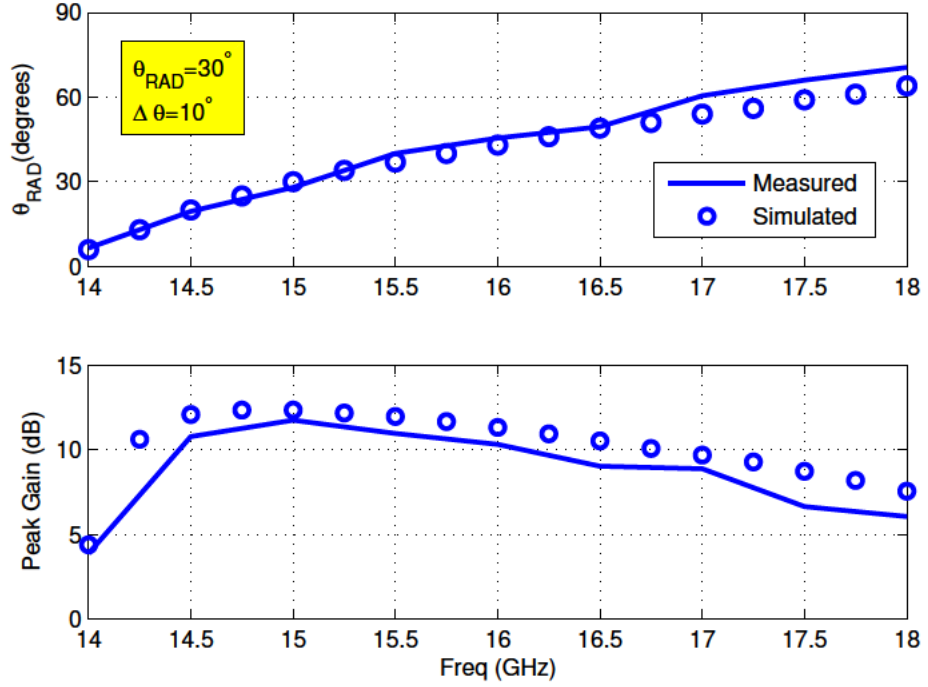


Figure 2.11: Measured and simulated frequency dispersion of  $\theta_{\text{RAD}}$  and gain for the antenna with  $\theta_{\text{RAD}} = 30^\circ$  and  $\Delta\theta = 10^\circ$  at 15 GHz.

## 2.4 Conclusion

The ability to control the leaky-mode complex propagation constant in a PLWA has been shown in this chapter. This antenna combines the feasibility to flexibly choose the pointing angle and the beamwidth while keeping optimum high radiation efficiency, and with the advantage of using a complete planar technology. The proposed design is based on a substrate integrated waveguide (SIW) which

cavity width  $W$  and periodicity between via-holes  $P$  can be varied to simultaneously control the leaky-mode phase and leakage constant. In order to validate the theoretical results obtained with commercial full-wave software, five prototypes operating at 15 GHz have been built and measured, showing very good agreement between theory and experiments. In three designs the pointing angle was kept constant and the beamwidth was varied, whereas for the other two the beamwidth was fixed for different pointing angles, at the design frequency of 15 GHz. All prototypes showed 90% radiation efficiency, demonstrating the capability of a planar LWA to obtain a versatile radiation diagram with high radiation efficiency in a simple, low-cost and effective way.



## **Chapter 3**

# **Analysis of 1-D Leaky-Wave Line Sources**

A transverse equivalent network is developed in this chapter to efficiently analyze the substrate integrated waveguide leaky-wave antenna SIW LWA shown in the previous Chapter 2. For this purpose, precise modeling of the SIW posts for any distance between vias is essential to obtain accurate results. It is shown how Marcuvitz closed-form expressions are not valid for short distances due to the small-obstacle approximation, making necessary a full-wave based modeling of the radiating posts' equivalent impedance. A detailed parametric study is performed obtaining leaky-mode dispersion curves as function of the main geometrical dimensions of the antenna. These new results provide physical insight into the working mechanism of the antenna and predict important effects, such as coupling with higher-order channel-modes for wide radiating strips, or the increase in the cross-polarization level for thick substrates. Design curves are obtained for an efficient design of the antenna pointing angle and directivity. Full-wave simulations and experimental results on fabricated prototypes operating at 15 GHz validate the proposed model.

### 3.1 Introduction

Leaky-Wave antennas (LWAs) can be efficiently designed by obtaining the complex propagation constant of the radiating leaky mode ( $k = \beta - j\alpha$ ) as function of frequency and the main geometrical parameters of the antenna [82]. Recently, a novel planar LWA in substrate integrated waveguide (SIW) technology was proposed (see Fig. 3.1a), showing the interesting feature of simultaneous control over the leaky-mode phase and leakage rate by only modifying the SIW printed-circuit dimensions [91], while keeping its single-layer planar nature. Previous printed-circuit LWAs, such as the first higher-order mode microstrip [61], [62] or the half-mode microstrip [71], [72] LWAs did not provide this flexible control over the leaky mode, thus suffering from limitations in the tailoring of the radiation pattern and radiation efficiency. The results and designs presented in [91] were obtained from simulations of the 3D CAD model of the antenna using finite element method (FEM) commercial EM solver HFSS [90].

In this chapter, a transverse equivalent network (TEN) (shown in Fig. 3.1b) is developed for the efficient analysis and design of this SIW LWA. As it is well known, the transverse resonance method (TRM) is a modal approach extensively used to obtain leaky-mode dispersion curves which assist in the direct design of LWAs [82], [92]–[94], being this modal alternative much more efficient if compared with the aforementioned analysis of the LWA using full-wave FEM simulations of its complete 3D CAD model. Furthermore, detailed parametric modal curves can be obtained to study the effect of all the geometrical parts of the antenna, and to give physical insight into the working principles and design rules of the LWA. With these main objectives in mind, in Section 3.2 is described the developed TEN, which was first proposed in [95] and it is here enhanced to accurately model the radiating posts' equivalent impedance for any distance between SIW vias. It is shown that the small-obstacle limit of Marcuvitz' analytical model [89, pp. 285–289] (used in a previous SIW LWA [45]), is overcome with the pro-

posed TEN, which is validated with full-wave simulations. Section 3.3 of this chapter presents a parametric study of the antenna, illustrating the influence of the main geometrical parameters and reporting important effects such as coupling with higher-order channel-modes for wide radiating strips, or the increase in the cross-polarization level for thick substrates. These dispersion data are used in Section 3.4 to obtain design curves that allow for an efficient and optimized design of the LWA, which is validated with experimental results on fabricated prototypes operating at 15 GHz. Finally, Section 3.5 summarizes the main conclusions of this chapter.

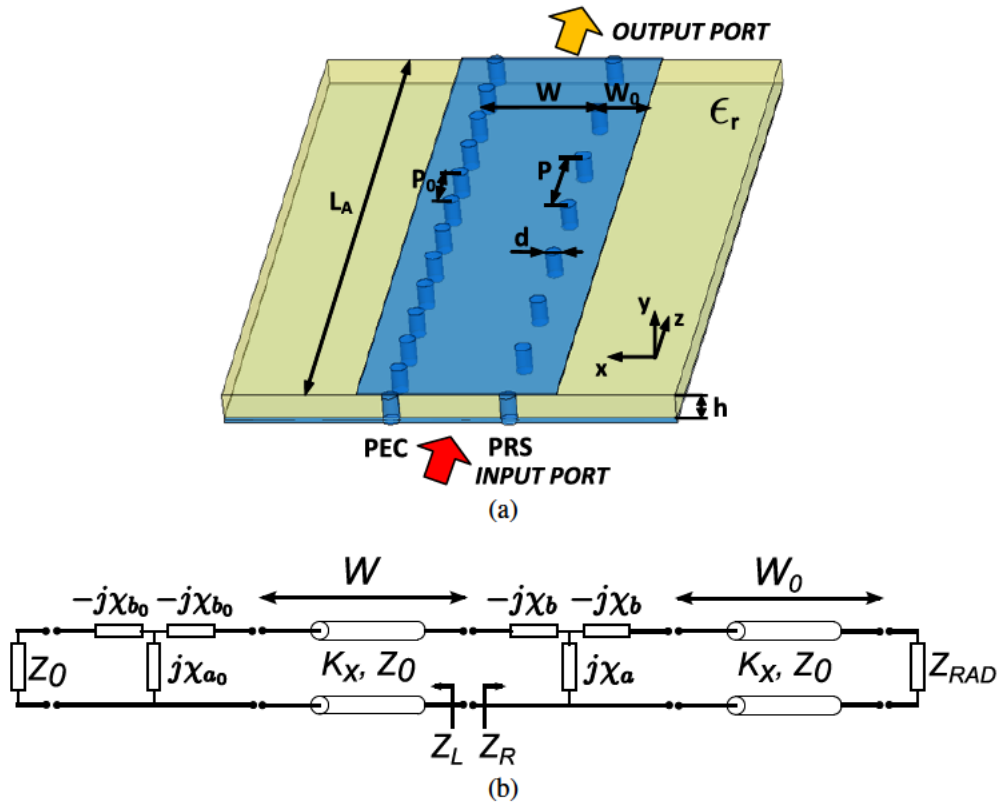


Figure 3.1: a) Scheme of the novel SIW LWA with its main geometrical parameters. b) Associated TEN of the cross section of the SIW LWA.

## 3.2 Development of Transverse Equivalent Network

The scheme of the proposed TEN is shown in Fig. 3.1b. Two sections of transmission lines of length  $W$  and  $W_0$  model the SIW width and the radiating strip width, respectively. This strip is terminated on its right side by an equivalent impedance  $Z_{\text{RAD}}$  which characterizes the radiating discontinuity due to the truncation of the upper plate in a dielectric filled parallel-plate waveguide. The closed-form approximation for the case of electrically thin substrates, which was proposed by Kuester et al. in [96], is used to model  $Z_{\text{RAD}}$ . Connecting the SIW and the radiating strip sections, there is a T network that models the row of metallic cylinders of diameter  $d$  and separated at a distance  $P$ , and is composed of one parallel inductor and two series capacitors (with respective reactances  $X_a$  and  $X_b$ ), as it was proposed by Marcuvitz [89, pp. 285–289]. Similar equivalent T impedance network is used at the left side of the SIW to model the row of metallic ports with period  $P_0$ , which is connected to the characteristic impedance  $Z_0$  of the parallel-plate dielectric substrate. Due to the small-obstacle approximation of the Marcuvitz's model, these posts reactances need to be obtained with a more accurate method (at least for  $P/d < 5$ ) than the analytical one proposed by Marcuvitz.

As it was shown in Chapter 2, the period  $P_0$  is fixed to  $P_0/d = 2$  in order to create a totally-reflective wall as usually done in SIW circuits [3], while the period  $P$  is a design parameter which is varied in the range  $P/d = [2 - 7]$  to modify the transparency of this partially-reflective sheet (PRS), and to obtain control over the leakage rate [6], [45]. Therefore, an accurate modeling of the posts' reactances for any distance  $P$  is required for the rigorous analysis and design of the proposed LWA.

### 3.2.1 Accurate Modeling of Partially Reflective Inductive Posts

To overcome the restrictions of Marcuvitz's model, the reactances  $X_a$  and  $X_b$  are extracted from an accurate full-wave analysis of the reflection coefficient  $\rho_P$  of

a periodic row of metallic posts under TE plane-wave incidence, as illustrated in Fig. 3.2.

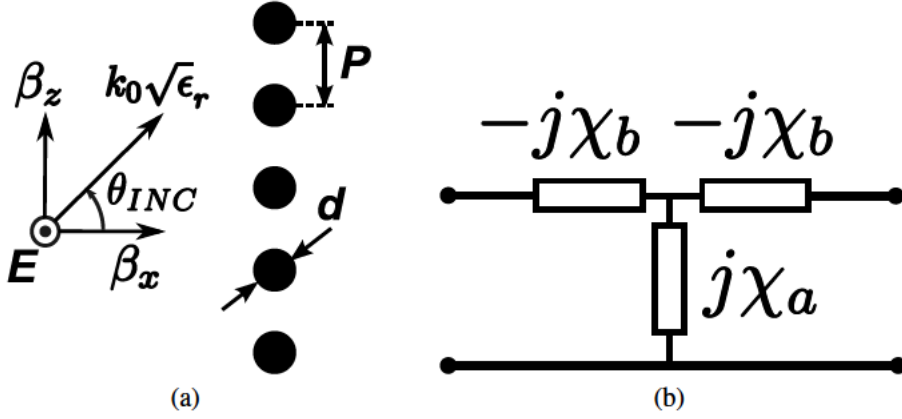


Figure 3.2: a) Scheme of TE plane-wave incidence on a row of periodic metallic posts. b) Equivalent T-circuit model proposed by Marcuvitz [89, pp. 285–289].

This analysis is based on an efficient electric field integral equation (EFIE) technique, which uses the Green's function of a periodic distribution of electric current filaments accelerated with Kummars' method [97]–[99]. The reflection coefficient is then computed for the incidence angle  $\theta_{INC}$  (see Fig. 3.2a), and the rest of the geometrical parameters ( $P$ ,  $d$ , and  $\epsilon_r$ ). Hence, the associated complex impedance can be then derived from  $\rho_P$ :

$$\overline{Z}_P(P, \theta_{INC}) = \frac{Z_P}{Z_0} = \frac{1 + \rho_P(P, \theta_{INC})}{1 - \rho_P(P, \theta_{INC})} = \overline{R}_P(P, \theta_{INC}) + j\overline{X}_P(P, \theta_{INC}) \quad (3.1)$$

Next, the real and imaginary parts that form this impedance,  $R_P(P, \theta_{INC})$  and  $X_P(P, \theta_{INC})$ , are compared with the T network proposed by Marcuvitz [89, pp. 285–289] and shown in Fig. 3.2b. After some algebraic manipulations, where it has been taken into account that the T model is ended by the characteristic impedance  $Z_0$  of a TE-polarized wave, the following equations relate the normalized reactances  $\overline{X}_a$  and  $\overline{X}_b$  to the real and imaginary parts of  $\overline{Z}_P$ ,  $\overline{R}_P$  and  $\overline{X}_P$ , thus

expressing their dependence on  $P$  and  $\theta_{\text{INC}}$ :

$$\overline{X}_a(P, \theta_{\text{INC}}) = \frac{X_a}{Z_0} = \sqrt{\overline{R}_P(P, \theta_{\text{INC}}) \left[ 1 + \left( \frac{\overline{X}_P(P, \theta_{\text{INC}})}{1 - \overline{R}_P(P, \theta_{\text{INC}})} \right)^2 \right]} \quad (3.2)$$

$$\overline{X}_b(P, \theta_{\text{INC}}) = \frac{X_b}{Z_0} = \overline{X}_a(P, \theta_{\text{INC}}) - \frac{\overline{X}_P(P, \theta_{\text{INC}})}{1 - \overline{R}_P(P, \theta_{\text{INC}})} \quad (3.3)$$

Fig. 3.3 shows with circles the values of the normalized reactances  $\overline{X}_a$  and  $\overline{X}_b$  obtained from Eqs. (3.1)–(3.3) as function of  $P$  for  $\theta_{\text{INC}} = 30^\circ$ , at the analysis frequency of 15 GHz and for  $\epsilon_r = 2.2$  and  $d = 1$  mm. Results obtained from Marcuvitz closed-form expressions for an inductive array of cylindrical posts [89, pp. 285–289] are also included in continuous line. For large separations ( $P > 5$  mm), good agreement is observed between both approaches, observing how  $\overline{X}_a$  increases and  $\overline{X}_b$  decreases as the distance between posts is enlarged. However, as the posts are located in closer proximity, Marcuvitz' results become less accurate due the small-obstacle approximation involved in the derivation of his formulas. The limit mentioned by Marcuvitz ( $P/d > 5$  [89]) is coherent with the results plotted in Fig. 3.3. Particularly, it can be observed that  $\overline{X}_a$  becomes

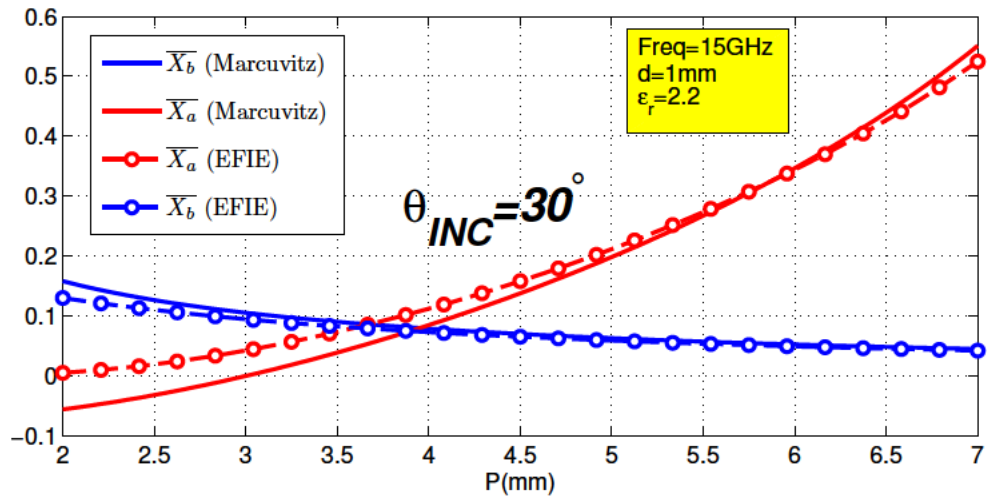


Figure 3.3: Equivalent T network reactances as function of  $P$  for  $\theta_{\text{INC}} = 30^\circ$ .

negative for  $P < 3$  mm, which has not physical meaning since it would model a negative inductance. Similar results were obtained for other angles of incidence, observing that for larger values of  $\theta_{\text{INC}}$  the inaccuracies are even more remarkable, as also mentioned by Marcuvitz in his model. The numerical approach proposed in this chapter can accurately obtain the inductance and capacitance of the array of metallic posts for any value of  $P$  and  $\theta_{\text{INC}}$ , which is essential for the analysis and design of the proposed SIW LWA.

Fig. 3.4 shows the reflection coefficient,  $\rho_P$ , associated to the scenario of TE plane-wave incidence studied in Fig. 3.3, varying  $P$  for three different values of  $\theta_{\text{INC}}$ . Results obtained using commercial full-wave software CST [100] are also plotted, validating the numerical technique proposed to model the array of vias for any value of  $P$  and  $\theta_{\text{INC}}$ . As expected, the array behaves as a totally reflective sheet for small values of  $P$ , and it becomes more transparent as the posts are separated. Moreover, it is observed that for  $P \approx 3.5$  mm there is change in the array behavior from capacitive (negative reflection phase for  $P < 3.5$  mm) to inductive (positive reflection phase for  $P > 3.5$  mm). This result is in coherence with Fig. 3.3, where a crossing between  $\overline{X_a}$  and  $\overline{X_b}$  curves is obtained for  $P \approx 3.5$  mm. Again, the range of validity of Marcuvitz impedance only for  $P > 5$  mm is evident from Fig. 3.4.

### 3.2.2 Development of an Accurate TEN

Once the accurate model of  $X_a$  and  $X_b$  has been obtained for any incident angle  $\theta_{\text{INC}}$  and any period  $P$  and  $P_0$ , it can be introduced in the TEN shown in Fig. 3.1b. The equivalent radiation impedance  $Z_{\text{RAD}}$  is given by Kuester et al. in [96] and it has closed-form expressions as function of the angle of incidence  $\theta_{\text{INC}}$ , the substrate thickness  $h$  and its relative permittivity  $\epsilon_r$ . On the other hand, the impedances of the transmission lines sections can be readily expressed from their respective lengths  $W$  and  $W_0$ , and using the transverse wavenumber  $k_x$  and

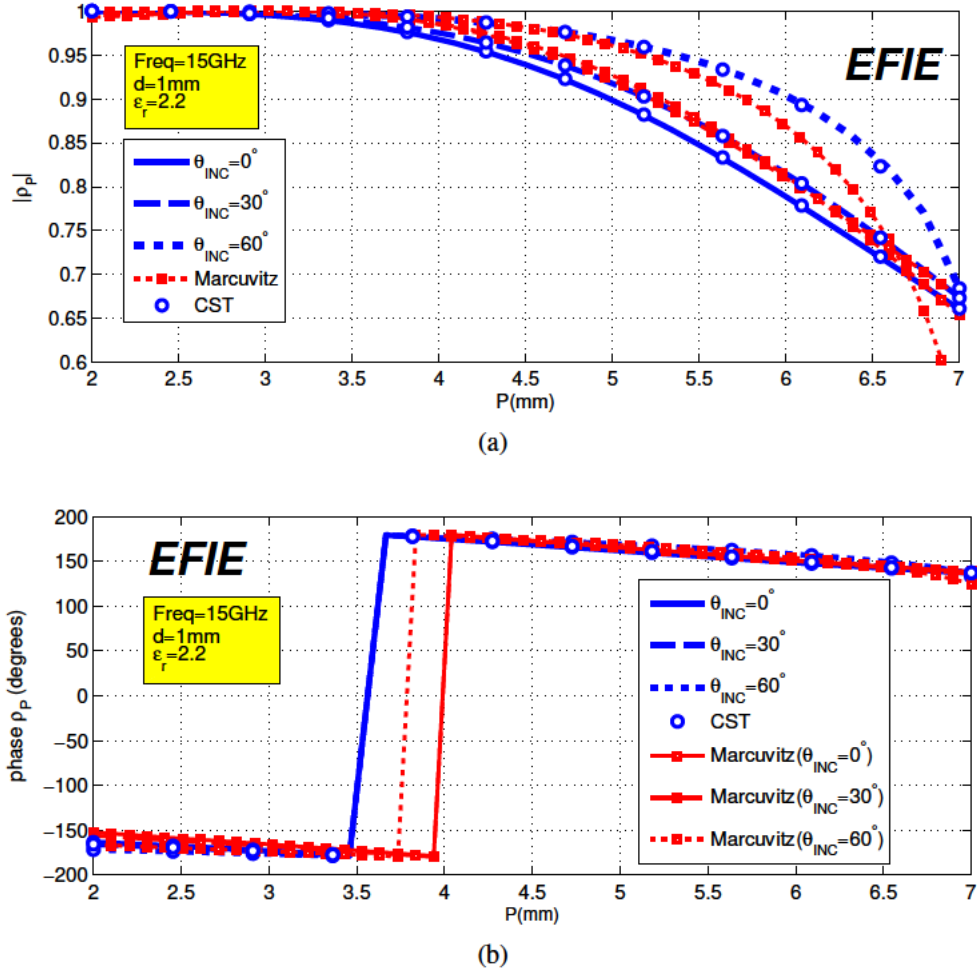


Figure 3.4: Response of the reflection coefficient as function of  $P$  for several incident angles: a) magnitude and b) phase.

the characteristic impedance of a TE-polarized wave:

$$Z_0(\theta_{INC}) = \frac{\omega \mu_0}{k_x(\theta_{INC})} \quad (3.4)$$

where  $k_x$  can be related to the longitudinal wavenumber  $k_z$ , by the following expression where  $k_0$  is the free-space wavenumber and  $\epsilon_r$  the substrate permittivity (see Fig. 3.2a):

$$k_x(\theta_{INC}) = \sqrt{k_0^2 \epsilon_r - k_z^2(\theta_{INC})} \quad (3.5)$$

Finally, the transverse resonance equation (TRE) can be expressed at the reference plane shown in Fig. 3.1b as:

$$Z_L(k_z) + Z_R(k_z) = 0 \quad (3.6)$$

which must be solved for the unknown leaky-mode complex longitudinal wavenumber  $k_z$ :

$$k_z(\theta_{\text{INC}}) = \beta_z(\theta_{\text{INC}}) - j\alpha \quad (3.7)$$

It must be noticed that the internal angle of incidence  $\theta_{\text{INC}}$  is related to the leaky-wave phase constant  $\beta_z$  (see Fig. 3.2a) by:

$$\sin \theta_{\text{INC}} \approx \frac{\beta_z}{k_0 \sqrt{\epsilon_r}} \quad (3.8)$$

Since all the discrete components represented in the TEN of Fig. 3.1b are dependent on  $\theta_{\text{INC}}$ , they can also be expressed as function of the unknown leaky-wave phase constant  $\beta$  using (3.8). Also, since  $k_x$  is related to  $\beta$  and  $\alpha$  by (3.5) and (3.7), the propagation in the equivalent transmission line sections can also be expressed as function of the unknown longitudinal phase and attenuation constants of the leaky mode. Therefore, the problem of finding the leaky mode solution is equivalent to the minimization of (3.6) in the complex plane  $(\beta - j\alpha)$  [82], for any frequency and dimensions of the studied LWA.

As an example, Fig. 3.5 shows the leaky mode normalized phase and attenuation constants ( $\beta/k_0$  and  $\alpha/k_0$ ) as frequency is varied from 12 GHz to 18 GHz, and for different values of  $P$ . The rest of geometrical parameters of the studied LWA are kept fixed and they are summarized in the inset of Fig. 3.5. Results obtained from the proposed TEN are compared with HFSS, showing good agreement for all values of  $P$ . It must be noticed that the internal incidence angle  $\theta_{\text{INC}}$  is modified as the solution of  $\beta$  changes, according to (3.8). Therefore, an accurate model of the posts for any value of  $P$  and  $\theta_{\text{INC}}$  is essential for the leaky-mode analysis

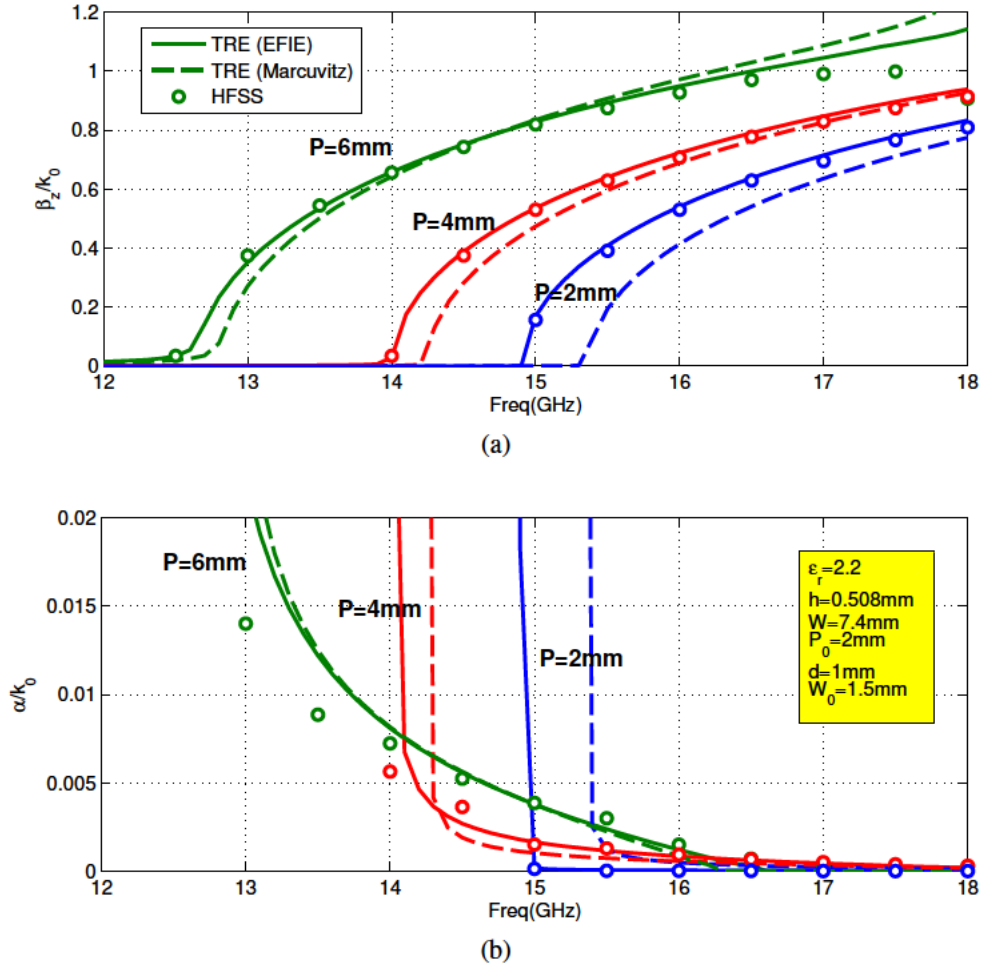


Figure 3.5: a) Normalized phase constant. b) Normalized leakage rate as function of frequency and different values of  $P$ .

of the proposed antenna. Also, modal results obtained when Marcuvitz analytical impedance is used instead of the more accurate full-wave model for  $X_a$  and  $X_b$  are also plotted. As expected, higher disagreement is observed for lower values of  $P$ , due to Marcuvitz' aforementioned small-obstacle approximation, while our TEN provides good results for both the phase and attenuation constants when compared to HFSS. Particularly, strong discrepancies in the leaky phase constant are observed for the  $P = 2\text{ mm}$  curve, while for the  $P = 6\text{ mm}$  curve the results are more similar to the other two techniques compared in Fig. 3.5.

### 3.3 Parametric Dispersion Curves

In order to characterize the behavior of the proposed SIW LWA as its main geometrical parameters are varied, several dispersion curves at a fixed design frequency (15 GHz) have been obtained. These results will provide physical insight into the working mechanism of the antenna and they will help in the design process. In each subsection, it is shown the effect of a parameter in the leaky-mode normalized leakage rate  $\alpha/k_0$  and its associated radiation angle  $\theta_{\text{RAD}}$  given by [82]:

$$\sin \theta_{\text{RAD}} \approx \frac{\beta}{k_0} \quad (3.9)$$

#### 3.3.1 Effect of Distance Between Reflective Posts $P$

For a fixed design frequency of 15 GHz, Fig. 3.6 illustrates the effect of the distance between the PRS posts' distance  $P$ , for different SIW widths  $W$ . As expected, when  $P$  is increased the PRS wall becomes more transparent, thus increasing the leakage rate (see Fig. 3.6b). However, it is also observed how for periods larger than  $\approx 5.5$  mm the leakage rate starts to decrease. This effect is due to the leaky mode is radiating very close to endfire ( $\theta_{\text{RAD}}$  tending to  $90^\circ$  in Fig. 3.6a), eventually transforming into a surface-wave [82], with null leakage rate from  $P \approx 7$  mm.

The combination of the previous effects make the leakage rate to behave as shown in Fig. 3.6b, so that for values of  $P = [2 - 6]$  mm the increase of transparency is responsible for the rise in  $\alpha/k_0$ , while for  $P > 6$  mm the transition from leaky to surface wave make  $\alpha/k_0$  to decrease. As it is also observed in Fig. 3.6a, the increase in  $P$  also affects the pointing angle, increasing  $\beta/k_0$  and therefore  $\theta_{\text{RAD}}$  (e.g. from  $10^\circ$  to  $60^\circ$  for  $W = 7.4$  mm as the distance  $P$  is enlarged from 2 mm to 6 mm). Good agreement is observed between HFSS and the proposed model.

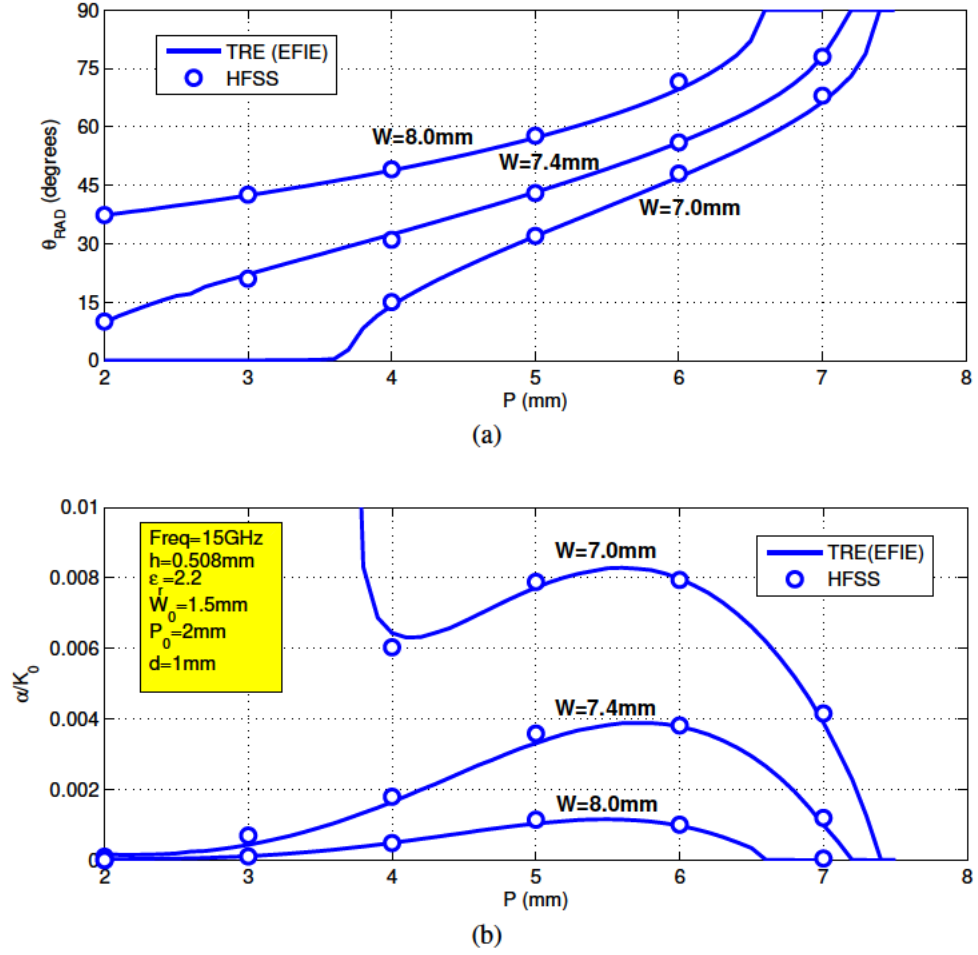


Figure 3.6: a) Pointing angle of the main beam. b) Normalized leakage rate as function of the separation between posts  $P$  and for different widths  $W$ .

### 3.3.2 Effect of SIW Width $W$

As described in Chapter 2, the simultaneous variation of  $P$  and  $W$  allows a flexible control over  $\theta_{\text{RAD}}$  and  $\alpha/k_0$  in a wide range of values. This is illustrated in Fig. 3.7, showing dispersion plots as  $W$  is continuously varied from 6.8 mm to 7.8 mm, for several discrete values of  $P$  between 2 mm and 6 mm. As previously explained and illustrated in Fig. 3.6, higher values of  $P$  in the range  $[2 - 6]$  mm provide higher leakage rates and increasing pointing angles. The SIW width  $W$  is the proper parameter which allows steering the radiation angle at the desired value,

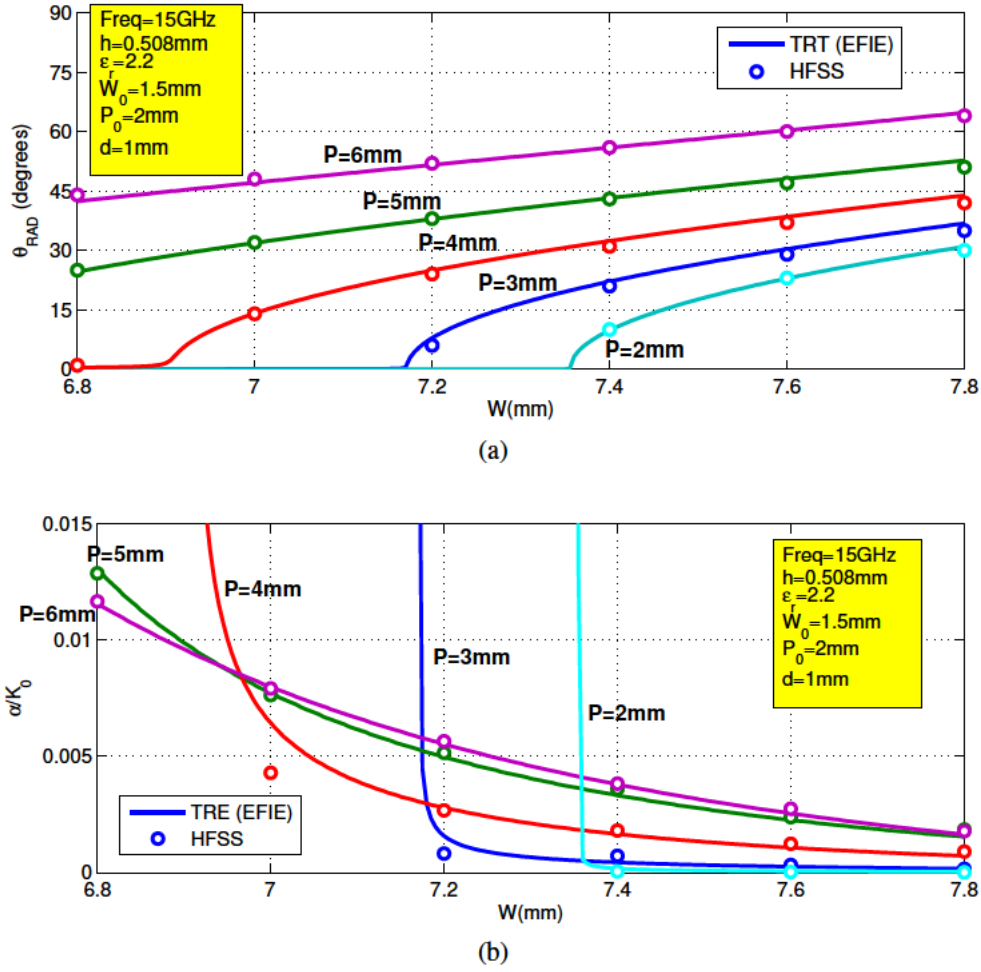


Figure 3.7: a) Pointing angle of the main beam and b) normalized leakage rate as function of the width  $W$  and for different separation between posts  $P$ .

since it determines the cutoff frequency of the  $\text{TE}_{10}$ -like leaky mode. As happens in any SIW [3], [6], [45] or microstrip [61], [62], [71], [72] LWA, lower strip widths  $W$  provide higher leaky-mode cutoff frequencies, and therefore lower values of  $\theta_{\text{RAD}}$  for a fixed frequency and  $P$ , as shown in Fig. 3.7a. For a constant value of  $P$ , decreasing  $W$  not only decrease  $\theta_{\text{RAD}}$ , but also increase  $\alpha/k_0$  (see Fig. 3.7b) as it is common to a leaky wave radiating at angles closer to broad-side [82]. Fig. 3.7 shows good agreement between HFSS results and the proposed TEN for all the range of  $W$  and  $P$ , showing variation in  $\theta_{\text{RAD}}$  from  $0^\circ$  to  $65^\circ$ , and

in  $\alpha/k_0$  from 0 to 0.012. The sudden rise in  $\alpha/k_0$  observed in Fig. 3.7b for the lower values of  $P$  as  $W$  is decreased, is due to the reactive nature of the leaky wave below cutoff (in this range the attenuation constant  $\alpha/k_0$  is due to stored reactive energy and not to radiation leakage [82]). The same immersion in the reactive regime was observed in Fig. 3.5b as frequency was lowered.

### 3.3.3 Effect of Radiating Strip Width $W_0$

The strip of width  $W_0$  acts as a transition from the fields which come from the SIW PRS wall and which reach the radiating discontinuity occurring at its edge. A standing-wave periodic behavior is expected as  $W_0$  is varied, as it happens in previous stub-loaded LWAs [84], [92], [101], [102] in which a section of parallel-plate guide makes the transition from the leaky waveguide to the radiating open-end. However, higher-order channel-guide leaky-modes resonating in this width of parallel-plate will appear as  $W_0$  is increased, as reported in [84], [92], [101], [102]. This is illustrated in Fig. 3.8, showing how the SIW leaky mode (continuous blue line) has a periodic variation in  $\theta_{\text{RAD}}$  and  $\alpha/k_0$  as  $W_0$  is increased. In dashed red lines, the dispersion curves for higher-order channel leaky modes are also plotted. As it happened with  $W$  for the SIW mode,  $W_0$  determines the channel-modes cut-off frequency. As a result, these higher-order modes do not have a periodic standing-wave behavior with  $W_0$ , but  $\theta_{\text{RAD}}$  increases and  $\alpha/k_0$  decreases as  $W_0$  is augmented (as it happened for the SIW mode when  $W$  was varied, see Fig. 3.7). Particularly, it can be extracted from Fig. 3.8 that the first channel-mode appears at  $W_0 = 2.5$  mm, the second one has a cut-off at  $W_0 = 10$  mm, the third one at  $W_0 = 17.5$  mm, and the fourth one at  $W_0 = 25$  mm. Thus, each increment of  $\Delta W_0 = 7.5$  mm (which approximately corresponds to  $\lambda/2$  in the substrate at 15 GHz), a new higher-order channel-mode appears.

The emergence of higher-order leaky modes is an undesired effect for two reasons. First, single-leaky-mode operation is desired to assure that the pointing angle and radiation efficiency of the LWA is due to the SIW leaky-mode which

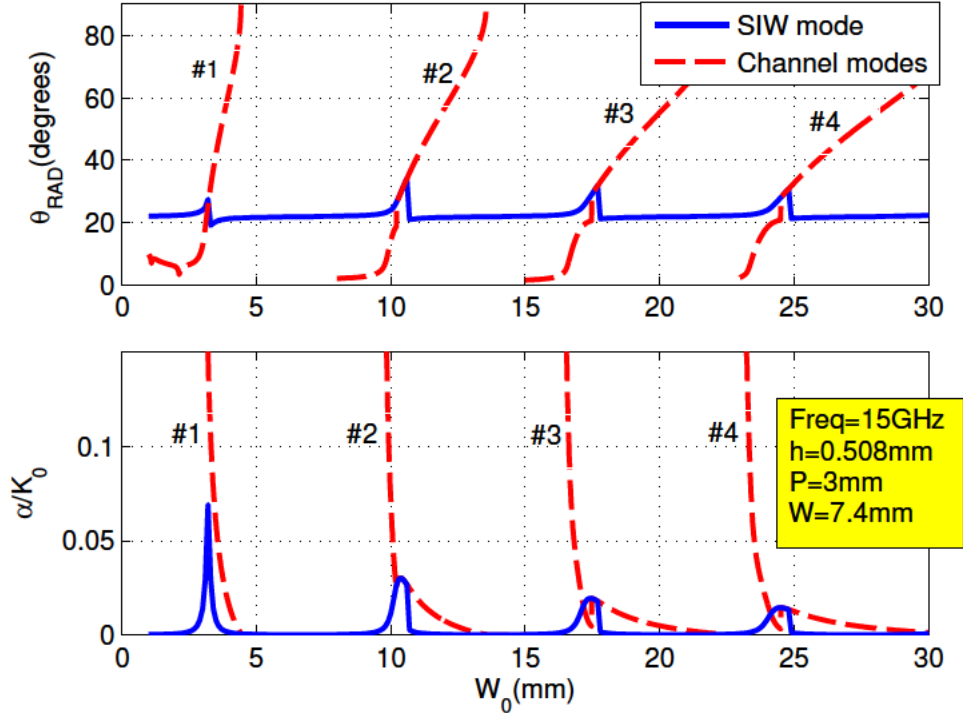


Figure 3.8: Dispersion curves as function of the radiating strip width  $W_0$  for SIW leaky mode and higher-order channel-guide leaky modes.

prescribed phase and leakage constants, thus allowing a prearranged direct design. Excitation of any higher-order leaky mode would translate in the appearance of an extra beam radiating at an unwanted direction, and a loss of gain in the desired scanning angle. The second reason to avoid multimode operation has to do with the unwanted coupling effect between our desired SIW leaky mode and the unwanted channel-guide modes. This coupling is illustrated in Fig. 3.9, where a detailed plot of the dispersion of the dominant SIW mode and the first-higher-order channel-mode is given as function of the radiating strip width  $W_0$  for a range from 1 mm to 5 mm.

As reported in previous studies [84], [92], [101], [102], these two leaky modes couple when  $\beta$  and  $\alpha$  of both modes have similar values, producing the exotic-looking dispersion curves shown in Fig. 3.9, where it is observed an interchange

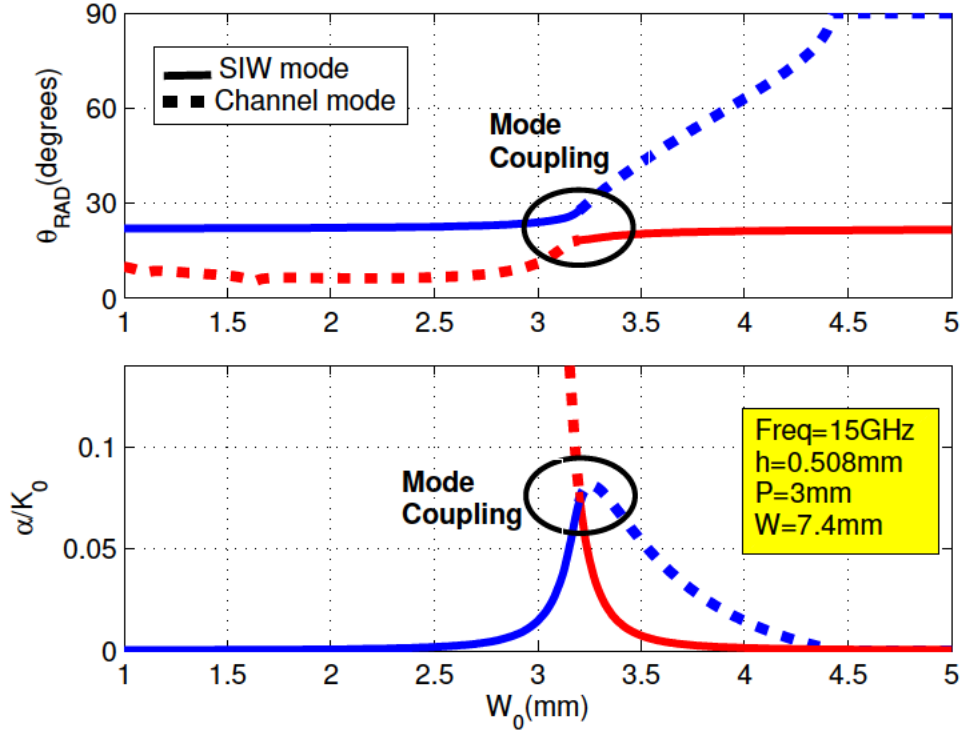


Figure 3.9: Detail of coupling effect between SIW and channel leaky modes as function of the radiating strip width  $W_0$ .

in their wavenumber values. The periodic variation of the leaky mode as  $W_0$  is increased, is plotted in Fig. 3.10 for the different values of  $P$ . Moreover, the results obtained with the TRE (EFIE) technique are compared with 3D HFSS full-wave simulations, showing the validity of the proposed model and the accuracy in the prediction of this quasi-periodic coupling phenomenon.

The parallel-plate strip region of width  $W_0$  serves to eliminate the vertical component of higher-order electric fields, allowing the radiated beam to possess purer horizontal polarization and thus a higher cross-polarization discrimination (XPD) as  $W_0$  is increased, as it is shown in Fig. 3.11 [101]. Minimum XPD level of 14 dB is obtained for  $W_0 = 0$  mm, and it can be increased over 20 dB for  $W_0 > 6$  mm. Also, Fig. 3.11 shows that lower values of  $P$  provide higher XPD levels.

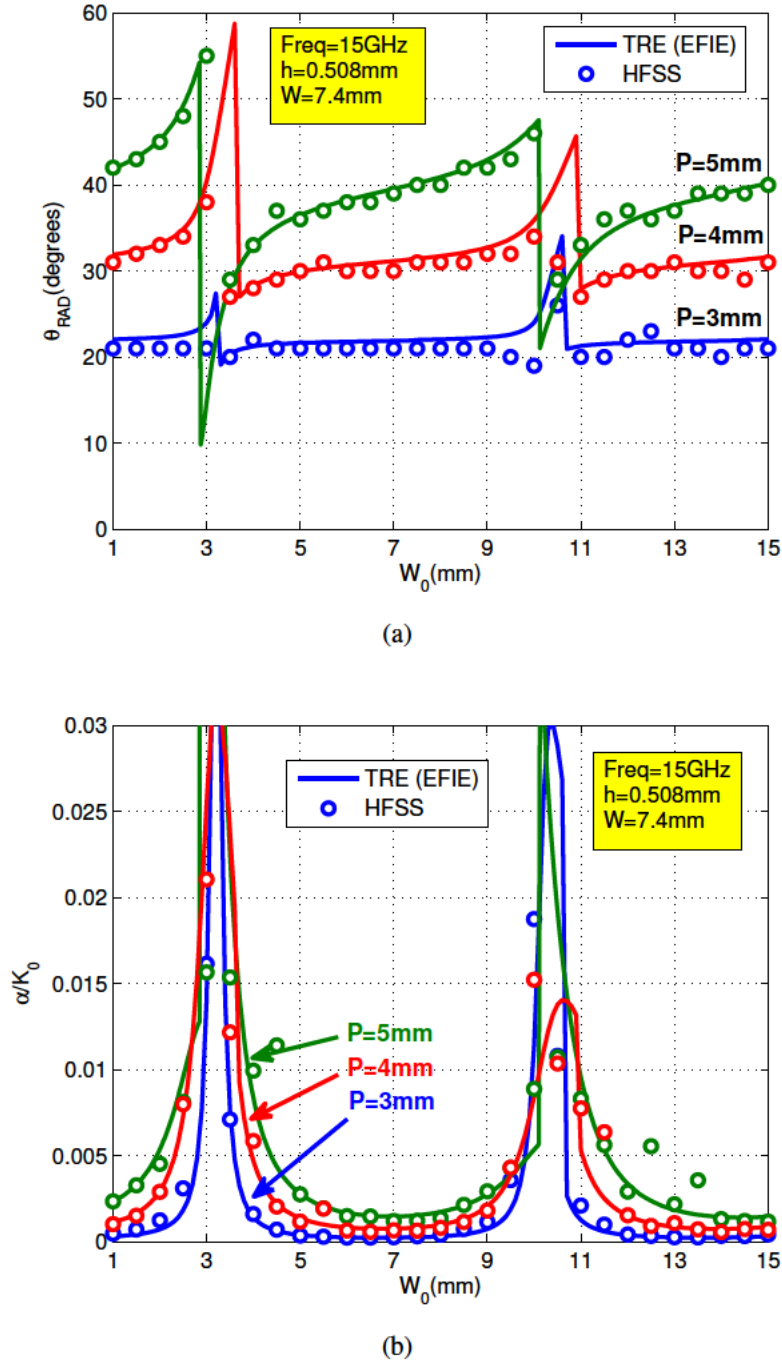


Figure 3.10: a) Pointing angle of the main beam and b) normalized leakage rate as function of the radiating strip width  $W_0$  and for different separation between posts  $P$ .

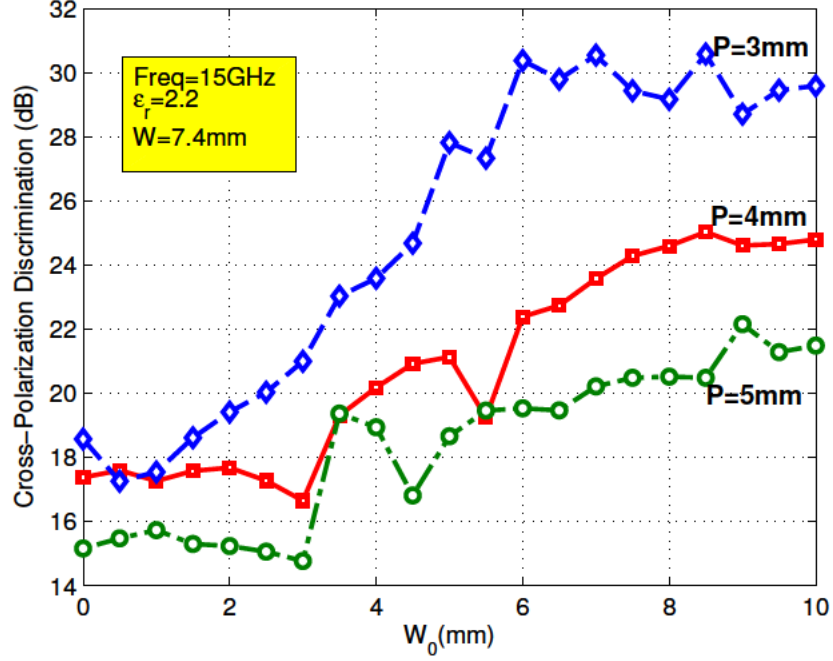


Figure 3.11: Dependence on the polarization discrimination level with  $W_0$ .

At the same time, multimode coupling problems must be avoided by choosing  $W_0 < 3$  mm (which approximately corresponds to  $\lambda/4$  in the substrate at 15 GHz), as it was shown in Fig. 3.9. An optimum value of  $W_0 = 1.5$  mm is chosen to minimize undesired coupling effect while assuring minimum XPD level.

### 3.3.4 Effect of $h$

The dependence on the leaky mode with the substrate thickness  $h$  is shown in Fig. 3.12, where the results obtained with the TRE (EFIE) are compared and validated with HFSS. As it is observed, the pointing angle  $\theta_{\text{RAD}}$  remains almost constant for each value of  $P$  as  $h$  is increased. However, the leakage rate is increased due to the higher transparency of the quasi-magnetic wall created at the radiating strip discontinuity, as accurately modeled by Kuester [96] radiation impedance  $Z_{\text{RAD}}$  (see Fig. 3.1b). In addition, it is observed how the range of validity of the

closed-form approximation for thin-substrates ( $k_0 h \leq 0.2$ ) proposed in [96] is reasonably acceptable for even thicker substrates. On the other hand, this higher leakage rate due to the thicker substrate has the inconvenient of increasing the cross-polarization level, therefore decreasing the XPD discrimination for higher  $h$  as it shown in Fig. 3.13. Again, lower values of  $P$  provide higher XPD levels, as it happened in Fig. 3.11. Therefore, it is important to have a trade-off between higher leakage values and higher XPD levels. Commercial substrates with  $h = 1.57$  mm and  $\epsilon_r = 2.2$  offer XPD level over 5 dB for  $W = 7.4$  mm and  $P > 5$  mm, and provide leakage rates up to  $\alpha/k_0 = 0.02$ .

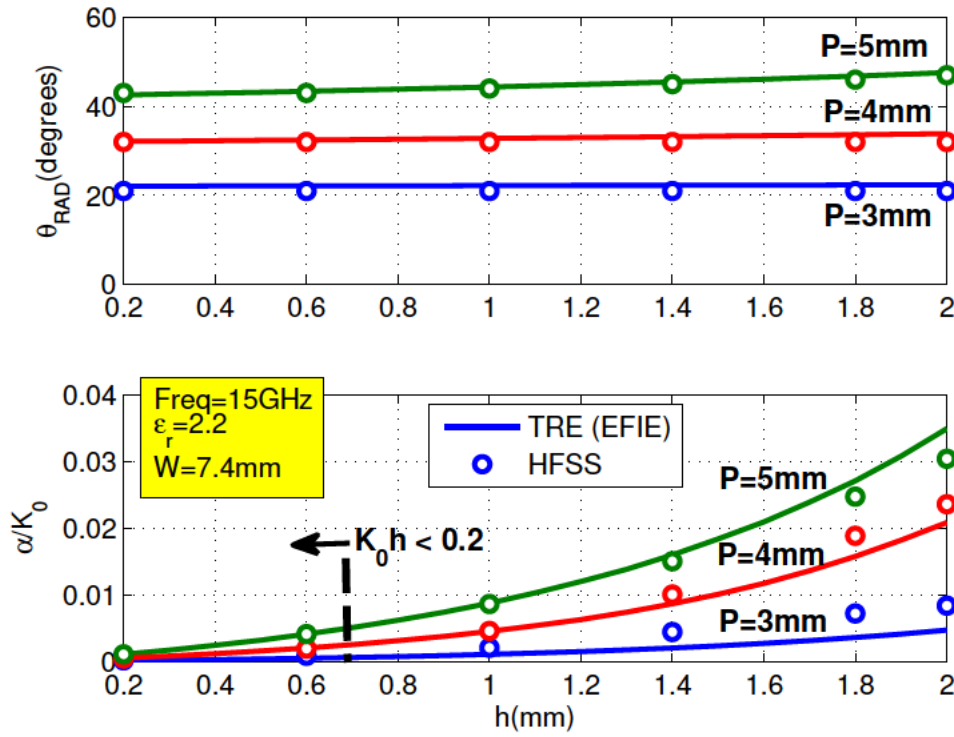


Figure 3.12: Effect over the leaky mode as the thickness of the substrate is increased.

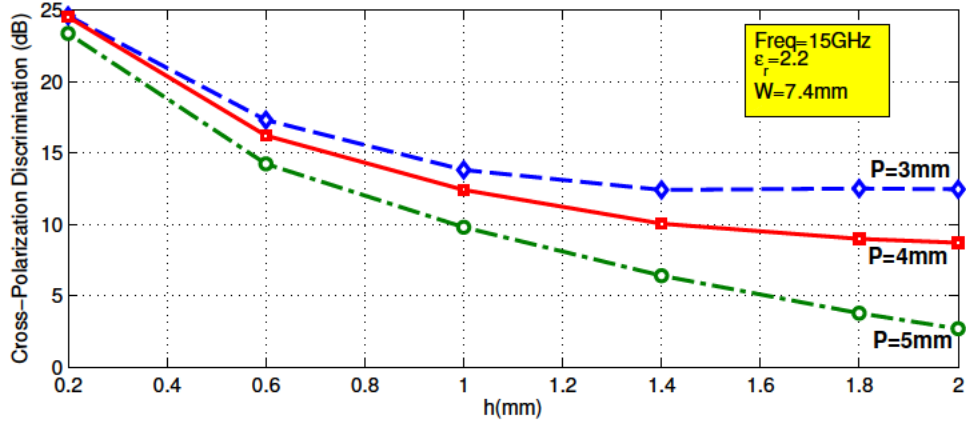


Figure 3.13: Dependence on the polarization discrimination level with  $h$ .

### 3.4 Design Curves and Experiments

In this section two-dimensional dispersion charts are presented to assist in the design of the physical dimensions of several SIW LWAs with flexible control over the scanning angle and the beamwidth [91]. These leaky-modal design curves are validated with experimental results shown in Chapter 2.

#### 3.4.1 Design Curves

As it has been illustrated by the dispersion results presented in the previous section, the two main parameters which allow a simultaneous control of the leaky-mode phase and leakage rates are  $W$  and  $P$  (since the variation of  $W_0$  is not recommended due to the coupling and cross-polarization effects described in Section 3.3.3). An efficient design technique consists of the plot of a two-dimensional dispersion charts [103] as the one shown in Fig. 3.14. Constant- $\theta_{\text{RAD}}$  and constant- $\alpha/k_0$  curves are plotted with continuous black lines and dashed red lines respectively, as  $W$  and  $P$  are simultaneously swept in all the range of useful values ( $W$  from 7 mm to 8 mm, and  $P$  from 2 mm to 6 mm, while the rest of parameters are fixed to  $\epsilon_r = 2.2$ ,  $h = 1.57$  mm,  $d = 1$  mm,  $P_0 = 2$  mm and  $W_0 = 1.5$  mm) and the design frequency is set to 15 GHz.

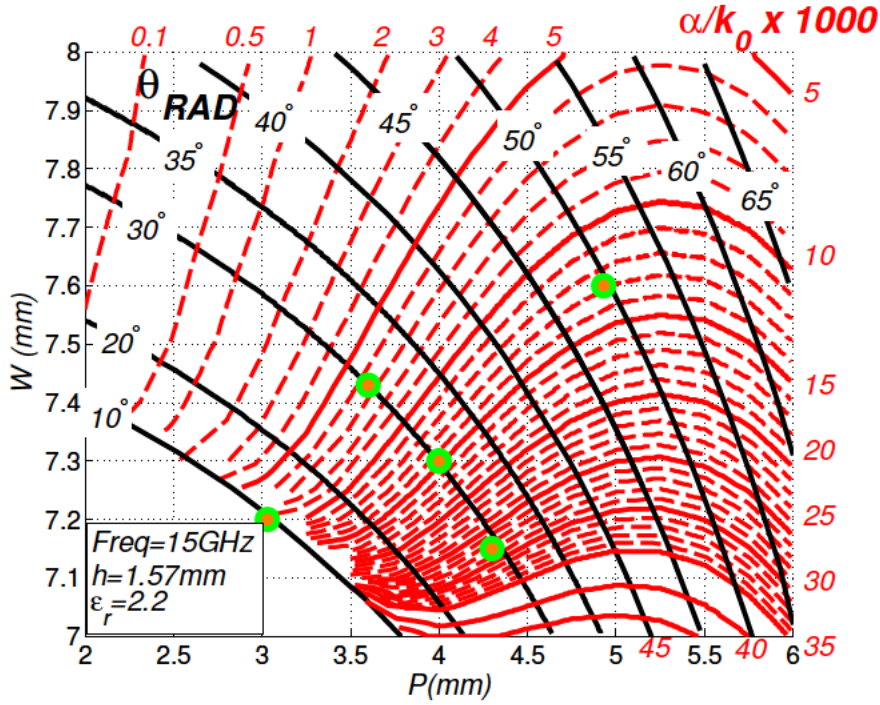


Figure 3.14: Two-dimensional dispersion chart for SIW LWA, including in circles the dimensions of the five manufactured antennas in [91].

Using this 2D dispersion chart shown in Fig. 3.14, the couple of dimensions  $(W, P)$  which provide any requested pair of values  $(\theta_{\text{RAD}}, \alpha/k_0)$  can readily be identified. As an example, it is shown with circles in Fig. 3.14 five different designs points which correspond to the LWAs reported in Chapter 2. These five design points are represented in Fig. 3.14 with green circles, and they correspond to the set of dimensions  $(W, P)$  which were designed in [91] using HFSS to provide the requested values of  $\theta_{\text{RAD}}$  and  $\alpha/k_0$ . As it can be seen, three designs points lie in the constant  $\theta_{\text{RAD}} = 30^\circ$  curve but with different leakage rates, so that the scanning angle is kept constant while the directivity (and beamwidth  $\Delta\theta$ ) is varied as explained in [91]. The other three points lie in three different scanning curves  $\theta_R = 10^\circ, 30^\circ$ , and  $50^\circ$ , and with the appropriate leakage rate values to provide  $\theta_{\text{RAD}} = 10^\circ$  beamwidth and 90% radiation efficiency. The designed dimensions match the ones which were obtained in [91] with 3D full-wave iterative

optimization (trial and error) using HFSS. Therefore, this procedure based on a 2D dispersion chart of the leaky mode can be used as a practical way for obtaining the geometrical dimensions in an arbitrary leaky-wave device, since the computational cost needed for the modal dispersion approach is clearly much lower than the trial-and-error followed in [91]. However, it is important to note that this procedure still shows some limitations due to the necessity of sweeping a wide range of values for  $W$  and  $P$  that later will not be used. In order to improve this fact, a synthesis technique, which directly relates the geometrical dimensions of the structure to the leaky mode, will be presented in Section 4.1. In this manner, the leaky mode can be computed in a more straightforward way than the 2D dispersion chart presented in this section, but with the drawback of only being valid for similar TENs to the one shown in Fig. 3.1b.

### 3.4.2 Experimental results

In order to provide further validation of the results shown along the previous sections, Fig. 3.15 depicts the radiation patterns in polar form obtained for these five SIW LWA designs reported in Chapter 2. The experimental radiation patterns (dashed line) obtained from fabricated prototypes [91] have been compared to theoretical ones (continuous red line) obtained by applying the technique described in Appendix A for calculating the radiation pattern of a 1-D leaky-wave line source, which makes use of the leaky mode computed by using the TEN presented in this chapter.

Fig. 3.15a illustrates the  $H$ -plane radiation patterns for the three designs lying in the  $\theta_{\text{RAD}} = 30^\circ$  curve with different leakage rates, showing the increase in the main beam width as  $\alpha$  is increased. Good agreement is observed between experimental and theoretical far-fields. On the other hand, Fig. 3.15b illustrates the three LWAs designed with similar beamwidth and different scanning angles  $\theta_{\text{RAD}} = 10^\circ, 30^\circ$  and  $50^\circ$ . Again, good agreement is observed between experiments and leaky mode results. Therefore, it can be concluded that the proposed

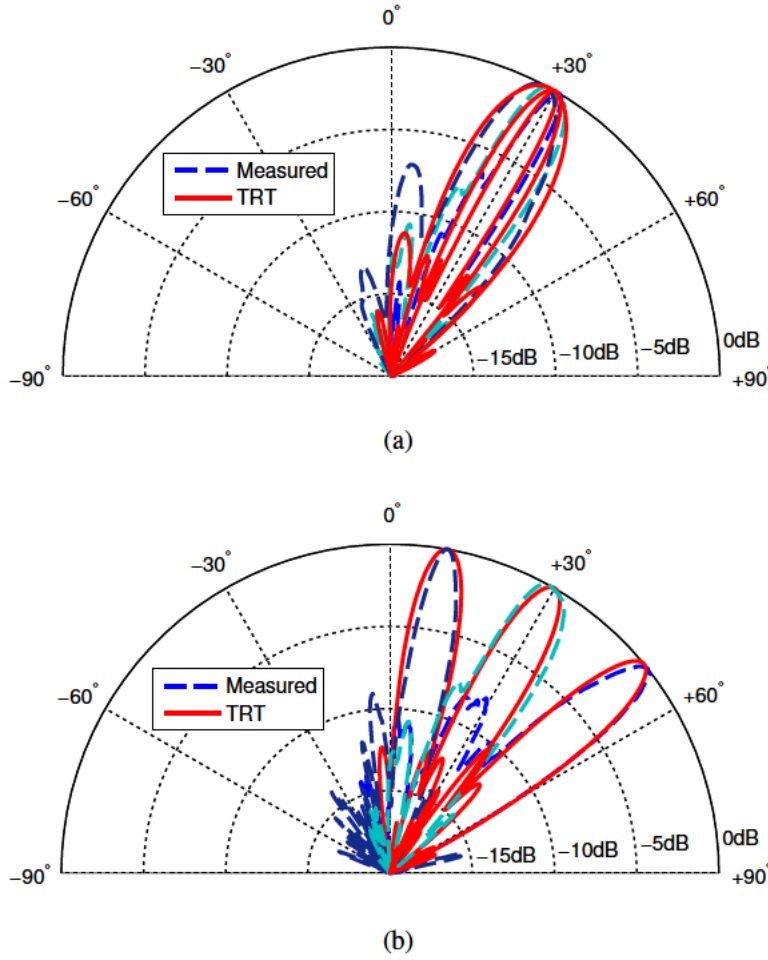


Figure 3.15: Measured and simulated  $H$ -plane radiation diagrams at 15 GHz:  
a) Variation of the beamwidth  $\Delta\theta$  for a constant pointing angle  $\theta_{RAD} = 30^\circ$ .  
b) Variation of the pointing angle  $\theta_{RAD}$  for a constant beamwidth  $\Delta\theta = 10^\circ$ .

TEN serves as a powerful tool for the accurately analysis and efficient design of this promising type of planar LWA in SIW technology.

Finally, with the purpose of showing the flexibility of this TEN for different frequencies, the frequency scanning response of the main radiated beam is shown in Fig. 3.16 for the three antennas with different pointing angle used in [91] and shown in Fig. 3.15b. Good agreement is observed between the scanning predicted from the TEN (continuous line) and measured results (circles).

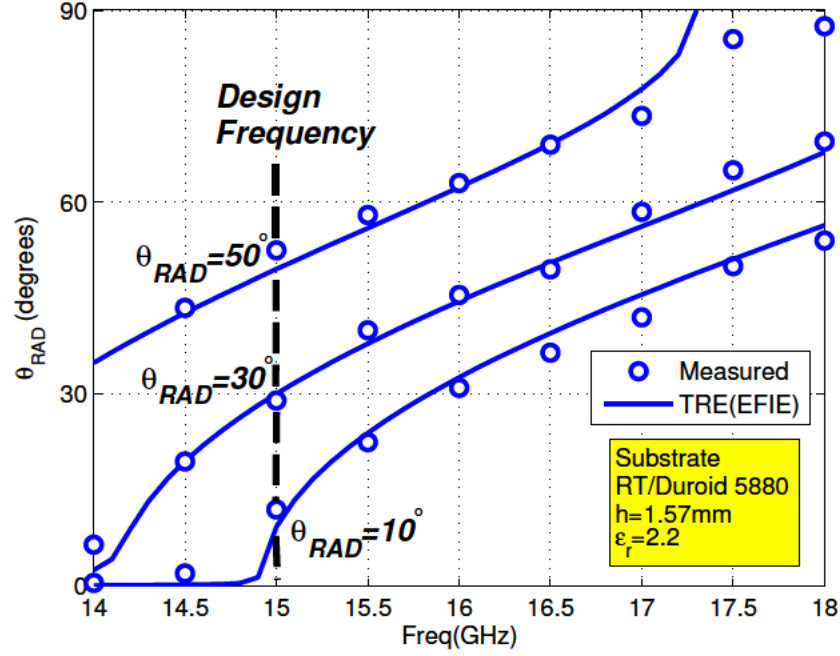


Figure 3.16: Measured and simulated frequency scanning responses for the three antennas designed in [91] to radiate at  $\theta_{RAD} = 50^\circ$ ,  $30^\circ$ , and  $10^\circ$  at the frequency of 15 GHz.

### 3.5 Conclusion

In this chapter a transverse equivalent network (TEN) has been proposed to efficiently analyze the planar LWA (PLWA) presented in the previous Chapter 2. This PLWA is formed by two row of metallic post, similarly to a substrate integrated waveguide (SIW) but with the particularity that one of these rows is sparse enough to allow the pass of energy through a small section of dielectric-filled parallel plate waveguide, which finally produces the radiation at the truncation of its upper plate. Both rows of metallic posts are rigorously analyzed by means of an electric field integral equation (EFIE) technique, which allows accurately modeling and extracting their equivalent inductive and capacitive impedances as function of the unknown incident angle, and thus employing them in the TEN. Moreover, the behavior of this computed impedance is compared with the model

proposed by Marcuvitz, and the limitations of this last model are addressed. It has been shown that a full-wave based model is needed to accurately obtain the behavior of the metallic posts for any values of the period between posts, especially for close posts ( $P/d < 5$ ) and larger incident angles. Once the posts' equivalent impedances have been efficiently formulated for any period  $P$  and any incidence angle  $\theta_{\text{INC}}$ , it has been shown that the TEN associated to the SIW LWA transverse plane gives accurate dispersion results for the leaky-mode complex propagation constant as function of frequency or any geometrical parameter of the antenna. As a result, it has been studied the influence of the main antenna dimensions, showing that the radiating strip width  $W_0$  must be studied in detail to avoid the appearance of unwanted higher-order channel modes, while assuring horizontal linear polarization with elevated XPD. Another trade-off study must be done for the substrate thickness  $h$  and relative constant  $\epsilon_r$ , which must be thick and low-permittivity enough to provide high values of leakage rate, again taking care of the cross-polarization discrimination level. Then, the SIW width  $W$  and the distance between radiating posts  $P$  can be designed using two-dimensional dispersion charts to obtain the couple of dimension  $(W, P)$  which provide the desired values of scanning angle  $\theta_{\text{RAD}}$  and leakage rate  $\alpha/k_0$ , at the design frequency. Experimental results on fabricated prototypes have shown the degree of accuracy and effectiveness of the proposed TEN analysis and design technique. In this way, it has been presented an efficient and powerful tool to analyze and design this promising type of planar LWA in SIW technology, as it will be demonstrated along the next chapters.



# **Chapter 4**

## **Synthesis of Tapered Planar LW Devices**

In this chapter, the synthesis of tapered planar leaky-wave devices is shown. In particular, in Section 4.1 a synthesis technique based on holographic concepts is applied for the design of several leaky-wave antennas, e.g. scanning SIW antenna with reduced sidelobe level, synthesis of broadbeam shaped radiation patterns, generation of radiation nulls and synthesis of near-field focusing patterns. The benefits of controlling both amplitude and phase of the radiated fields are demonstrated in Section 4.2 by correcting the radiation pattern for the case of conformal antennas. In addition, several applications such as an angular bandpass filter in Section 4.3, near-field focusing inside a parallel-plate waveguide in Section 4.4, and a quasi-optical multiplexer in Section 4.5 have been developed. All designs have been manufactured and measured, and the results have been compared to full-wave simulations obtained with commercial software HFSS.

## 4.1 Holographic Pattern Synthesis With Modulated SIW LWAs

Here, the synthesis of one-dimensional (line-source) leaky-wave antennas (LWAs) in substrate integrated waveguide (SIW) technology with modulated geometry is presented, demonstrating the capability to flexibly tailor the radiated fields pattern both in near- and far-field regimes. The synthesis technique is inspired in holographic concepts, which are related to the existence of modulated leaky waves. A systematic design algorithm to obtain the requested modulation of the SIW width and distance between posts to synthesize the desired radiation pattern is described. Several design examples operating at 15 GHz are reported and experimentally validated, showing the power and versatility of the proposed holographic SIW technology.

### 4.1.1 Introduction

In the last few years, increased interest and expectations have arisen among the electromagnetic community regarding the actual possibility to artificially control the propagation properties of electromagnetic waves, developing new concepts such as metamaterials (MM) or transformation optics (TO) [104]. In the field of antenna engineering, the effort is concentrated in the suitable engineering of radiative metasurfaces, so that the radiation pattern is flexibly controlled. This is related to the concept of holographic antennas (HAs) [105], [106], in which a modulated holographic surface generates an objective radiation pattern when it is excited from a known reference field. This intricate relation between microwave holography, metasurfaces, and leaky waves is explained in detail in recently published papers such as [107] or [108]. Basically, the working mechanism of HAs can be interpreted as a transformation of a guided surface wave (SW) into a radiating leaky wave (LW) [107], as illustrated in Fig. 4.1a. The modulation of the

holographic surface geometry is responsible of the generation of this LW, which ultimately creates the objective radiation pattern. Particularly, the use of printed-circuit holographic surfaces has gained interest due to their low cost, low profile, easy modulation, and direct integration of the SW feeder in the antenna substrate [108]–[112].

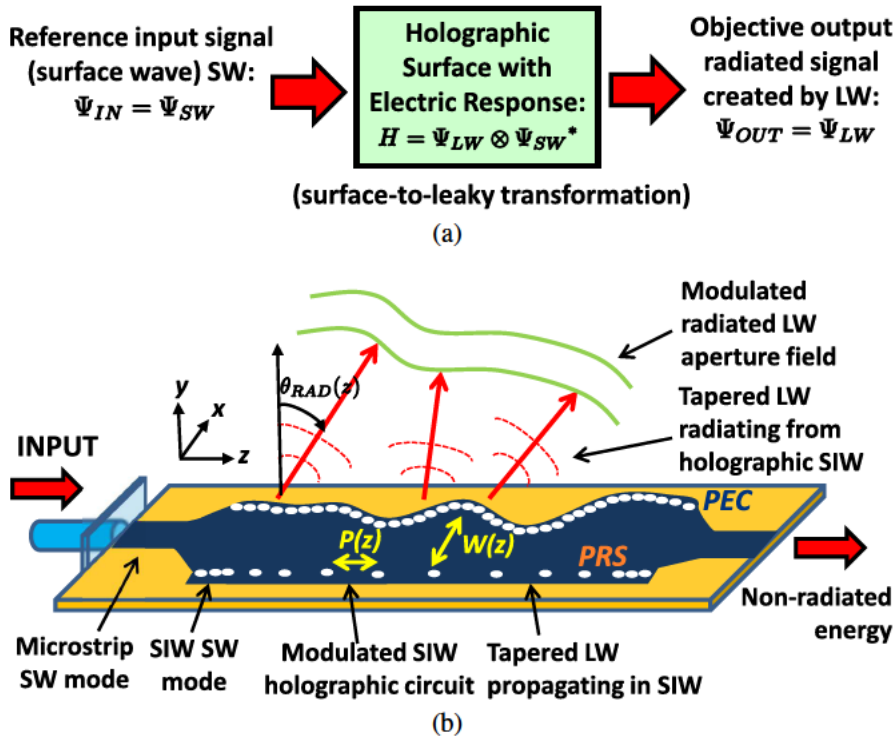


Figure 4.1: a) Holography concepts. b) Scheme of modulated SIW antenna.

In this section an approach based on holographic concepts has been applied to the design of modulated substrate integrated waveguide (SIW) line-source leaky-wave antennas (LWAs), as sketched in Fig. 4.1b. Building on the SIW LWA presented in [91], here it is employed a fast and accurate numerical synthesis technique to develop novel antenna designs with modulated LW apertures, and hence demonstrating the synthesis of unusual radiation patterns in this technology. Nevertheless, the first theoretical work on sinusoidally modulated LWAs was proposed by Oliner&Hessel in 1959 [113], and more recently this has been applied to the

width-modulated microstrip line [114]–[116] and the gap-modulated strip-grating [117]. All these holographic designs are restricted to sinusoidal modulations of the printed circuit, and as a result they are limited to the synthesis of coherent radiation patterns which radiate at a specified angle in the far-field [107]–[117]. However, in this section the synthesis of arbitrary objective radiation patterns is shown, as a result of the flexible modulation of the SIW circuit which is not limited to sinusoidal functions. Section 4.1.2 describes a numerical synthesis technique, which allows for efficiently obtaining the arbitrary modulation of the SIW width  $W(z)$  and distance between posts  $P(z)$  (see Fig. 4.1b), in order to create any desired complex (amplitude and phase) aperture distribution. In Section 4.1.3, several designs examples are reported and experimentally verified, demonstrating the holographic synthesis of unconventional radiation patterns (such as broadbeam shaping in the far-field, generation of wide radiation nulls, or near-field focusing) using modulated SIW antennas.

#### 4.1.2 Synthesis of Modulated Holographic SIW LWA

As it is well-known [6], SIW technology allows guiding a  $TE_{10}$ -like surface wave (SW) inside a dielectric substrate by properly arranging close metal posts. This SW is the reference input signal which excites our modulated SIW holographic line. As it is represented in Fig. 4.1b, the SIW has two main geometric variables which are modulated along its length  $z$ : the width  $W(z)$  of the SIW printed circuit fenced by a perfect electric conductor (PEC) wall and a partially reflective surface (PRS), and the distance  $P(z)$  between the metallic posts located close to a radiating side, which form the PRS. As it was demonstrated in Chapter 2, these two variables ( $W$ ,  $P$ ) allow the transformation of the SW into a LW, with flexible and simultaneous control over the radiation angle  $\theta_{RAD}$  and the normalized leakage rate  $\alpha/k_0$ .

In this way, here it is proposed the modulation of the SIW printed circuit, so that the SW-to-LW transformation can be accurately controlled at any longitudinal

point  $z$  of the radiating aperture, creating any complex aperture distribution of the form:

$$E_{\text{RAD}}^{\text{APERT}}(z) = M(z) \cdot e^{j\phi(z)} \quad (4.1)$$

whose amplitude  $M(z)$  and phase  $\phi(z)$  terms can be respectively related to the modulation functions of the LW leakage rate  $\alpha(z)$  and pointing angle  $\theta_{\text{RAD}}$  by [82]:

$$\alpha(z) = \frac{1}{2} \frac{|M(z)|^2}{\frac{1}{\eta} \int_0^{L_A} |M(\tau)|^2 d\tau - \int_0^z |M(\tau)|^2 d\tau} \quad (4.2)$$

$$\beta(z) = k_0 \sin \theta_{\text{RAD}}(z) = -\frac{\partial \phi(z)}{\partial z} \quad (4.3)$$

where  $\eta$  is the radiation efficiency and  $L_A$  is the antenna radiating length. From (4.2) and (4.3), it can be obtained the modulation of the LW longitudinal complex wavenumber  $k_z$  along the antenna length, which is needed to synthesize any desired complex aperture distribution (4.1):

$$k_z^{\text{LW}}(z) = k_0 \sin \theta_{\text{RAD}}(z) - j\alpha(z) \quad (4.4)$$

The most intriguing part of the holographic synthesis design comes when one wants to relate the desired electromagnetic modulation of the LW (4.4) with the physical modulation of the holographic surface. Obviously, this step depends on the type of LWA being used, and requires a modal analysis tool able to obtain the dispersion of the LW in the structure under study. Closed-form transcendental dispersion equations were obtained by Oliner and Hessel in [113], but they were valid only for sinusoidal modulations, and these equations provided the requested modulation of the equivalent surface reactance, but not the final modulated geometry.

Here it is used the transverse equivalent network (TEN) developed in Chapter 3, which is similar to the one described in [118]. The TEN relates the main dimensions of the SIW structure with the transverse wavenumber  $k_x$ , as it can be

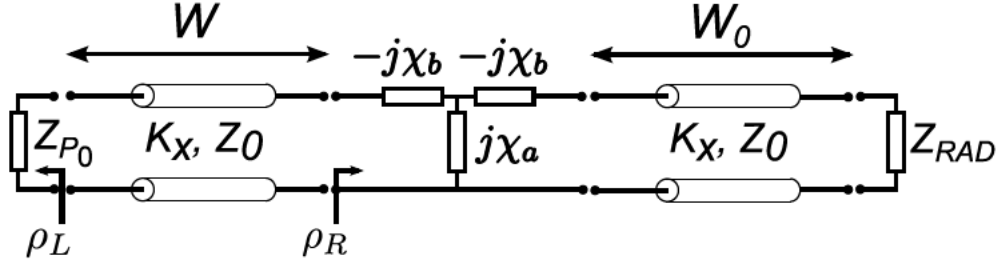


Figure 4.2: Transverse equivalent network with its associated lumped elements for the SIW LWA.

seen in Fig. 4.2. Particularly, the SIW width  $W$  and the transverse length  $W_0$  of the upper plate extending beyond the PRS are represented. In addition, the row of metallic posts acting as PRS and with arbitrary period  $P$  has been modeled with a T-network formed by the reactances  $\chi_a$  and  $\chi_b$ , which have been determined by applying the method of moments technique used in [118]. The modulation of the LW longitudinal wavenumber  $k_z^{\text{LW}}(z)$  (4.4) corresponds to a variation of the LW transverse wavenumber  $k_x^{\text{LW}}(z)$  given by:

$$k_x^{\text{LW}}(z) = \sqrt{k_0^2 \epsilon_r - k_z^{\text{LW}2}(z)} = \beta_x(z) + j\alpha_x(z) \quad (4.5)$$

Eq. (4.5) describes the values for the LW complex transverse wavenumber  $(\beta_x, \alpha_x)$  required at each longitudinal position  $z$  of the holographic antenna. It is important to note that the impedance mismatch between sections with different dimensions is not considered in this approach. However, due to the smooth changes in the geometry along the  $z$ -axis, this effect can be neglected and the TEN still leads to accurate results in a modulated geometry. Both  $\beta_x$  and  $\alpha_x$  can be related to the equivalent reflection coefficients presented by the posts located at each side of the SIW antenna,  $\rho_L$  and  $\rho_R$  (see Fig. 4.2), by using the following transverse resonance equation:

$$\rho_L(P_0, k_x) \cdot \rho_R(P, k_x) \cdot e^{-2j(\beta_x + j\alpha_x)W} = 1 \quad (4.6)$$

It must be noticed the dependence on (4.6) with the two geometric design parameters  $W$  and  $P$ . Particularly, the distance between posts  $P$  determines the equivalent reflection coefficient of the right side of the SIW  $\rho_R$ , which also depends on  $\beta_x$  since it governs the internal incidence angle as explained in [118]. Similarly,  $\rho_L$  can be numerically obtained for the dimensions of the non-radiative posts and any value of  $\beta_x$ . On the other hand, the SIW width  $W$  only appears in the complex exponential of (4.6), and can be expressed as a function of the posts' reflectivity by taking the magnitude of (4.6):

$$W = -\frac{1}{2\alpha_x} \ln (|\rho_L(P_0, k_x)| \cdot |\rho_R(P, k_x)|) \quad (4.7)$$

In the same way, taking the phase of (4.6) it can express the next equation:

$$\phi_L(P_0, k_x) + \phi_R(P, k_x) = 2\pi + 2\beta_x W \quad (4.8)$$

and inserting (4.7) in (4.8) it finally obtains the following transcendental equation:

$$\begin{aligned} \phi_{TRE} = \phi_L(P_0, k_x) + \phi_R(P, k_x) - 2\pi \\ + \frac{\beta_x}{\alpha_x} \ln (|\rho_L(P_0, k_x)| \cdot |\rho_R(P, k_x)|) = 0 \end{aligned} \quad (4.9)$$

which must be numerically solved for the unknown value of  $P$  that satisfies (4.9) for the requested values of  $\beta_x$  and  $\alpha_x$ . In order to clarify the aforementioned procedure for obtaining  $W$  and  $P$ , Fig. 4.3 shows an example for a value of  $\theta_{\text{RAD}} = 30^\circ$  and  $\alpha/k_0 = 0.06$ , while the following design parameters are used:  $f = 15$  GHz,  $h = 0.508$  mm,  $\epsilon_r = 2.2$ ,  $W_0 = 1.5$  mm and  $P_0 = 2$  mm (see [91, Fig. 2a] for a detailed scheme of these dimensions). It is observed as (4.9) (dashed line) is solved for  $P = 6.83$  mm, which corresponds to a value of  $W = 5.63$  mm as is illustrated in continuous line by using (4.7). It is important to highlight that solving (4.9) involves a one-dimensional numerical search with respect to  $P$ , avoiding the much more complicated two-dimensional search in the complex

plane which must be performed for leaky-mode dispersion analysis [82], [118]. Once  $P$  is found, the SIW width  $W$  is directly derived from (4.7), and in this way it obtains the pair of dimensions  $(P, W)$  which produce the desired values of  $\beta_x$  and  $\alpha_x$  (and thus  $\theta_{\text{RAD}}$  and  $\alpha$ ) at any longitudinal position  $z$  of the holographic SIW LWA (4.5).

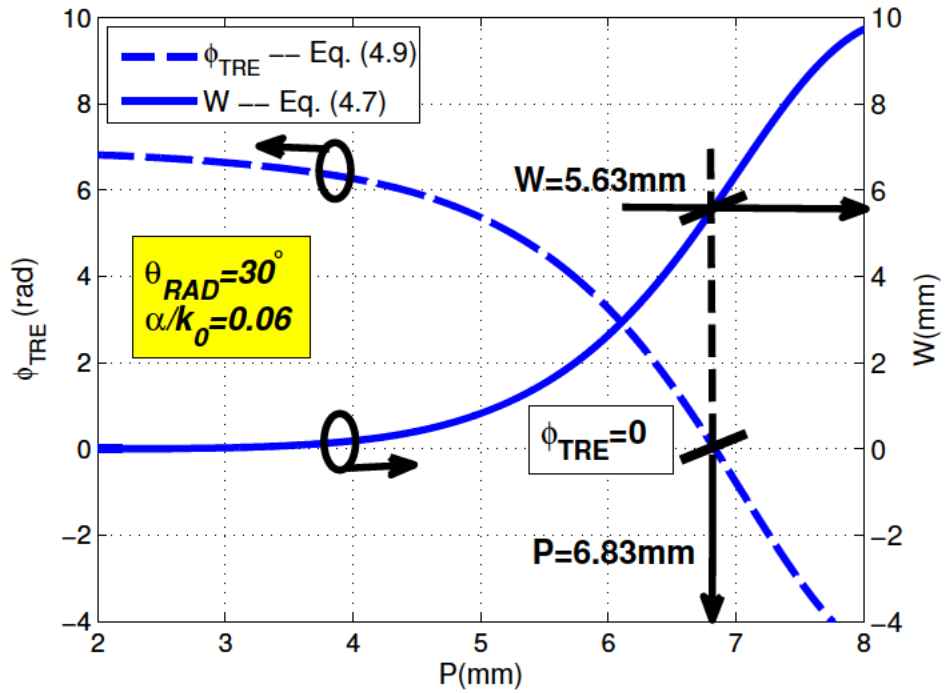


Figure 4.3: Synthesis procedure for obtaining  $W$  and  $P$  given the rest of design parameters.

In the following Section 4.1.3, several design examples illustrate the success of the proposed SIW modulation technique to synthesize arbitrary radiation patterns. For each objective LW aperture distribution (4.1)–(4.3), it will be shown the modulated SIW layout  $(P(z), W(z))$  which is obtained after solving (4.7) and (4.9), as illustrated for the design example in Fig. 4.3. Also, measured results on fabricated prototypes will experimentally validate the designs.

### 4.1.3 Design Examples

All the designs have been manufactured in commercial substrate Taconic TLX-5 with  $\epsilon_r = 2.2$ ,  $\tan \delta = 0.0009$ , and  $h = 0.508$  mm thickness, for a design frequency of 15 GHz and radiation efficiency  $\eta = 90\%$ . All the prototypes are fed by microstrip-to-SIW transitions, which have been optimized with HFSS, as described in [91]. The other fixed parameters are: posts' diameter  $d = 1$  mm, non-radiative posts' distance  $P_0 = 2$  mm, and radiating strip width  $W_0 = 1.5$  mm. As explained, the two variable geometrical parameters which must be modulated to synthesize the desired objective radiation patterns are  $W$  and  $P$ .

#### Scanning SIW Antenna With Reduced Sidelobe Level

The first example involves the synthesis of a  $L_A = 6.75 \lambda_0 = 135$  mm-long aperture field with constant pointing angle  $\theta_{\text{RAD}}(z) = 30^\circ$  and modulated cosine-type amplitude distribution  $M(z)$  at the frequency of 15 GHz. As it is well known [82], this tapered aperture field corresponds to a radiation pattern which is focused at the desired constant angle and with sidelobe level  $SLL = -23$  dB.

Fig. 4.4a shows the requested variation in the LW pointing angle  $\theta_{\text{RAD}}(z)$  and normalized leakage rate  $\alpha(z)/k_0$ , while Fig. 4.4b represents the SIW modulation functions  $P(z)$  and  $W(z)$  obtained when applying the proposed synthesis method. As it can be seen, the separation of the radiating posts must be increased up to  $P = 7$  mm at  $z = 100$  mm to provide maximum normalized leakage  $\alpha/k_0 = 0.06$ , while the antenna edges must be illuminated with negligible leakage which corresponds to a small separation between posts of  $P = 2$  mm. On the other hand, the SIW width must also be modulated from  $W = 7.8$  mm at the edges to  $W = 5.5$  mm at  $z = 100$  mm, in order to correct for the phase aberrations and keep a constant pointing angle  $\theta_{\text{RAD}}(z) = 30^\circ$  along the whole holographic aperture. Fig. 4.4c illustrates the resulting layout with increased scale in the  $x$ -axis to emphasize the modulation of  $W$  and  $P$  along the SIW, while a photograph of

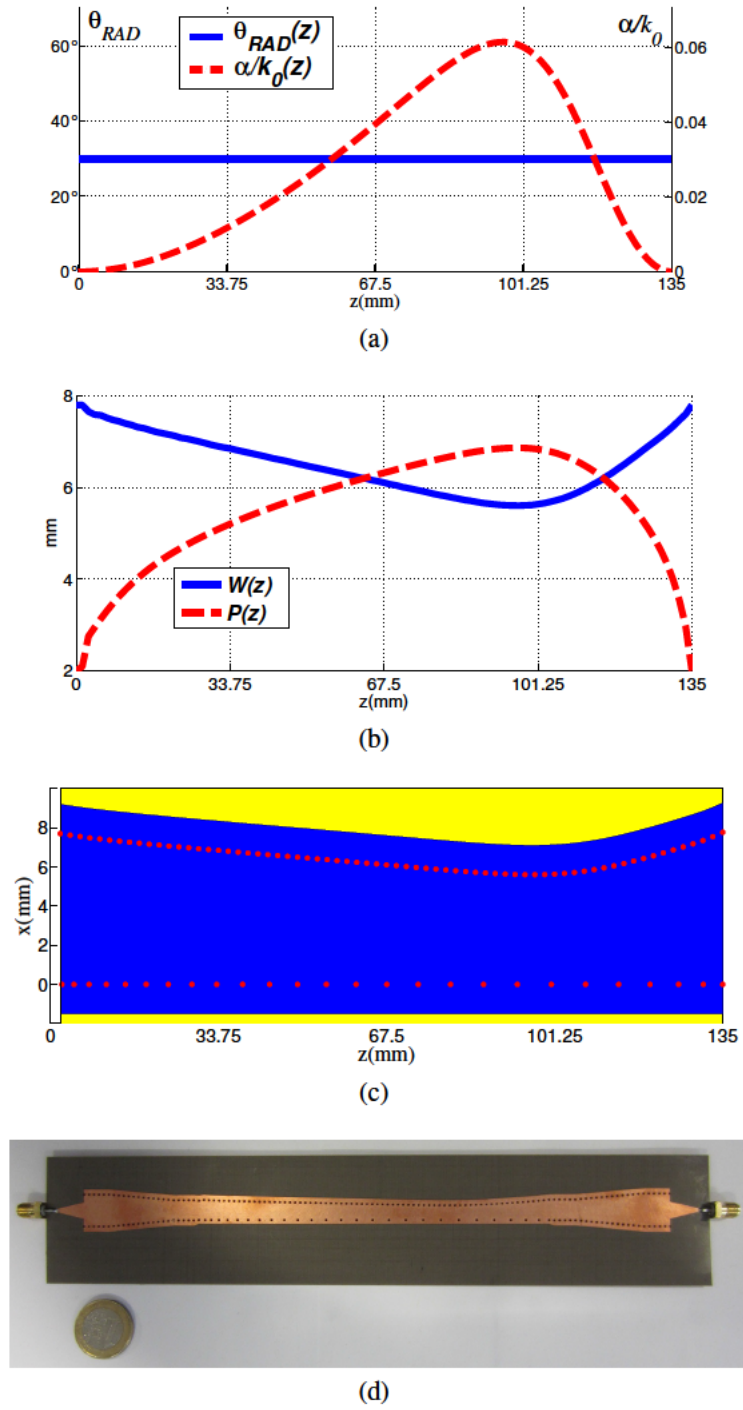


Figure 4.4: a) Modulated LW aperture functions. b) Modulated dimensions. c) Layout and d) manufactured prototype of reduced SLL SIW antenna.

the fabricated prototype including the SMA connectors and the transitions from microstrip-to-SIW is shown in Fig. 4.4d.

The corresponding measured  $S$ -parameters of the antenna shown in Fig. 4.4 are represented in Fig. 4.5. As shown in Fig. 4.1b and Fig. 4.4d, microstrip-to-SIW transitions are used to feed and load the antennas, which allows a direct connection from a SMA connector. Good impedance matching at the design frequency of 15 GHz is observed ( $S_{11} = -25$  dB). Moreover, a  $\eta \approx 90\%$  radiation efficiency deduced from measured values of gain (G) and directivity (D) ( $\eta = G/D$ ) is obtained, which is in agreement with the value of  $S_{21} = -10$  dB and the radiation efficiency derived from the  $S$ -parameters [82], after compensating the material losses with values obtained from full-wave simulations of a lossy model:

$$\eta = 1 - e^{-2\alpha L_A} = 1 - (|S_{11}|^2 + |S_{21}|^2) \quad (4.10)$$

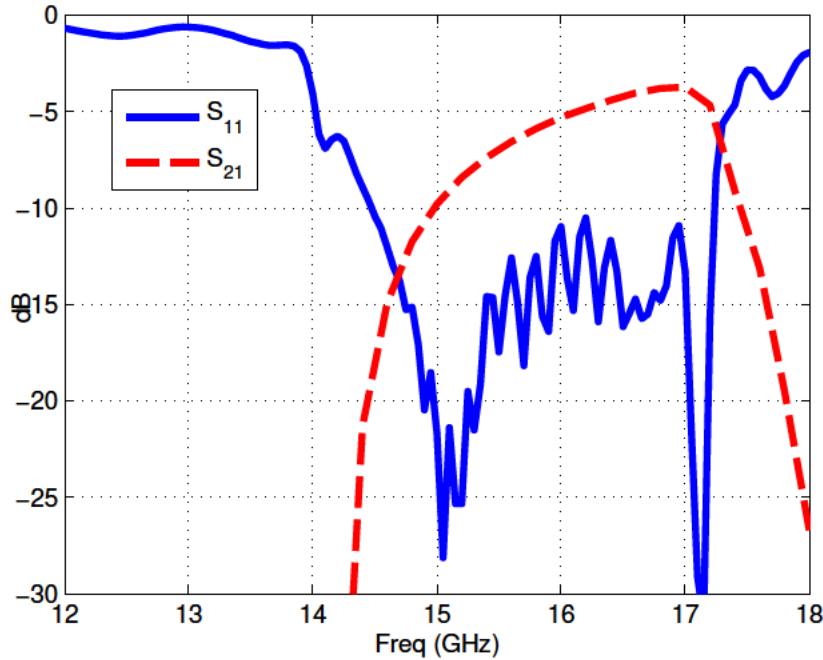


Figure 4.5: Measured  $S$ -parameters for the SIW antenna with reduced SLL and pointing at  $30^\circ$  for the design frequency of 15 GHz.

Fig. 4.6a compares the theoretical objective radiation pattern and the measured one, showing very good agreement in the scanning angle, the main beam width, and the SLL. In Fig. 4.6b, the radiation pattern of the modulated SIW antenna is compared to the one obtained for a non-modulated SIW LWA scanning at the same angle [91], showing the improvement from  $SLL = -8$  dB to  $SLL = -23$  dB. Similar low SLL scanning designs have been recently reported in SIW technology by modulating the offset position of a long slot etched on the broadside of the SIW [119]. However, the modulation of a single geometrical parameter does not allow an independent control for the amplitude and phase of the fields at the aperture, and thus [119] is limited to significant synthesis restrictions. This is of key importance when precise modulation of both amplitude and phase of the aperture fields is requested [120], as it is shown in the following less-conventional synthesis examples.

### Synthesis of Broadbeam Shaped Radiation Patterns

The synthesis of scanned broadbeam radiation patterns from a modulated LW was theoretically proposed in [121], and later in [122] some designs were performed using a slotted leaky waveguide. However, no experimental results have been reported so far to demonstrate this in practice. As it is explained in [120]–[122], the simultaneous modulation of the LW pointing angle and leakage rate is required to obtain an equalized broadbeam which covers a wide angular region, while presenting high rejection out of it. As an example, here it designs an aperture of length  $L_A = 20 \lambda_0 = 400$  mm, with  $-3$  dB beamwidth in the range  $\theta_{RAD} = [15^\circ, 45^\circ]$ , and  $-10$  dB rejection at  $\theta_{RAD} = [10^\circ, 50^\circ]$  at the frequency of 15 GHz. To synthesize this objective radiation function, the LW pointing angle must be modulated with a diverging phase function covering the angular range  $\theta_{RAD}(z) = [10^\circ, 50^\circ]$ , as shown in Fig. 4.7a. Simultaneously, the leakage rate must be varied to produce uniform radiated power per unit angle, obtaining the curve for  $\alpha(z)/k_0$  also plotted in Fig. 4.7a. Using these functions, the curves for the holographic SIW circuit

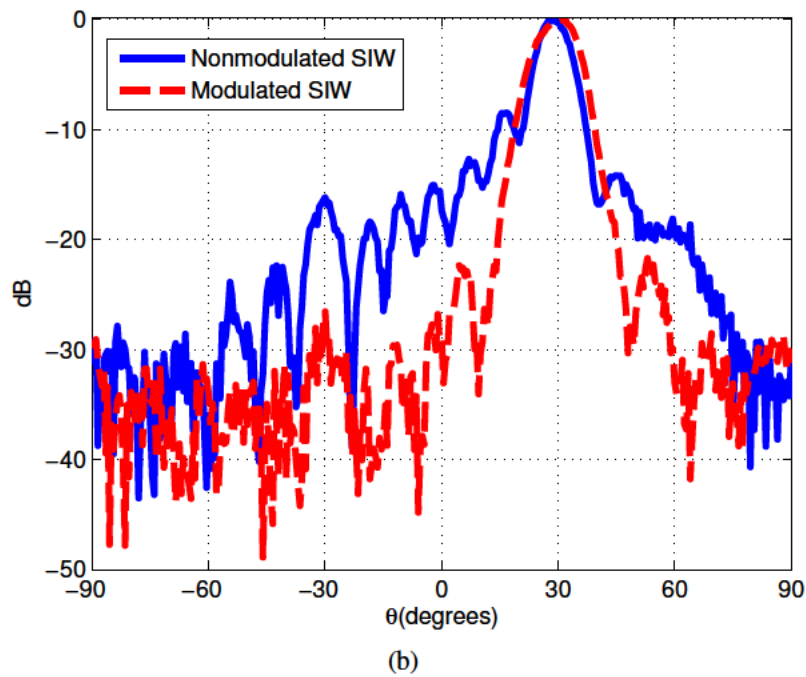
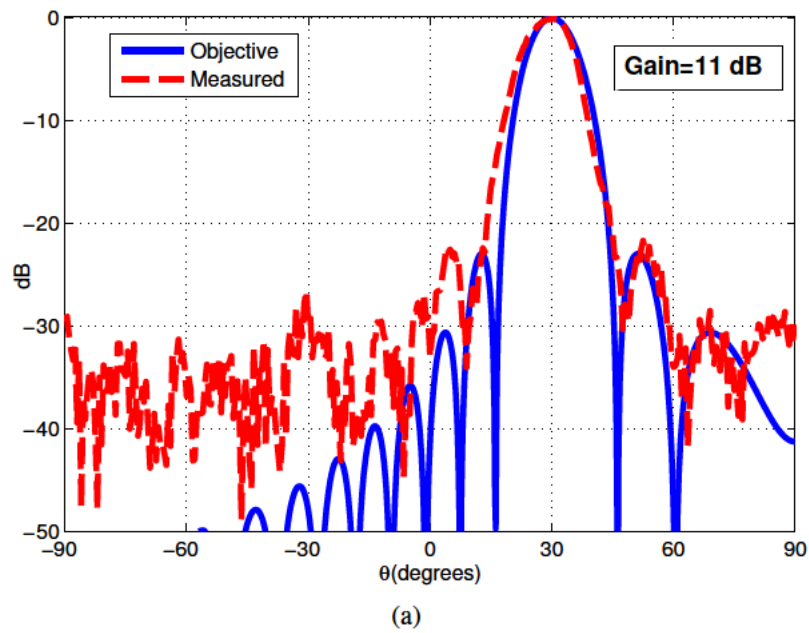


Figure 4.6: a) Objective and measured radiation pattern of reduced SLL SIW antenna for the design frequency of 15 GHz. b) Comparison with a measured non-modulated SIW LWA.

modulation  $P(z)$  and  $W(z)$  represented in Fig. 4.7b are obtained. The variations of  $P(z)$  follow the profile of  $\alpha(z)/k_0$ , with more sparse vias where higher leakage is requested. On the other hand, the variations of  $W(z)$  are needed to create the requested increasing function  $\theta_{\text{RAD}}(z)$  for each value of  $P(z)$  and  $\alpha(z)/k_0$ .

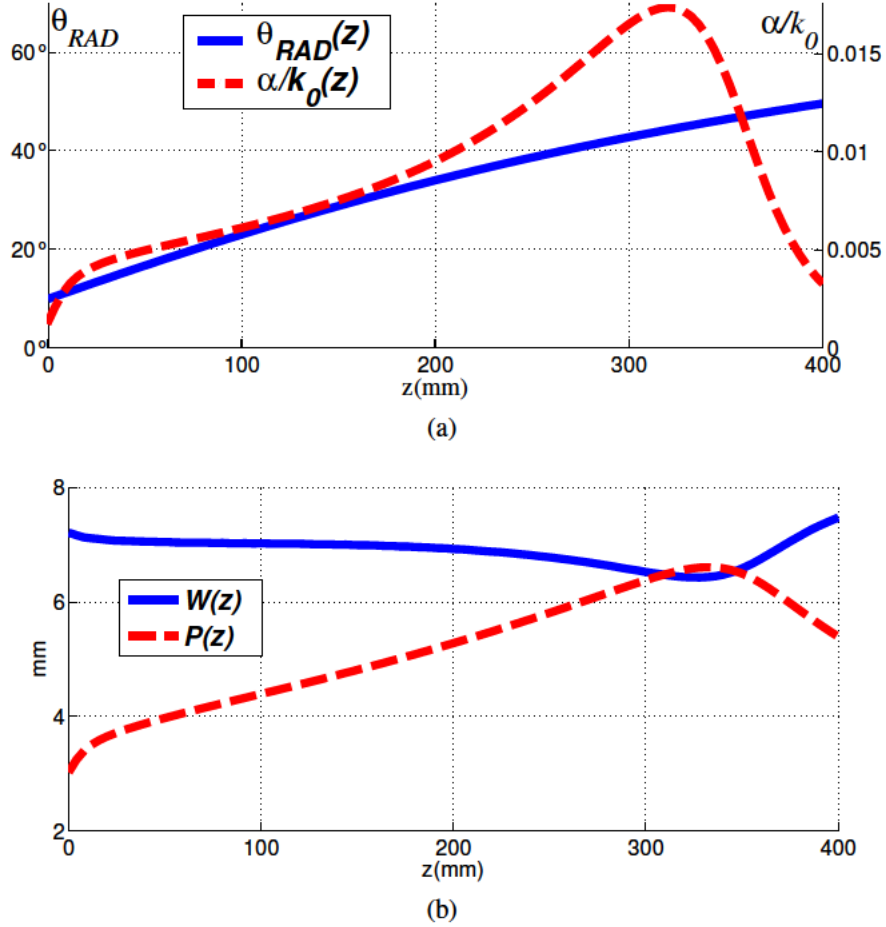


Figure 4.7: a) Modulated LW aperture functions and b) modulated dimensions for broadbeam SIW antenna.

Fig. 4.8 shows the measured  $S$ -parameters for the prototype antenna modulated with the geometry functions  $W(z)$  and  $P(z)$  of Fig. 4.7b. A good matching  $S_{11} < -10$  dB is achieved for the range of frequencies from 15 GHz to 17.5 GHz. In particular,  $S_{11} = -15$  dB and  $S_{21} = -15$  dB are obtained for the design frequency of 15 GHz, providing the desired  $\eta \approx 90\%$  (4.10).

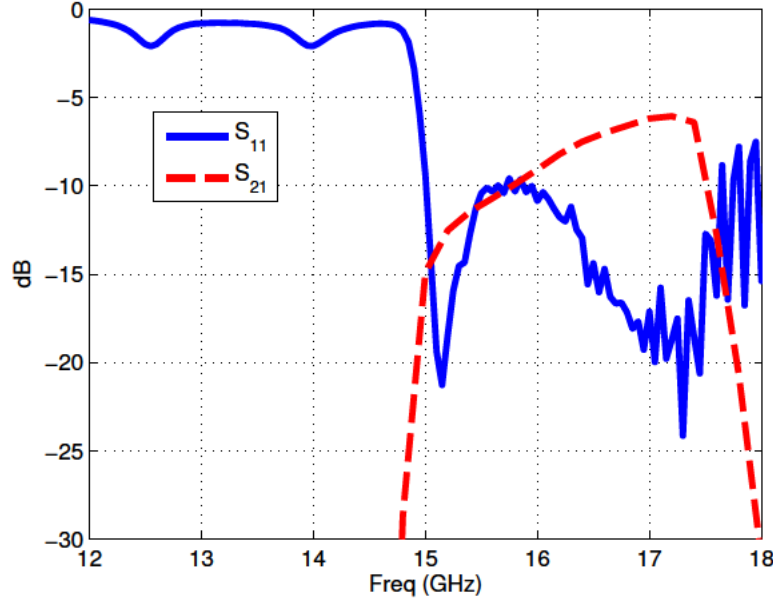


Figure 4.8: Measured  $S$ -parameters for the SIW antenna with broadbeam for the design frequency of 15 GHz.

The objective radiation pattern is plotted with blue line in Fig. 4.9, showing the flat main beam covering the prescribed wide angular region  $\theta_{\text{RAD}} = [15^\circ, 45^\circ]$ , and with high roll-off out of it. The measured radiation pattern agrees very well with theory, showing a bit broader beam (which might be caused by fabrication tolerances) and a reflected lobe at mirrored angles (produced by reflections at the end of the antenna). Nevertheless, the agreement is satisfactory, demonstrating with experiments the practical implementation of a modulated LWA which synthesizes the broadbeam concept.

### Generation of Radiation Nulls

Another unusual type of LW modulation was proposed in [123] to synthesize radiation nulls in wide angular regions. For this purpose, the LW pointing angle and leakage rate must be varied in a very demanding manner, with more abrupt variations as the specified null is deeper and wider [123]. Here, it is experimentally demonstrated the possibility to synthesize such challenging LW variations.

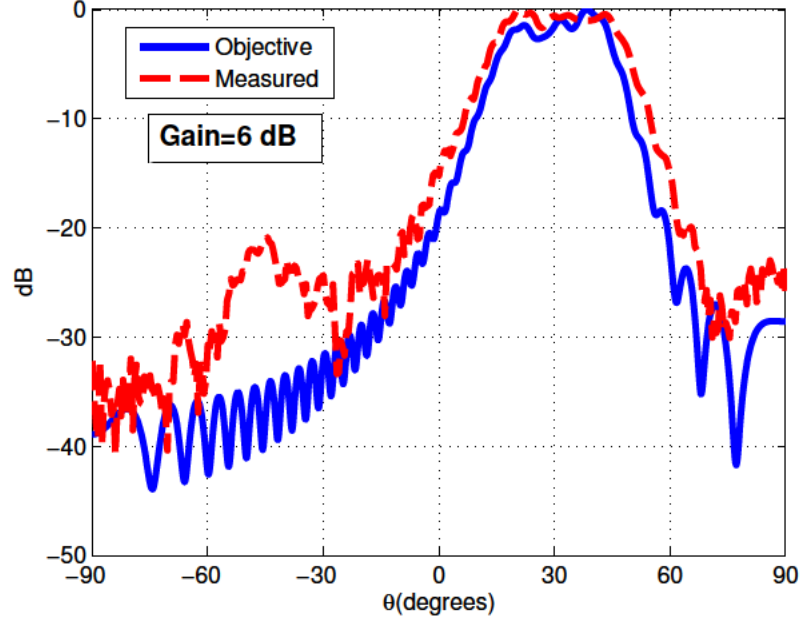


Figure 4.9: Objective and measured radiation pattern of broadbeam SIW antenna for the design frequency of 15 GHz.

As an example, the broadbeam radiation pattern shown in Fig. 4.9 is chosen as the objective function, which is modified with the addition of a  $-20$  dB radiation null in the angular range  $\theta_{\text{RAD}} = [0^\circ, 10^\circ]$  at the frequency of 15 GHz. In this way, it is aimed a growth in the rejection out from the main shaped beam, what may be used to mitigate interferences present in the prescribed angular region or to increase FMCW radar resolution. The requested modulation of the LW to synthesize this objective is shown in Fig. 4.10a, where the aforementioned abrupt and severe variations (peaks and dips) for both  $\theta_{\text{RAD}}(z)$  and  $\alpha(z)/k_0$  functions can be seen. These LW electrical specifications are transformed to SIW circuit geometry, obtaining the functions  $P(z)$  and  $W(z)$  plotted in Fig. 4.10b. As it can be seen, the holographic SIW circuit reproduces in its modulated geometry the requested peaks and falls.

Once the values of  $W$  and  $P$  have been correctly synthesized and its corresponding layout printed, the corresponding  $S$ -parameters of the prototype antenna

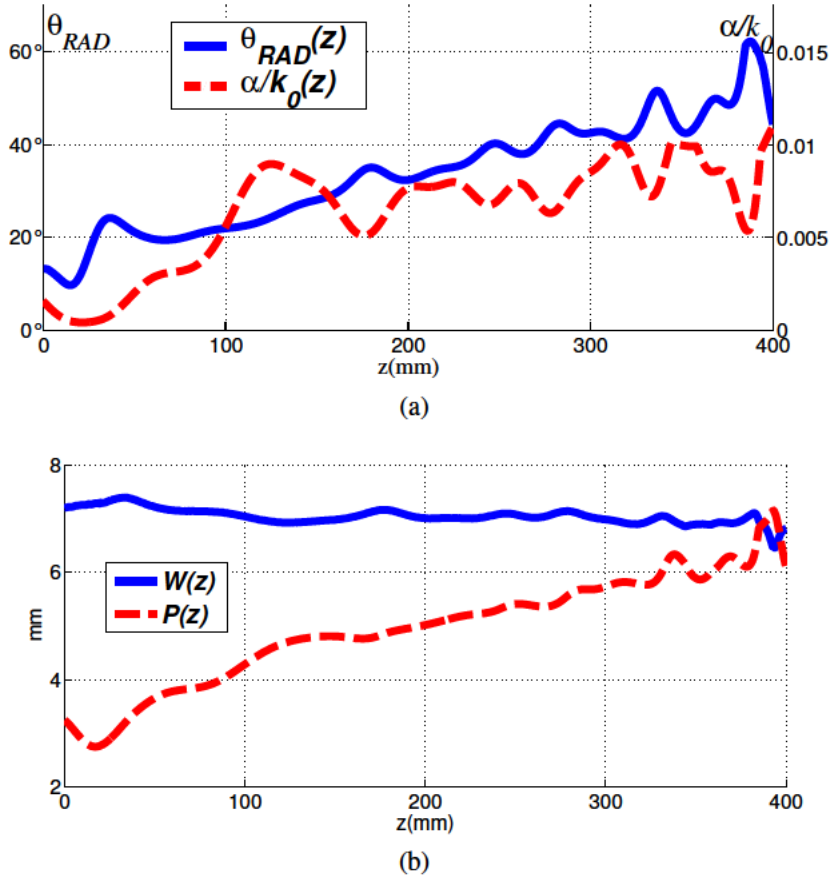


Figure 4.10: a) Modulated LW aperture functions and b) modulated dimensions for broadband SIW antenna with radiation null.

are measured as shown in Fig. 4.11. It is observed how the  $S_{11}$  is below  $-10$  dB for the entire range of frequencies from 15 GHz to 18 GHz. Moreover, very good matching  $S_{11} = -25$  dB is obtained for the design frequency of 15 GHz, while keeping  $S_{21} < -10$  dB to assure that 90% of the power has been radiated.

The theoretical objective and the measured radiation pattern are represented in Fig. 4.12, showing excellent agreement and thus demonstrating the power of the proposed holographic SIW technology to synthesize very demanding radiation specifications. As desired, a radiation null in the prescribed range  $[0^\circ, 10^\circ]$  has been successfully created, resulting in an increased rejection in this angular zone if compared to the pattern shown in Fig. 4.9.

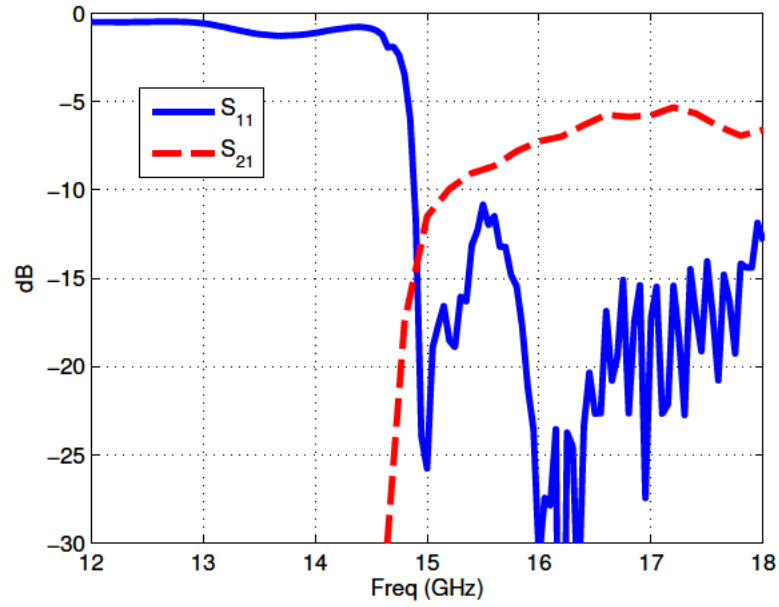


Figure 4.11: Measured  $S$ -parameters for the SIW antenna combining a broadbeam pattern with a radiation null.

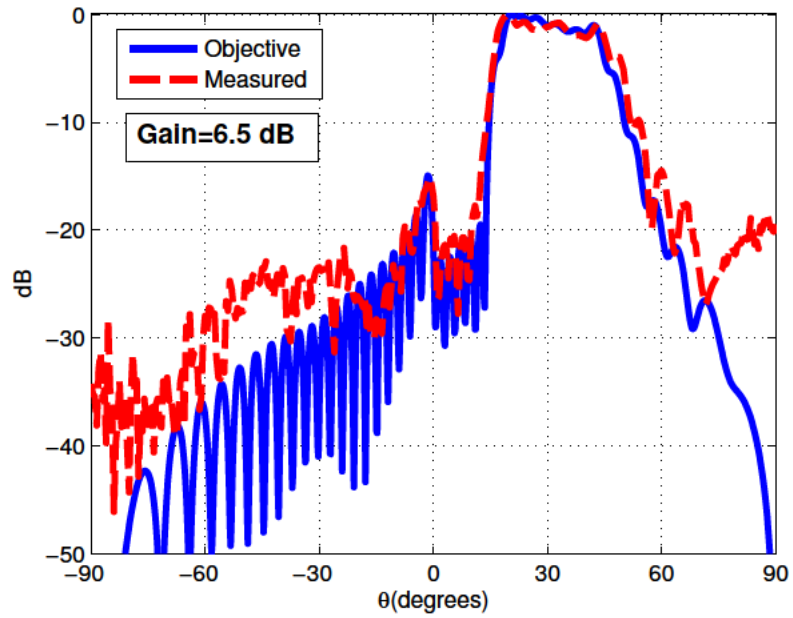


Figure 4.12: Objective and measured radiation pattern of broadbeam SIW antenna with radiation null for the design frequency of 15 GHz.

### Synthesis of Near-field Focusing Patterns

The last unconventional example is dedicated to the synthesis of near-field focusing patterns from a rectilinear LWA. As explained in [121], [124], this can be done by properly modulating the LW pointing angle so that a converging phase front is created, while the leakage rate must be varied to obtain uniform illumination and thus optimize the focusing efficiency. Here it presents the design of a holographic leaky-lens in SIW technology, showing the practical implementation of the theoretical concepts reported in [121], [124]. A holographic near-field focused annular/spiral modulated-slot antenna has also been presented in [125], [126], following a two-dimensional topology similar to the well-known radial line slot array (RLSA) [127]. However, the topology and technology of the designs of [125], [126], are utterly different to the ones presented in this thesis, which are one-dimensional LWAs based on modulated SIW technology. An aperture length  $L_A = 7.5 \lambda_0 = 150 \text{ mm}$  with a focal point at  $[z_F = 8 \lambda_0 = 160 \text{ mm}, y_F = 3 \lambda_0 = 60 \text{ mm}]$  at the frequency of 15 GHz has been chosen. Using the theoretical expressions of [124], this leads to the modulation of the LW shown in Fig. 4.13a. As it can be seen, the LW pointing angle must be modulated with a converging phase function varying from  $\theta_{\text{RAD}} = 65^\circ$  at the beginning of the antenna to  $\theta_{\text{RAD}} = 22^\circ$  at the end, and with a leakage rate function also plotted in Fig. 4.13a. The resulting modulation of the SIW circuit is represented in Fig. 4.13b, where it is particularly illustrative to see how the SIW width must be modulated from wider values ( $W = 8 \text{ mm}$ ) to narrower values ( $W = 6 \text{ mm}$ ) to provide the requested decreasing function for  $\theta_{\text{RAD}}(z)$ .

The theoretical objective near-field pattern obtained with an in-house code developed in [124] is represented in Fig. 4.14a, showing with a 10 dB scale the intensity of the fields for the  $zy$ -plane (see reference axes in Fig. 4.1b) in the vicinity of the 150 mm-long antenna (which is located at the bottom-left corner). As it can be seen, an ellipsoidal focal region whose maximum intensity is situated around the specified focal point ( $z = 160 \text{ mm}, y = 60 \text{ mm}$ ) is theoretically synthesized

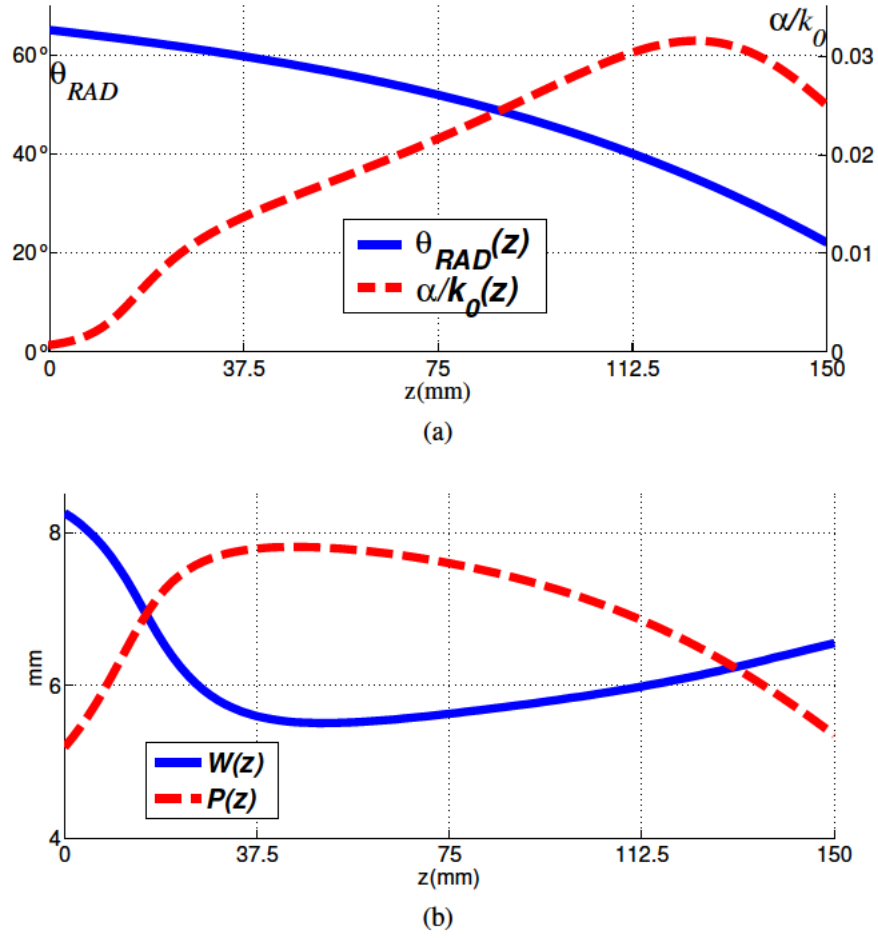


Figure 4.13: a) Modulated LW aperture functions and b) modulated dimensions for SIW antenna with near-field focusing pattern.

with the modulated LW fields. Moreover, this focusing pattern has been measured by using a near-field chamber and the near-field intensity pattern obtained is represented in Fig. 4.14b, showing very good agreement with the objective pattern, and thus demonstrating the capacity of the proposed holographic SIW to synthesize a rectilinear leaky-wave lens.

Finally, the measured input matching (continuous blue line) and insertion loss (red dashed line) of the SIW antenna are shown in Fig. 4.15 as function of frequency. As it can be seen, matching below  $-10\text{ dB}$  is obtained for the entire region from 15 GHz to 17.5 GHz. On the other hand, at the design frequency of

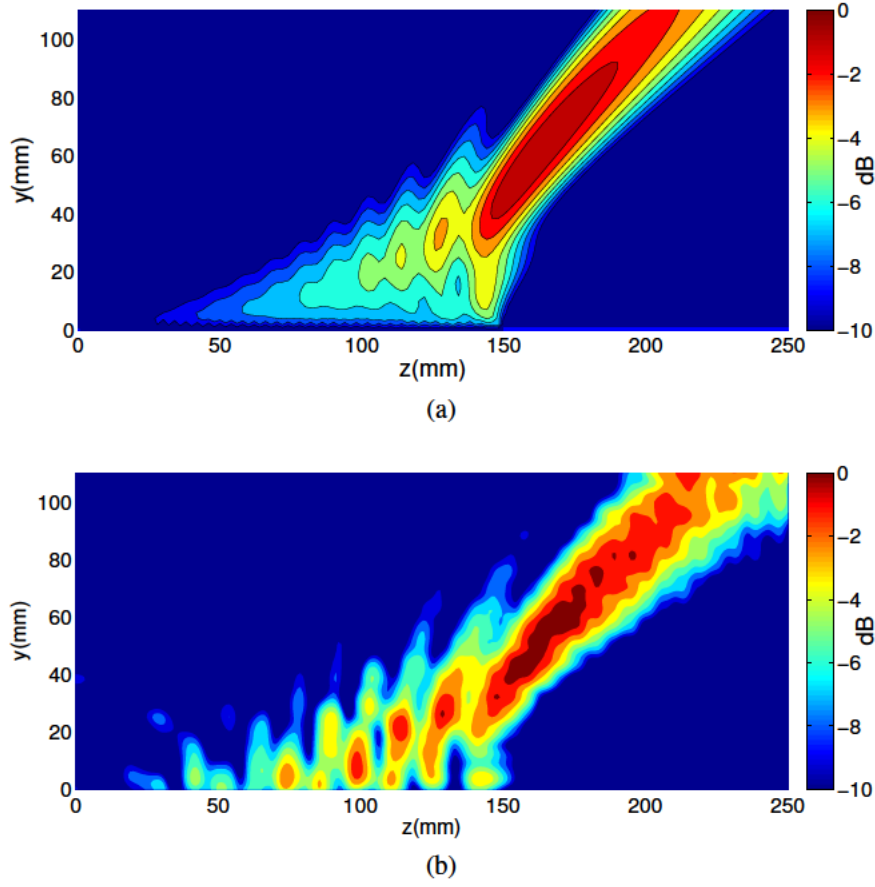


Figure 4.14: a) Objective and b) measured near-field pattern for focused SIW antenna for the design frequency of 15 GHz.

15 GHz the measured  $S_{21}$  is also below  $-10$  dB, thus confirming the  $\eta = 90\%$  radiation efficiency (4.10) for the proposed rectilinear leaky-wave lens.

#### 4.1.4 Conclusion

In this section it has been demonstrated the ability to control the complex aperture leaky-wave fields radiated by holographic antennas in substrate integrated waveguide (SIW) technology. From the transverse equivalent network of the structure, a transcendental close-form equation has been developed, which must be numerically solved to obtain the modulated dimensions of the SIW (width  $W$  and

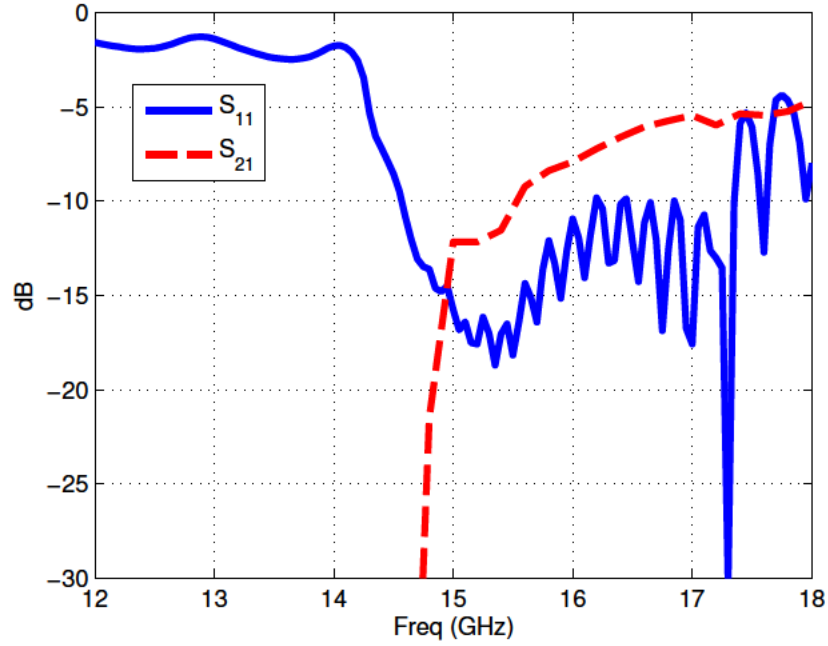


Figure 4.15: Measured  $S$ -parameters for the SIW antenna with near-field focusing pattern for the design frequency of 15 GHz.

distance between posts  $P$ ) that provide the requested variations in the complex leaky fields. This systematic design algorithm has been applied to the synthesis of unconventional radiation patterns and PCB compatible designs for antennas with low sidelobes or radiation nulls adjacent to the radiation peak have been produced, providing cost efficient routes to interference mitigation and FMCW radar resolution. Likewise, low cost techniques have been presented for tailoring the radiation pattern and hence optimising coverage. Moreover, near-field focusing patterns have been experimentally demonstrated, releasing pathways for spatial signal multiplexing or focused curing and hyperthermia. All these designs require the simultaneous and independent control over the aperture phase and amplitude distributions. Previous holographic designs were limited to sinusoidal modulations, and thus could not allow for the synthesis of arbitrarily modulated aperture fields. Prototypes have been fabricated, and the measured results have experimentally confirmed the concept of holographic synthesis in modulated SIW tech-

nology. This flexible control over the synthesis of arbitrary radiation patterns is demonstrated using a modulated planar printed-circuit antenna in SIW technology, which is simply fed from a microstrip line. The proposed SIW holographic technology presents low losses, high radiation efficiency, easy modulation of its geometry, and direct integration with planar circuits, making it very appropriate for the millimeter waveband.

## 4.2 Conformal Tapered Substrate Integrated Waveguide Leaky-Wave Antenna

In this section, it demonstrates the capability to conform a substrate integrated waveguide leaky-wave antenna (SIW LWA) along an arbitrarily curved line by suitably tapering the leaky mode along the antenna length. In particular, it is shown that by means of locally adjusting the pointing angle of the radiated wave, a coherent plane-wave front in the far-field region can be obtained. Combined with the capability to taper the leakage rate along the antenna, this allows designing antennas with high illumination efficiency, which provides higher directivity when compared with previous conformal LWAs such as the half-mode microstrip LWAs (HMLWAs). These concepts have been validated with both measured and simulated results involving the proposed conformal SIW LWA as well as three different configurations of HMLWA: conformal tapered HMLWA, conformal non-tapered HMLWA and conventional rectilinear HMLWA. The antennas have been designed to operate at 15 GHz, and in the case of the SIW LWA an analysis of its frequency scanning response has been performed.

### 4.2.1 Introduction

Conformal antennas are essential in applications where the generation of high directional patterns is required over curved surfaces, such as those encountered in

mobile platforms (e.g. airplanes, automobile, trains) [128]. Phased arrays offer a suitable solution for such applications due to their capability to control the phase of each element individually and therefore provide beamforming agility. Despite such advantages, phased arrays are typically driven by phase shifters, leading to increased cost and manufacturing complexity. Due to their characteristics of high-gain and easy-feeding, leaky-wave antennas (LWAs) [82] offer an interesting solution for conformal high-gain narrowband applications (bandwidths  $BW < 5\%$ ), which avoid the use of complex corporate feeding networks.

On the other hand, conformal designs need to be curved along a predetermined geometry while keeping a directive scanning radiation pattern. Therefore, they need to have flexibility to tailor their radiation pattern according to the prescribed geometry. Planar LWAs have widely proved their capability to taper the leaky mode along the antenna length for a large variety of applications [82], [91], [117], [129]–[134]. Moreover, some planar designs based on half-mode microstrip LWAs (HMLWAs) [72], [135]–[137] and metamaterials transmission lines [138], [139] have been proposed for use on conformal surfaces. Despite the advantageous characteristics of these solutions, they lack the capability of independently controlling the amplitude and phase of the radiated fields at the antenna aperture. Thus, they cannot provide optimum amplitude distribution for a given antenna length, which translates in loss of radiation and illumination efficiency.

In this section, the use of a conformal LWA, which is based on substrate integrated waveguide (SIW) technology [1], is proposed for the design of optimum high-gain planar conformal LWAs. The recently proposed SIW technology allows structures based on equivalent rectangular waveguides to be integrated in conventional printed circuit boards (PCBs). Unlike previous designs of conformal SIW antennas [55], [140], the proposed solution dispenses the need for distributed networks for the adjustment of individual elements phase and amplitude, hence leading to significant savings in complexity and cost.

A schematic view of the proposed conformal SIW LWA is represented in

Fig. 4.16, together with a lateral view that illustrates the curvature radius  $R$  of the antenna. The SIW LWA is fed by a microstrip line (port 1). Appropriate modulation of the leaky wave's complex propagation constant along the antenna enables recovering a plane wave-front in the far field independently of the curvature radius  $R$ . In addition, the control over the amplitude distribution [91], [141] allows an efficient illumination of the antenna aperture and the optimization of the antenna efficiency, thus overcoming the limitation of previous planar alternatives like the HMLWA.

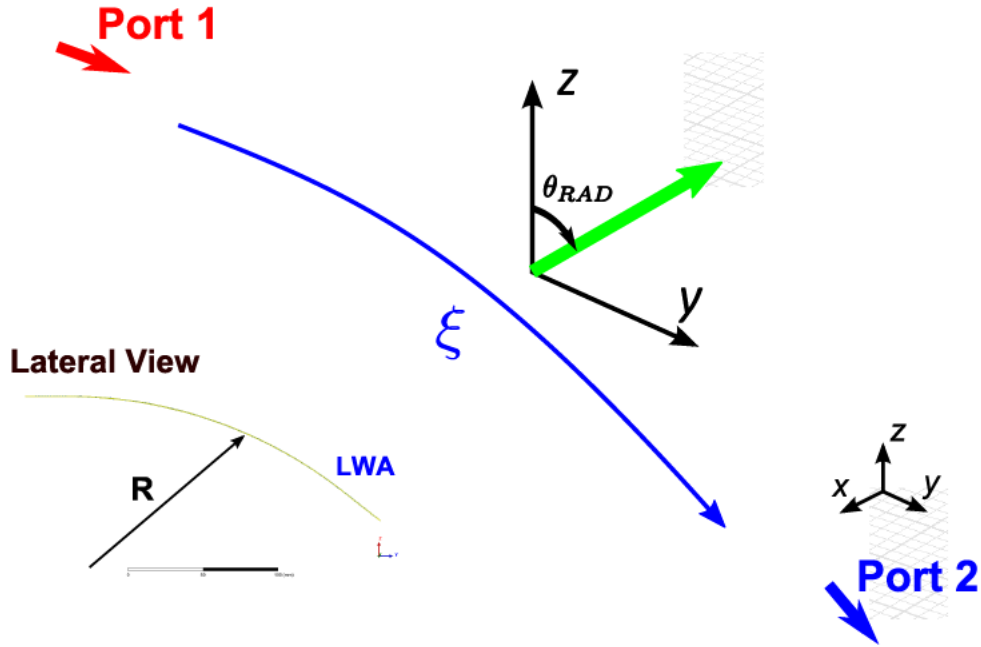


Figure 4.16: Scheme of the conformal tapered SIW LWA and its lateral view.

With the aim of showing the benefits of designing tapered antennas along curved surfaces, an analysis of the main characteristics of the proposed conformal SIW LWA and three types of HMLWA has been carried out. By means of comparing those, it is demonstrated that a suitable modulation along the antenna aperture is required to avoid any deviations in the radiation pattern of the conformal antenna caused by the curved geometry. Measured results on fabricated prototypes operating at 15 GHz have been compared with simulations and theory for

the tapered SIW LWA and three different configurations of HMLWA: (1) conformal tapered HMLWA, (2) conformal non-tapered HMLWA and (3) conventional rectilinear HMLWA.

The rest of the section is organized as follows: Section 4.2.2 describes the technique for tapering the LW mode in order to obtain a suitable radiation pattern in a conformal surface. Furthermore, the tapered designs for the cases of the conformal HMLWA and SIW LWA are presented. In Section 4.2.3 the measured radiation patterns of the different proposed cases of HMLWA and SIW LWA are compared, illustrating the flexibility of the SIW LWA to be conformed and to taper the radiated fields both in amplitude and phase. Next, the frequency scanning response of the designed conformal tapered SIW LWA, is shown in Section 4.2.4. Finally, the conclusions of this section are summarized in Section 4.2.5.

#### 4.2.2 Design of Conformal Tapered LWAs

The radiation properties in tapered LWAs are mainly determined by the leaky mode [82], which is defined by a complex propagation constant that may locally vary along the antenna longitudinal position  $\xi$ :

$$k_{\text{LW}}(\xi) = \beta_{\text{LW}}(\xi) - j\alpha_{\text{LW}}(\xi) \quad (4.11)$$

where  $\alpha_{\text{LW}}$  stands for the leakage rate and  $\beta_{\text{LW}}$  for the phase constant, which determines the leaky-wave angle  $\theta_{\text{LW}}$  of the main radiated beam according to:

$$\sin \theta_{\text{LW}} \approx \beta_{\text{LW}}/k_0 \quad (4.12)$$

In the case of rectilinear (non-curved) LWAs [82],  $\beta_{\text{LW}}(\xi)$  is kept constant in order to obtain a uniform pointing angle  $\theta_{\text{LW}}$  along the whole antenna length  $L_A$ , and therefore generate a plane wave-front scanning at a constant angle  $\theta_{\text{RAD}}$ , and thus  $\theta_{\text{RAD}} = \theta_{\text{LW}}$ .

For the case of conformal surfaces, as illustrated in Fig. 4.16, the leaky mode needs to be varied along the curved profile  $\xi$  for keeping a constant pointing angle  $\theta_{\text{RAD}}$  in the far-field. To this aim, (4.12) can be modified for adapting the local radiation angle  $\theta_{\text{LW}}$  to the curved profile  $\xi$  [142]:

$$\frac{\beta_{\text{LW}}}{k_0}(\xi) = \sin(\theta_{\text{RAD}} - \theta_{\text{zn}}(\xi)) \quad (4.13)$$

where  $\theta_{\text{zn}}(\xi)$  stands for the normal vector to the curved surface, which can be obtained from the local slope of the curved shape:

$$\theta_{\text{zn}}(\xi) = -\arctan \frac{\partial Z}{\partial y}(\xi) \quad (4.14)$$

From the previous equation, it can be noted that larger radii demand smaller corrections for the normal vector  $\theta_{\text{zn}}(\xi)$ . Therefore, smoother variations of the phase constant  $\beta_{\text{LW}}(\xi)$  are required along the antenna length. However, it is important to note that the design procedure can be successfully applied to arbitrary radii lengths and radiation angles  $\theta_{\text{RAD}}$ , since the variation on  $\beta_{\text{LW}}(\xi)$  is independent on the type of technology chosen. It is further noted that the above are valid to the extent that the leaky wave mode is the sole source of far-field radiation.

Fig. 4.17 shows a geometrical interpretation of (4.13) and (4.14). In particular, an example case of a curved surface with radius  $R = 15\lambda_0$  and antenna length of  $L_A = 10\lambda_0$  is used. The desired radiation angle has been fixed to  $\theta_{\text{RAD}} = 45^\circ$ , which gives a local radiation angle  $\theta_{\text{LW}}$  that varies from  $45^\circ$  at the  $y = 0$  end of the antenna gradually increasing to  $7^\circ$  at the other end, as illustrated in dashed-red line in Fig. 4.17. This variation of the local radiation angle is consequence of the variation of the normal vector to the curved surface  $\theta_{\text{zn}}$  (4.14), which is represented in dashed-blue line and varies from  $0^\circ$  at the beginning of the antenna to  $38^\circ$  at the far-end.

On the other hand, the leakage rate  $\alpha_{\text{LW}}(\xi)$  in (4.11) must be also varied to obtain any requested amplitude function of the aperture fields  $M(\xi)$ , and for any

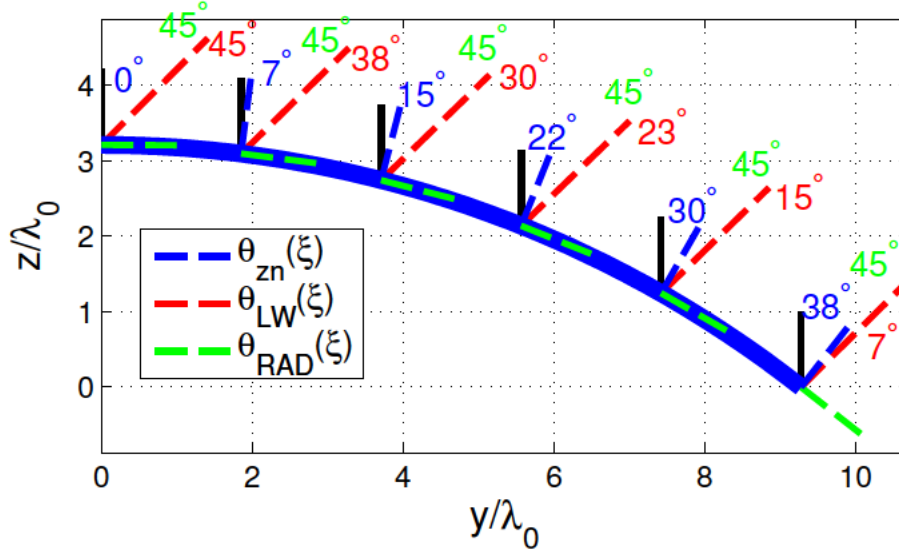


Figure 4.17: Geometrical variation of the main angles for a conformal LWA of length  $L_A = 10\lambda_0$  over a cylindrical surface with radius  $R = 15\lambda_0$  and radiating at  $\theta_{\text{RAD}} = 45^\circ$  for the design frequency of 15 GHz.

radiation efficiency  $\eta_{\text{RAD}}$  [82]:

$$\alpha_{\text{LW}}(\xi) = \frac{1}{2} \frac{|M(\xi)|^2}{\frac{1}{\eta_{\text{RAD}}} \int_0^{L_A} |M(\tau)|^2 d\tau - \int_0^\xi |M(\tau)|^2 d\tau} \quad (4.15)$$

With the purpose of demonstrating the flexibility to synthesize tapered illumination functions in conformal antennas, a quasi-uniform aperture illumination function  $M(\xi)$  shown in Fig. 4.18a has been synthesized for  $\eta_{\text{RAD}} = 90\%$ .  $M(\xi)$  is designed to reduce the diffraction at both extremes of the antenna and improve its matching. It is important to mention that due to the curved geometry some differences in the amplitude of the radiated fields could appear with respect to the non-curved case. However, for practical cases with radii larger than the antenna length  $L_A$ , these differences can be neglected as demonstrated by the analysis theory for conformal tapered LWAs developed in [142]. The corresponding variations of  $\alpha_{\text{LW}}(\xi)$  and  $\theta_{\text{LW}}(\xi)$  for the aforementioned antenna length of  $L_A = 200 \text{ mm} = 10\lambda_0$  are represented in Fig. 4.18b.

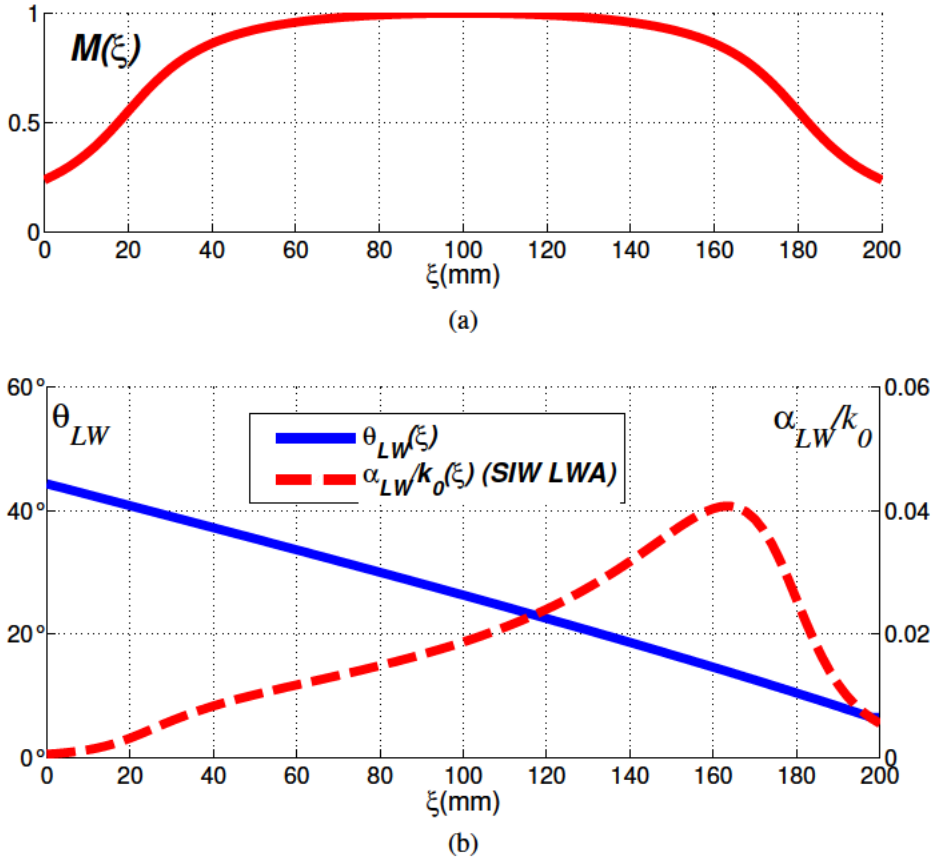


Figure 4.18: Conformal LWA of length  $L_A = 10\lambda_0$ : a) quasi-uniform amplitude aperture illumination function, and b) tapered scanning angle and leakage rate along the antenna length.

The above described method to obtain the leaky mode along a curved surface is next demonstrated by means of two different types of conformal LWAs. First design is based on a HMLWA [135]–[137], whereas for the second one is used a SIW LWA [91]. The curve profile is the same as the one used in Fig. 4.17, with a radius of  $R = 15\lambda_0 = 300$  mm and antenna length of  $L_A = 10\lambda_0 = 200$  mm at the design frequency of 15 GHz. Next, the flexibility to taper both the amplitude and phase of the leaky mode (4.11) in the case of the proposed conformal SIW LWA will be shown, as opposed to earlier HMLWA solutions where only the phase constant can be adjusted.

### Conformal Tapered Microstrip Half-Mode LWA

The first design is based on a microstrip half-mode LWA, which can be suitably conformed along a curved surface by tapering its width  $W$ . In this manner, the leaky-wave angle  $\theta_{LW}$  can be adjusted to correct the curve radius [136].

With the use of a transverse equivalent network (TEN) of a cross-section of the HMLWA [63], the complex propagation constant can be obtained as function of its geometrical parameters. The width  $W$  is then tapered to obtain the requested pointing angle, as shown in Fig. 4.19a. It can be observed how the width  $W$  varies from  $W = 3.92$  mm at the beginning of the antenna ( $\xi = 0$  mm) for providing an angle of  $\theta_{LW} = 45^\circ$ , to  $W = 3.36$  mm at the far-end ( $\xi = 200$  mm), which provides a radiation angle of  $\theta_{LW} = 7^\circ$ . Moreover, the layout of the designed antenna is shown in Fig. 4.19b, where the blue color represents the metal top layer, the red circles the metallic via-holes, and the yellow color the substrate.

Despite the capability of HMLWA to adjust the propagation constant, the leakage rate  $\alpha_{LW}$  is given by the value of  $\beta_{LW}$  and the substrate's properties [143], which does not allow the synthesis of any aperture distribution of the radiated fields. In particular, thicker substrates provide higher leakage rates for the same scanning angle and the same frequency of operation [143] and unless there is a suitable technology to adjust the height of the substrate along the HMLWA, the aperture distribution cannot be independently controlled to achieve, for example, the one represented in Fig. 4.18a. Instead, the designer is left to choose optimum substrate parameters for the entire HMLWA.

The impact of the lack of control over  $\alpha_{LW}$  is illustrated in Fig. 4.19c, where the leakage rate for a HMLWA with a tapered quasi-uniform illumination along the antenna has been represented in pink dash-dot line and the obtained value of  $\alpha_{LW}$  for the tapered HMLWA is represented in red dashed line. In order to obtain a leakage rate approaching the function shown in Fig. 4.18b, and since the only parameter to vary the leakage rate is the substrate, a thin commercial substrate with thickness  $h = 0.254$  mm,  $\epsilon_r = 2.2$  and  $\tan \delta = 0.0009$  has been selected as

an optimum trade-off. However, the leakage rate values obtained are higher than those requested by Fig. 4.18, which leads to a lower illumination efficiency.

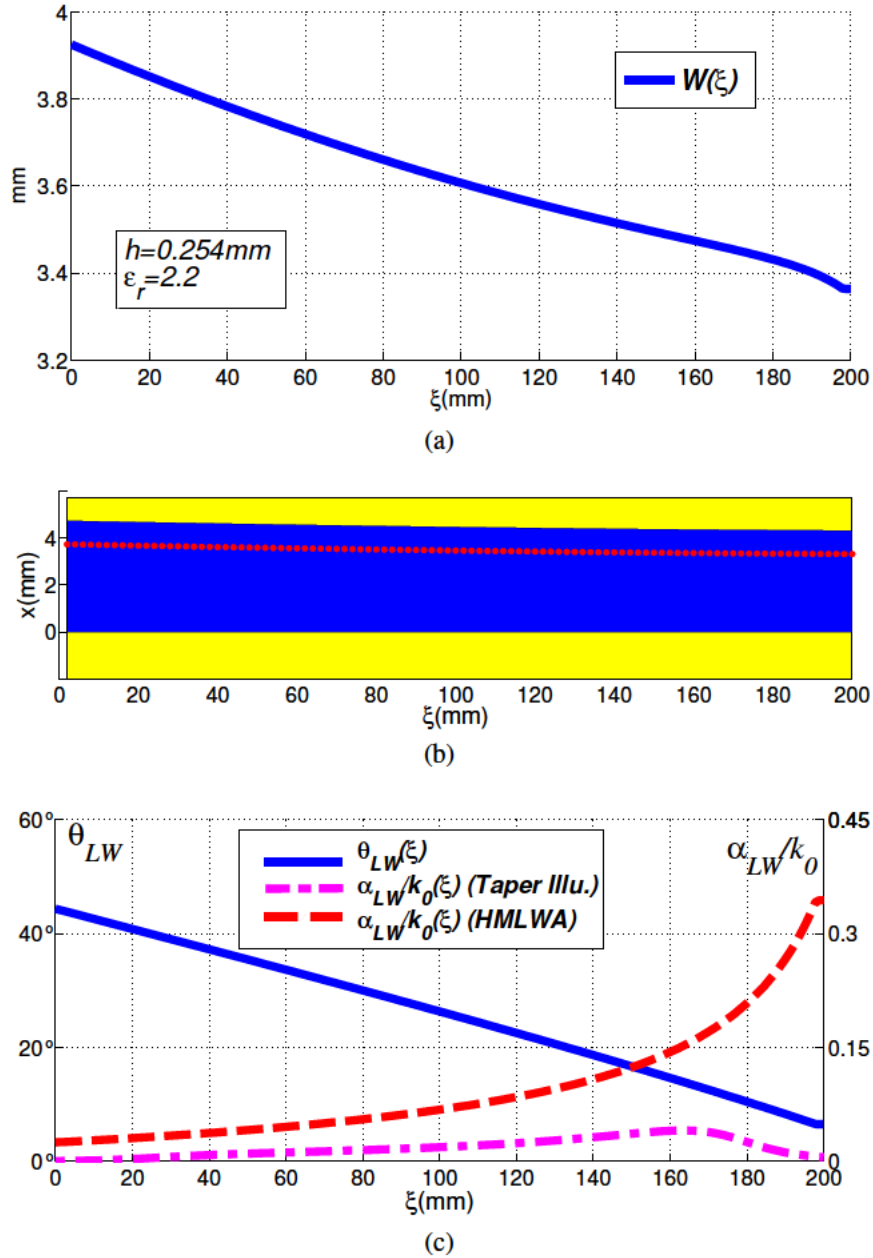


Figure 4.19: Conformal tapered HMLWA: a) modulation of  $W$  along the antenna length, b) corresponding layout for the tapered HMLWA, and c) synthesized and objective leaky-mode's tapering functions at 15 GHz.

### Conformal Tapered SIW LWA

The second design is based on a SIW LWA with capability to independently control the amplitude and phase of the radiated fields (see Fig. 4.20). To this aim, both the width  $W$  and the period  $P$  of the SIW are varied, which allows modifying  $\beta_{\text{LW}}$  and  $\alpha_{\text{LW}}$  of the leaky mode propagating along the SIW [91]. The radiation angle  $\theta_{\text{RAD}}$  is primarily determined by the width,  $W$ , of the SIW, which strongly affects the phase constant  $\beta_{\text{LW}}$  and therefore modifies  $\theta_{\text{LW}}$  according to (4.12). On the other hand, the leakage rate  $\alpha_{\text{LW}}$  is mainly controlled by the separation  $P$  between posts of one of the rows of the SIW. Typically, larger separations between posts provide larger leakage rates, which allow an effective control over  $\alpha_{\text{LW}}$  as function of  $P$ . In this manner, by suitably modifying  $W$  and  $P$  along the SIW a wide range of values for  $\alpha_{\text{LW}}$  and  $\beta_{\text{LW}}$  can be obtained. Therefore, an arbitrary distribution of amplitude and phase along the antenna aperture can be designed with independence of the substrate used, while keeping high radiation efficiency.

In practice, the dependence of the leakage rate and phase constant on  $W$  and  $P$  is coupled and therefore for the case of this SIW LWA the tapered geometry has been obtained using a TEN of the cross section of the antenna [118]. By virtue of the capability to independently control the leakage rate and the phase constant, the substrate thickness is not limited to any value as in the HMLWA, which has allowed the selection of a thicker substrate compared with the HMLWA. In this example, a commercial substrate with thickness  $h = 0.508$  mm,  $\epsilon_r = 2.2$  and  $\tan \delta = 0.0009$  has been used. Likewise, by following the variations of the objective leaky-mode's tapering functions represented in Fig. 4.18b, both the width  $W$  and the separation between vias  $P$  have been modified along the antenna length as shown in Fig. 4.20a. This modulation of the SIW LWA geometry can be clearly observed in the layout view represented in Fig. 4.20b. Moreover, Fig. 4.20c shows characteristics of the leaky mode synthesized for obtaining the suitably conformed SIW LWA, according to the prescribed curve of Fig. 4.17. The flexibility to control the leaky mode of the SIW LWA is demonstrated by comparing the leakage

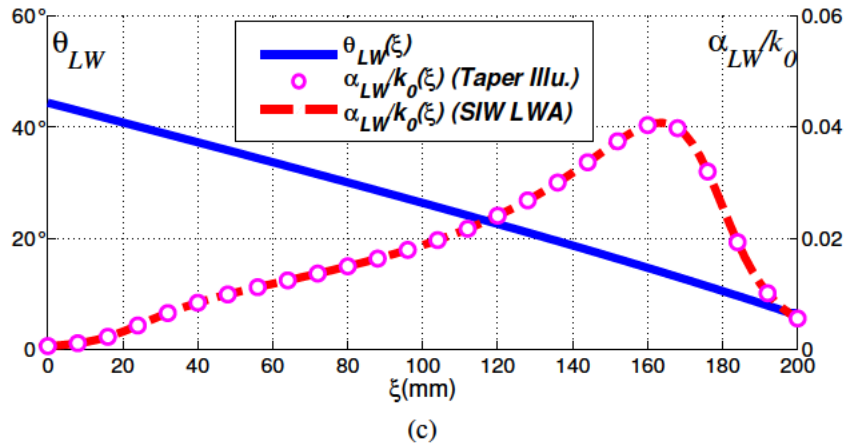
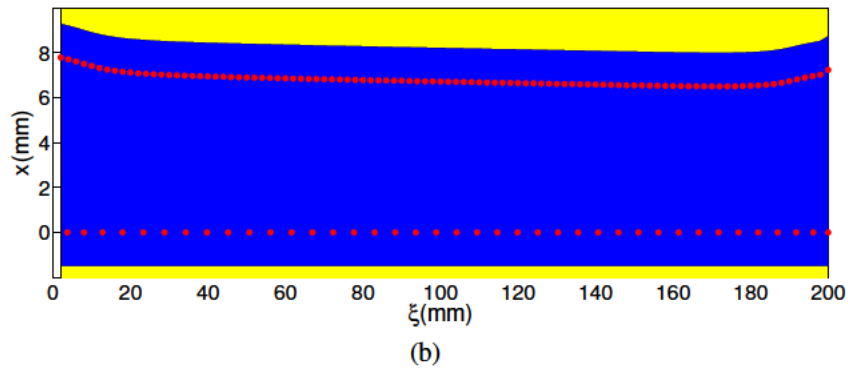
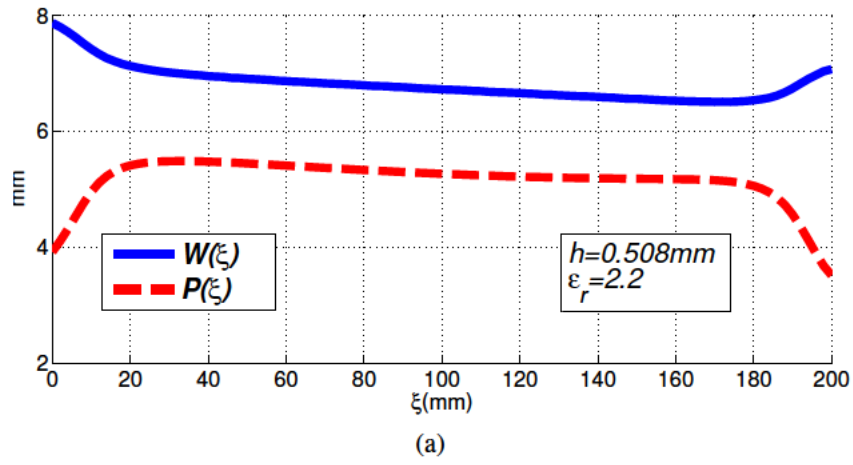


Figure 4.20: Conformal tapered SIW LWA: a) modulation of the width  $W$  and distance between posts  $P$  along the antenna length, b) corresponding layout for the tapered SIW LWA, and c) synthesized and objective leaky-mode's tapering functions at the design frequency of 15 GHz.

rate of the ideal tapered illumination function (pink circles) shown in Fig. 4.18, and the synthesized one (red dashed line). It is observed how  $\alpha_{LW}$  of the tapered SIW LWA follows the prescribed value of  $\alpha_{LW}$  shown in Fig. 4.18b. This figure further shows the variation of the radiation angle  $\theta_{LW}$  along the antenna length to conform the radiation pattern to the curve surface.

### 4.2.3 Measured Radiation Patterns

This subsection shows the radiation patterns at the design frequency of 15 GHz for the different proposed antennas. Simulated results obtained with commercial full-wave software HFSS have been compared with theoretical radiation patterns computed from the engineered leaky mode and with measurements. The conformal designs have also been compared with a rectilinear HMLWA to justify the tapering of the leaky mode. Both the SIW LWA and the HMLWA have been directly fed by a  $50\ \Omega$  microstrip transmission line, which has been tapered to reduce the mismatch [91]. The set-up used for measuring the far-field radiation patterns is shown in Fig. 4.21. It can be seen how the antenna is conformed along a curve surface with radius  $R = 300$  mm, which is inscribed over a foam panel.

The necessity to conform the radiation pattern in order to avoid diverging phase fronts is illustrated along this section with several examples. The first design shows a conventional rectilinear HMLWA with length  $L_A = 200$  mm and a uniform width  $W = 3.92$  mm, which provides a constant pointing angle of  $45^\circ$  along the antenna (see Fig. 4.19c). In Fig. 4.22 theoretical and simulated radiation patterns are compared with measurements for the design frequency of 15 GHz. Good agreement between results is observed. A reflected lobe appears at  $-45^\circ$  in the measured result, attributed to the mismatch at the far-end of the antenna. The level of the reflected lobe is  $-20$  dB below the main beam, which indicates a high radiation efficiency  $> 90\%$  [91].

The second design example shows the case of the same conventional rectilinear HMLWA used in Fig. 4.22, which is now conformed along a curved surface

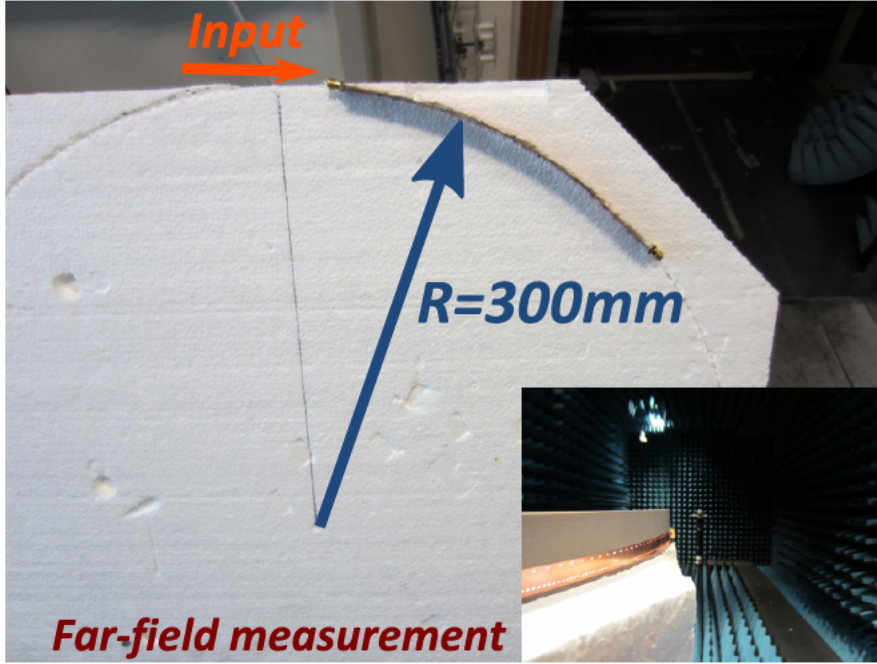


Figure 4.21: Photographs of the conformal antenna over a foam panel and the set-up used for measuring its radiation pattern.

of radius  $R = 300$  mm. Theoretical, simulated and measured radiation patterns are compared in Fig. 4.23, providing a good agreement and confirming the good quality of the measurements and its set-up. It can be clearly noticed how the directivity deteriorates as the main beam is now wider and shifted from  $45^\circ$  to  $60^\circ$ . This result exemplifies the need to taper the HMLWA in order to correct the surface curvature and recover a directive radiation pattern scanning at  $\theta_{\text{RAD}} = 45^\circ$ .

As described in Fig. 4.18, the HMLWA can be tapered to follow a prescribed radiation angle. For this example, it has been used the conformal surface shown in Fig. 4.17, which has a radius of  $R = 300$  mm. In order to correct the distorted radiation pattern of Fig. 4.23, the tapered design proposed in Fig. 4.18 has been used. In this manner, the HMLWA width is varied along the antenna length to provide the angle shown in Fig. 4.19c, which allows that the curvature of the conformal surface can be compensated. Likewise, the variation of the locally radiated angle allows recovering a plane-wave front, avoiding a diverging phase front, and

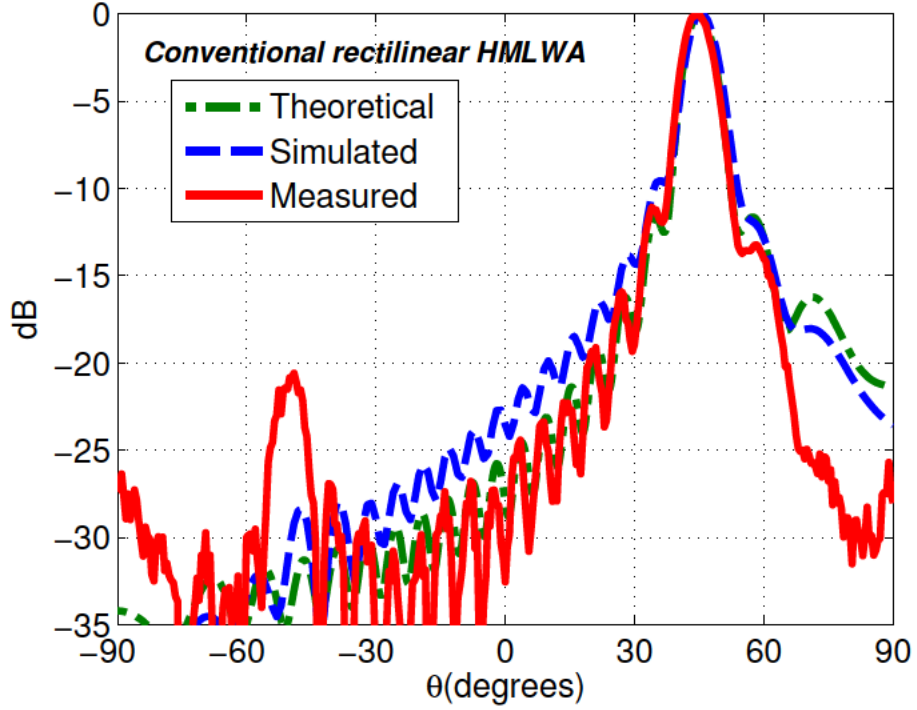


Figure 4.22: Theoretical, simulated and measured radiation patterns at the design frequency of 15 GHz for the conventional rectilinear HMLWA.

thus, a single narrow beam for the far-field radiation pattern can be obtained at the desired angle of  $\theta_{\text{RAD}} = 45^\circ$ .

Theoretical, simulated and measured radiation patterns are compared in Fig. 4.24, showing good agreement between results and confirming the success in tapering the leaky mode, and recovering the desired radiation pattern pointing at  $45^\circ$ .

The last design shows the SIW LWA detailed in Fig. 4.19, which in addition to have the capability to vary the radiated angle as the HMLWA, allows the control in the amplitude of the radiated fields. In this way, the amplitude aperture distribution can be tapered, as shown in Fig. 4.20c. This control over the aperture distribution allows obtaining higher aperture illuminations which provide higher directivities. Moreover, the tapered apertures can also be designed to improve the matching or reduce the SLL [141]. Fig. 4.25 shows a comparative between the-

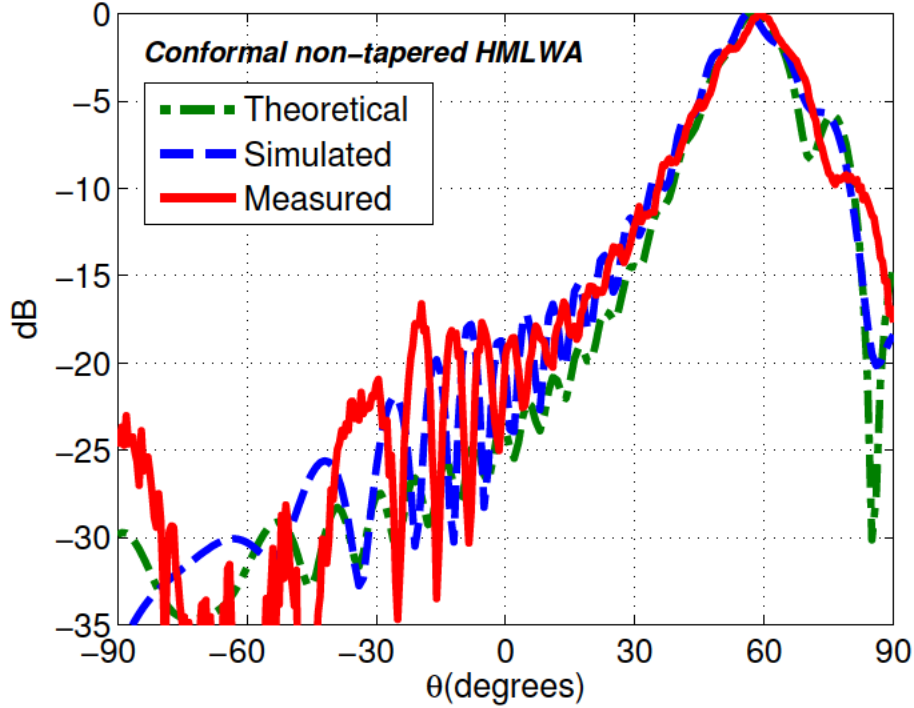


Figure 4.23: Theoretical, simulated and measured radiation patterns at the design frequency of 15 GHz for the conformal non-tapered HMLWA.

oretical, simulated and measured radiation patterns for the case of the conformal SIW LWA. The agreement between results is good, demonstrating the capability to conform the SIW LWA and correct its radiation pattern. It is noticed how a narrow main beam pointing at  $45^\circ$  has been obtained for the design frequency of 15 GHz.

With the purpose of illustrating the effect of the curvature over the phase-front, the radiated near fields for the three proposed designs, i.e. the conventional rectilinear HMLWA, the conformal non-tapered HMLWA, and the conformal tapered SIW LWA, are represented in Fig. 4.26. These plots have been obtained by using a modal tool developed in [142]. As it can be seen in Fig. 4.26a, the rectilinear LWA produces a coherent plane-wave propagating towards the prescribed scanning angle of  $45^\circ$ . However, when the LWA is bent to the described arc, the phase fronts

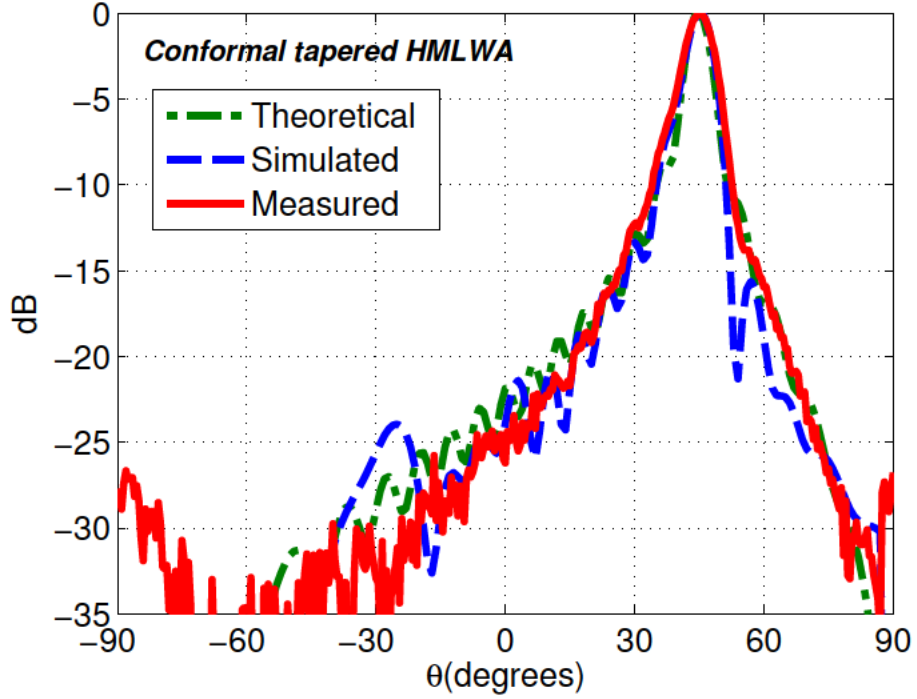


Figure 4.24: Theoretical, simulated and measured radiation patterns at the design frequency of 15 GHz for the conformal tapered HMLWA.

also suffer from this divergence, as it is clearly illustrated in Fig. 4.26b, producing as a result the distorted far-field radiation pattern plotted in Fig. 4.23.

To avoid this diverging phase-front the leaky mode must be properly tapered to correct for this curvature and restore the desired coherent plane-wave focusing at  $45^\circ$  in the far-field. Fig. 4.26c shows the simulated near-fields created by the conformal tapered LWA. It can be seen that the emitted fields present a uniform plane-wave phase front propagating at the desired scanning angle of  $45^\circ$ , despite the curved shape of the LWA, which provides a non-distorted far-field radiation pattern as illustrated in Fig. 4.25.

In addition, in order to summarize the measured results, the far-field radiation patterns for the three different designs over the conformal surface, i.e. the conformal non-tapered HMLWA, and the conformal tapered HMLWA and SIW LWA,

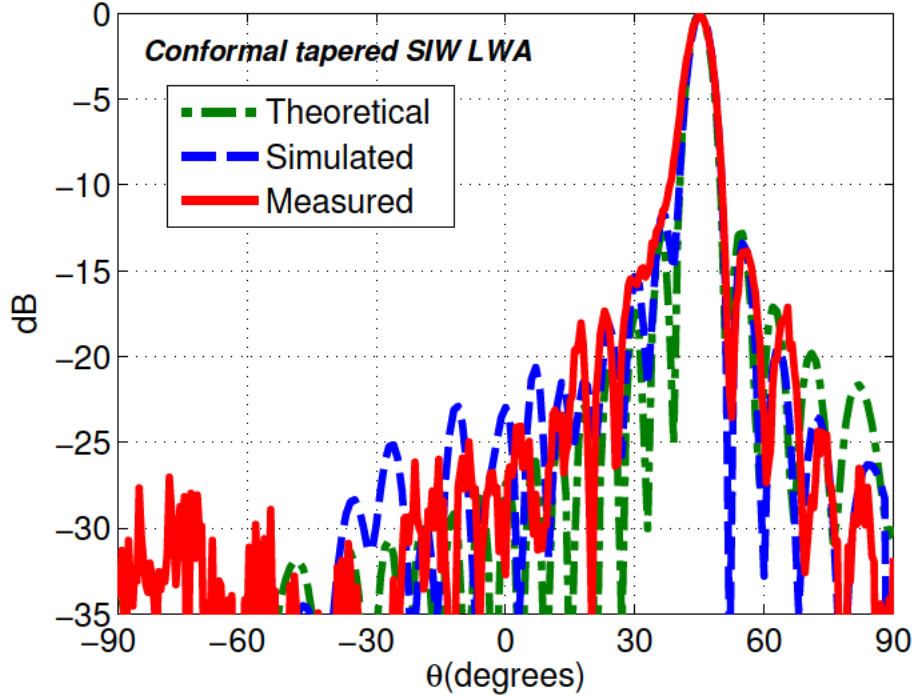
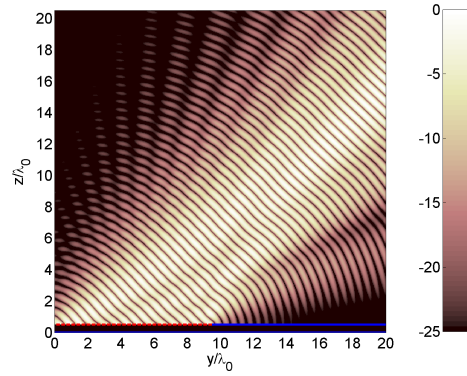


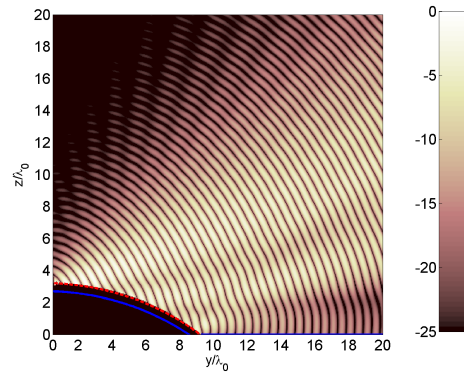
Figure 4.25: Theoretical, simulated and measured radiation patterns at the design frequency of 15 GHz for the conformal tapered SIW LWA.

are compared in Fig. 4.27. It can be noticed from the conformal tapered HMLWA and SIW LWA radiation patterns, the necessity to correct the radiation angle along the antenna length with the aim of compensating the curved surface and to keep a constant pointing angle at  $45^\circ$ .

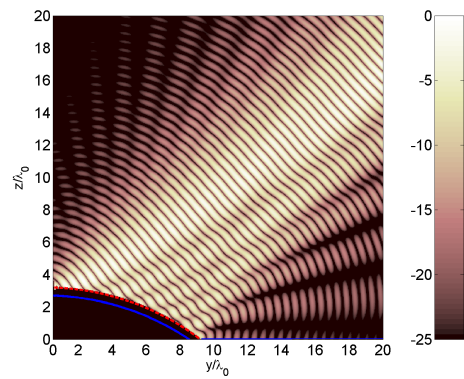
Moreover, it is observed that for case of the SIW LWA the beamwidth  $\Delta\theta$  is reduced due to a higher illumination efficiency compared to the tapered HMLWA. In particular, the conformal tapered HMLWA shows a  $-3$  dB beamwidth of  $\Delta\theta = 8^\circ$ , which is reduced to  $\Delta\theta = 6^\circ$  for the conformal tapered SIW LWA. As explained previously, the control of the amplitude distribution has allowed to design an antenna with a higher aperture illumination, which is translated into a higher directivity in addition of providing a wider flexibility to choose the antenna substrate.



(a)



(b)



(c)

Figure 4.26: Near-field radiation patterns for the designed: a) non-tapered rectilinear HMLWA, b) non-tapered conformal HMLWA, and c) tapered conformal LWA, with an antenna length of  $L_A = 10\lambda_0$  at the design frequency of 15 GHz.

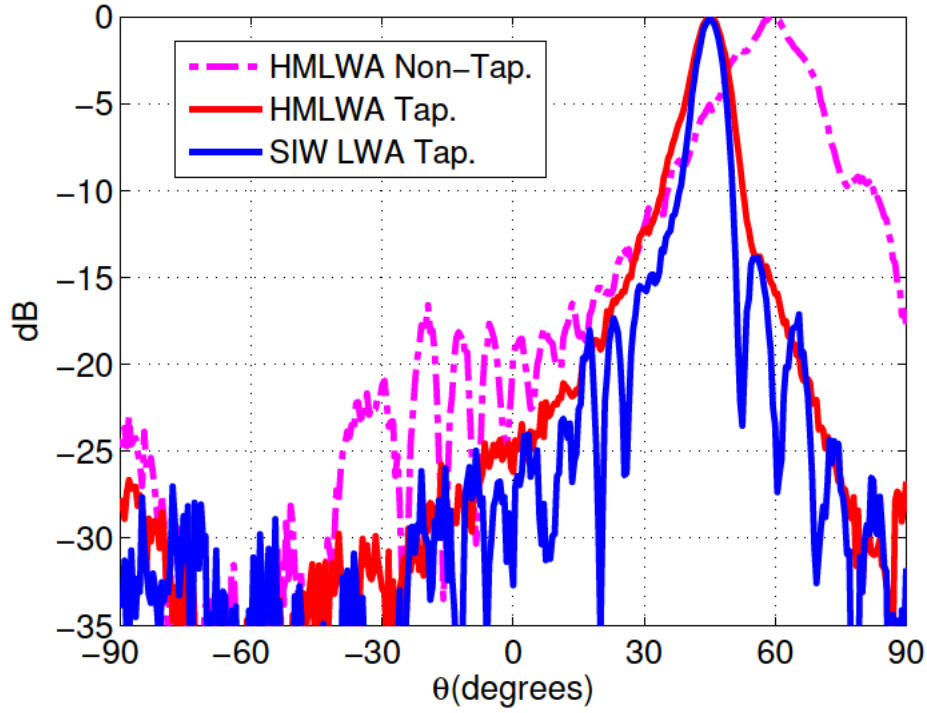


Figure 4.27: Measured radiation patterns at the design frequency of 15 GHz for the conformal designs of a non-tapered HMLWA, tapered HMLWA and tapered SIW LWA.

#### 4.2.4 Conformal SIW LWA Frequency Scanning Response

Next, an analysis of the measured frequency scanning properties of the conformal tapered SIW LWA is presented, including gain, input matching, radiation patterns, and scanning angle. The SIW LWA described in Fig. 4.19 has been used, which has an antenna length of  $L_A = 200$  mm and a radiation angle of  $45^\circ$  for the design frequency of 15 GHz when is conformed over a cylindrical surface of radius  $R = 300$  mm.

First, the normalized radiation patterns measured at several frequencies are shown in polar form in Fig. 4.28. A frequency range from 14 GHz to 18 GHz has been chosen to cover the complete operational band of the SIW LWA. As shown, at 14 GHz the radiation pattern (in dashed blue line) is pointing at  $20^\circ$  while for increasing frequency the angle moves towards endfire, in accordance with the

typical frequency scanning response presented by LWAs [91]. It is further important to note that the radiation pattern is kept similar in term of beamwidth  $\Delta\theta$  for the different frequencies, mainly from 14.5 GHz. This effect is explained by the quasi-linear dependence on the propagation constant with the frequency, which also increases the pointing angle (4.12) in a similar way for all the sections of the antenna. Therefore, the antenna can radiate with similar performances at several frequencies. However, the leakage rate typically decreases with the frequency which provides lower radiation efficiency and lower gain. This frequency scanning operation could be interesting for applications which require performing spatial and frequency scanning like automotive radars.

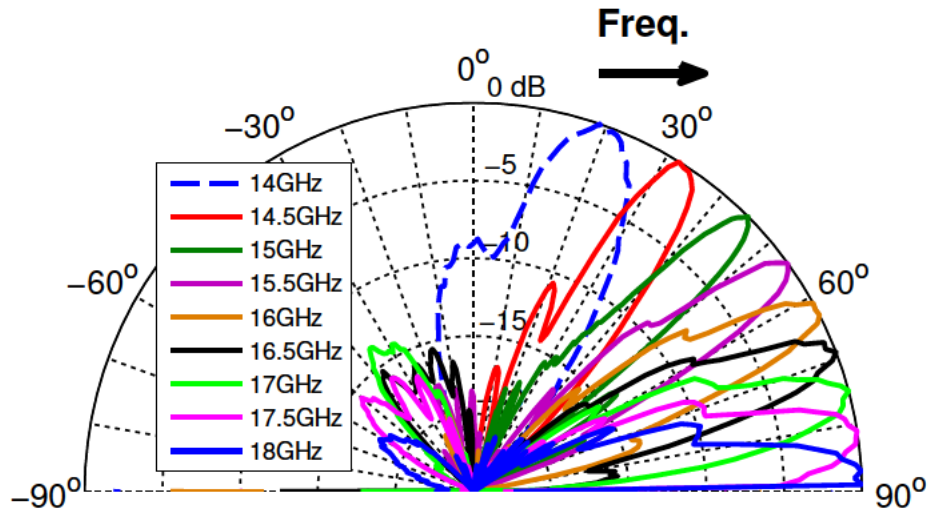


Figure 4.28: Measured radiation patterns for the conformal tapered SIW LWA for a range of frequencies from 14 GHz to 18 GHz.

The behavior of the radiation angle with the frequency is summarized in Fig. 4.29. It can be seen how  $\theta_{\text{RAD}}$  moves from  $20^\circ$  at 14 GHz to  $90^\circ$  at 18 GHz, whereas for the design frequency of 15 GHz the aforementioned angle of  $45^\circ$  has been obtained. Moreover, measured results are compared with simulations, obtaining a good agreement between them.

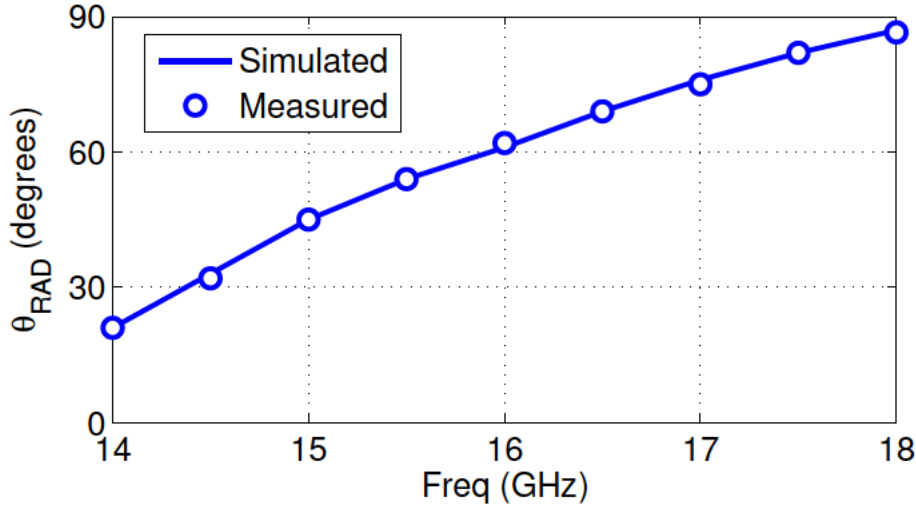


Figure 4.29: Measured and simulated frequency scanning response of the radiation angle  $\theta_{RAD}$  for the conformal tapered SIW LWA.

Fig. 4.30 shows the simulated (continuous line) and measured (circles) gain for the normalized radiation patterns represented in Fig. 4.28. As shown, the maximum gain is obtained at the design frequency of 15 GHz with a value of 13 dB. It can be also observed that the gain decreases around 14 GHz for an angle of  $20^\circ$ . This gain reduction is mainly due to the leaky mode is now closer to the "reactive mode" region [82], which causes a fast decay of the leaky wave along the transmission line and thus a smaller illuminated length of the SIW LWA. From 15 GHz the radiation efficiency begins to decrease, which is translated into a lower gain. However, a gain value around 10 dB is kept until a frequency of 18 GHz, which provides an angle close to endfire.

Finally, the measured S-parameters (continuous line) of the SIW LWA are compared with simulations (dashed line) in Fig. 4.31. A good input matching  $S_{11} = -25$  dB is observed at the design frequency of 15 GHz, with a low transmission coefficient  $S_{21} = -15$  dB, as consequence of the high designed radiation efficiency [91]. The input matching is kept below  $-10$  dB for the range from 14.5 GHz to 18 GHz, which ensures low reflection losses for the complete operational band of the antenna. On the other hand, the increasing value of the  $S_{21}$  with

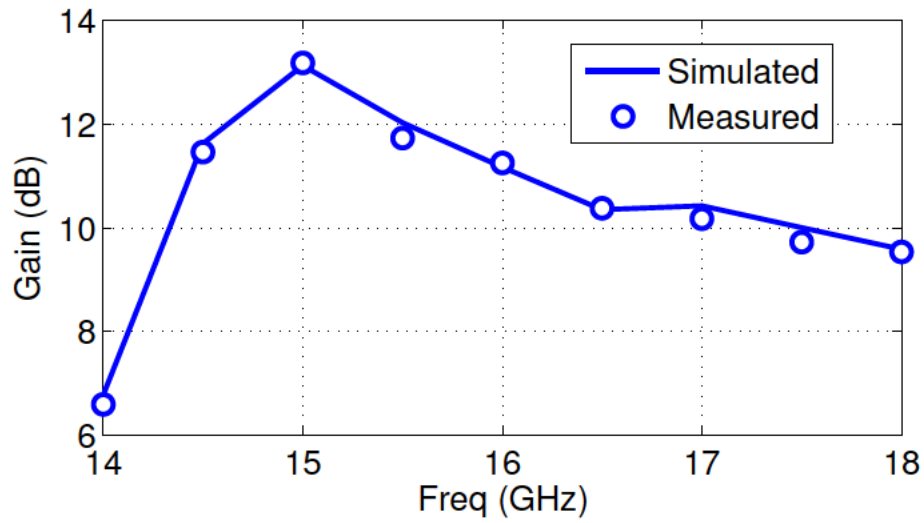


Figure 4.30: Measured and simulated frequency dispersion of the peak gain for the conformal tapered SIW LWA.

the frequency indicates that the radiation efficiency decreases, which is results to lower values of gain shown in Fig. 4.30.

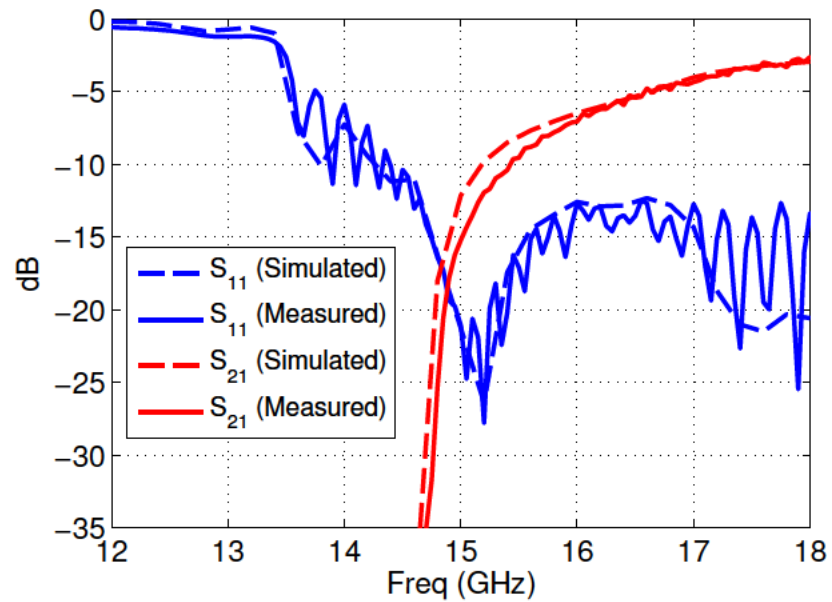


Figure 4.31: Measured and simulated S-parameters for the range of frequencies from 12 GHz to 18 GHz for the conformal tapered SIW LWA.

#### 4.2.5 Conclusion

The design of a conformal substrate integrated waveguide leaky-wave antenna (SIW LWA), which exhibits the capability to taper the amplitude and phase of the fields radiated at the antenna aperture, has been shown in this section. The tapered SIW LWA has been compared with other planar conformal alternative such as the half-mode LWA (HMLWA), which lacks the capability to control the leakage rate. As a result, the flexibility to taper leaky mode in the proposed conformal SIW LWA has allowed obtaining higher illumination efficiency and restoring the high-gain frequency scanning response despite the curved surface. The necessity to perform a tapered design for conformal antennas has been demonstrated by comparing the radiation pattern of a conformal non-tapered HMLWA with the tapered designs of the HMLWA and the SIW LWA. Three antenna prototypes operating at 15 GHz have been manufactured and measured: 1. Conventional HMLWA, 2. Tapered HMLWA, and 3. Tapered SIW LWA. Theoretical, simulated and measured radiation patterns have been compared obtaining good agreement between them, which assures the good quality of the prototypes and the set-up used in the far-field measurements. Finally, an analysis of the frequency scanning response of the SIW LWA has been performed in the range from 14 GHz to 18 GHz.

### 4.3 Quasi-Elliptic Angular Bandpass Filter Using a Single-Layer Modulated SIW Travelling-Wave Line

The design of a novel compact planar angular bandpass filter that integrates in a single-layer SIW device the radiating and filtering functionalities in both angular and frequency domains is reported in this section. The synthesis of the sharpened quasi-elliptic angular response is based on the proper tapering of the leaky wave that propagates through the modulated SIW line. The theory is proven with ex-

periments performed on fabricated prototypes, demonstrating an improvement of 17 dB in the angular rejection for a  $20\lambda_0$ -long filter covering the range  $[20^\circ, 40^\circ]$  at 15 GHz. The bandpass filtering mechanism is also demonstrated, showing a bandwidth of 700 MHz which results from the inherent spatial-frequency dispersion of the leaky wave propagating through the designed SIW filter.

### 4.3.1 Introduction

Frequency and angular filtering capabilities have been traditionally obtained on frequency-selective surfaces (FSS) [144], which combine radiation and spatial/frequency filtering functionalities by using at least two different subsystems (the antenna and the FSS). The shaping of the FSS angular/frequency response is typically based on cavity-filter synthesis techniques, so that more selective patterns are normally obtained by stacking a higher number of resonant FSS layers to increase the filter order [144]–[152]. Based on this concept, several technologies such as layered dielectrics [144], multilayered coupled printed circuits [145] (including cascaded substrate integrated waveguide (SIW) cavities [146], [147]), metal strip/patch gratings [148], [149], or metal grids [150], have been proposed. In all cases, the filter volume and complexity increase as more demanding specifications are added in spatial and frequency domains, resulting in an increased number of cascaded resonant FSS layers [144]–[152].

With the purpose of reducing the complexity and volume of these previous designs, a simple, compact, planar SIW angular bandpass filter, which integrates in one single-layer travelling-wave line the radiating and the angular/frequency filtering mechanisms, is proposed. An schematic view of the proposed filtering system is shown in Fig. 4.32, illustrating the design scanning angle  $\theta_0$  and the signal operating frequency  $f_0$ . This single-layer SIW is in charge of generating an angular width  $\Delta\theta$  around  $\theta_0$  in the space domain, and a pass bandwidth  $BW$  around  $f_0$  in the frequency domain.

The design is based on the synthesis of a selective angular pattern cover-

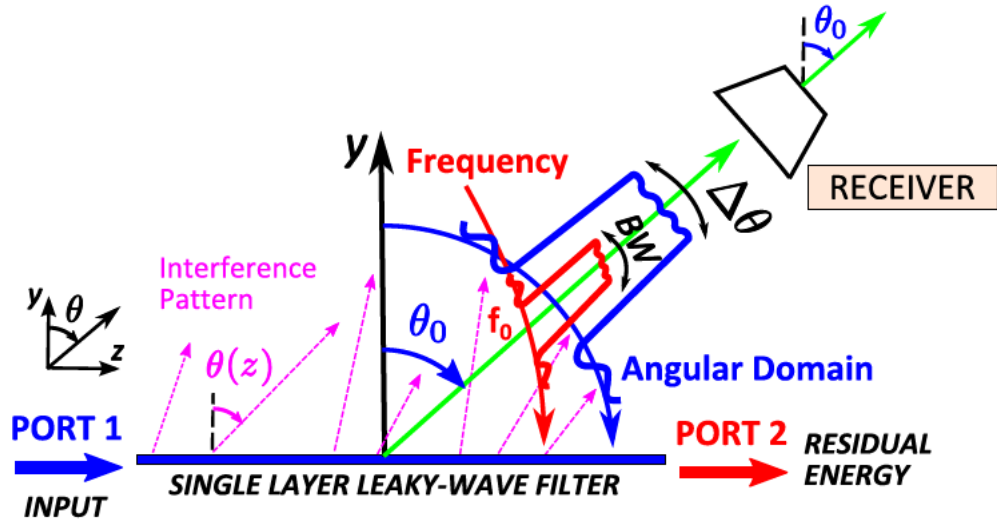


Figure 4.32: Scheme of the single-layer filter scanning at a prescribed angular  $\theta_0$  and operating at a given central frequency  $f_0$ .

ing a specified wide angular region, and with high angular rejection out from it. First designs were conceived from curved leaky-wave antennas (LWAs) by Ohtera [153]. Later, Burghignoli et al.[121] proposed a technique to obtain angular shaping by modulating the leaky-wave (LW) complex propagation constant along a rectilinear aperture. However, here the ability to obtain a broadbeam radiation pattern with one single radiation null proposed in [154], has been widened to generate for the first time selective angular patterns by using a tapered substrate integrated waveguide (SIW) [91], [141], which can be directly scalable at millimeter bands [155]–[157]. Moreover, the angular selectivity has been combined with its frequency dispersion characteristic in order to demonstrate theoretical and experimentally the design of a novel single-layer device with both spatial and frequency filtering functionalities.

Some of the main applications of these spatial/frequency filtering functionalities can be found in the design of analog signal processing (ASP) circuits [158]–[166], due to the necessity to obtain low-cost circuits at microwave/millimeter-wave frequencies and avoid unaffordable over-Gbps/Tbps sampling [166]. Many of these proposals are based on the spatial-frequency decomposition inherent to

surface and leaky waves [161]–[163]. In all these cases, a dispersion engineering approach is used to control the coupled frequency-angular response of the modes propagating in textured engineered materials, with the aim to integrate different functionalities in one single device [161]–[165].

The section is distributed as follows: Section 4.3.2 describes the theoretical concepts for the angular synthesis of Chebyshev and quasi-elliptic angular responses, which are based on the modulation of a travelling leaky wave [123]. In Section 4.3.3, this is applied to the practical modulation of a substrate integrated waveguide (SIW) [91] operating at 15 GHz, showing experimental data which confirms the theory. Section 4.3.4 demonstrates that a bandpass frequency response is inherently obtained from this simple device. Finally, Section 4.3.5 summarizes the conclusions of the section.

### 4.3.2 Synthesis of Quasi-Elliptic Angular Response

The design of Chebyshev angular filters from a modulated leaky wave was theoretically proposed in [121]. Likewise, the required variations of the leaky mode along the SIW need to be related with its complex aperture field distribution:

$$E_{\text{RAD}}^{\text{APERT}}(z) = M(z) \cdot e^{j\phi(z)} \quad (4.16)$$

whose amplitude  $M(z)$  and phase  $\phi(z)$  terms can be respectively obtained as function of the LW leakage rate  $\alpha(z)$  and pointing angle  $\theta_{\text{RAD}}$  by [82]:

$$\alpha(z) = \frac{1}{2} \frac{|M(z)|^2}{\frac{1}{\eta} \int_0^L |M(\tau)|^2 d\tau - \int_0^z |M(\tau)|^2 d\tau} \quad (4.17)$$

$$\beta(z) = k_0 \sin \theta_{\text{RAD}}(z) = -\frac{\partial \phi(z)}{\partial z} \quad (4.18)$$

where  $\eta$  is the radiation efficiency. Therefore, the modulated complex aperture distribution (4.16) can now be synthesized from the tapered values of the complex

wavenumber  $k_z$  along the SIW length:

$$k_z^{LW}(z) = k_0 \sin \theta_{\text{RAD}}(z) - j\alpha(z) \quad (4.19)$$

Fig. 4.33 illustrates the angular responses obtained when applying this modulation technique [121] with different filter lengths  $L$ , for the synthesis of a broad-beam centered at an angle  $\theta = 30^\circ$  with a  $-3$  dB beamwidth of  $\Delta\theta = 25^\circ$ . Clearly, one needs to enlarge  $L$  to synthesize a more selective Chebyshev angular response while keeping the same angular width. This is summarized in Table 4.1, which illustrates the rejection (measured as the linear slope in dB/ $^\circ$  to fall from  $-3$  dB to  $-10$  dB), as a function of  $L$ .

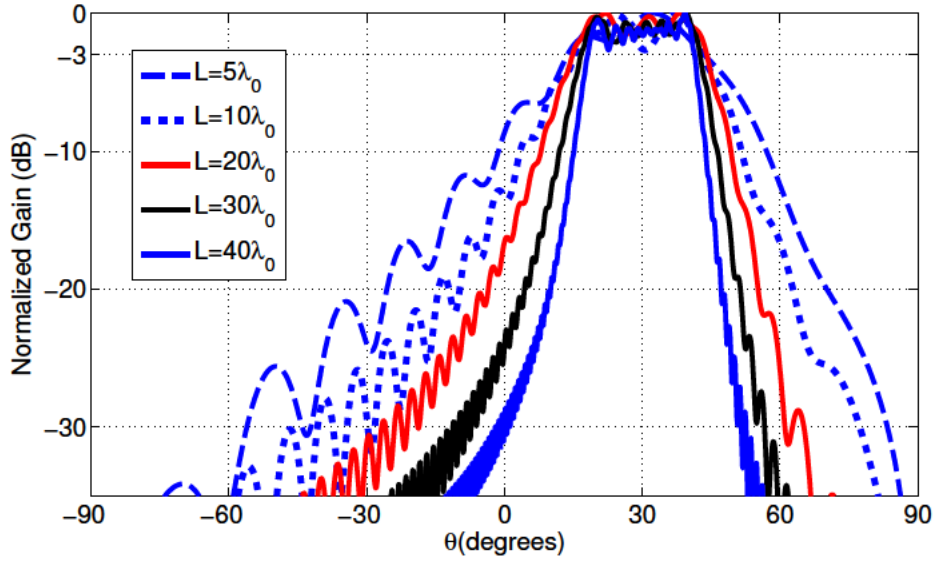


Figure 4.33: Chebyshev angular filtering response as a function of filter length  $L$ .

Table 4.1: Relation between angular rejection and filter length.

Length $L$	$5\lambda_0$	$10\lambda_0$	$20\lambda_0$	$30\lambda_0$	$40\lambda_0$
Rejection dB/ $^\circ$	0.5	0.7	1	1.5	2.4

The standard modulation technique proposed in [121] can be modified with the addition of more demanding specifications to the synthesis, so that a quasi-elliptic

filter response with increased angular rejection can be obtained without the need of increasing the filter length [123]. This process has been summarized in the flowchart shown in Fig. 4.34. First, the initial values of the leaky mode ( $\alpha_{INI}$ ,  $\beta_{INI}$ ) for obtaining a Chebyshev response with a prescribed  $\theta$  and  $\Delta\theta$  are determined by using the technique described in [121]. Then, the calculated radiation pattern for ( $\alpha_{INI}$ ,  $\beta_{INI}$ ) is modified according to the required specifications (in terms of the angular region for the main broad-beam and its two surrounding transmission nulls) for a more selective response [123]. Afterwards, the quasi-elliptic angular response is expressed as function of a complex aperture field distribution (4.16), which can be related from (4.17) and (4.18) with its corresponding values for the leaky mode. Finally, the required modulated values of  $\alpha$  and  $\beta$  must be translated to a suitable geometry with enough flexibility to follow the variations of the leaky mode along the length of the angular filter [91].

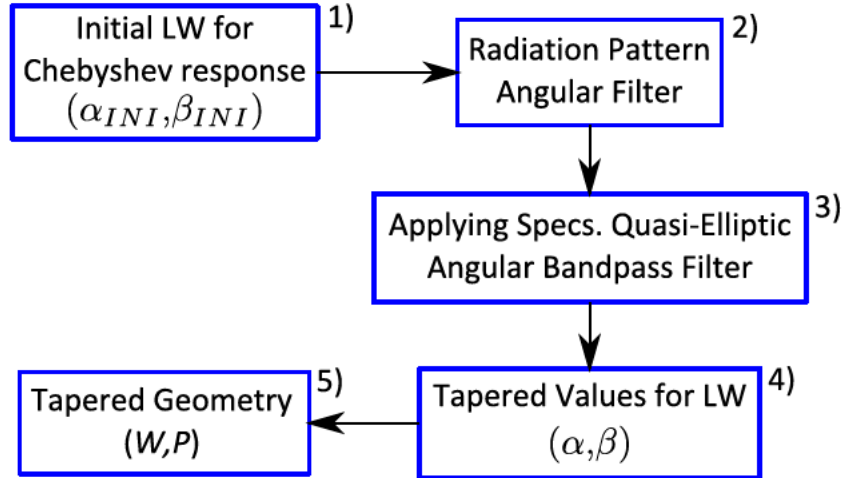


Figure 4.34: Flowchart for the synthesis of a quasi-elliptic bandpass filter.

An example of the previous design process is illustrated in Fig. 4.35, where the theoretical angular pattern obtained for a  $20\lambda_0$ -long filter is plotted in magenta with the following specifications: a main broad-beam with a  $-3$  dB width covering the angular range  $\theta = [20^\circ, 40^\circ]$ , and two surrounding transmission nulls below  $-20$  dB in the angular regions  $\theta = [0^\circ, 15^\circ]$  and  $\theta = [45^\circ, 60^\circ]$  (these

specs are plotted with green dashed lines in Fig. 4.35). This angular response has been created using the numerical technique for the synthesis of radiation nulls in rectilinear tapered LWAs proposed in [123]. It can be seen how the designed quasi-elliptic  $20\lambda_0$ -long angular filter has the same rejection ( $2.4 \text{ dB}/^\circ$ ) than a Chebyshev-type  $40\lambda_0$ -long one (plotted in blue line) because of the addition of the null specs. As a result, the rejection has been improved by 17 dB compared to the Chebyshev angular filter with the same length  $L = 20\lambda_0$ . Out from these null regions, the quasi-elliptic  $20\lambda_0$  filter follows the same radiation profile of the conventional Chebyshev  $20\lambda_0$ -long filter (plotted in dashed red line), as it can be also seen in Fig. 4.35 for  $\theta < 0^\circ$ . This is due to the fact that our design is based on a Chebyshev  $20\lambda_0$  in which null specs have been added only to the prescribed angular regions.

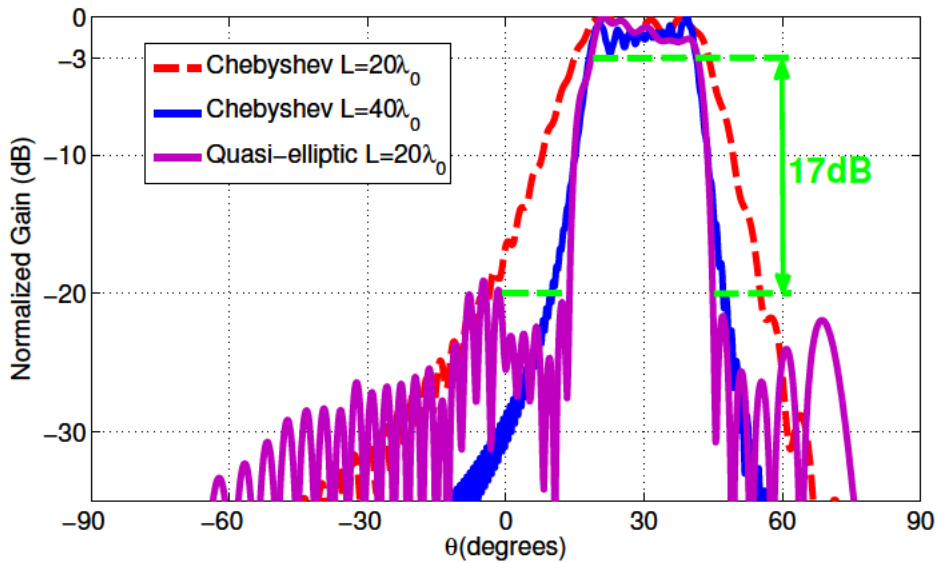


Figure 4.35: Synthesis of radiation nulls to increase the angular rejection.

The requested simultaneous tapering functions for the leaky-wave pointing angle  $\theta_{\text{RAD}}(z)$  and normalized leakage rate  $\alpha(z)/k_0$  to synthesize the two  $20\lambda_0$ -long filter designs of Fig. 4.35 are shown in Fig. 4.36. The standard Chebyshev tapering is plotted with continuous lines and it is compared to the proposed novel

tapering (plotted with dashed lines) with addition of radiation nulls for quasi-elliptic response synthesis. The Chebyshev-type tapering [121] involves a quasi-linear increase in the locally-tapered pointing angle covering the angular region  $\theta_{\text{RAD}}(z) = [10^\circ, 50^\circ]$  as shown in Fig. 4.36a, and a tapered modulation of the leakage rate shown in Fig. 4.36b, which provides uniform radiated power per unit angle in the aforementioned interval. As it can be seen in Fig. 4.36, these smooth tapering functions are modified with abrupt variations in both  $\theta_{\text{RAD}}(z)$  and  $\alpha(z)/k_0$  to synthesize the requested radiation nulls for the quasi-elliptic angular filter, wherein stronger variations are needed for wider and deeper null specs as explained in [123].

### 4.3.3 Design of an Angular Bandpass Filter With Modulated SIW LWA

The final stage of the design process in order to obtain an angular bandpass response with higher angular selectivity, consists in translating the electrical modulations of the leaky-wave complex propagation constant into their geometrical modulations of the filter cross section along its length  $z$ . For this, it is required a leaky-wave transmission line topology that possesses enough degrees of freedom to simultaneously and independently control  $\theta_{\text{RAD}}$  and  $\alpha/k_0$ . The microstrip line [167] and the slotted waveguide [122] have been theoretically proposed with this objective in mind, but no experimental data has been reported so far to demonstrate this possibility. Here it proposes the use of a modified SIW, which has recently shown the capability to flexibly control  $\theta_{\text{RAD}}$  and  $\alpha/k_0$  by properly designing the SIW width  $W$  and the separation between vias  $P$  [91], [141], as sketched in Fig. 4.37a.

In this way, the requested leaky-wave modulation of Fig. 4.36 is transformed into the SIW geometry modulation functions  $W(z)$  and  $P(z)$  shown in Fig. 4.37b, for both  $20\lambda_0$  tapered designs (Chebyshev and quasi-elliptic). The design fre-

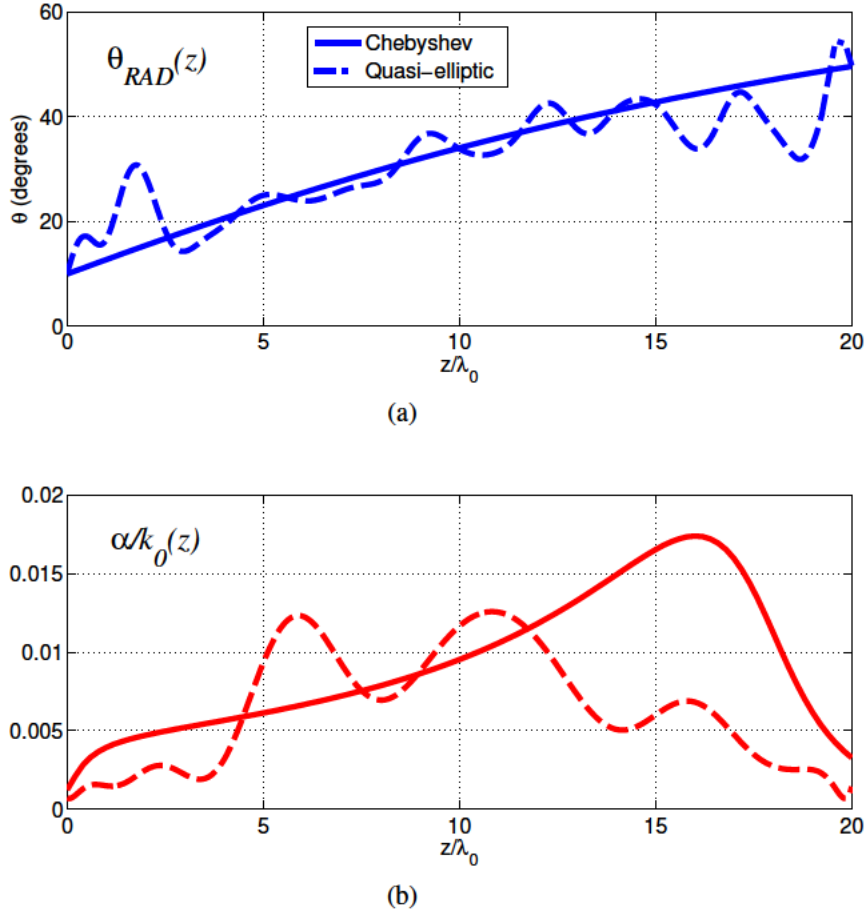


Figure 4.36: Tapering of leaky wave a) local pointing angle and b) local leakage rate for the synthesis of Chebyshev and quasi-elliptic angular responses.

quency is 15 GHz ( $\lambda_0 = 20$  mm), and commercial Taconic TLP-5 substrate with  $\epsilon_r = 2.2$ ,  $\tan \delta = 0.0009$  and  $h = 0.508$  mm is used for the SIW. The other fixed parameters are: posts' diameter  $d = 1$  mm, non-radiative posts' distance  $P_0 = 2$  mm, and radiating strip width  $W_0 = 1.5$  mm (see Fig. 4.37a). As it can be seen in Fig. 4.37b, the Chebyshev tapered design requests a smooth modulation of the SIW width  $W$  and the distance between posts  $P$ . On the contrary, the proposed addition of radiation nulls is translated into more abrupt modulations in  $W(z)$  and  $P(z)$ , which follow the variations in the leaky-wave tapering functions  $\theta_{RAD}(z)$  and  $\alpha(z)/k_0$  shown in Fig. 4.36.

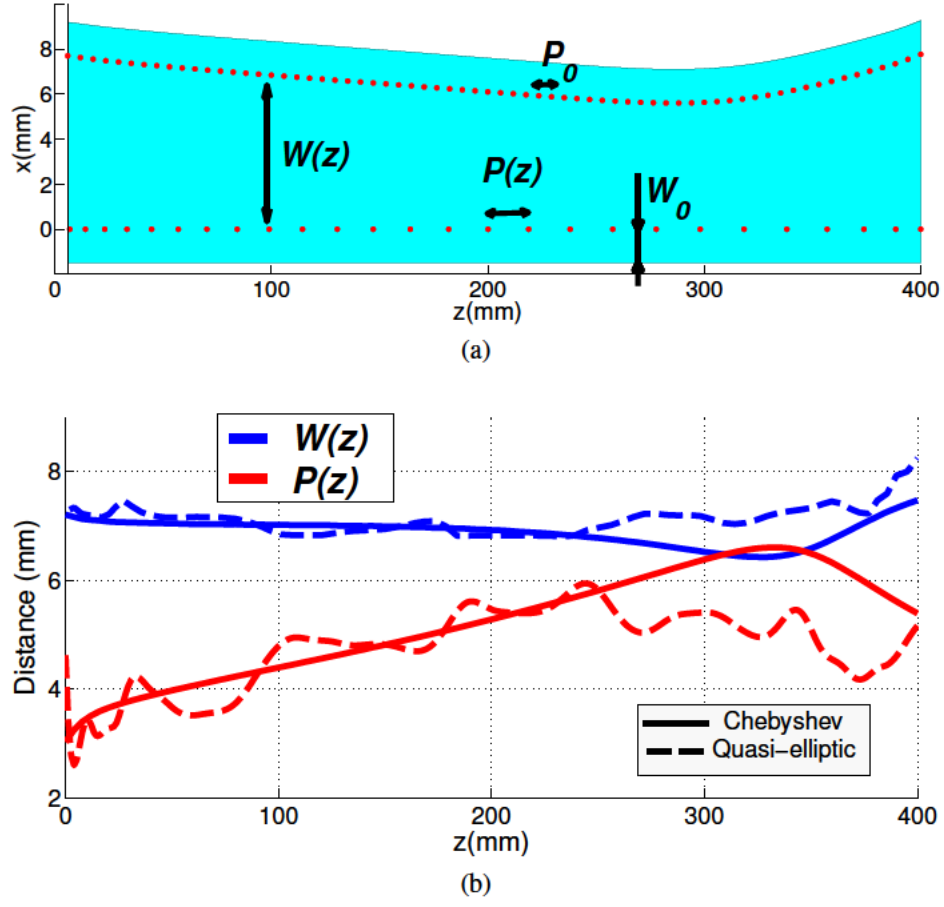


Figure 4.37: a) Scheme of modulated SIW filter with  $L = 20\lambda_0 = 400$  mm. b) Modulation of SIW dimensions to synthesize Chebyshev and quasi-elliptic angular responses.

A photograph of a fabricated modulated SIW prototype of length  $L = 20\lambda_0 = 400$  mm is shown in Fig. 4.38a. In addition, Fig. 4.38b shows the corresponding simulated (HFSS) leaky-mode propagating-fields inside this modulated SIW line. As it can be seen, the guided wavelength  $\lambda_g(z)$  varies along the  $20\lambda_0$  length of the device, showing longer  $\lambda_g$  at the radiating SIW input and shorter  $\lambda_g(z)$  at the end. Recalling the well-known relation between  $\lambda_g(z)$  and the locally modulated leaky-wave pointing angle  $\theta_{\text{RAD}}(z)$ [82]:

$$\sin \theta_{\text{RAD}}(z) \approx \frac{\lambda_0}{\lambda_g(z)} \quad (4.20)$$

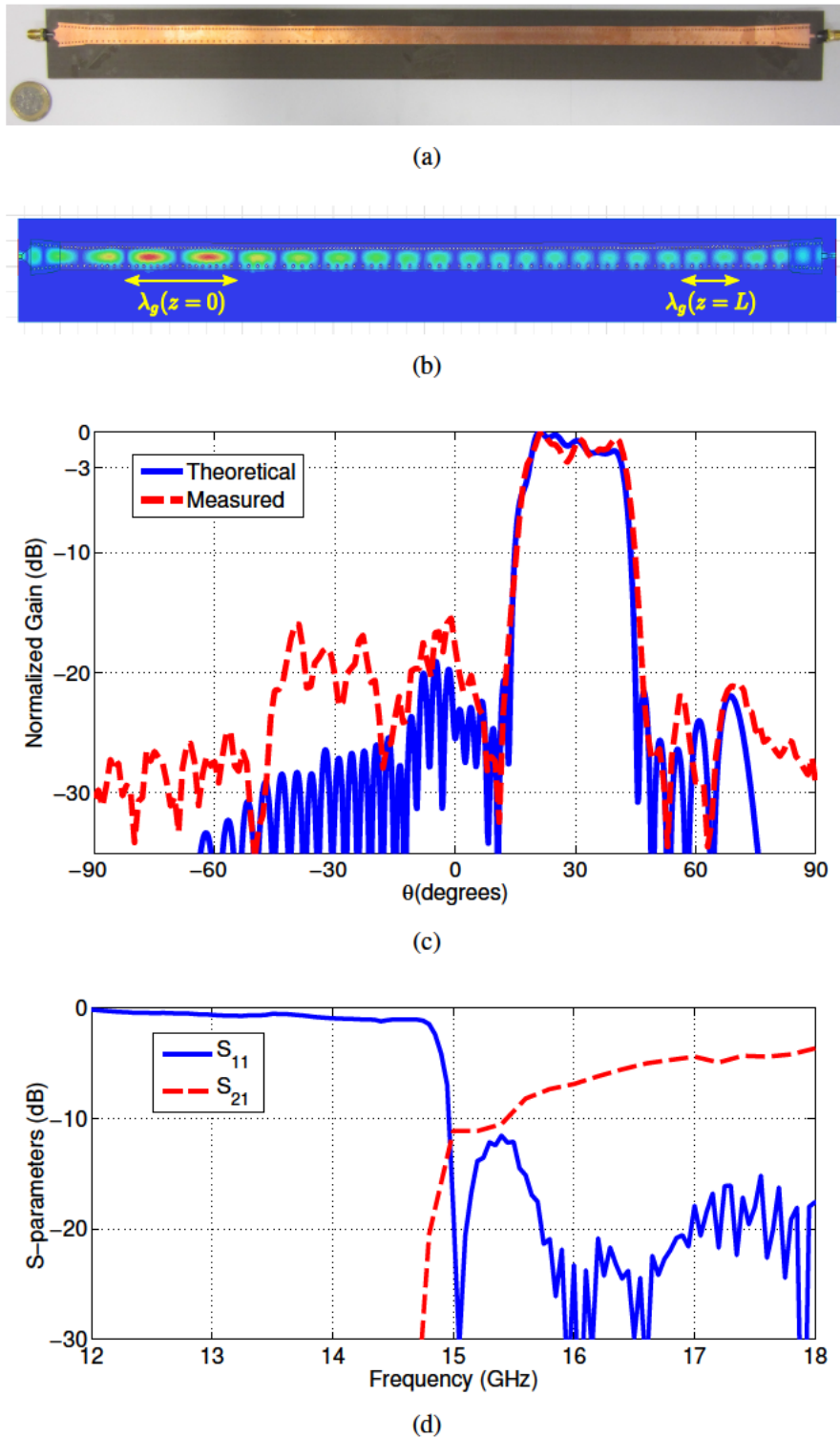


Figure 4.38: a) Manufactured modulated SIW quasi-elliptic filter. b) Simulated propagating leaky-mode electric field. c) Measured far-field angular pattern at 15 GHz. d) Measured input matching and return loss.

It can readily see from the simulations of Fig. 4.38b that the designed tapered SIW does effectively modulate the local scanning angle along the longitudinal  $z$ -direction to obtain an increasing function of  $\theta_{\text{RAD}}(z)$  as the one shown in Fig. 4.36a. The measured angular pattern at the design frequency of 15 GHz for the quasi-elliptic design (dashed red line) is compared with theory (continuous blue line) in Fig. 4.38c. As it can be seen, the agreement between experiments and the objective pattern is very good, showing the successful synthesis of a very selective main shaped beam covering the prescribed  $-3$  dB angular region  $\theta = [20^\circ, 40^\circ]$ , and with the desired sharp angular decay. Some discrepancies are observed at the angular range in the backward quadrant  $\theta = [-20^\circ, -40^\circ]$ , due to the leaky wave reflected at the far end of the SIW line (which emits energy at mirrored angles with respect to the main beam). The SIW is directly fed by a microstrip transmission line, which has been tapered to reduce the mismatch [91]. The measured input matching  $S_{11}$  and transmission  $S_{21}$  coefficients are also reported in Fig. 4.38d, showing good matching  $S_{11} \approx -20$  dB at the design frequency of 15 GHz, and a low  $S_{21} \approx -10$  dB as a result of the high designed radiation efficiency ( $\eta = 1 - |S_{11}|^2 - |S_{21}|^2$ ) [91].

Simulated radiated fields in the elevation  $zy$ -plane ( $H$ -plane, in an area of  $50\lambda_0 \times 50\lambda_0$ ) are represented in Fig. 4.39 to give more physical insight into the synthesis of the angular selective response. Both Chebyshev (Fig. 4.39a) and quasi-elliptic (Fig. 4.39b) SIW filter designs have been analyzed to illustratively show the similarities and differences in their respective radiated-field angular patterns. As it can be seen, both cases show the synthesis of a diverging radiated field that covers the specified angular region  $[20^\circ, 40^\circ]$  with quasi-uniform radiated power per unit angle. However, the transition from light to shadow is more abrupt and discernible in the quasi-elliptic case, due to the higher rejection created by destructive interference of radiated fields at directions which are immediately adjacent to the light zone. To stress this difference, white dashed lines mark radiation directions of  $10^\circ$  and  $50^\circ$ , showing a stronger reduction in the near-field intensity level

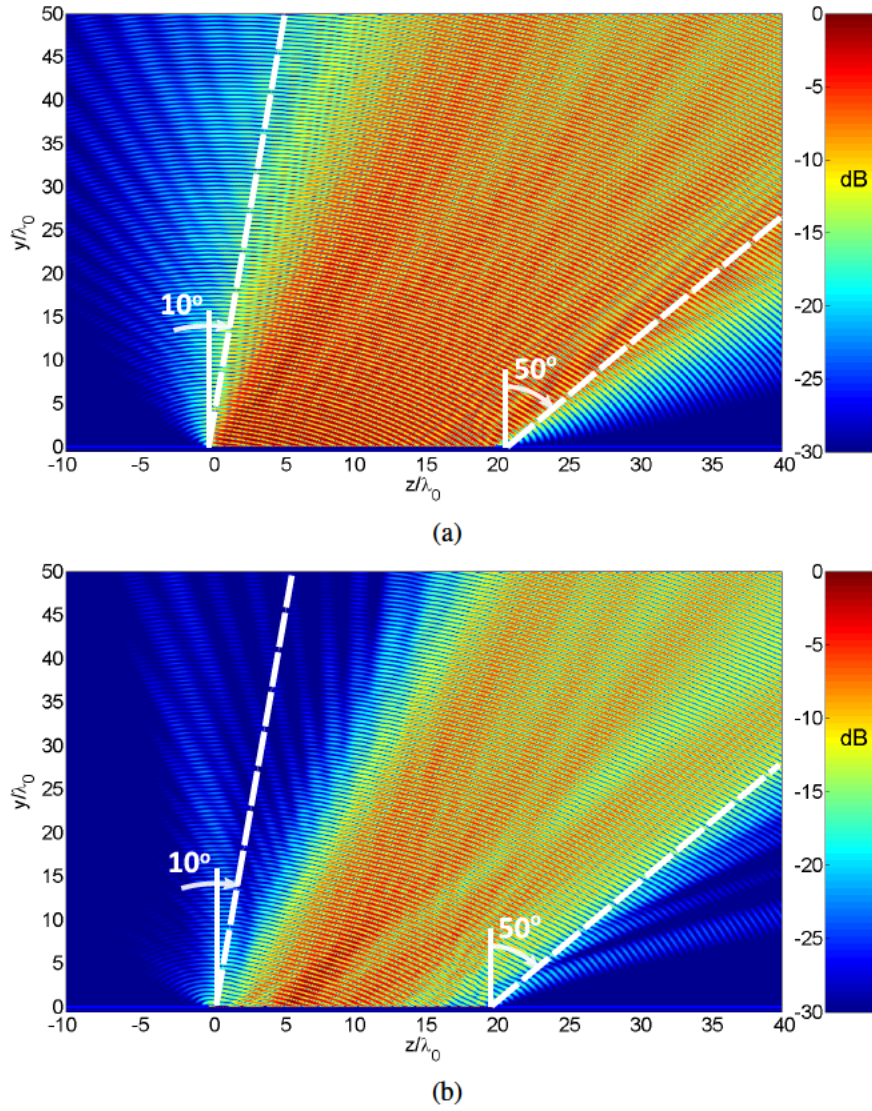


Figure 4.39: Simulated near-field patterns in the  $zy$ -plane radiated by the modulated SIW filters: a) Chebyshev design. b) Quasi-elliptic design.

(20 dB below) for the quasi-elliptic filter than for the the Chebyshev design.

This reduction in the near-field pattern is in coherence with the far-field patterns shown in Fig. 4.40. Clearly, the introduction of radiation null specifications for the quasi-elliptic filter has increased the roll off from 1 dB/° to 2.5 dB/° compared to the Chebyshev design, while using the same filter length ( $L = 20\lambda_0$ ). From these results, the synthesis of a selective angular response from a practi-

cal modulated rectilinear SIW device and the increase in the angular rejection by using leaky-wave selective null synthesis techniques have been demonstrated.

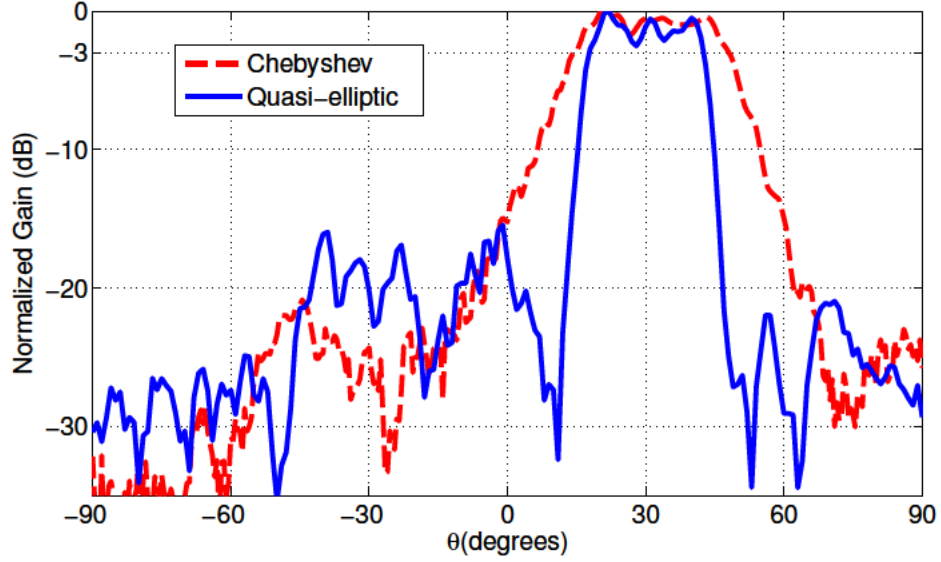


Figure 4.40: Measured far-field patterns at 15 GHz for Chebyshev and quasi-elliptic angular responses.

#### 4.3.4 Frequency Bandpass Filter Response

The frequency response of angular filters is also of key importance to permit a desired bandwidth and to reject unwanted signals. Design of filters on both angular and frequency domains is not a simple task, and only a few works have treated the simultaneous synthesis of angular bandpass filters [148], [152]. Leaky modes scan the direction of the main beam towards endfire as frequency is increased as a result of their inherent frequency-spatial dispersion [82]. This property has been exploited in some recent works to conceive integrated circuits that perform spatial-spectral filtering for analog signal processing [161]–[165]. This is a general aspect that also applies to this SIW leaky-wave angular filter. This can be seen in Fig. 4.41, which plots the measured gain patterns as frequency is varied from 15 GHz to 18 GHz for the quasi-elliptic angular filter design. Below

14.8 GHz the SIW presents cutoff as it can be observed by the high input mismatch ( $S_{11} > -1.5$  dB) in Fig. 4.38d, resulting in a rapid drop of the overall filter angular gain. As frequency is increased, the synthesized selective angular response at 15 GHz emerges, and then the central angle is scanned towards endfire with a scanning ratio of  $15^\circ/\text{GHz}$  as shown in Fig. 4.41.

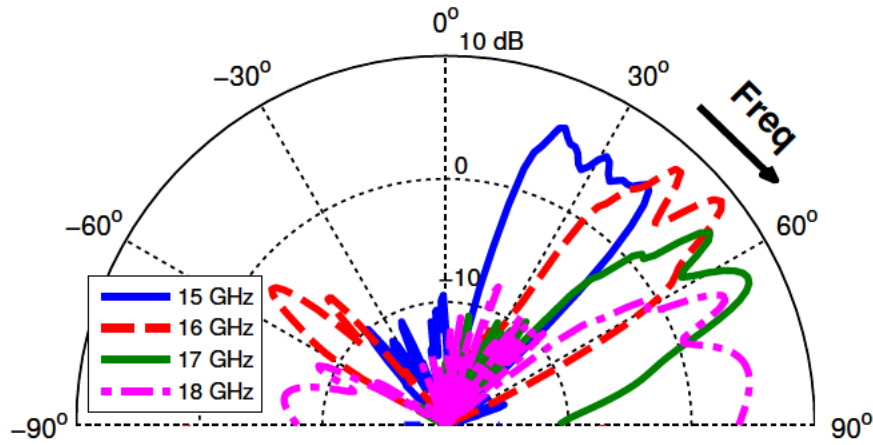


Figure 4.41: Measured angular gain patterns at different frequencies for the quasi-elliptic SIW filter design.

As a result of this scanning behavior, the electromagnetic response for the fixed design observation angle of  $\theta_0 = 30^\circ$  and around the design frequency of 15 GHz is of the type of a bandpass filter. This is demonstrated by the measured gain at  $\theta_0 = 30^\circ$  for frequencies between 14 GHz and 17 GHz plotted in Fig. 4.42. The gain has been measured in the far-field region by using a gain-comparison method for the set-up shown in Fig. 4.32. A well-defined bandpass response is demonstrated, with a  $-3$  dB bandwidth of 700 MHz centered at 15.25 GHz, which is in agreement with the simulated results (red dashed line). The lower bandpass frequency limit is determined by the aforementioned SIW cutoff, which rejects frequencies below 14.8 GHz. Then, the pass band is originated by the transit of the designed selective angular response of width  $\Delta\theta = 20^\circ$ , which scans half of its angular width below  $30^\circ$  ( $\Delta\theta/2 = 10^\circ$ ) at the aforementioned scanning ratio (SR) of  $15^\circ/\text{GHz}$ . In this way, the resulting bandwidth BW for the design observation

angle of  $\theta_0 = 30^\circ$  can be approximated by:

$$BW \approx \frac{\Delta\theta/2}{SR} \quad (4.21)$$

which provides a value of  $BW = 667$  MHz in coherence with the measured bandwidth reported in Fig. 4.42. Moreover, it can be seen that the out-of-band rejection is weaker for the upper band than for the lower band. This asymmetry is due to the different nature on the rejection mechanism for these two bands: clearly the lower stopband due to the SIW cutoff provides higher rejection ( $G = -30$  dB at 14 GHz) than the rejection due to the scanning of the angular response at high frequencies ( $G = -12$  dB at 16 GHz).

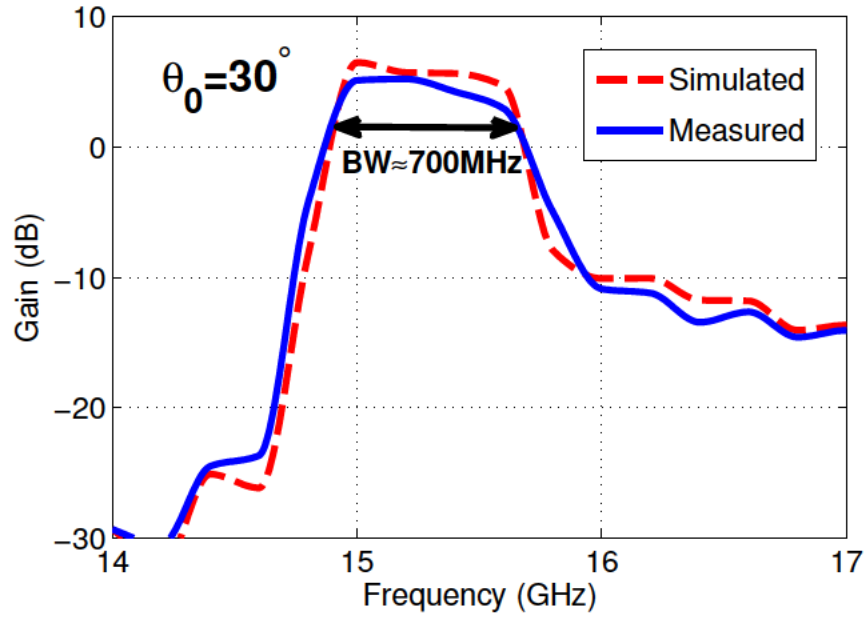


Figure 4.42: Measured and simulated bandpass filtering responses (gain versus frequency) for the quasi-elliptic SIW filter designed at 15 GHz and  $\theta_0 = 30^\circ$ .

Nevertheless, it is worth noting that the bandwidth,  $BW$ , of the synthesized bandpass response can be controlled once the angular width  $\Delta\theta$  has been chosen, by proper selection of the leaky-mode scanning ratio ( $SR$ ) according to (4.21).

The scanning ratio, SR, (also known as frequency sensitivity [82]) is given by the angular dispersion curve  $\theta(f)$  of the leaky mode propagating on the studied transmission medium. With the purpose of showing the flexibility to choose different scanning ratios, and thus, to control the BW, the leaky-mode dispersion curves for the designed SIW filter and three different substrate's permittivities ( $\epsilon_r = 2.2$ , 4.5 and 10) are shown in Fig. 4.43. The modal scanning responses have been obtained using the modal tool developed in [118] for the central section of the filter, which scans at the central design angle of  $\theta_0 = 30^\circ$  for the operating frequency of 15 GHz. From the derivative of  $\theta(f)$  at 15 GHz, three different leaky-mode scanning ratios are obtained depending on the substrate used ( $\epsilon_r = 2.2$ ,  $SR \approx 15^\circ/\text{GHz}$ ), ( $\epsilon_r = 4.5$ ,  $SR \approx 30^\circ/\text{GHz}$ ) and ( $\epsilon_r = 10$ ,  $SR \approx 80^\circ/\text{GHz}$ ). This relationship between the SR and the BW has been experimentally demonstrated for the designed SIW filter with  $\epsilon_r = 2.2$ , which agrees with the measured result shown in Fig. 4.42.

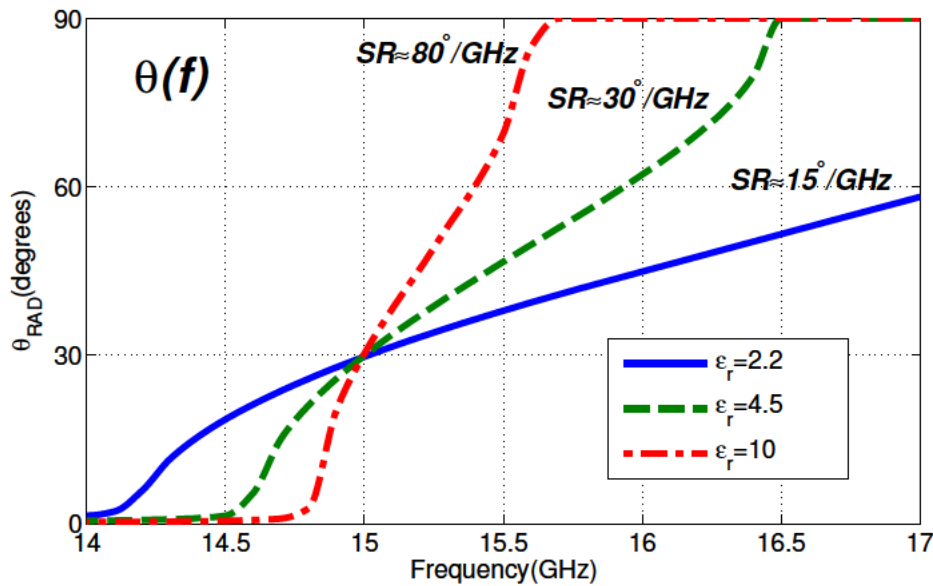


Figure 4.43: Angular-frequency dispersion curve of the leaky mode propagating in the designed SIW angular bandpass filter for the three different substrate's permittivities ( $\epsilon_r = 2.2$ , 4.5 and 10).

Therefore, dispersion engineering techniques can be used to tune the leaky-mode scanning ratio, and thus modify the frequency bandwidth BW for a given angular width  $\Delta\theta$  according the design equation (4.21). By simply choosing the SIW dielectric permittivity, one can strongly control the scanning ratio as demonstrated in [143]. Also, the addition of high impedance surface (HIS) sheets [168] can further increase the SR to reduce the filter BW. Conversely, the SR can be decreased by means of novel passive [169]–[171] or active [172] artificial transmission lines with reduced beam squint, so that the resulting BW could be notably increased. However, it is also important to note that in order to obtain the same angular response at the design frequency, the iterative process followed in Fig. 4.34 needs to be applied for each scanning ratio.

To finalize, Fig. 4.44 summarizes the performance of the proposed SIW device covering the whole angular and frequency ranges. It shows the measured gain with a colorbar as a function of frequency ( $y$ -axis), and for different far-field observation angles  $\theta$  ( $x$ -axis). The frequency scanning response which couples the frequency and the angular filtering behaviors becomes evident in this figure: it is readily observed the wide red-colored trace of angular width  $\Delta\theta = 20^\circ$  which moves from central  $\theta = 30^\circ$  at 15 GHz to  $\theta = 60^\circ$  at 17 GHz, in coherence with Fig. 4.41. This figure also helps to geometrically relate the magnitudes involved in (4.21); namely the angular width  $\Delta\theta$ , the scanning ratio SR, and the resulting bandwidth BW. It is also graphically observed how the  $\Delta\theta = 20^\circ$  angular-wide main beam synthesized around  $\theta = 30^\circ$  at 15 GHz moves towards endfire at a ratio  $SR = 15^\circ/\text{GHz}$  as frequency is increased, creating for  $\theta = 30^\circ$  a pass band with frequency bandwidth  $BW = 700 \text{ MHz}$ . Moreover, it must be pointed out that it can be observed in Fig. 4.44 a reflected lobe created by the filter far-end discontinuity which emits energy at mirrored angles from the main spatial direction. However its level is well 10 dB below the main angle for all frequencies (as it can be also seen in Fig. 4.41).

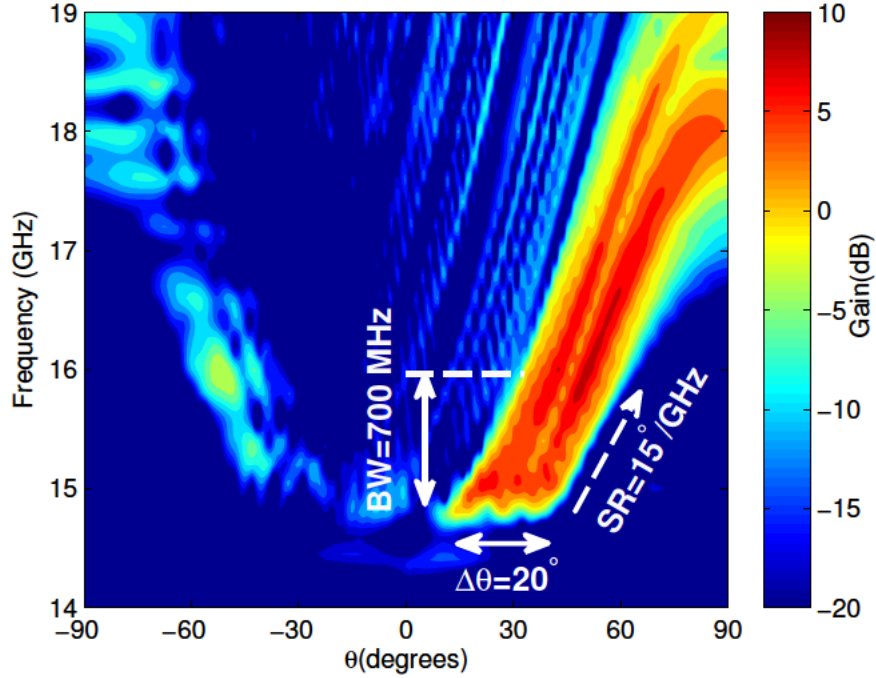


Figure 4.44: Measured angular bandpass filtering performance for the quasi-elliptic SIW filter design. Gain is represented by an intensity colorbar,  $\theta$  (degrees) is in  $x$ -axis, and frequency (GHz) is in  $y$ -axis.

### 4.3.5 Conclusion

The synthesis of a quasi-elliptic angular bandpass filter in a single-layer low-profile modulated SIW transmission line has been presented in this section. Measured results on a fabricated 400 mm-long filter prototype operating at 15 GHz with  $20^\circ$  angular width and 700 MHz bandwidth have validated the theory. It has been shown an improvement in the angular rejection of 17 dB due to the insertion of nulls in the angular domain. Moreover, it has been shown that a well-shaped bandpass filtering in the frequency domain is simply produced as a consequence of the leaky-mode scanning sensitivity. It has been demonstrated that the resulting bandwidth of 700 MHz is directly related to the angular width and the spatial-frequency dispersion of the leaky mode propagating on the SIW filter. As a result,

the selectivity in both angular and frequency domains can be independently tuned by means of dispersion engineering over the leaky-mode scanning ratio. Compared to previous angular bandpass filter technologies based on cascaded resonant FSS, this travelling-wave SIW device integrates in one single planar substrate the radiating and the filtering properties in both angular and frequency domains. This device is thus an important contribution to integrate different functionalities in one single device, thus reducing complexity and volume for analog signal processing circuits. Moreover, this SIW technology can be directly scalable at millimeter bands, where novel simple alternatives for low-loss filtering/multiplexing are requested.

#### **4.4 Properties of Microwave Near-Field Focusing of Width-Tapered Microstrip LWAs**

The possibility of microwave near-field focusing using a simple width-tapered microstrip leaky-wave antenna is theoretically and experimentally proven in this section. The design procedure to obtain the modulation of the microstrip width along the antenna length is described, illustrating the conditions and limitations for optimum focusing at a certain focal point and using a given substrate. A  $7.5\lambda_0$ -long microstrip lens is designed to operate at 15 GHz, and its focusing properties are studied. An array of two in-phase microstrip lenses located front-to-front is proposed to obtain a symmetric focusing pattern with higher spatial resolution. Theoretical and experimental results demonstrate the optimum synthesis of a focusing region with focal length of  $3\lambda_0$ , presenting focal width of only  $0.33\lambda_0$ , and focal depth of  $1.25\lambda_0$ . Finally, it is reported the frequency focus-scanning performance in the range 14-17 GHz. All these features make the proposed microstrip lens a simpler alternative solution to focused planar phased-arrays.

### 4.4.1 Introduction

Near-Field focusing leaky-wave antennas (LWAs), also known as leaky-wave lenses (LWLs), have recently been proposed [121], [124], [167], [173]–[175]. The main advantage of LWLs when compared with conventional focused phased-array apertures [176]–[181], is its simple feeding mechanism, avoiding costly and lossy distribution networks. The first approaches of LWL made use of curved LWAs to obtain a converging phase front [173], [174]. Later [121], a rectilinear configuration of LWL based on the appropriated tapering of the leaky-mode pointing angle was proposed. Different LWAs technologies have been tentatively proposed to conceive rectilinear LWLs, such as the composite right/left handed microstrip [175], the microstrip line [167], or the slotted waveguide LWA [124]. These rectilinear versions of LWL avoid the need to curve the leaky structure, which can be complicated and even undesired for certain applications. However, the synthesis of rectilinear LWLs is more demanding than for the conformal LWL case, in the sense that one needs to properly taper the leaky-mode complex propagation constant along the length of the LWA [121], [124]. It must be noticed the similarities between the proposed half-width microstrip line, and the slotted dielectric waveguide [124]. Certainly, from an electromagnetic point of view, the half-width microstrip can be seen as a limiting case of the slot line in which one of its metallic fins tends to zero. As a result, the same leaky-mode analysis tool used in [124] can be used in the present case to study a microstrip line embedded in parallel plates. On the other hand, the capability to demonstrate the near-field focusing performance of planar microstrip lines have been extensively pursued [121], [124], [167], [173]–[175], due to its simplicity, low-cost, low-profile, easy adjustment, and direct feeding and integration with other planar circuits (when compared, for instance, with more bulky dielectric waveguides as [124]). Therefore, the proposed structure provides a systematic and robust design of near-field focusing from a simple width-modulated microstrip line, which is demonstrated by experimental results.

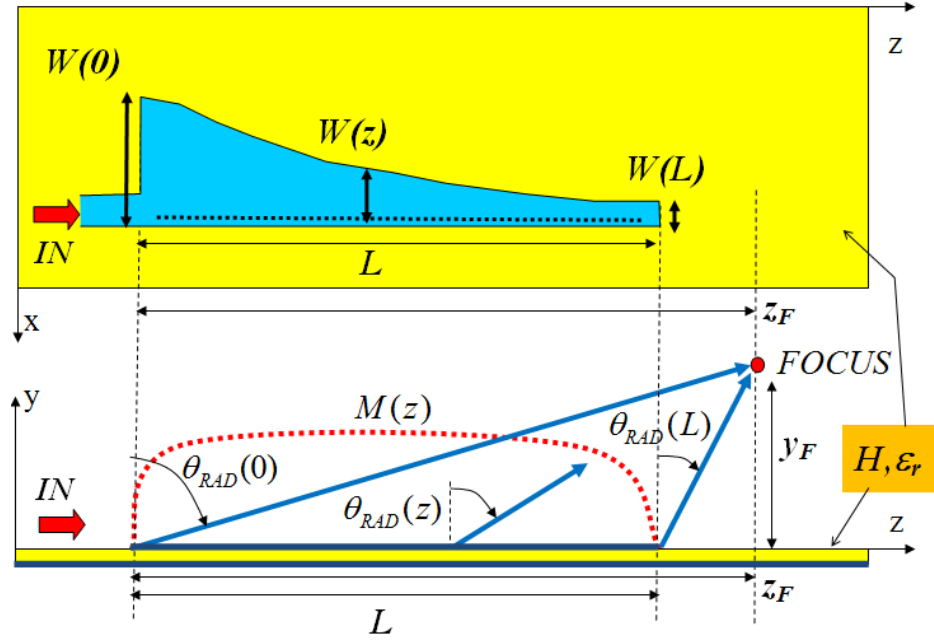


Figure 4.45: Scheme of width-tapered microstrip leaky-wave lens (MLWL).

The section is distributed as follows. In Section 4.4.2, it is theoretically described how a microstrip leaky-wave lens (MLWL) can be conceived by appropriately modulating the strip width  $W$  along the microstrip length as shown in Fig. 4.45. The limitations of microstrip technology in implementing near-field focusing through leaky waves are also explained in this section, together with the conditions that assure optimum focusing for a certain focal point and a given planar substrate. In Section 4.4.3, the synthesis technique is applied to the design of a practical MLWL using commercial substrate and operating at 15 GHz, showing experimental results that confirm the theory. Particularly, Section 4.4.3 describes the near-field measurement set-up, which makes use of a parallel-plate medium. Fig. 4.51 reports the results obtained for a single MLWL, while Fig. 4.53 illustrates how the arrangement of two MLWL located front-to-front allows to obtain a symmetrical near-field pattern with increased focusing resolution. In Fig. 4.59, it is studied the scanning of the focused region when frequency is varied in the range 14 GHz-16 GHz, showing how the focal length can be tuned by simply changing

the operating frequency. Finally, Section 4.4.4 summarizes the conclusions of this work.

#### 4.4.2 Focusing Conditions in a Microstrip LWA

The theory needed to analyze and design a tapered rectilinear LWL was introduced in [121] using some approximate ray-optics expressions, and lately more accurately derived in [124]. The leaky-wave complex propagation constant must be varied along the longitudinal position of the rectilinear antenna ( $z$ -axis in Fig. 4.45), so that both the pointing angle  $\theta_{\text{RAD}}$  and the normalized leakage rate  $\alpha(z)/k_0$  are  $z$ -dependent functions:

$$k(z)/k_0 \approx \sin \theta_{\text{RAD}}(z) - j\alpha(z)/k_0 \quad (4.22)$$

For a given LWL length  $L$ , radiation efficiency  $\eta_{\text{RAD}}$ , optimum aperture distribution, and focal point  $(z_F, y_F)$ , the functions  $\theta_{\text{RAD}}(z)$  and  $\alpha(z)/k_0$  are derived using closed-form expressions [121], [124]. For instance, Fig. 4.46 shows the requested tapering for a rectilinear LWL of length  $L = 20\lambda_0$  with a focal point at  $(z_F = 25\lambda_0, y_F = 25\lambda_0)$  and  $\eta_{\text{RAD}} = 90\%$ . As the leaky-wave advances along the LWL length,  $\theta_{\text{RAD}}$  is decreased and  $\alpha(z)/k_0$  is increased, as indicated by the arrows in Fig. 4.46.

As explained in [124], the most difficult part to conceive a practical rectilinear LWL is the design of the modulated dimensions of the LWA which synthesize the requested variation of  $\theta_{\text{RAD}}(z)$  and  $\alpha(z)/k_0$ . This step relies on the choice of a LWA technology that has enough geometrical degrees of freedom to simultaneous and independent control  $\theta_{\text{RAD}}$  and  $\alpha/k_0$  in a sufficient large range of values [121], [124]. For instance, a slotted leaky waveguide was chosen in [124] to theoretically design a rectilinear LWL due to this property. On the contrary, it is well-known the lack of simultaneous control over phase and attenuation constants of the operating  $\text{EH}_1$  leaky mode in microstrip leaky-wave antennas (MLWAs) [60]–[63]. This

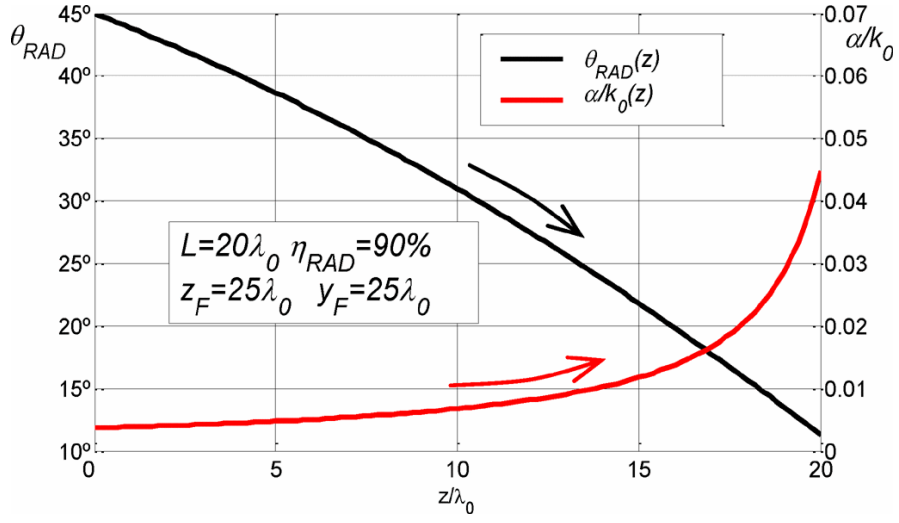


Figure 4.46: Tapering of leaky mode to synthesize a rectilinear LWL.

is due to its simplicity, since only a geometrical parameter can be tapered using printed-circuit techniques, namely the microstrip width  $W$ . The same occurs for the half-width MLWA [71], [72], [182], which is a simplification of the original MLWA by inserting a metallic wall in one side of the strip. Fig. 4.47 show results for the  $EH_1$  leaky mode of a half-width MLWA, in a substrate with height  $H = 0.254$  mm and relative dielectric constant  $\epsilon_r = 2.2$ . The strip width  $W$  values are in the range  $W = [3 \text{ mm} - 5 \text{ mm}]$  for leaky-mode operation in the 15 GHz band. These leaky-mode frequency dispersion results were obtained from a simple but accurate transverse equivalent network (TEN) extensively used in the analysis and design of MLWAs [62], [63], [71], [72], [182].

As it can be seen in Fig. 4.47a, the MLWA provides a simple mechanism to control the pointing directions  $\theta_{RAD}$  of the leaky mode by simply modifying the printed-strip width  $W$ . At a fixed design frequency, wider strips provide higher values of  $\theta_{RAD}$  (up to endfire radiation) while narrower strips radiate at lower  $\theta_{RAD}$  (near broadside). On the other hand, the variation of  $\alpha/k_0$  with  $W$  follows the common dispersion relation of a leaky mode [62], i.e. lower  $\theta_{RAD}$  provide higher  $\alpha/k_0$ , while higher  $\theta_{RAD}$  offer lower  $\alpha/k_0$  (which ultimately provides  $\alpha/k_0 = 0$

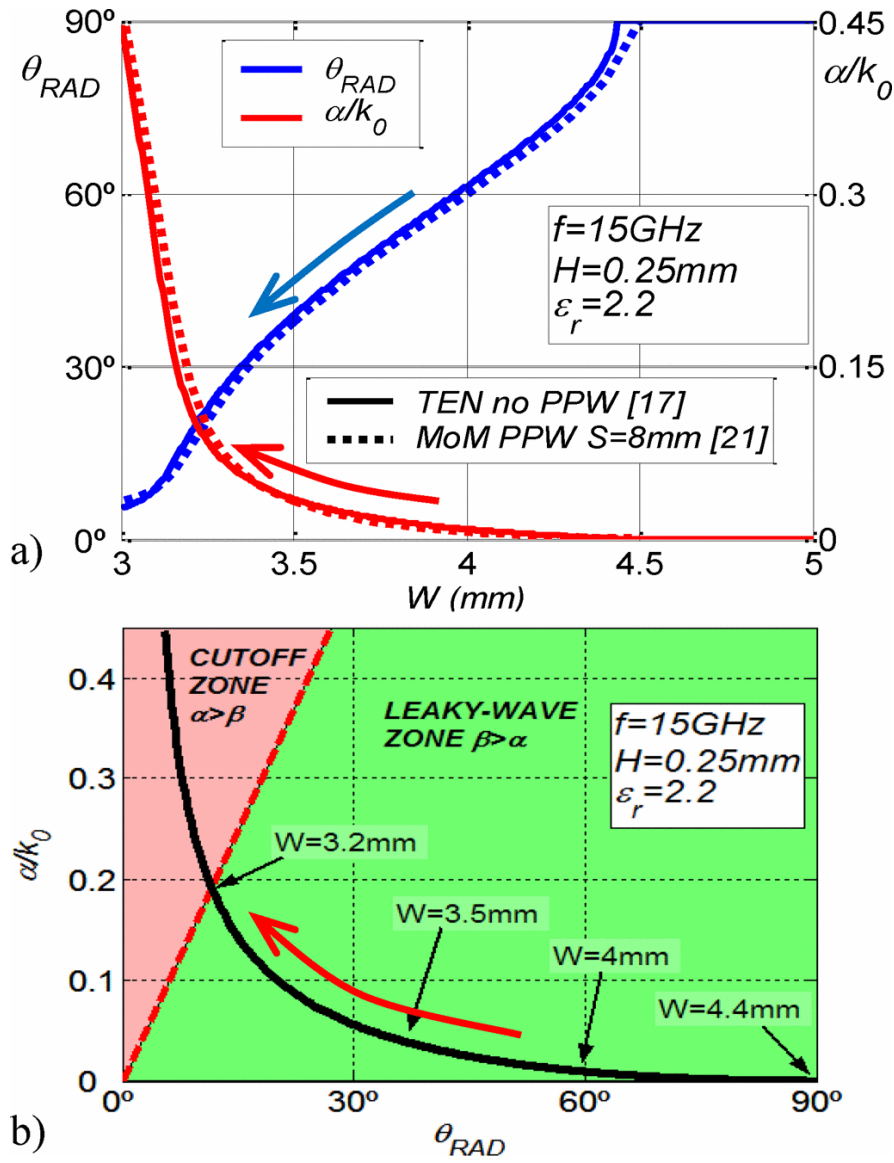


Figure 4.47: a) Microstrip leaky-mode dispersion with strip width  $W$  at 15 GHz. b) Characteristic curve  $\alpha/k_0 - \theta_{RAD}(W)$  for substrate with  $H = 0.254\text{mm}$  and  $\epsilon_r = 2.2$ .

when  $\theta_{RAD} = 90^\circ$ , see Fig. 4.47). Due to the lack of more geometrical variables,  $\theta_{RAD}$  and  $\alpha/k_0$  cannot be independently adjusted for a given dielectric substrate. This dependence is represented by the characteristic curve that relates the couple of values  $(\theta_{RAD}, \alpha/k_0)$  obtained for each strip width  $W$ , as shown in Fig. 4.47b.

This curve is characteristic of the microstrip  $\text{EH}_1$  leaky mode in a particular substrate  $(H, \epsilon_r)$  and frequency of operation. For any substrate, this curve always represents that decreasing values of  $W$  provide decreasing values of  $\theta_{\text{RAD}}$  and increasing values of  $\alpha/k_0$ , as highlighted by the direction of the red arrow plotted in Fig. 4.47b. On the other hand, the tapering of  $\theta_{\text{RAD}}$  and  $\alpha/k_0$  requested in a LWL design is always characterized by decreasing  $\theta_{\text{RAD}}(z)$  and increasing  $\alpha(z)/k_0$  functions, as also indicated by the arrows drawn in Fig. 4.46. Therefore, by decreasing the strip width  $W$  as the leaky wave advances along the longitudinal direction of the MLWA  $z$ , it can decrease  $\theta_{\text{RAD}}$  and increase  $\alpha/k_0$ , which is in consistency with the synthesis of a near-field focused aperture. The question is whether the tapering of width  $W$  can exactly match the requested coupled variations of  $\theta_{\text{RAD}}$  and  $\alpha/k_0$  for any LWL design. The response is negative in a general case.

To clarify this point, Fig. 4.48 repeats the characteristic curve of our MLWA in the selected substrate (Fig. 4.47b), but with the addition of the  $\alpha/k_0$ - $\theta_{\text{RAD}}$  characteristic curves for different LWL designs. For instance, for the tapering of the LWL shown in Fig. 4.46 ( $L = 20\lambda_0$ ,  $\eta_{\text{RAD}} = 90\%$ ,  $z_F = 25\lambda_0$ ,  $y_F = 25\lambda_0$ ), it is obtained the  $\alpha/k_0$ - $\theta_{\text{RAD}}$  characteristic curve plotted with magenta dashed-dotted line (LWL1) in Fig. 4.48. As it can be seen, this characteristic curve does not match the curve for our MLWA (shown in black continuous line in Fig. 4.48). However, by changing the LWL design specifications (lens length  $L$  and the focal position  $z_F$ ,  $y_F$ ) while keeping optimum radiation and aperture efficiencies, one can obtain different characteristic curves, as shown in Fig. 4.48 for two new LWL designs.

Particularly, LWL3 design ( $L = 7.5\lambda_0$ ,  $\eta_{\text{RAD}} = 90\%$ ,  $z_F = 9.3\lambda_0$ ,  $y_F = 4.3\lambda_0$ ) shown with red dotted line in Fig. 4.48) requests a  $\alpha/k_0$ - $\theta_{\text{RAD}}$  function which overlaps the  $\alpha/k_0$ - $\theta_{\text{RAD}}$  characteristic curve of our MLWA. In this way, the MLWA strip width  $W$  can be tapered to synthesize a LWL with the specifications of LWL3. This is illustrated in Fig. 4.49, where the theoretical optimum taper-

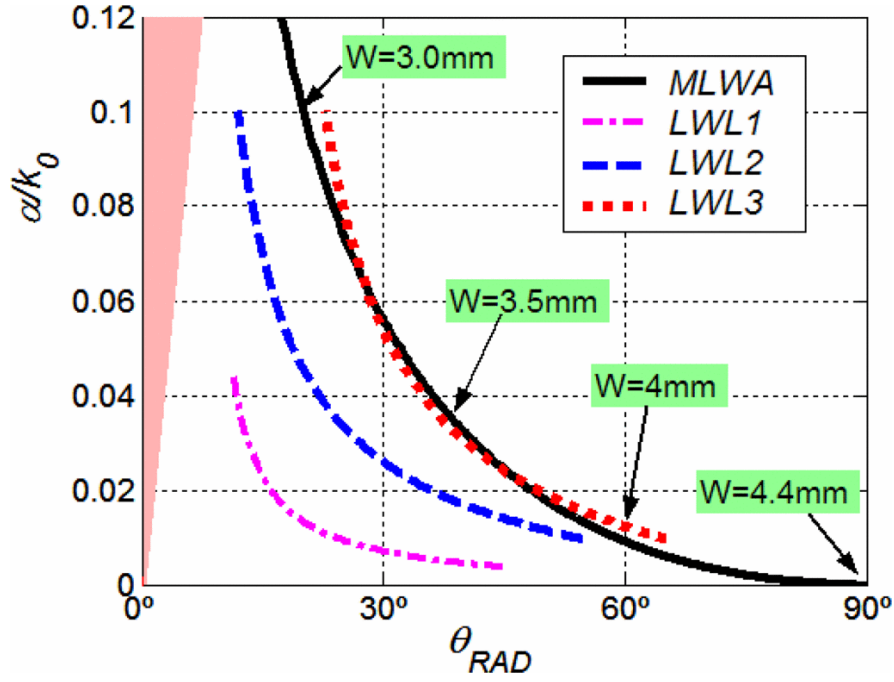


Figure 4.48: Characteristic curves for MLWA ( $f = 15$  GHz,  $H = 0.254$  mm,  $\epsilon_r = 2.2$ ) and different designed leaky-wave lenses (LWL1  $L = 20\lambda_0$ ,  $z_F = 25\lambda_0$ ,  $y_F = 25\lambda_0$ , LWL2  $L = 7.5\lambda_0$ ,  $z_F = 8.8\lambda_0$ ,  $y_F = 6.2\lambda_0$ , LWL3  $L = 7.5\lambda_0$ ,  $z_F = 9.3\lambda_0$ ,  $y_F = 4.3\lambda_0$ ).

ing functions  $\theta_{\text{RAD}}(z)$  and  $\alpha(z)/k_0$  of LWL3, are compared with the tapered leaky-mode functions obtained by modifying the strip width  $W(z)$  in the studied MLWA. As it can be seen,  $W(z)$  must be varied from  $W = 4.1$  mm at the input of the MLWA to  $W = 3.2$  mm at the far end ( $L = 7.5\lambda_0$ ) so that  $\theta_{\text{RAD}}(z)$  is successfully modulated from  $\theta_{\text{RAD}} = 65^\circ$  to  $\theta_{\text{RAD}} = 22^\circ$ , while  $\alpha(z)/k_0$  is tapered from  $\alpha/k_0 = 0.01$  to  $\alpha/k_0 = 0.1$  to provide 90% radiation efficiency and optimum aperture distribution. Therefore it is concluded that a width-modulated microstrip line printed on a given substrate can only provide optimum focusing (with optimal radiation and aperture efficiencies) for certain design specification (lens length and focal position). Obviously, different values of  $H$  and  $\epsilon_r$  give two more degrees of freedom to choose the more appropriate substrate for other design specifications. Probably due to these restrictions, width-tapered microstrip lines

have been used for the synthesis of broadbeam, broadband MLWAs [129], [167], [183], but no practical designs of MLWLs have been demonstrated so far.

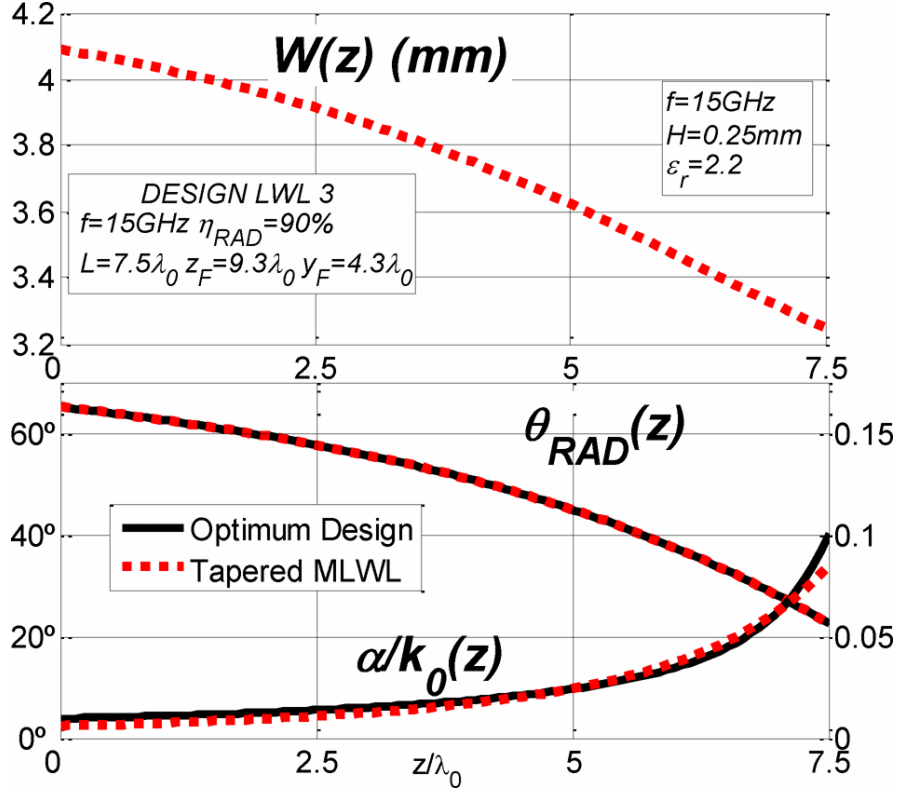


Figure 4.49: Tapering of MLWA width  $W(z)$  ( $f = 15\text{ GHz}$ ,  $H = 0.254\text{ mm}$ ,  $\epsilon_r = 2.2$ ) to synthesize a LWL with  $L = 7.5\lambda_0$ ,  $z_F = 9.3\lambda_0$ ,  $y_F = 4.3\lambda_0$ .

### 4.4.3 Experimental Demonstration

#### Measurement set-up: MLWL inside Parallel Plates

The proposed analysis and design theory is confirmed in this section by fabricating the rectilinear MLWL and then measuring the radiated near fields. To this end, metallic parallel plates surrounding the tapered MLWL and separated at a distance  $S = 8\text{ mm}$  have been used. The parallel-plate waveguide (PPW) is essential to prevent radiated fields from spreading laterally (towards the  $x$ -direction), which would degrade the focusing efficiency of the synthesized two-dimensional

(2D) near-field pattern. A 1D LWA is a line source that provides focusing in one plane (2D focusing) [62], [63], no matter this focusing is created in the near- or far-field regime (a fan-beam is created in the latter case). A more practical microwave lens with 3D free space near-field focusing pattern can be obtained from the arrangement of several width-tapered microstrip lines in a conventional parallel phased-array fashion [62], [71], [72], [182], as done in recent designs of planar microwave lenses [176]–[178]. Besides, the use of the PPW has practical interest in certain applications such as hyperthermia [184] and heating [185], where a confined environment is required for safety reasons (so that the metallic walls prevent from uncontrolled high-power lateral radiation). Moreover, in some curing applications it is needed an uniform field pattern in the vertical direction, so that the samples are carried by a horizontal conveyor belt which passes through a PPW, as done in the present work. Nevertheless, this work does not intend to show the applicability of focusing inside parallel plates, but aims to demonstrate the near-field focusing characteristics of a single modulated microstrip line. The PPW medium is quite convenient to this end. The scheme of the laterally-shielded MLWL is shown in Fig. 4.50a, together with an outline of the  $\text{EH}_1$  leaky electric field inside the half-width MLWA and radiating into the parallel-plate waveguide (PPW), as shown in Fig. 4.50b. The accurate leaky fields in this laterally-shielded microstrip structure can be analyzed using the Method of Moment (MoM) code developed in [186], and are represented in Fig. 4.50c.

The  $\text{EH}_1$  leaky-mode electric field lines shown in Fig. 4.50c confirm the draft of Fig. 4.50b. The vertical ( $y$ -directed) lines of the  $\text{EH}_1$  microstrip mode (resonating below the strip and inside the dielectric slab and shown with continuous red lines in Fig. 4.50b) transform into a weak horizontal ( $x$ -directed) quasi-TEM leaky-wave propagating inside the PPW air region (dashed red lines in Fig. 4.50b), due to the fringed fields created at the strip open-end (dotted red lines in Fig. 4.50b). If the distance between the parallel-plates satisfies  $S < \lambda_0/2$ , only this TEM fields are above cutoff in the PPW, obtaining pure horizontal ra-

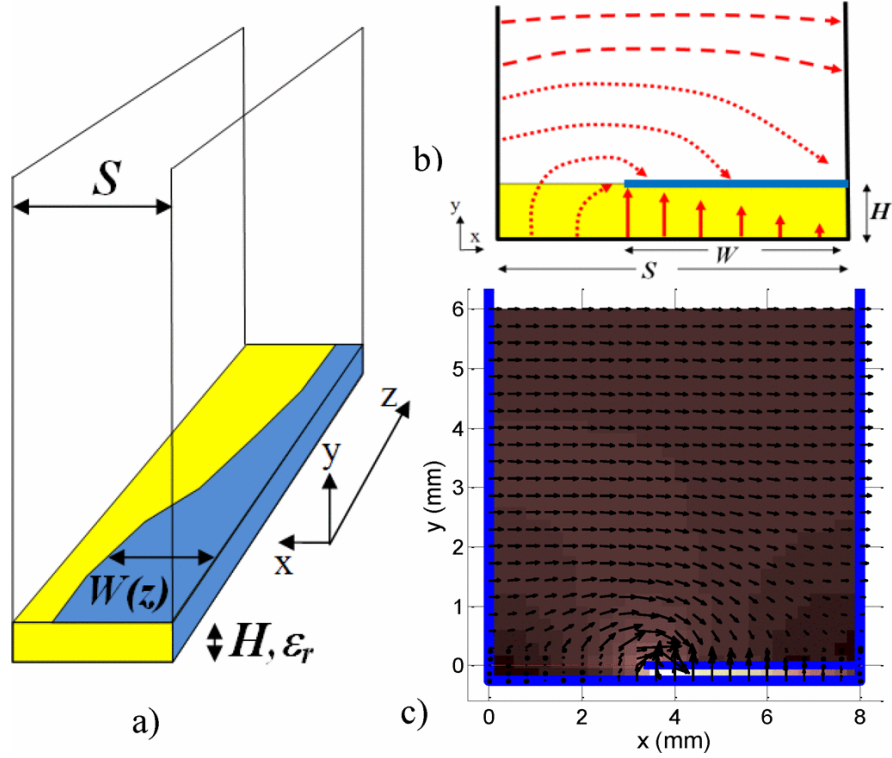


Figure 4.50: a) MLWL embedded in parallel plates. b) Leaky-mode electric field lines. c) Field plot [186] for  $S = 8$  mm,  $W = 4.5$  mm,  $f = 15$  GHz,  $H = 0.254$  mm,  $\epsilon_r = 2.2$ .

diated leaky-fields with no variation in  $x$ . Therefore, the parallel plates create a non-dispersive medium for the radiated leaky fields, which become invariant with respect to  $x$ , so that a pure 2D focusing pattern in the  $zy$ -plane can be obtained. Moreover, the dispersion of the  $EH_1$  leaky mode in this hybrid microstrip-PPW structure computed with [186] is plotted in Fig. 4.50a with dotted lines, showing similar results than in the absence of the PPW. Therefore, the effect of the parallel plates in the width-tapering of the leaky-mode is negligible, and the synthesis technique of Section 4.4.2 can be used for the design of the MLWL embedded in the PPW.

Moreover, the parallel plates will be used as a supporting structure for measuring the near fields, as shown in the pictures of Fig. 4.51. For this purpose, holes of diameter  $D = 4.2$  mm  $= 0.21\lambda_0$  and separated a distance  $d = 6.35$  mm  $= 0.32\lambda_0$

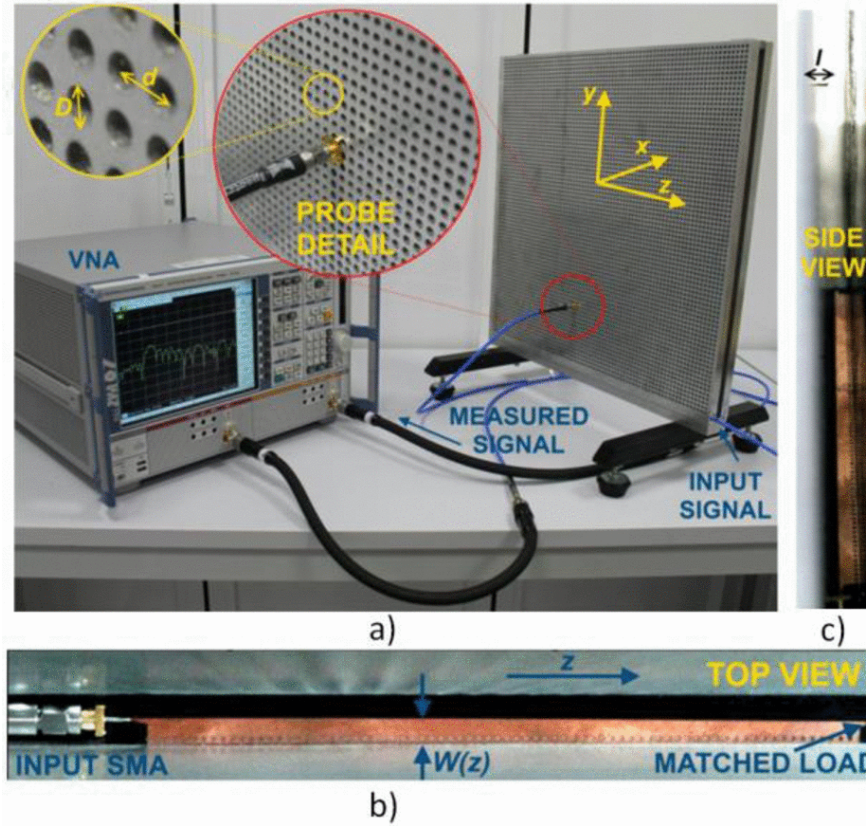


Figure 4.51: Photograph of fabricated width-modulated MLWL and parallel plates near-field measurement set-up.

are drilled in one of the plates. A coaxial probe is manually inserted in the holes to sample the near fields in the  $zy$ -plane. Since the coaxial probe penetrates a sub-wavelength length  $l = 2.9 \text{ mm} = 0.15\lambda_0$  (see Fig. 4.51c) and the holes have sub-wavelength diameter, it is assured that the perturbation of the holes and the probe have minimum impact in the focusing pattern created by the MLWL inside the PPW. Also, it is worth noting that the sampling distance satisfies the Nyquist condition  $d < \lambda_0/2$ . The width-tapered microstrip lens was fabricated on commercial substrate Rogers RT/duroid 5880 ( $H = 0.254 \text{ mm}$ ,  $\epsilon_r = 2.2$ ,  $\tan \delta = 0.0009$ ), using metallic vias of 1 mm diameter and separated 2 mm to create the half-width metallic side. Fig. 4.51b and Fig. 4.51c shows photos of the fabricated MLWL prototype inside the PPW. It can be observed the input SMA connector and the

matching load. A Vector Network Analyzer (VNA) is used to feed the MLWL at its input port and measure the sampled near fields from the coaxial probe. This system allows accurate and stable positioning of the sampling probe, providing precise measurement of the near-fields amplitude and phase distribution in the  $zy$ -plane, as it will be shown next.

### Single MLWL

If a single rectilinear MLWL is embedded in the PPW, a tilted 2D focusing pattern must be obtained as illustrated in Fig. 4.45. Fig. 4.52 shows the near-field pattern in the  $zy$ -plane with  $-10$  dB scale, for the MLWL designed in Section 4.4.2 at the frequency of 15 GHz. Leaky-mode theory [124] (Fig. 4.52a), full-wave HFSS simulations [90] (Fig. 4.52b), and measured results (Fig. 4.52c), show good agreement. It is demonstrated that the designed  $7.5\lambda_0$ -long width-tapered MLWA creates an ellipsoidal tilted focal region in the vicinity of the specified focal point  $z_F = 9.3\lambda_0$ ,  $y_F = 4.3\lambda_0$ . The focal point  $(9.3\lambda_0, 4.3\lambda_0)$  is marked with a red circle in Fig. 4.52a. The well-known focal shift effect [124] can be observed, resulting in a maximum field intensity point (marked with a green circle in Fig. 4.52a) located at  $(8\lambda_0, 3\lambda_0)$ , which is closer to the radiator than the expected focal point. The 3 dB focal region covers a tilted ellipsoid with approximate depth of focus  $3\lambda_0$  and focus width  $1\lambda_0$ . The simulated and measured input matching of the MLWL embedded in the PPW is represented in Fig. 4.53, showing  $S_{11}$  below  $-10$  dB in the 12 GHz to 20 GHz frequency band.

Using amplitude and phase information, one can obtain the time-varying near fields [187], so that the phase fronts can be represented at a given moment. Fig. 4.54 shows the theoretical, HFSS simulated, and measured time-varying near fields, illustrating how the fields emanate from the MLWL and converge at the focal point. Again, good agreement is observed between theory and experiments.

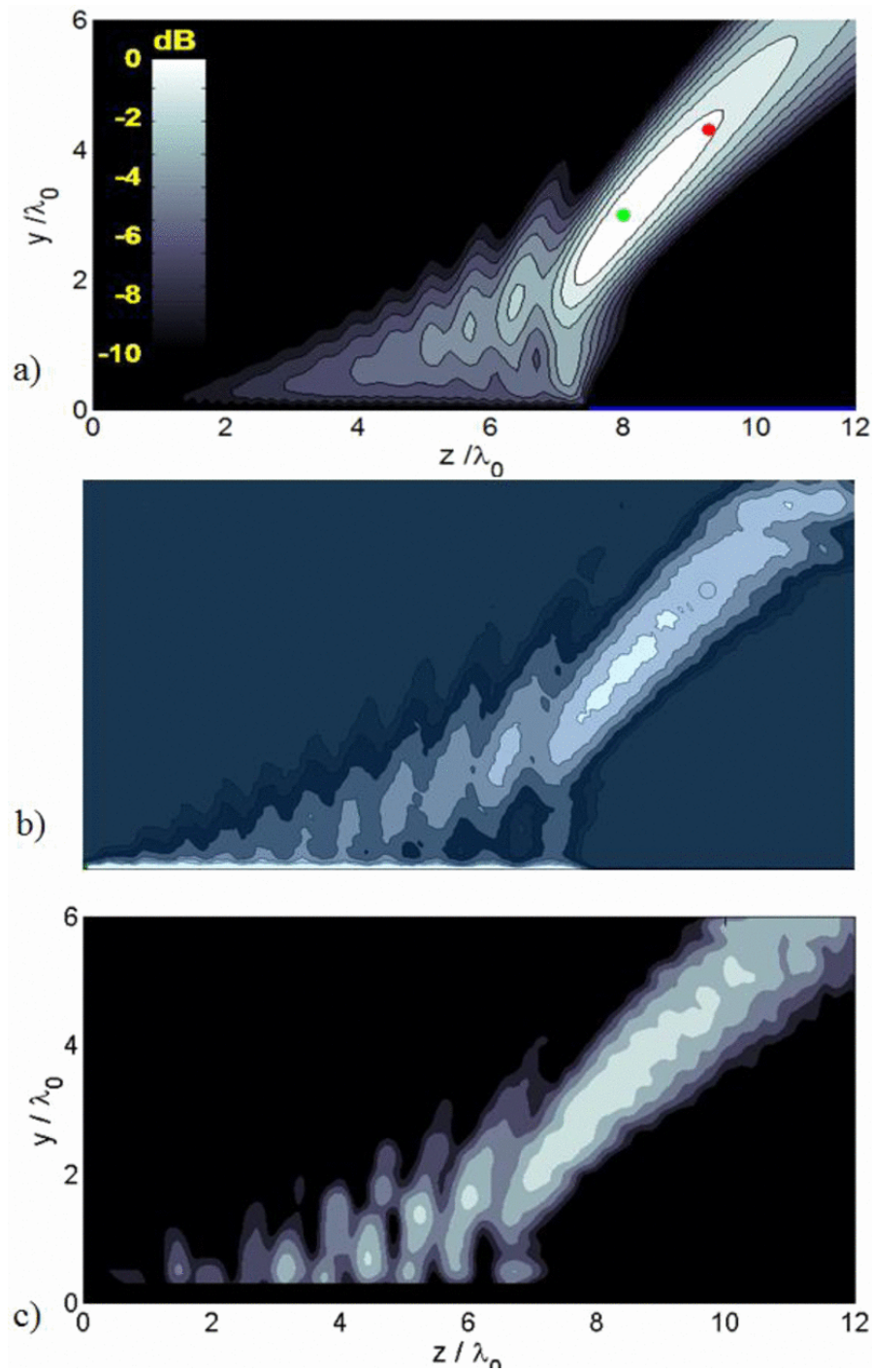


Figure 4.52: a) Theoretical, b) simulated (HFSS) and c) measured focusing pattern for the single MLWL at 15 GHz.

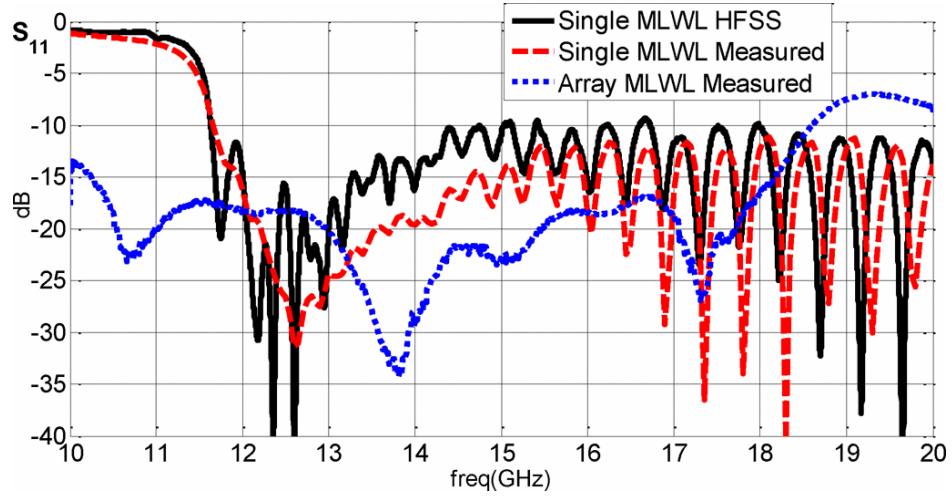


Figure 4.53: Simulated and measured matching for single lens and array of two MLWLs.

#### Front-to-Front In-Phase Array of MLWLs

In order to obtain a symmetric (non tilted) focal region with increased resolution, two identical MLWLs are arranged front-to-front as shown in Fig. 4.55. They are separated at a distance  $D = 1\lambda_0$  so that by in-phase feeding each MLWL, a mirrored focusing pattern with constructive interference at  $z = 8\lambda_0, y = 3\lambda_0$  must be created.

This array set-up is represented in the photograph of Fig. 4.56, where it is observed the power divider and the coaxial cables which feed in-phase the two MLWLs. The array input matching measured by the VNA is represented in Fig. 4.53, showing a different response to the one of the single MLWL ( $S_{11} < -10$  dB from 10 GHz to 18 GHz) due to the divider. The theoretical, simulated and measured near fields at 15 GHz are shown in Fig. 4.57 with  $-20$  dB scale. The agreement between leaky-mode theory, full-wave HFSS results, and experiments is very good.

A symmetrical focusing pattern is successfully generated by the array, observing cylindrical phase-fronts converging at a focal point located at the middle between the two MLWLs  $z_F = 8\lambda_0$ , and with the expected focal length  $y_F = 3\lambda_0$ . The array configuration provides higher focusing resolution (lower size of the fo-

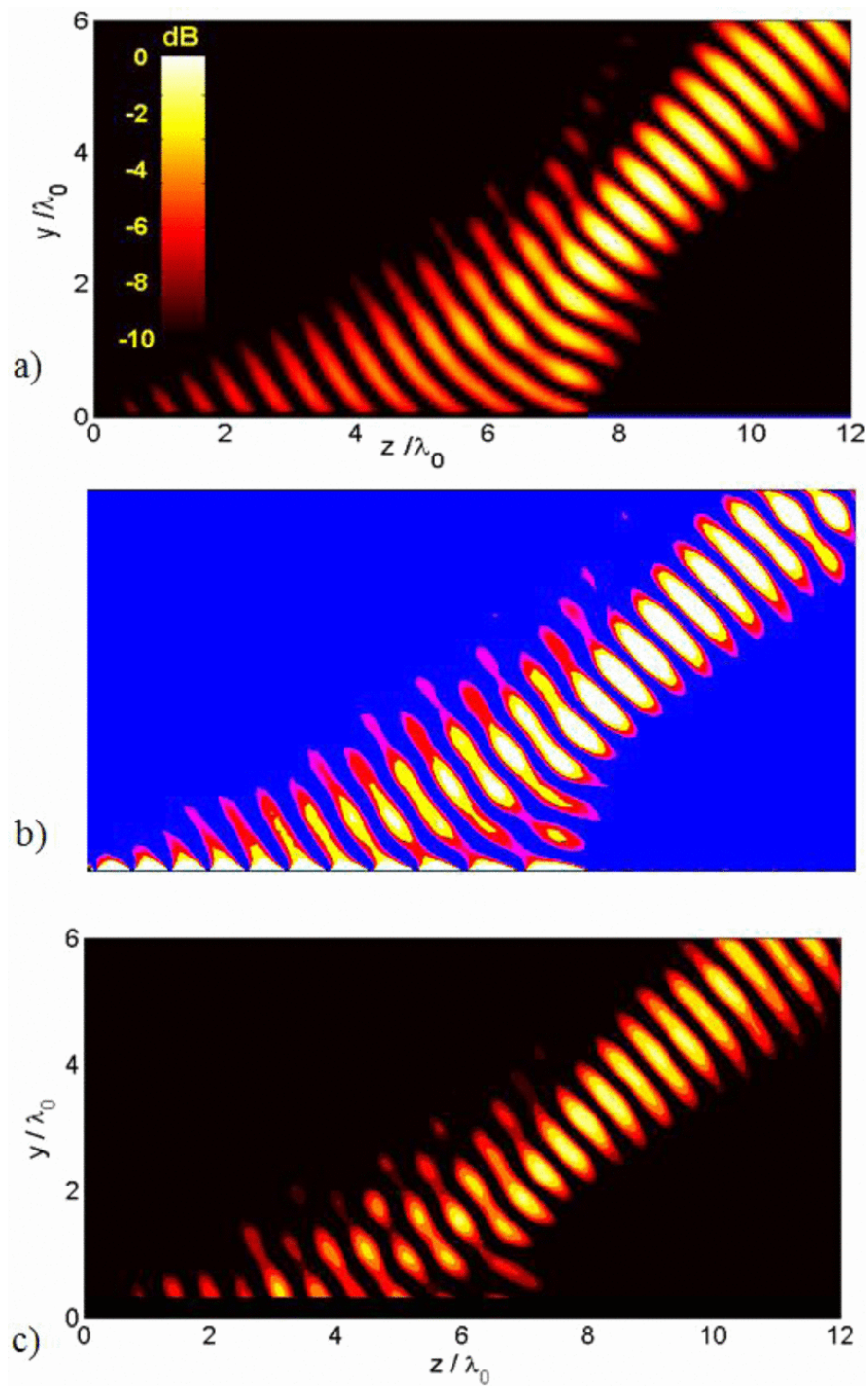


Figure 4.54: a) Theoretical, b) simulated (HFSS) and c) measured time-varying near fields for the single MLWL at 15 GHz.

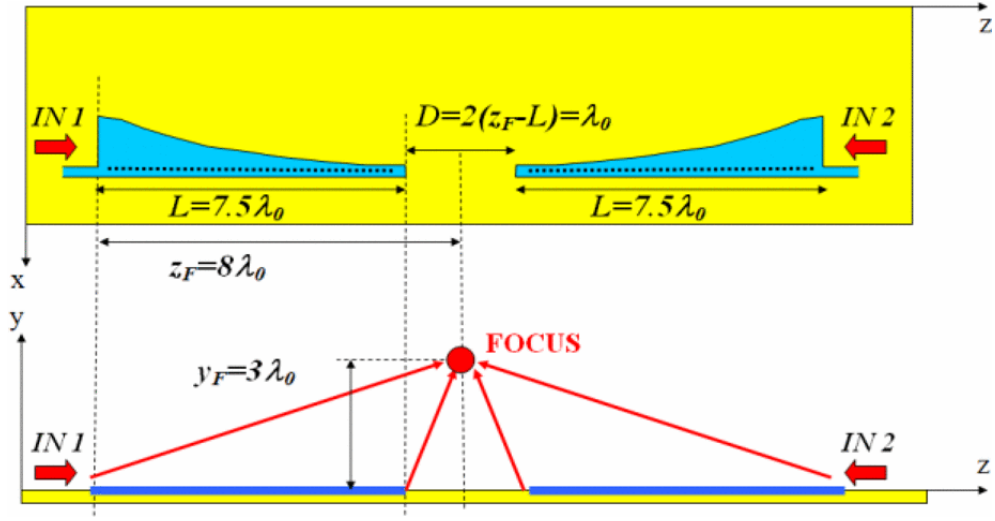


Figure 4.55: Scheme of two MLWLs placed front-to-front.

cal region) than the single lens, as it corresponds to a focused aperture with double length. This improvement is illustrated in Fig. 4.58, where the focusing patterns of the single MLWL and the array of two in-phase MLWLs are superimposed. As it can be seen, the size of the focal region has been substantially reduced. It also becomes evident the symmetry of the focusing pattern when compared to the tilted field distribution generated by the single MLWL.

To compare theoretical and measured results in a more quantitative way, axial cuts ( $y$ -line at  $z = z_F = 8\lambda_0$ ) and transverse cuts ( $z$ -line at  $y = y_F = 3\lambda_0$ ) of the array focusing pattern are plotted in Fig. 4.59a and Fig. 4.59b, respectively. Again, very good agreement is observed in both cuts between experiments, full-wave simulations, and leaky-mode theory. The discrepancies with leaky-mode theory are due to radiation by discontinuities which are only taken into account in the full-wave simulations of the complete 3D CAD model of the lenses performed with HFSS. Nevertheless, excellent agreement is observed at the points close to the focal region, confirming the design of a MLWL with optimized aperture efficiency. Due to this success in the synthesis of the desired amplitude and phase aperture distributions, it is obtained 3 dB focal width of only  $\Delta z = 0.33\lambda_0 =$

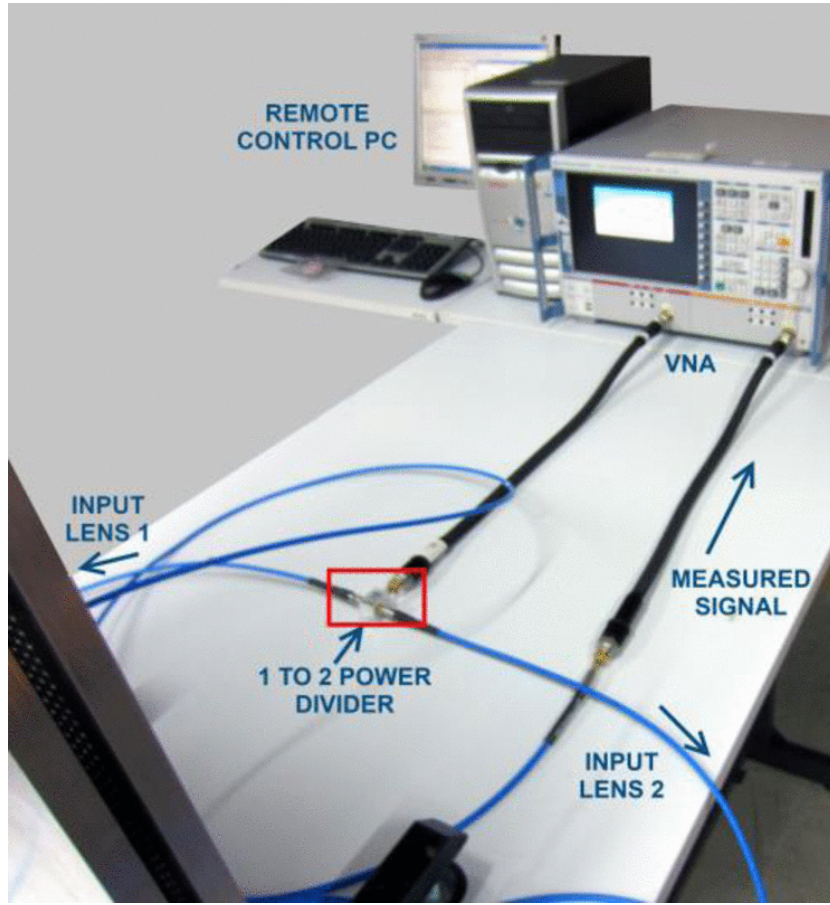


Figure 4.56: Measurement set-up for the array configuration.

6.7 mm and 3 dB focal depth  $\Delta y = 1.25\lambda_0 = 25$  mm. Sidelobe level in the transverse cut is  $-3$  dB, while the forelobe and aftlobe levels in the axial cut are approximately  $-9$  dB.

### Frequency-scanning of the Focal Region

As it is well known [60]–[63], [71], [72], [182], microstrip leaky-wave antennas (MLWAs) vary the far-field radiation pattern with frequency due to the strongly dispersive nature of the  $\text{EH}_1$  leaky mode, showing a scanning of the main radiated beam from broadside to endfire direction as frequency is increased. Similarly, it was theoretically demonstrated in [124] that a focused LWL creates a frequency-

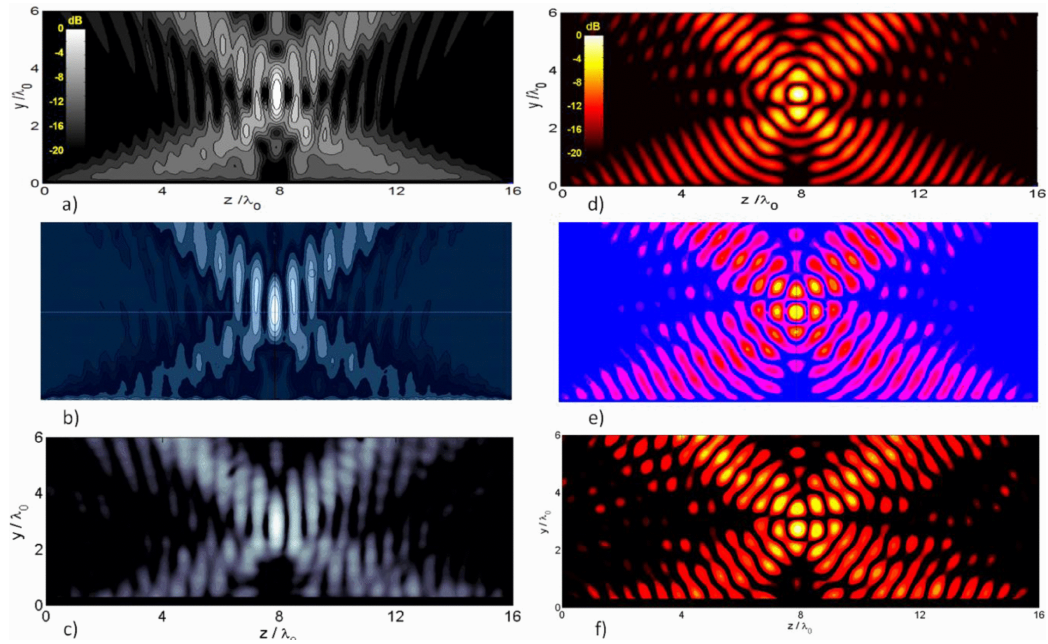


Figure 4.57: a) Theoretical, b) simulated (HFSS) and c) measured focusing pattern and corresponding time-varying near-fields for the array of two MLWLs at 15 GHz.

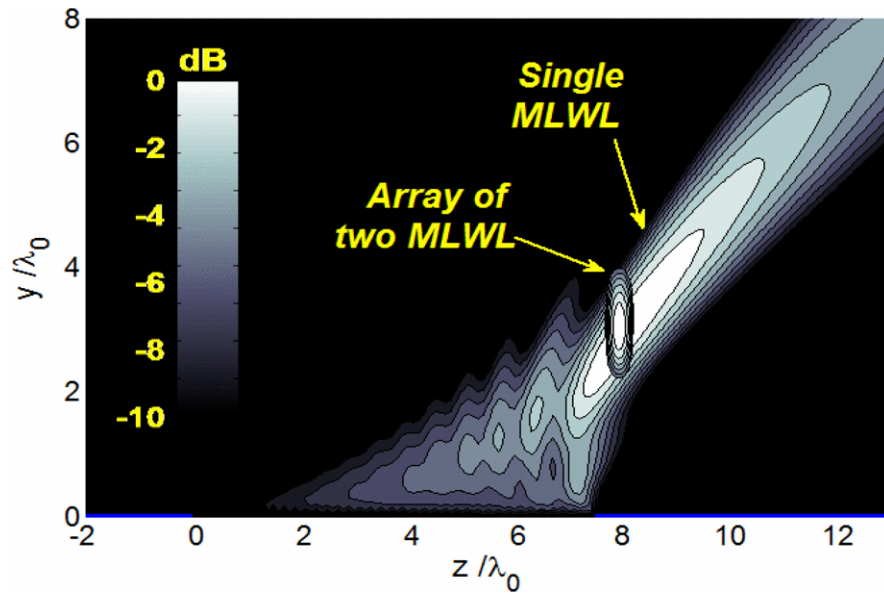


Figure 4.58: Comparison between theoretical focusing patterns of single and array of two MLWLs at 15 GHz, obtained from leaky-mode theory.

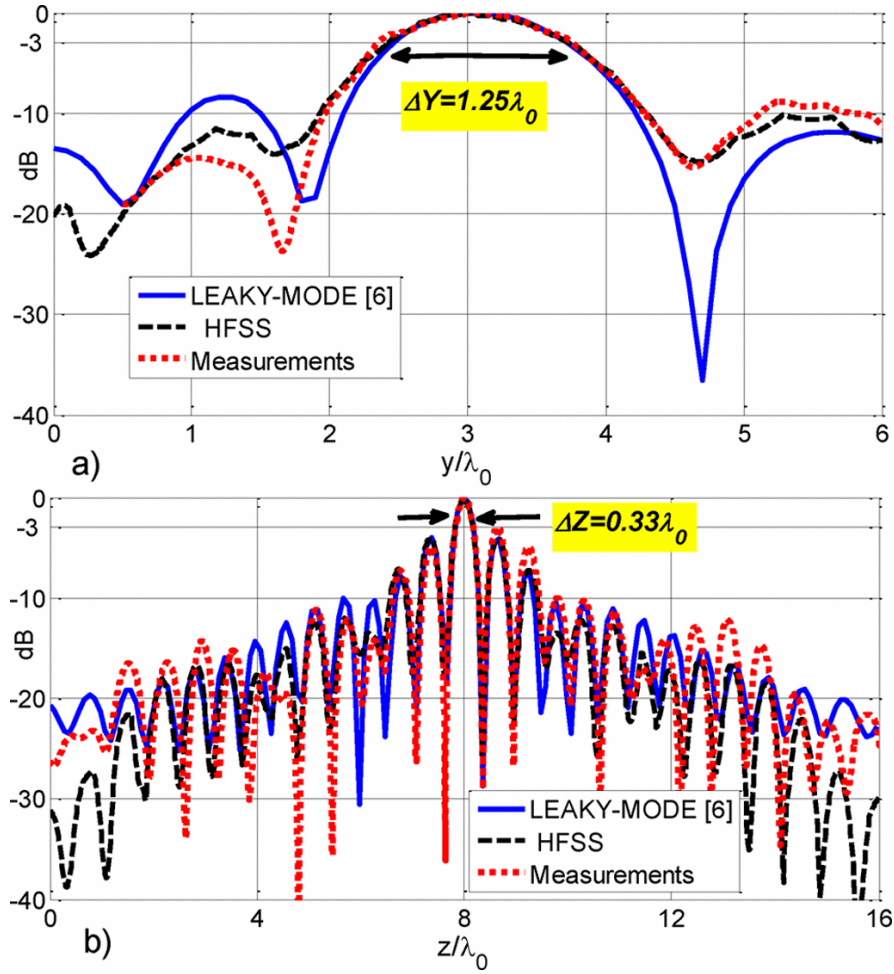


Figure 4.59: Theoretical and measured a) axial and b) transverse cuts at 15 GHz.

steerable focusing region which is scanned in the near-field towards the aperture as frequency is increased. Here it presents experimental results that confirm this general theory for the case of our MLWL. Fig. 4.60a shows with  $-6$  dB scale the variation of the measured focusing pattern of the single MLWL for three frequencies around the design frequency: 14 GHz, 15 GHz and 16 GHz. As it can be seen, the tilted focal region moves in the  $zy$ -plane from (140 mm, 80 mm) at 14 GHz, to the design focal point (160 mm, 60 mm) at 15 GHz, and then to (160 mm, 40 mm) for 16 GHz. Fig. 4.60b shows the resulting near-field pattern for the array of two MLWLs. As it can be seen, for 15 GHz and 16 GHz a single main focused region

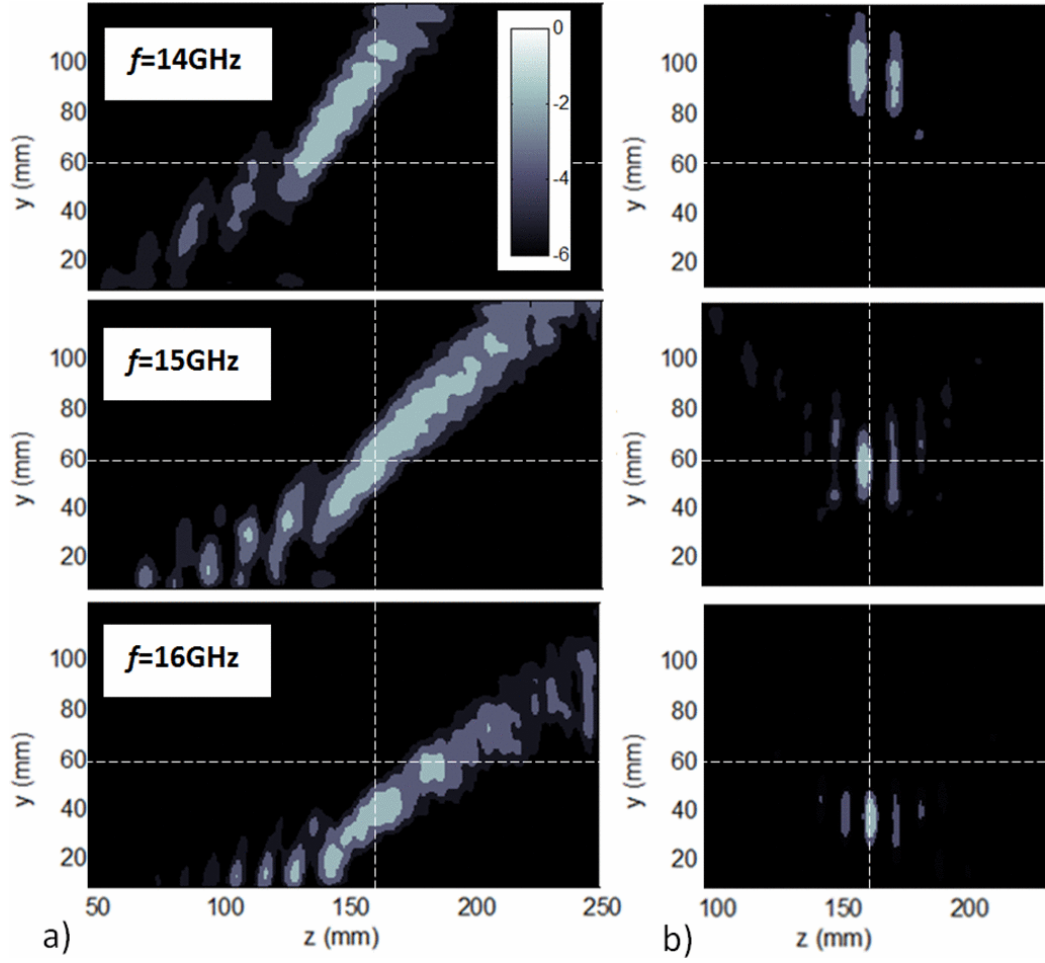


Figure 4.60: Measured frequency scanning of the focusing region around the design frequency a) single MLWL b) array of two MLWLs.

is obtained at the middle point between the two lenses  $z = 160$  mm, and with decreasing focal height from  $y = 60$  mm at 15 GHz to  $y = 40$  mm at 16 GHz, as a result of the coalescence of the two beams at the same point. However, at 14 GHz there are two main focal regions at the same focal height ( $y = 100$  mm) but separated at two different transverse positions,  $z_1 = 152$  mm and  $z_2 = 168$  mm. This is due to the fact that the two beams created by each MLWL do not merge at the same transverse point, creating two focal points instead of a single focus. This phenomenon is general for any array of focused LWLs, and it is the equivalent

in the near-field regime to the splitting-condition occurring in LWAs radiating at broadside in the far field [188]. As a result, scanning bandwidth with a single focus is limited, in our case to the range from 14.2 GHz to 17 GHz.

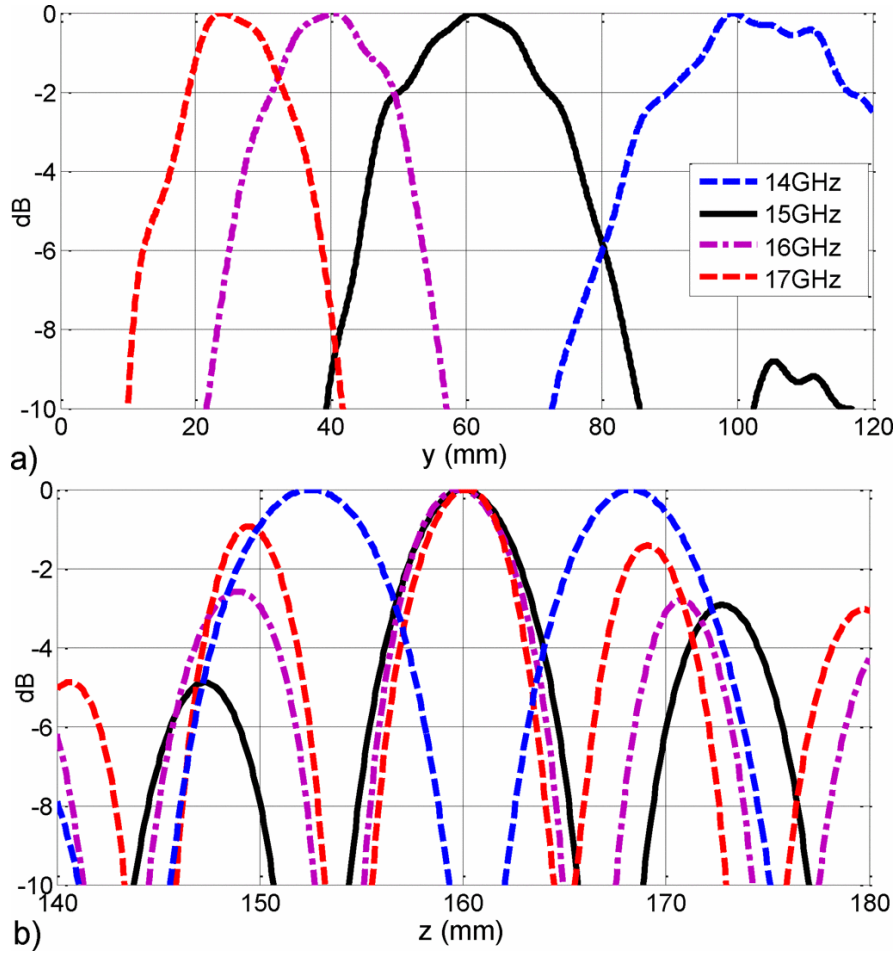


Figure 4.61: Measured a) axial and b) transverse cuts as frequency is varied for the array of two MLWLs.

The measured axial and transverse near-field cuts as frequency is varied from 14 GHz to 17 GHz are plotted in Fig. 4.61a and Fig. 4.61b, respectively. The axial cuts clearly show the aforementioned decrease in the focal height from  $y_F = 100$  mm at 14 GHz to  $y_F = 26$  mm at 17 GHz. It is also evident from Fig. 4.61a the corresponding well-known [189] decrease of the focal depths for lower focal lengths, obtaining a change from  $\Delta y = 39$  mm at 14 GHz to  $\Delta y = 17.5$  mm at

17 GHz. The transverse cuts along the  $z$ -direction in Fig. 4.61b are obtained at the respective focal heights  $y_F$  for each frequency. From Fig. 4.61b, it can be readily seen that a single focal region at the central longitudinal point  $z = 160$  mm is obtained for frequencies between 15 GHz and 17 GHz, presenting a focal width which also decreases as frequency increases (from  $\Delta z = 6.9$  mm at 15 GHz to  $\Delta z = 5.4$  mm at 17 GHz). At 14 GHz, it is certainly observed the aforementioned splitting from one single focus to two focal regions located at  $z_1 = 152$  mm and  $z_2 = 168$  mm, and a local field minimum is obtained at the central position  $z = 160$  mm.

Finally, Fig. 4.62 represents the variation with frequency of the focal height  $y_F$ , focal depth  $\Delta y$ , and focal width  $\Delta z$ , highlighting the single-focus bandwidth. Measured results are consistent with  $\text{EH}_1$  leaky-mode dispersion theory, showing the continuous scanning of the focal height  $y_F$  from 100 mm to 26 mm in the range 14 GHz-17 GHz, and the corresponding decrease in the focal depth  $\Delta y$  and width  $\Delta z$ .

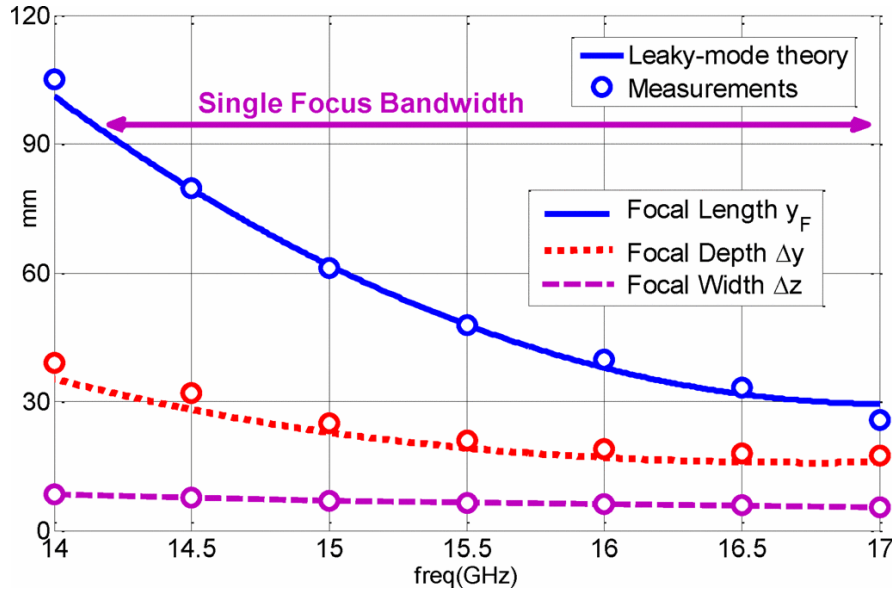


Figure 4.62: Variation of focal length, depth and width with frequency for the array of two MLWLs.

The tuning of the focal length a frequency is varied by simply using the dispersive properties of the  $\text{EH}_1$  microstrip leaky mode, is an alternative solution to more complicated fixed-frequency tuning schemes used in printed-circuit focused arrays. For instance in [180], a RFID tunable near-field focused phased-array antenna operating at 5.8 GHz was proposed using three circular arrays of eight printed dipoles. The corporate distribution network of phased-array solutions is clearly a much more complex subsystem (formed in the case of [180] by two phase shifters, one 1:4 power divider, and four 1:8 power divider), than the simple feeding system needed by frequency-scanned MLWLs. In [179], a focus-scanning strip-grating LWA was proposed to steer the focus at 2.4 GHz by using FET switches connected to each strip of the array. Also in this case, a complex electronic system is required to control the bias of each FET. Again, frequency-scanned MLWLs offer a much simpler approach since there is no need to use active circuits, being this difference more obvious as the size of the focused aperture increases (which is needed for higher focusing resolution, as in the case studied in this work with a total length of  $16\lambda_0 = 32$  cm, see Fig. 4.55).

However, the frequency-scanning of the focal distance is useful only for those applications in which it is not crucial to keep constant the operating frequency. This might include microwave hyperthermia applicators [184], non-contact (remote) sensors [185], or wireless power transmission systems [190]. Moreover, this focusing frequency response can be a desirable feature for new emerging applications, such as electrical prisms operating as spectral-spatial demultiplexers [191], or microwave analog real-time spectrum analyzers [163].

#### 4.4.4 Conclusion

In this section, it has been demonstrated the ability of a width tapered microstrip leaky-wave antennas to synthesize a near-field focusing pattern. The interest relies in its simplicity: by only decreasing the width of a microstrip line along its length, a leaky wave can be tapered to provide an aperture-field distribution with

converging quadratic phase and equiangular amplitude illumination. An efficient synthesis technique for the modulation of the strip width has been developed by using dispersion results of the  $\text{EH}_1$  microstrip leaky mode. It has been explicitly illustrated the limitations of microstrip technology in implementing near-field focusing through leaky waves as a result of the lack of simultaneous and independent control over phase and attenuation constants. In this way, the optimum focusing pattern is determined by the characteristic dispersion curve of the  $\text{EH}_1$  leaky mode in the selected substrate.

An optimum near-field focused pattern with focal height  $3\lambda_0 = 60$  mm has been synthesized at 15 GHz using commercial substrate with  $H = 0.254$  mm and  $\epsilon_r = 2.2$ , and using two  $7.5\lambda_0$ -long microstrip lines arranged front-to-front and separated a distance of  $1\lambda_0$  (total length 320 mm). The width-tapered microstrip lenses have been fabricated, and parallel plates have been located at both lateral sides to avoid dispersion of the radiated fields in the transverse direction, and to help in the near-field measurement campaign. The near-field patterns have been measured using a coaxial probe that samples the  $zy$ -plane through subwavelength holes which have been drilled in one of the plates. Very good agreement has been obtained between the theoretical focusing pattern and experimental results, obtaining at 15 GHz a focal width of only  $0.33\lambda_0 = 6.7$  mm, and focal depth of  $1.25\lambda_0 = 25$  mm, thus indicating the success in the synthesis of an optimum focusing pattern. Finally, the frequency-scanning behavior of the microstrip lens has been studied, showing a decrease of the focal length from  $y_F = 100$  mm at 14 GHz to  $y_F = 26$  mm at 17 GHz, which is in coherence with the dispersion of the  $\text{EH}_1$  tapered leaky mode.

The proposed width-tapered microstrip leaky-wave lens avoids the use of complex and lossy distribution networks associated to focused phased-arrays. It is also a much simpler solution compared to previous curved leaky lenses, and it presents lower profile and easier fabrication if compared to leaky lenses based on modulated waveguides. Also, the design methodology and fabrication simplicity is bet-

ter than leaky lenses based on metamaterial concepts. Finally, it is also remarkable that the scanning of the focus by just varying the frequency is a much simpler tuning technique than the use of active tuning components, when the application is not restricted to a fixed operation frequency.

## **4.5 Quasi-Optical Multiplexing Using Leaky-Wave Near-Field Focusing Techniques in Substrate Integrated Waveguide Technology**

This section describes a quasi-optical multiplexing technique in substrate integrated waveguide (SIW) technology. It is based on the frequency dispersion response (spectral-spatial decomposition) of the fundamental SIW leaky mode, which emanates from the SIW and radiates inside the host dielectric substrate. Full-wave simulations in the 10 GHz-20 GHz band demonstrate that the rejection between channels can be increased and the insertion losses reduced by using near-field focusing techniques.

### **4.5.1 Introduction**

Recently, an increased interest over the use of artificial dispersion-engineered 1D and 2D transmission mediums with application to microwave near-field focusing [161], diplexing [192], analog Fourier transform [162], multiplexing [191], or real-time spectrum analyzer [163] has been given. All these designs are based on the spatial-spectral decomposition which results from the frequency-dispersive propagation constant along the studied medium. By suitably engineering the dispersion of the transmission line, a specified spatial filtering response can be obtained in which each frequency is routed to a different spatial direction. This type of device has also been recalled as an electrical prism [191], due to the analogy with optical prisms. All previous designs [161]–[163], [191], [192] are based on

the use of artificial metamaterial transmission lines, where the dispersion of the propagating modes is controlled by the components which constitute the lattice unit cell.

In this work, it is proposed the use of a simpler substrate integrated waveguide (SIW) transmission line to conceive a planar microwave multiplexer based on the dispersion of the fundamental leaky mode [193]. As it is shown in Fig. 4.63a, the SIW can radiate inside the host substrate if the distance between posts  $P$  of one of its side walls is large enough, as originally proposed in [45] to conceive SIW leaky-wave antennas. This radiation is in the form of a TE surface leaky wave (polarized along  $x$  according to Fig. 4.63a), which propagates through the dielectric substrate at a given angle  $\theta_d$  (given by  $\beta/k_d \approx \sin \theta_d$  where  $k_d = k_0\sqrt{\epsilon_r}$  is the substrate wavenumber and  $\beta$  is the leaky-mode phase constant along the  $z$ -axis), and with a given leakage rate  $\alpha$  (Np/m). Also, it was demonstrated in [91] that the variation of the SIW width  $W$  and posts' distance  $P$  provides simultaneous control over  $\theta_d$  and  $\alpha$ , thus allowing flexible design of the far-field radiation pattern.

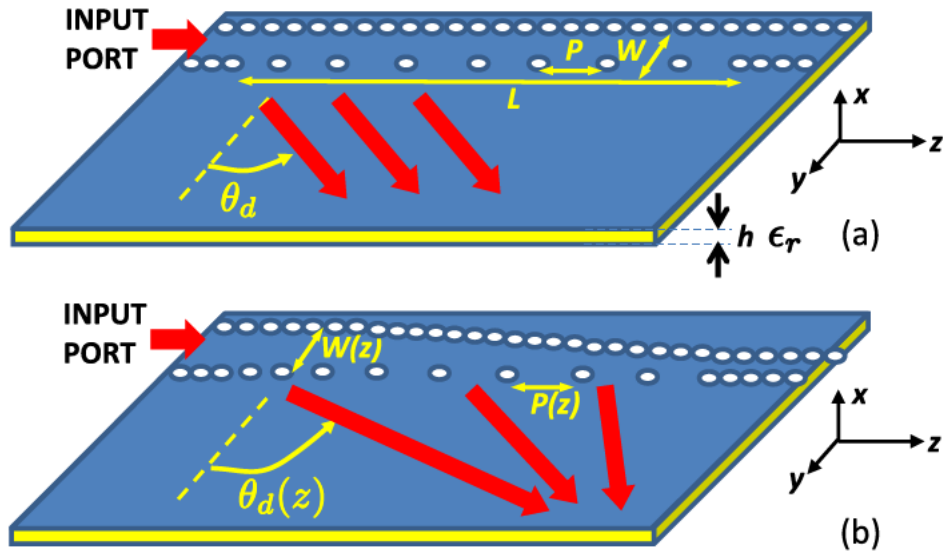


Figure 4.63: Scheme of leaky SIW radiating inside the integrated substrate: a) Uniform SIW and b) Modulated SIW with near-field focusing.

The section is distributed as follows. Section 4.5.2 describes the working mechanism of the proposed multiplexer, illustrating with simulations the design of a uniform SIW leaky-wave multiplexer operating in the 10 GHz to 20 GHz microwave band. Section 4.5.3 presents a variation of this first uniform design, by modulating the  $W$  and  $P$  of the SIW along its length as shown in Fig. 4.63b. The modulation is needed to synthesize a focusing two-dimensional wave [194], which near-field focus can be steered with frequency as proposed in [124]. Moreover, the required geometrical variations are obtained by using a transverse equivalent network of the structure, which allows an efficient computation of the leaky mode as function of the main parameters of the SIW. Finally, full-wave simulated results for both uniform and non-uniform SIW multiplexers are compared, and in this way, it is theoretically proven that the modulated SIW provides higher rejection between channels and reduced losses than the uniform design, for a similar operational bandwidth and size.

### 4.5.2 Uniform SIW Multiplexer

First it studies the case of a uniform SIW with the following parameters according to Fig. 4.63a:  $h = 0.508$  mm,  $\epsilon_r = 2.2$ ,  $L = 100$  mm,  $W = 8.5$  mm,  $P = 6.5$  mm, and diameter of vias  $d = 1$  mm. As shown in Fig. 4.64, the fundamental mode of the SIW radiates in the substrate with a frequency-scanned angle varying from  $\theta_d = 5^\circ$  at 11 GHz to  $\theta_d = 52^\circ$  at 17 GHz. Thus, this SIW structure behaves as a spectral-spatial decomposer [161]–[163], [191], [192] which splits different frequencies to separate angular regions in the  $zy$ -plane, as illustrated in the near-field plots obtained with HFSS in Fig. 4.65a for 11 GHz, 14 GHz and 17 GHz.

For the design of a practical multiplexer, one must choose the location of the output ports to extract the signals for each frequency channel. First, one must decide the distance  $D$  measured along the  $y$ -axis from the SIW radiating wall, see Fig. 4.65a. Obviously, shorter values of  $D$  provide more compact devices. However, a minimum distance  $D$  is needed to obtain sufficient separation between

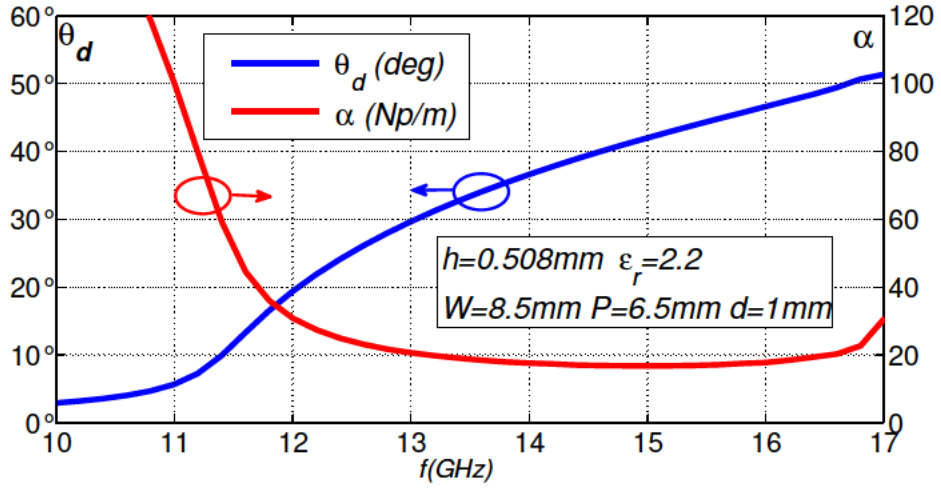


Figure 4.64: Frequency-dispersion of the leaky mode for a uniform SIW.

channels (spatial resolution) for a given angular scanning. As a practical example, Fig. 4.68a shows the near-field patterns (magnitude of electric field (V/m) expressed in dB) obtained along the  $z$ -axis for  $y = D = 60$  mm (see horizontal line in Fig. 4.65a), as frequency is varied from 11 GHz to 17 GHz. The near fields concentrate in a spatial region which is shifted towards the right side as frequency rises, due to the frequency-scanning mechanism demonstrated in Fig. 4.65a. From the longitudinal position where the maximum near-field intensity occurs at each frequency, one can obtain the longitudinal location  $z_0$  of the output ports for the different channels, as shown with arrows in Fig. 4.68a.

Finally, the frequency variation of the near-field measured at each  $z_0$  position is plotted in Fig. 4.69a for the range from 10 GHz to 20 GHz. As it can be seen, the SIW acts as an electrical prism which provides a bandpass response for each output port  $z_0$  with a maximum level at its corresponding frequency, in coherence with Fig. 4.68a. However, the rejection between channels is quite poor, and the shape of the bandpass responses strongly degrade as frequency is increased, limiting its performance as a practical multiplexer.

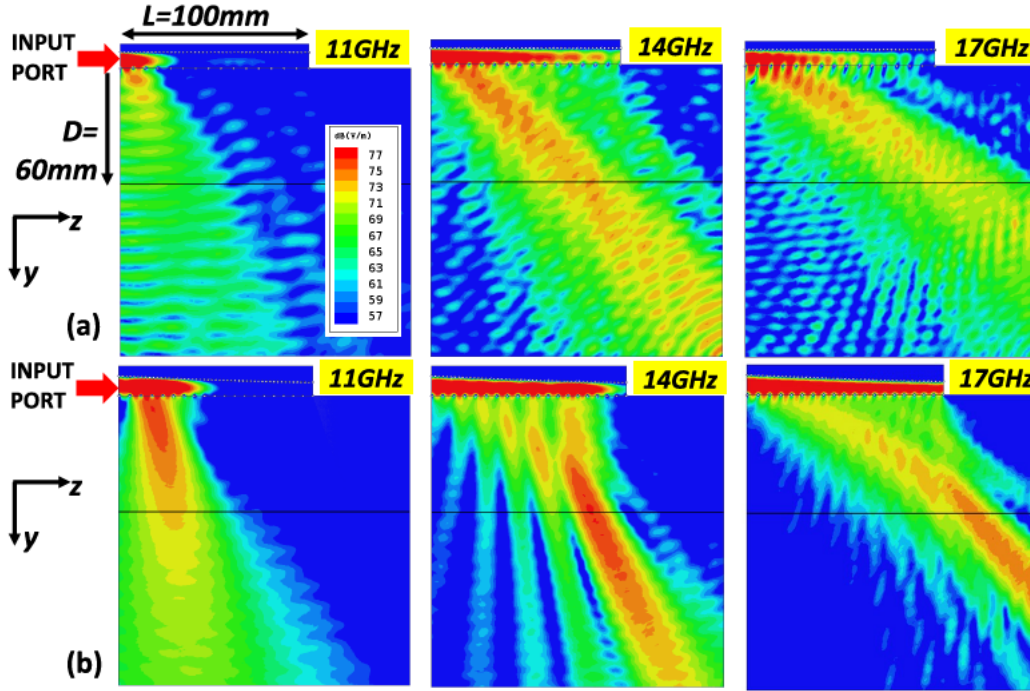


Figure 4.65: Near-field distributions in the  $zy$ -plane for 11 GHz, 14 GHz and 17 GHz: a) Uniform SIW and b) Modulated SIW.

### 4.5.3 Modulated SIW Multiplexer

The multiplexing performance can be improved by properly modulating the SIW width  $W(z)$  and posts distance  $P(z)$  along the leaky SIW length to obtain a near-field focus (see Fig. 4.63b), as originally demonstrated in [124] (the radiating length is kept unchanged to  $L = 100$  mm). The modulated SIW dimensions to synthesize a focus at  $z_F = 100$  mm,  $y_F = 66$  mm for the design frequency of 15 GHz were obtained by applying the procedure described in [124] to the particular case of a leaky SIW [91]. To this aim, the SIW LWA has been modified in order to only radiate inside of the host substrate. Moreover, this SIW multiplexer can be analyzed by using a similar TEN to the one described in Section 3.2, but expressing the row of metallic posts as an equivalent impedance,  $Z_P$ , formed by the combination of the T-model equivalent circuit for the row of posts (see Fig. 3.2b) with the characteristic impedance,  $Z_0$ , for the dielectric-filled PPW. As a result,

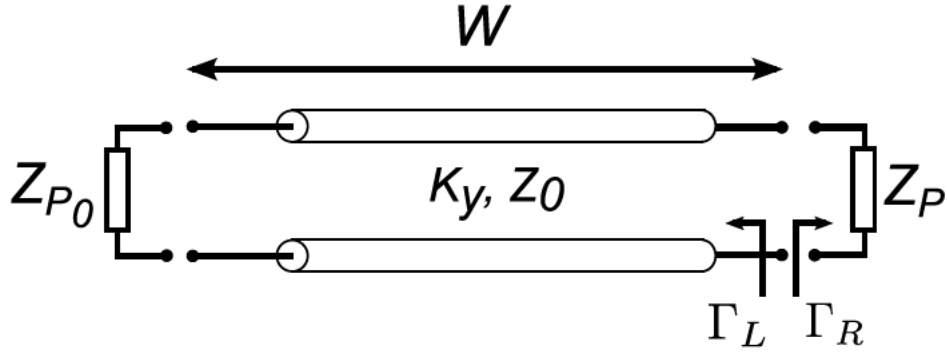


Figure 4.66: Scheme of the proposed TEN for the SIW multiplexer.

the transverse equivalent network (TEN) can be represented in the form showed in Fig. 4.66, and its corresponding transverse resonance equation (TRE) can be expressed as

$$\Gamma_L(k_z) \cdot \Gamma_R(k_z) = 1 \quad (4.23)$$

which must be solved for the unknown leaky-mode complex longitudinal wavenumber  $k_z$  in order to obtain the geometrical variation for  $W(z)$  and  $P(z)$ . The required modulations of the SIW in order to synthesize the prescribed focusing pattern are represented in Fig. 4.67.

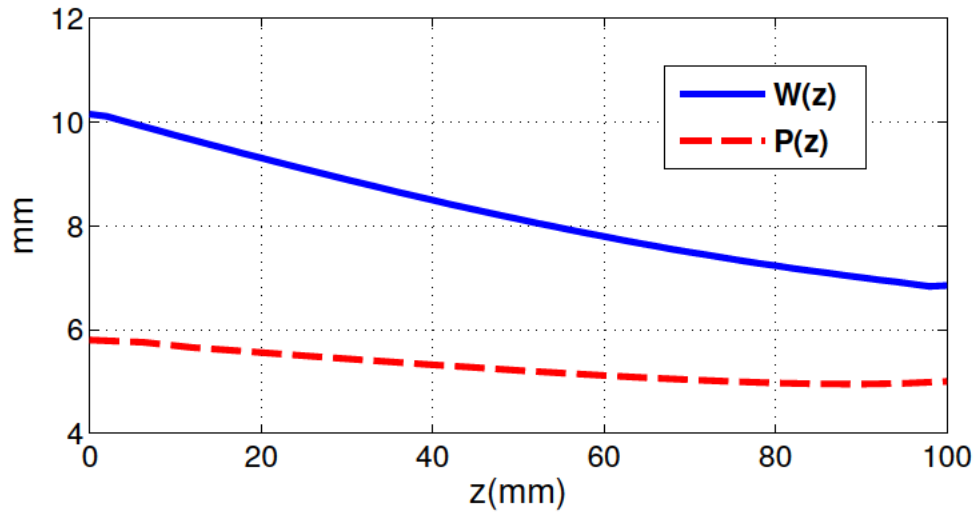


Figure 4.67: Tapered dimensions ( $W$  and  $P$ ) as function of the radiating length for the modulated SIW multiplexer.

Fig. 4.65b shows the simulated near-fields, observing the appearance of a focused region which is scanned in the  $zy$ -plane as frequency is varied as first reported in [124]. Fig. 4.68b shows the resulting field cut in the  $y = D = 60$  mm horizontal line. If it compares the field plots of Fig. 4.68a and Fig. 4.68b, two key differences can be appreciated. First, the field distributions are more concentrated in the space for Fig. 4.68b, resulting in lower beam widths and thus higher spatial isolation. One might think that larger apertures  $L$  provide increased directivity and reduced main beam width without the need of modulating the SIW line, as it is commonly done in the design of leaky-wave antennas [45], [91], [163]. However, since the radiation pattern is obtained in the far-field, a much higher far-field distance  $D$  is needed to obtain the focused pattern as  $L$  is increased (the Fraunhofer limit is  $2L^2/\lambda$ , which in our case would lead to  $D = 50\lambda_0 \approx 1.5$  m at 15 GHz).

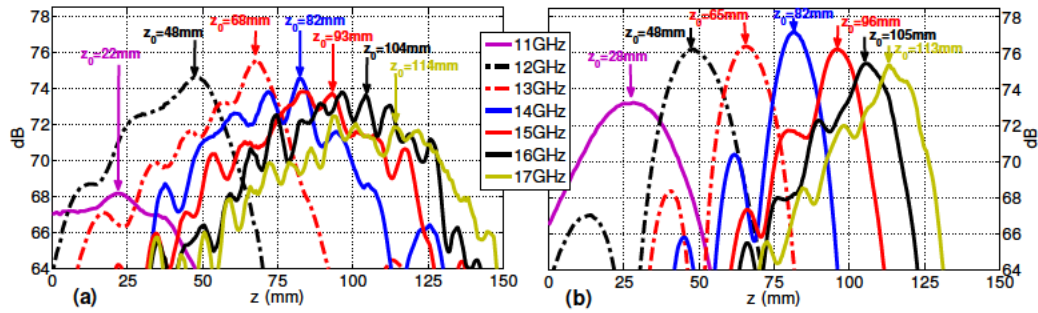


Figure 4.68: Near-field distributions along the  $z$ -axis for  $y = D = 60$  mm as frequency is varied: a) Uniform SIW and b) Modulated SIW.

It is worth mentioning that the modulated SIW design creates a focused distribution similar to the one obtained with a uniform SIW leaky-wave antenna which is focused at infinity, but at a much shorter focal distance  $D = y_F = 66$  mm at 15 GHz, as shown in Fig. 4.65. The second effect is that the field density (V/m) level increases in the order of 2 dB due to this higher concentration of the near fields, reducing the insertion losses due to spherical-wave spreading. Consequently in Fig. 4.69b, the frequency responses at the sampling output ports show more defined bandpass shapes, with higher rejection between channels and in-

creased peak field levels. Therefore, this simple modulated SIW structure presents a promising solution to conceive a new type of multiplexers, especially at high frequencies where conventional cavity-based filtering devices are not affordable due to losses.

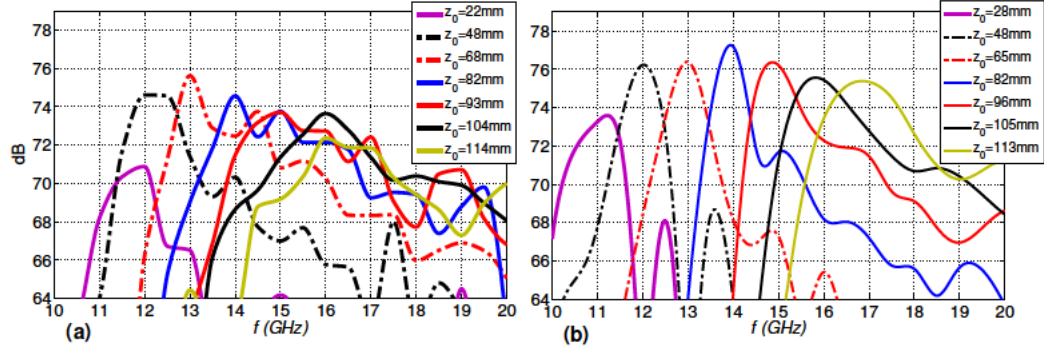


Figure 4.69: Near-field frequency response for  $y = D = 60$  mm at the sampling positions  $z_0$ : a) Uniform SIW and b) Modulated SIW.

# Chapter 5

## Radial Arrays

In this chapter, two different types of radial array configurations are presented. The first design is composed of eight 1-D SIW LWAs which have been radially arranged around a central feeding. Each of these 1-D SIW LWAs is designed to operate at the splitting point ( $\alpha = \beta$ ) of the leaky mode and, as a result of it, all the individual beams from each 1-D SIW LWA can merge into one providing a pencil beam radiation pattern at broadside direction, as will be shown in Section 5.1. The second design employs the same radial configuration with a single central feeding, but sinusoidally modulated half-mode LWAs are used instead of SIW LWAs. Due to the excitation of space harmonics caused by the periodic geometry of the antenna, the proposed structure can exhibit backward radiation. To this aim, the  $n = -1$  space harmonic is chosen and by means of a suitable modulation both in amplitude and phase, a near-field focusing over the center of the array is obtained, as demonstrated in Section 5.2. Both designs have been manufactured and measured, providing an experimental validation of the theoretical concepts exposed.

## 5.1 Pencil Beam Radiation Pattern From a Single Layer SIW LWA With Simple Feeding

A central feeding array radiating at broadside and manufactured in substrate integrated waveguide (SIW) technology is shown in this section. The single layer array consists of  $N = 8$  line-source leaky-wave antennas (LWAs), which are designed to satisfy the splitting condition ( $\alpha = \beta$ ) of the leaky mode. The LWAs are arranged in a radial configuration, in this manner, by properly designing the SIW width  $W$  and the spacing between SIW vias  $P$  for each SIW LWA, the leaky mode can be independently controlled to fulfill the splitting condition, and all the individual beams from each SIW LWA can merge into one at broadside direction ( $\theta = 0^\circ$ ) for a given design frequency. The two dimensional radiating surface allows obtaining a pencil beam radiation pattern, which is linearly polarized due to the radial arrangement. A prototype with a radiating length of  $L_A = 60$  mm for each SIW LWA, and a total radius of  $R = 73$  mm has been manufactured for a design frequency of 15 GHz. Input matching, gain, and radiation patterns at several planes have been measured and compared with full-wave simulations, obtaining good agreement between them.

### 5.1.1 Introduction

The capability to radiate at broadside direction with leaky-wave antennas (LWAs), has been widely used due to their easy feeding mechanism and high gain [82]. Principally, three different ways to obtain this broadside radiation ( $\theta = 0^\circ$ ) can be distinguished: I- With uniform-type LWAs satisfying the splitting condition ( $\beta = \alpha$ ) [188], [195], [196], II- Using the 1st high-order harmonic in periodic configurations [133], [197]–[201], and more recently III- By means of metamaterials [76], [202], [203]. Typically, most of these configurations have been based on one-dimensional (1D) LWAs, which provide a fan-beam radiation pattern [82].

However, a pencil beam radiation pattern can also be obtained when several LWAs line-sources are suitably arranged in a 2D plane and fed symmetrically [82], [133], [196], [200], [201], [204].

In this section, it uses the 2D configuration presented in [205], which by means of the flexible control of the leaky mode ( $k = \beta - j\alpha$ ) allows that the splitting condition ( $\beta = \alpha$ ) can be satisfied while keeping a high radiation efficiency independently of the antenna length  $L_A$  (type I [188]). The design is formed by arranging eight LWAs around a circumference of radius  $R_0$  in a radial fashion, which allows that all elements are fed in-phase, see Fig. 5.1a. The array is compatible with substrate integrated waveguide (SIW) technology, which assures the low-cost and low-profile of the complete structure [1]. Moreover, to keep a simple feeding of the array, and thus, avoiding corporate feeding networks [82], [196], [200], a through coaxial probe placed in the center of the array has been used. In this manner, its manufacture is simpler and more robust compared with blind probes [125].

Each element of the array can be considered as an independent 1D SIW LWA (see Fig. 5.1b), which by means of the control over its main geometrical parameters ( $W$  and  $P$ ) presents the capability to independently determine the phase and leakage constants of the leaky mode travelling along the structure [91]. As a result, an effective control over the leaky-mode components of amplitude and phase is obtained, which allows the determination of the radiation properties of the LWA [82]:

$$\sin \theta_{\text{RAD}} \approx \beta/k_0 \quad (5.1)$$

where  $k_0$  is the free-space wavenumber and  $\theta_{\text{RAD}}$  the angle of maximum radiation. Therefore, all the elements of the radial array can be designed to operate at the splitting point and radiate broadside. On the other hand, the use of the radial configuration allows that a pencil beam radiation pattern can be obtained. These radial configurations have been intensely employed in the literature for different applications, due to their capability to obtain large aperture illuminations [82],

[133], [196], [201], [204]. However, it is the first time to the author's knowledge that this flexible control of the splitting point, and thus, over the effective illuminated length of the antenna, has been obtained over a single-substrate, low-cost, low-profile and simple feeding SIW radial array.

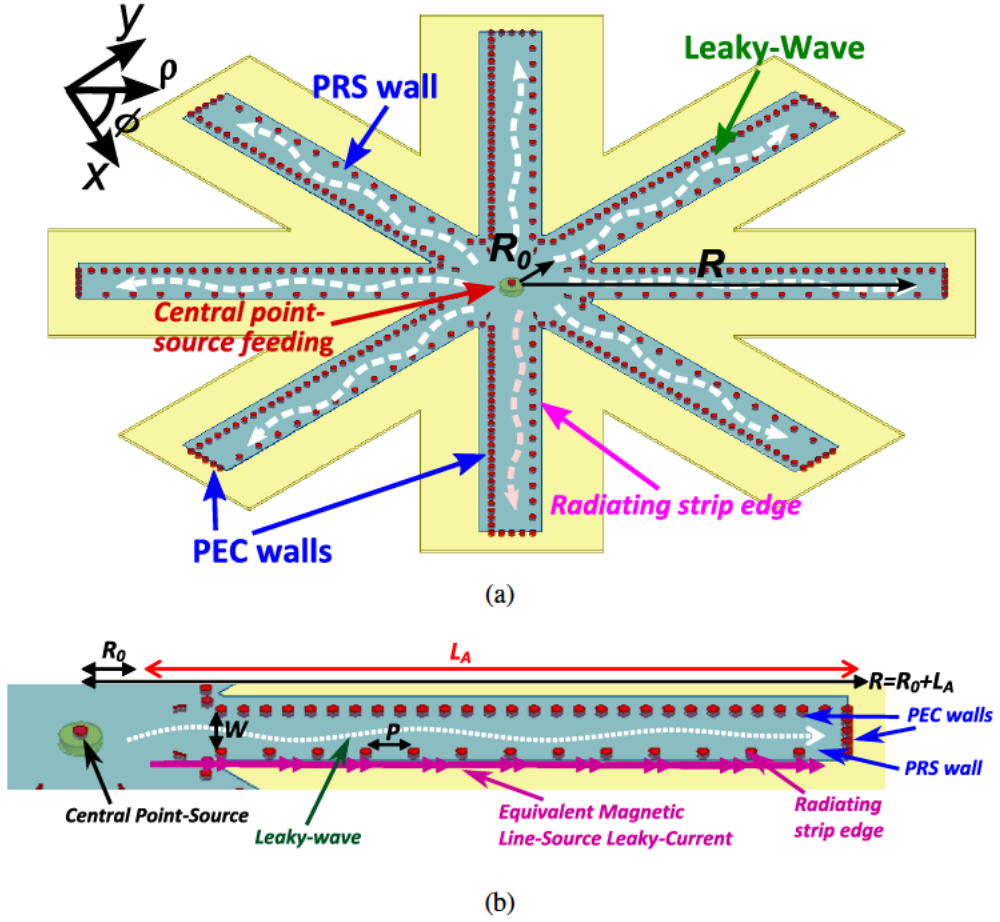


Figure 5.1: Scheme of a) radial array. b) SIW LWA element.

The rest of the section is organized as follows. Section 5.1.2 describes the design of the radial array, which is performed by an analysis of the leaky mode dispersion as function of the main geometrical parameters of the 1D SIW LWA. Section 5.1.3 shows the manufactured prototype for a radial array with  $N = 8$  SIW LWAs with a radiating length each of  $L_A = 3\lambda_0$  and a total radius of  $R = R_0 + L_A = 73\text{ mm}$  for the design frequency of 15 GHz (see Fig. 5.1).

Moreover, the reflection coefficient, the realized gain and the radiation patterns for different planes have been measured and compared with simulations obtained with commercial full-wave software. Finally, the conclusions of the work are summarized in Section 5.1.4.

### 5.1.2 Design of the Radial Array

The proposed structure is formed by an array of  $N = 8$  1D SIW LWAs arranged in a radial fashion and fed by a single coaxial probe. In this manner, when all the elements of the array fulfill the splitting condition, only one beam pointing at broadside is present in the radiation pattern [188]. To design the antenna to operate at this point, suitable values for the geometrical parameters of the 1D LWA must be chosen. Specifically, the  $TE_{10}$ -like mode propagating along the SIW becomes leaky due to one of the rows of metallic posts having a separation,  $P$ , large enough to allow the leakage of energy through these metalized vias. Hence, by controlling the separation between posts,  $P$ , a control over  $\alpha$  is obtained, and similarly, by varying the SIW width  $W$ , a main control over  $\beta$  is achieved. The complex propagation constant of the SIW LWA can be efficiently computed by analyzing a transverse section of the 1D SIW LWA by means of a modal tool based on the transverse resonance technique developed in [118]. This modal analysis allows the computation of the leaky mode as function of the main geometrical parameters of the structure (see Fig. 5.1b).

Moreover, in order to keep a high radiation efficiency ( $\eta_{\text{RAD}} \approx 0.90$ ) for a given element length  $L_A$ , an effective control of the leaky mode and therefore of the geometrical parameters is required. Since the radiation efficiency is ultimately given by  $\eta_{\text{RAD}} = 1 - e^{-4\pi \frac{\alpha}{k_0} \frac{L_A}{\lambda_0}}$ , the leaky mode needs to satisfy the following condition for broadside radiation with high (90%) radiation efficiency:

$$\frac{\alpha}{k_0} = \frac{\beta}{k_0} = \frac{0.184}{L_A/\lambda_0} \quad (5.2)$$

Therefore, the flexible control over the leaky mode needs to be performed both in the real and in the imaginary parts of the propagation constant, if we want to efficiently illuminate a given element length  $L_A$  and satisfy the splitting condition for broadside radiation. This control over the illuminated length of each element will allow us to choose the directivity of the array as function of  $L_A$  [205].

Next, in order to obtain the geometrical dimensions ( $W$  and  $P$ ) which provide the requested value of  $\alpha = \beta$  for a given element length  $L_A$ , the dispersion characteristics of the leaky mode will be studied for the case of the 1D SIW LWA showed in Fig. 5.1b. All the figures are shown for the design frequency of 15 GHz and a substrate with thickness  $h = 0.508$  mm and relative permittivity  $\epsilon_r = 2.2$ .

Fig. 5.2 shows the dispersion of the leaky mode, for three different separation between posts  $P = [4 \text{ mm}, 5 \text{ mm} \text{ and } 5.5 \text{ mm}]$  and as function of  $W$  in a range from 6 mm to 8 mm. As shown, the normalized phase constant  $\beta/k_0$  (blue dashed line) increases and the leakage rate  $\alpha/k_0$  (red solid line) decreases for larger  $W$ , which is related with a larger radiation angle  $\theta_{\text{RAD}}$  (5.1) [91]. Moreover, it is also observed that larger values of  $P$  provide higher leakage rates  $\alpha$  at the splitting point ( $\alpha = \beta$ ), passing from  $\alpha_1/k_0 = 0.03$  for  $P = 4$  mm to  $\alpha_3/k_0 = 0.12$  for  $P = 5.5$  mm. It is important to notice that this flexible control of the splitting point allows the design of passive LWAs radiating at broadside while keeping a high radiation efficiency independently of the antenna length according to (5.2). Although in some previous works certain control over the leakage rate or phase constant has been obtained [117], [133], [202], this capability to control the splitting point is the main contribution of the presented SIW LWA configuration, if compared to all previous planar radial-arrays of LWAs which lacked of such simultaneous and independent control over  $\alpha$  and  $\beta$  at broadside [82], [117], [133], [196], [201], [202], [204].

The final step in the design of the radial array antenna involves the election of the SIW LWAs dimensions  $W$  and  $P$  for any requested value of  $L_A$  which will define the array directivity  $D_A$  [205]. This step is illustrated in Fig. 5.3, which

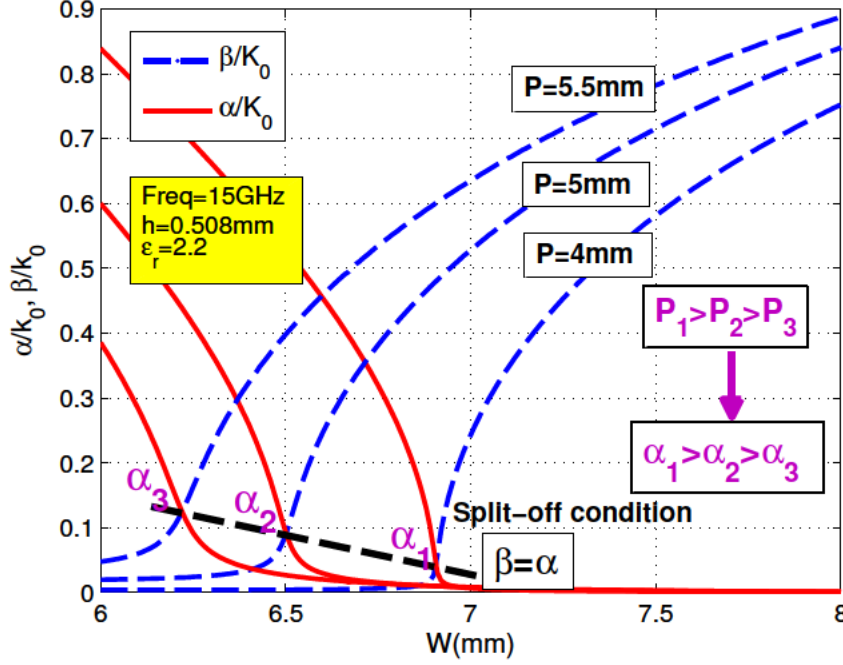


Figure 5.2: Leaky mode dispersion ( $\beta/k_0$  and  $\alpha/k_0$ ) as function of  $W$  and different values of  $P$ .

represents the corresponding values of  $W$  and  $P$  that satisfy the splitting condition ( $\alpha = \beta$ ), as a function of the antenna length  $L_A$  according to (5.2). The values of  $L_A$  are represented in the horizontal axis as a function of  $\lambda_0 = 20\text{ mm}$  at the design frequency of 15 GHz, and the physical dimensions for  $W$  and  $P$  are shown in mm in the left vertical axis. Moreover, the simulated values for the array directivity as function of  $L_A$  are represented with a dashed line at the right vertical axis. As expected, the array directivity  $D_A$  increases for larger illuminated lengths  $L_A$ . The corresponding values of  $\alpha/k_0 = \beta/k_0$  are also highlighted for several cases of  $L_A$ . In general, longer  $L_A$  requires lower leakage rates which are obtained with a smaller separation between SIW posts (lower values of  $P$  [91]). Likewise,  $W$  needs to be increased as  $P$  is decreased to keep the splitting point ( $\alpha = \beta$ ). In particular, a design with directivity of  $D_A = 14.6\text{ dB}$  requires an antenna with length of  $L_A = 3\lambda_0 = 60\text{ mm}$ ,  $W = 6.75\text{ mm}$  and  $P = 4.45\text{ mm}$ .

which corresponds to a value of  $\beta/k_0 = \alpha/k_0 = 0.061$ . On the other hand, an antenna with  $L_A = 6\lambda_0 = 120$  mm,  $W = 7$  mm and  $P = 3.66$  mm provides  $D_A = 17.28$  dB.

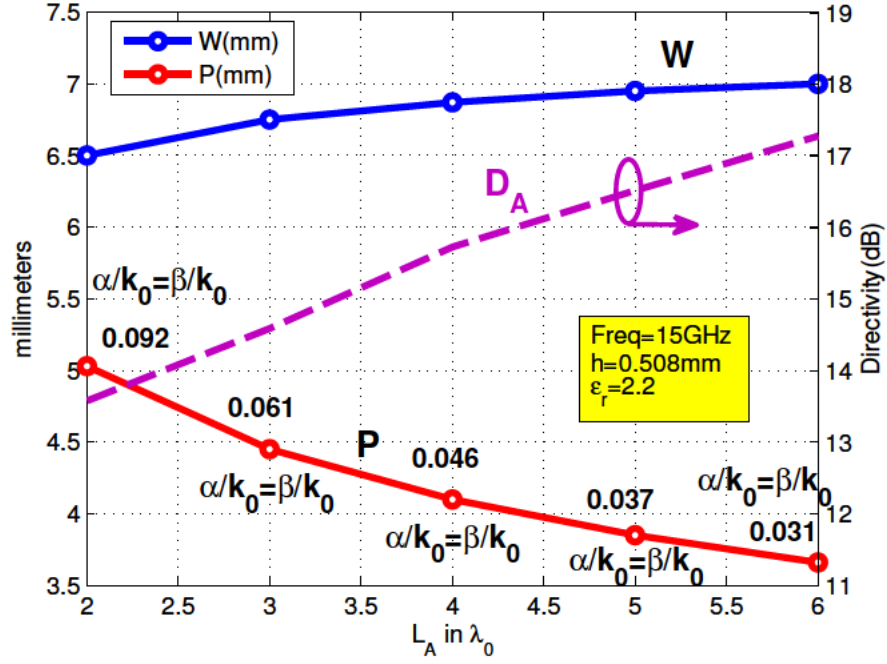


Figure 5.3: Synthesis procedure for obtaining broadside radiation ( $\alpha/k_0 = \beta/k_0$ ), as function of  $W$  and  $P$ , the 1D SIW LWA length  $L_A$  and its associated array directivity  $D_A$ .

### 5.1.3 Measured Results

A prototype based on the design procedure described in Section 5.1.2 has been manufactured and measured. A commercial substrate Taconic TLY-5 with  $\epsilon_r = 2.2$ ,  $\tan \delta = 0.0009$ , and  $h = 0.508$  mm thickness has been used. The element length has been fixed at  $L_A = 3\lambda_0$ , which corresponds to a theoretical array directivity  $D_A = 14.6$  dB for the main geometrical parameters  $W = 6.75$  mm and  $P = 4.45$  mm (see Fig. 5.3). The rest of the SIW geometrical parameters [91] are posts' diameter  $d = 1$  mm, non-radiative posts' distance  $P_0 = 2$  mm, and

radiating strip width  $W_0 = 1.5$  mm. With the purpose of maximizing the array directivity, the largest number of 1D SIW LWAs has been used ( $N = 8$ ), which has given a radius of  $R_0 = 13$  mm. Thus, the total radius of the array is  $R = R_0 + L_A = 13$  mm +  $3\lambda_0 = 73$  mm at the design frequency of 15 GHz. A photograph of the manufactured prototype in SIW technology is shown in Fig. 5.4, where the 8 LWAs and the central feeding can be observed.

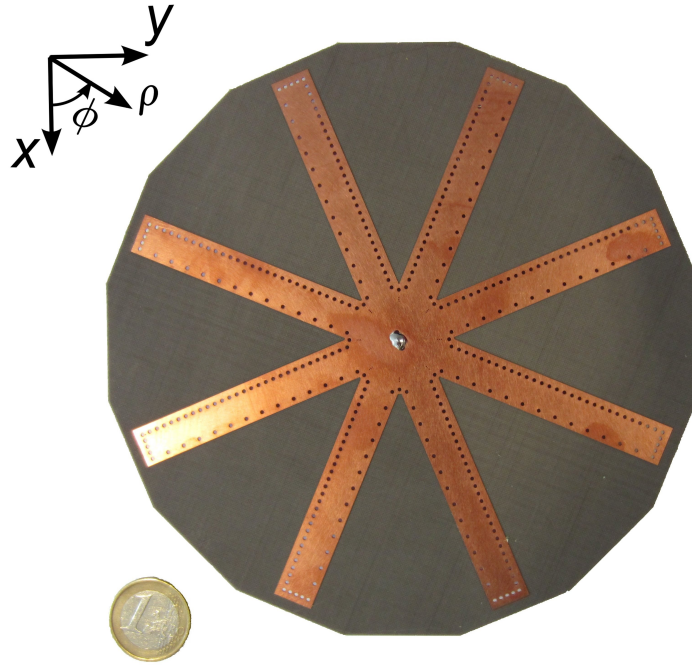


Figure 5.4: Top photographic view of the manufactured radial array for an antenna length  $L_A = 3\lambda_0 = 60$  mm and a total radius  $R = 73$  mm.

The simulated 3D radiation pattern of the array is shown in Fig. 5.5 for the design frequency of 15 GHz, together with the coordinate system used. As a result of the array configuration, a pencil beam radiation pattern pointing at broadside direction ( $\theta = 0^\circ$ ) is obtained. However, some side lobes also appear in the 3D pattern due to the non-uniformity along  $\phi$  of the radial configuration. As illustrated by the red arrow in Fig. 5.6, the resulting array is linearly polarized along the  $x$ -axis. This linear polarization is obtained by combining all the radiated fields

of the 1D LWAs, which are linearly polarized (the radiated electric field is represented for each element in Fig. 5.6 in black ( $\vec{E}$ )). Moreover, some of the elements have been mirrored so that their radiated fields reinforce the linear polarization of the array pattern  $\vec{E}_x$ . Due to all the 1D LWAs are not perfectly aligned to the  $x$ -axis some gain reduction is expected as consequence of polarization mismatches. It is important to note that this radial array arrangement allows for several polarizations, including circular or elliptical ones, to be obtained by adding a different phase-shift at the feeding section of each 1D LWA. This control over the requested phase-shift can be obtained e.g. by varying the distance of each 1D LWA respects to the center of the array according to a prescribed polarization pattern.

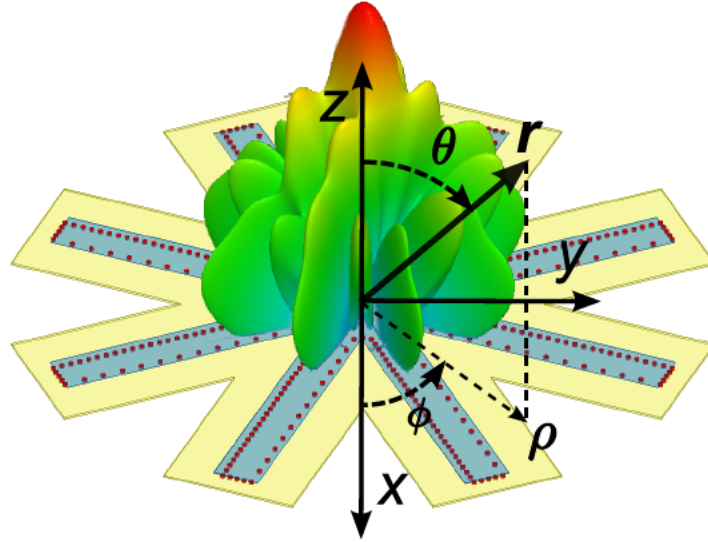


Figure 5.5: Three dimensional view of the radiation pattern formed by  $N = 8$  SIW LWAs of length  $L_A = 3\lambda_0$  for the design frequency of 15 GHz.

In order to support the theoretical approach given in Fig. 5.6 for determining the polarization of the complete array, Fig. 5.7 shows the simulated electric field vector,  $E(x,y,z)$  (V/m), on the surface of the air region that covers the array for two different phase representations. Specifically, the electric field is represented in Fig. 5.7a for a phase  $= 0^\circ$ , and it can be seen how the electric field vectors are

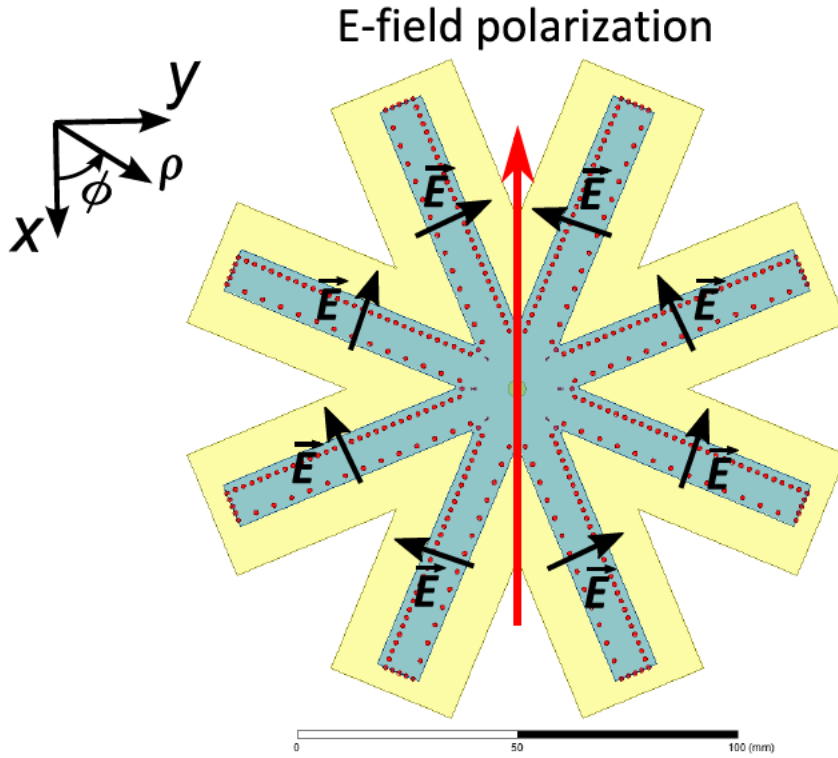


Figure 5.6:  $\vec{E}$  field polarization arrangement for each element of the array (black arrows), and resulting array polarization (red arrow).

oriented along the  $-x$  axis, whereas for phase  $= 180^\circ$  the vectors are oriented in opposite direction along the  $+x$  axis, as shown in Fig. 5.7b. Moreover, as a result of the radial arrangement, the maximum intensity of the radiated fields is located at the center of the array, as illustrated with red color vectors for both time phases in Fig. 5.7.

Fig. 5.8a shows the measured radiation pattern for the co-pol component ( $\vec{E}_\phi$ ) at  $\phi = 90^\circ$  ( $H$ -plane). The measured result is compared with full-wave simulations obtained with HFSS. Good agreement is observed between both curves, confirming the good quality of the measurements. Moreover, the radiation pattern shows a main beam with a beamwidth at  $-3$  dB of  $\Delta\theta \approx 9^\circ$ , and a side lobe level (SLL) of  $-10$  dB. On the other hand, the X-pol component ( $\vec{E}_\theta$ ) is represented in Fig. 5.8b for the same  $H$ -plane ( $\phi = 90^\circ$ ). It can be observed how the  $\vec{E}_\theta$  compo-

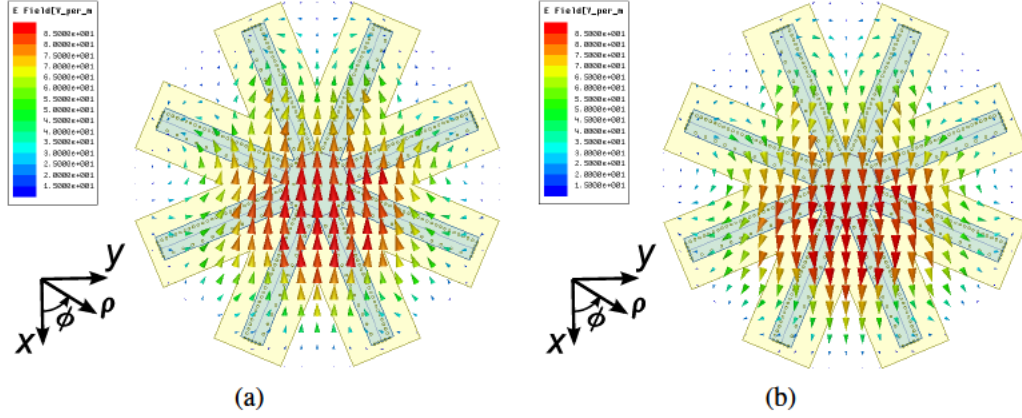


Figure 5.7: Simulated electric field vector,  $E(x,y,z)$  (V/m), over the array: a) time phase  $= 0^\circ$  and b) time phase  $= 180^\circ$ .

ment is null at broadside due to radial configuration shown in Fig. 5.6, however the X-pol increases reaching a maximum level of  $-10$  dB for the simulated radiation pattern and  $-5$  dB for the measured result, at an approximate angular direction  $\theta = \pm 30^\circ$ .

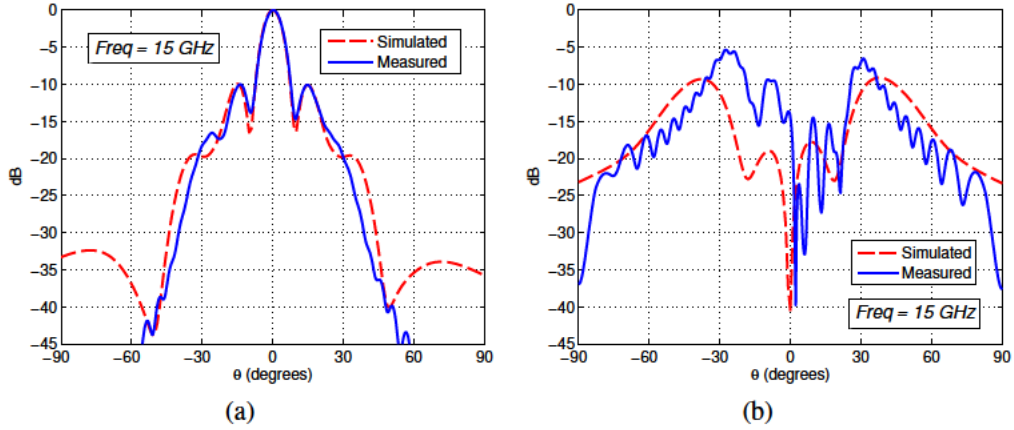


Figure 5.8: Measured and simulated radiation patterns: a) co-pol component ( $E_\phi$ ) at  $H$ -plane ( $\phi = 90^\circ$ ), and b) X-pol component ( $E_\theta$ ) at  $H$ -plane ( $\phi = 90^\circ$ ).

The  $E$ -plane radiation pattern ( $\phi = 0^\circ$ ) is also represented in Fig. 5.9 for both components  $\vec{E}_\theta$  (co-pol) and  $\vec{E}_\phi$  (X-pol). The measured result is represented in

solid line and the simulation in dashed line. Both simulations and measurements show a good agreement also for this plane. The  $E$ -plane radiation pattern presents a beamwidth of  $\Delta\theta \approx 13^\circ$  and a  $SLL \approx -7$  dB, which are higher compared to the ones obtained for the  $H$ -plane, and they are due to the non-uniformity of the radial array along  $\phi$ . Moreover, the X-pol component is below  $-35$  dB compared to the main component  $\vec{E}_\theta$  in the whole range of  $\theta$ . This low value for the X-pol component can be explained with the polarization configuration used (see Fig. 5.6), which provides a very low  $\vec{E}_\phi$  component at the  $E$ -plane. This measured broadside radiation pattern for  $\vec{E}_\theta$  at  $\phi = 0^\circ$ , demonstrates that 3D broadside radiation is obtained by using this radial configuration of 1D LWAs.

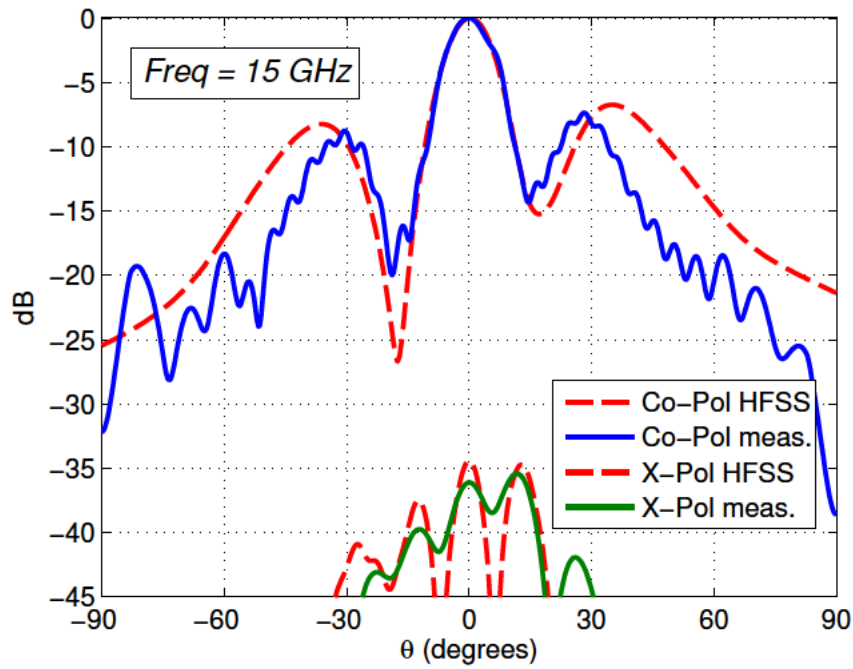


Figure 5.9: Measured and simulated radiation patterns for the co-pol component ( $E_\theta$ ) and X-pol component ( $E_\phi$ ) at  $E$ -plane ( $\phi = 0^\circ$ ).

The gain measured at broadside direction ( $\theta = 0^\circ$ ) is represented in Fig. 5.10 for the frequency range from 14.5 GHz to 15.5 GHz. The values of gain are compared with simulated ones, confirming again the good agreement between sim-

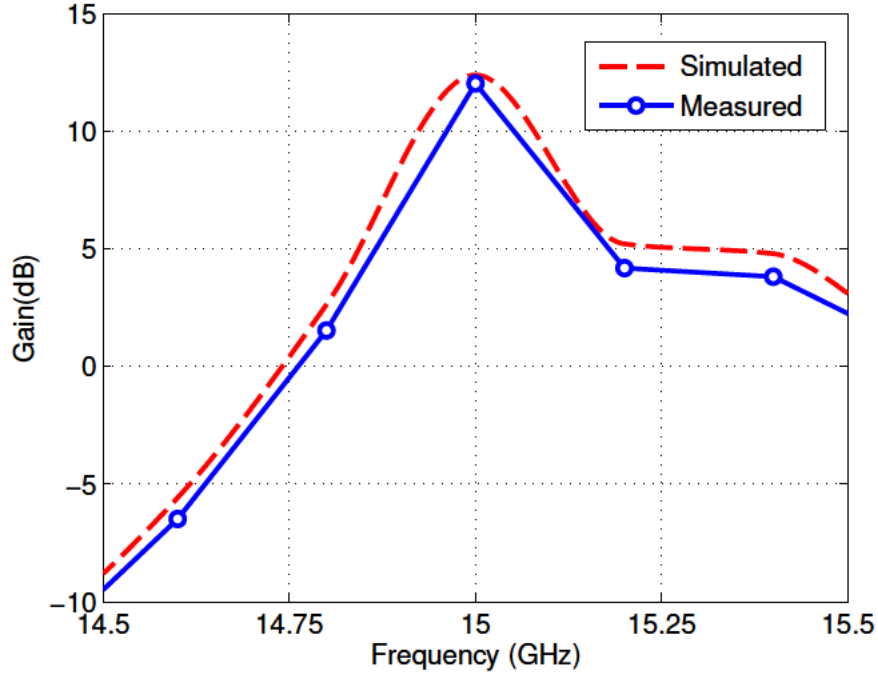


Figure 5.10: Measured and simulated gain values for the frequency range from 14.5 GHz to 15.5 GHz.

ulations and measurements. It can be observed how a maximum gain of 12 dB is obtained at the design frequency of 15 GHz, which if compared with the simulated values of the directivity in Fig. 5.3 provides an approximate value for the radiation efficiency of the complete array of  $\eta_{\text{RAD}} \approx G/D_A = 0.55$ . This difference between the radiation efficiency of each LWA and the obtained for the total array can be mainly attributed to polarization losses caused by the mismatch between the resulting polarization of the array and the polarization of each LWA, as illustrated in Fig. 5.6. The broadside gain is narrowband as it corresponds to most LWAs due to their strongly dispersive nature [82]. Below 15 GHz the SIW leaky line is below cutoff, as it can also be seen in the magnitude of the  $S_{11}$  parameter shown in Fig. 5.11. This makes the gain to rapidly drop below the design frequency. On the other hand, for frequencies above the splitting condition point, the radiation pattern of each 1D LWA scan forward and the pencil beam radiating

at broadside is lost [188], [204]. At this regime, the array can be used to provide a conical beam [204], but with a drop of the gain compared to broadside. Therefore, by only considering the radiation at broadside the proposed radial array provides a  $-3$  dB gain bandwidth from 14.85 GHz to 15.15 GHz ( $\approx 2\%$ ), which is smaller than the typical bandwidth of a single 1D LWA ( $\approx 5\%$ ).

Finally, the magnitude of the measured reflection coefficient (solid line) is shown in Fig. 5.11 and compared with simulations (dashed line). As previously mentioned, one of the advantages of this radial configuration is the simple feeding of the structure compared to more complex array distribution networks [196], [200]. In the proposed design, the feeding is done by a coaxial line placed in the center of the array. The inner conductor of the coaxial passes through the substrate and then is soldered with the metal top layer. The resulting feeding mechanism acts as a resonant cavity with eight output ports formed by the inputs of each 1D LWA. Due to this resonant feature of the feeding cavity, the input matching is narrowband as illustrated by the response of the reflection coefficient magnitude in Fig. 5.11. This narrow matching band of the structure is also related with the reduced gain bandwidth shown in Fig. 5.10. However, the measured result for the  $|S_{11}|$  is still below  $-20$  dB at 15 GHz, which provides a good input matching and allows a maximum gain at broadside.

#### 5.1.4 Conclusion

The capability to obtain controllable broadside radiation from a radial array configuration of substrate integrated waveguide (SIW) leaky-wave antennas (LWAs) has been demonstrated in this section. An example is employed that comprises an array formed by  $N = 8$  line-sources LWAs, which are arranged in an array fashion and are simply fed by a single coaxial line placed in the center of the array. In this manner, complex feeding networks are avoided to excite the array elements. The broadside radiation is achieved by fulfilling the splitting condition, which is based on having equal phase and leakage constants ( $\beta = \alpha$ ) for the leaky mode

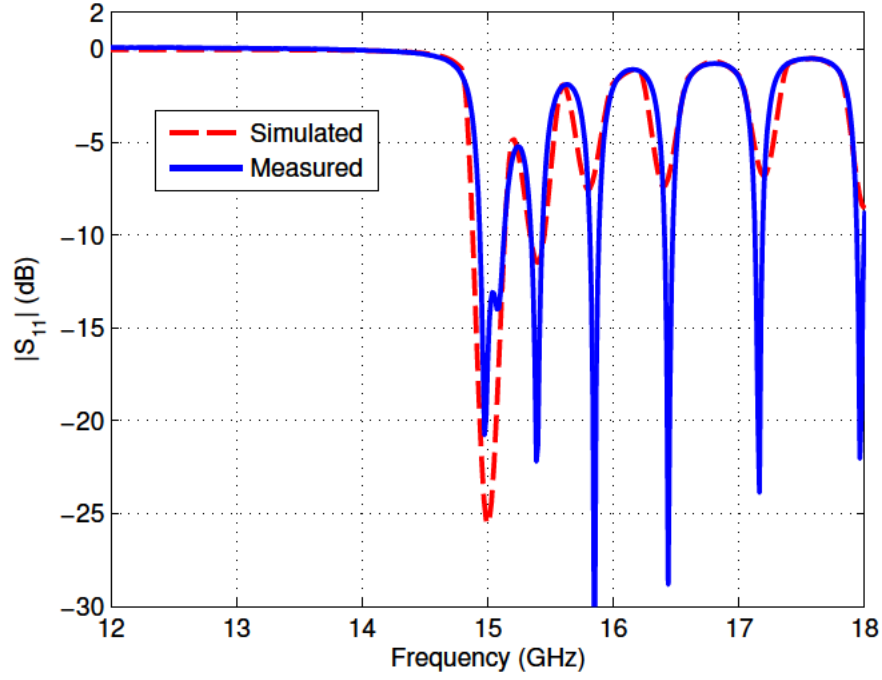


Figure 5.11: Measured and simulated  $|S_{11}|$ -parameter for the radial array of SIW LWAs, radiating broadside at the design frequency of 15 GHz.

propagating along the each SIW LWA ( $k = \beta - j\alpha$ ). Likewise, all beams merge into one at broadside direction ( $\theta = 0^\circ$ ) at a given design frequency. Besides, the flexibility to control the splitting point allows the efficient illumination of each SIW line, and thus obtaining high radiation efficiency and optimized gain independently of the selected antenna radius. A prototype with  $N = 8$  SIW LWAs with a length of  $L_A = 3\lambda_0 = 60$  mm and a total radius of  $R = 73$  mm for the design frequency of 15 GHz, has been manufactured. The reflection coefficient and the radiation patterns for different planes have been measured and compared with simulations, obtaining good agreement and showing a peak gain of 12 dB at 15 GHz, and a  $-3$  dB gain bandwidth of 2%. Despite its narrowband, this technology offers a low-profile, low-cost, easy feeding solution for directive radiation which can be easily integrated with planar circuits and used in higher frequency bands.

## 5.2 Non-Uniform Sinusoidally Modulated Half-Mode Leaky-Wave Lines for Near-Field Focusing Pattern Synthesis

A novel non-uniform sinusoidally modulated half-mode microstrip structure with application to near-field focused leaky-wave radiation in the backward Fresnel zone is proposed. First, it is presented a dispersion analysis of the constituent backward leaky wave in the sinusoidally modulated unit cell in half-width microstrip technology. This information is then used to design the finite non-uniform line that focuses the radiated fields at the desired point. Finally, eight similar line sources are arranged in a radial array to generate a three-dimensional focused spot located at the desired focal length over the simple central coaxial feeding. Simulated and experimental results are presented to validate the proposed simple approach.

### 5.2.1 Introduction

Sinusoidally modulated (SM) reactance surfaces were first proposed by Oliner and Hessel in 1959 as an elegant and canonical way to control the propagation of surface and leaky waves in periodic transmission media [113]. This seminal theoretical work assumed a sinusoidal variation of the equivalent surface reactance along the propagation direction that was soon applied to a variety of practical cases [206]–[211]. Recently, renewed interest is given to SM circuits in printed/planar technology due to their ability to control the propagation and radiation properties in low-cost artificial planar guides, arising the area of planar metamaterial dispersion engineering also referred to as metasurfing [108], [212], [213]. In this way, sinusoidally and linearly-chirped width-modulated microstrip lines have been proposed for enhanced control of the stopbands in microwave filters [114], [214], and to synthesize dispersive linear group delays with application to real-time analog

signal processing [215]. On the other hand, printed SM metasurfaces have also been proposed to control the radiation from leaky waves with application to directive holographic antennas [107], [110]–[112], [116], [117], [133], [134], [216], [217]. In all cases, it is essential to determine how to control the guiding and radiation characteristics of the constituent surface and leaky modes for each selected metasurface technology.

Some previous designs based on sinusoidally modulated microstrip lines [113], [117], [133], [217], metamaterial transmission lines [202] as well as periodic half-mode leaky-wave antennas (HMLWAs) [74], [218], [219] have shown the capability to radiate backward and to perform certain control over the phase or the amplitude of the radiated fields. As is well known [113], if the period of the structure is adequately chosen, the backward radiation comes from the existence of a backward leaky wave (negative scanning angle  $\theta_{\text{RAD}}$ ) associated with the  $n = -1$  space harmonic [the rest of harmonics are in the invisible spectrum (non radiating)]. The uniform value of the leaky-wave phase constant and leakage rate of an uniform SM LWA generates a linear-phase and exponential-amplitude aperture distribution that results in a plane-wave focusing at a given scanning angle  $\theta_{\text{RAD}}$  in the far-field zone (all sections of the LWA radiate at the same angle  $\theta_{\text{RAD}}$ ). All reported holographic SM microstrip LWAs [107], [110]–[112], [116], [117], [133], [134], [216], [217] have this uniform modulation and thus provide scanned beams focused in the far field.

In this work, a simultaneous control of both the phase constant and the leakage rate is employed to design a tapered illumination function, which is applied to obtain near-field focusing from an array of 1-D leaky-wave antennas (LWAs). Specifically, we propose the use of non-uniform (NU) SM LWAs to generate arbitrary aperture field distribution (magnitude and phase) that can synthesize near-field focused beams in the backward quadrant, as sketched in Fig. 5.12. To this aim, the uniform SM topology must be modified so that non-uniform SM unit cells scatter the electromagnetic waves with a defined non-uniform negative phase de-

lay in order to produce constructive interference at the desired point in the Fresnel zone, and with equalized amplitude for optimum aperture efficiency and side-lobe level. In particular, it is considered the case of NU SM microstrip half-width LWAs (HWLWAs) to taper the amplitude and phase of backward radiating leaky waves. The necessity of such tapering is illustrated with the design of a practical leaky-wave lens focused in the backward quadrant, which can thus be arranged in a radial-array fashion to obtain 3-D focusing using a simple central feeding as proposed in [220].

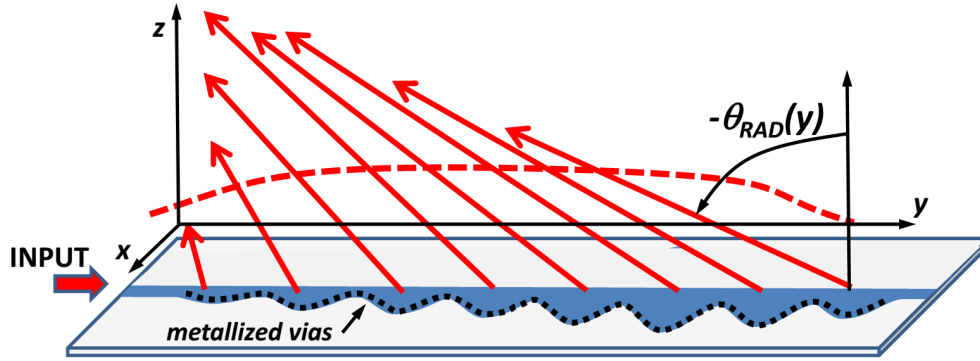


Figure 5.12: Scheme of the sinusoidally modulated HMLWA with a non-uniform taper performed to control in amplitude and phase the backward radiated waves.

The section is distributed as follows: Section 5.2.2 presents the dispersion analysis of the proposed SM half-width microstrip line and the design of the NU SM HWLWA to focus at a desired point in the backward region. Then, a central-fed radial-array of such NU SM HWLWAs is described in Section 5.2.3 to produce a 3-D near-field focused planar microwave lens. Section 5.2.4 reports the experimental results, showing the ability to create a 3-D focused beam at the desired location with the expected focal depth and focal width, and demonstrating the utility of NU SM microstrip lines for that purpose. Finally, the conclusions of this section are summarized in Section 5.2.5.

### 5.2.2 Analysis of the Sinusoidally Modulated HMLWA

With the aim of obtaining a radiating element with capability to radiate backward and with flexibility to control its complex illumination function, a conventional HMLWA with a sinusoidal modulation is proposed. The HMLWA is based on a microstrip line with one of its sides short-circuited by a perfect electric conductor (PEC) (see top view in Fig. 5.13a). In this manner, the first higher order leaky mode of the conventional microstrip line becomes the fundamental one in the HMLWA [62], [72]. The complex wavenumber of this fundamental leaky mode can be expressed as

$$k_y(y) = \beta_y(y) - j\alpha_y(y) \quad (5.3)$$

with  $\beta_y$  being the phase constant and  $\alpha_y$  the radiation rate, which are in general dependent on the local source coordinate ( $y$ ) along the LWA radiating length. From the value of  $\beta_y$  and its relation with the free-space wavenumber  $k_0$ , the radiation angle of the leaky mode can be determined [82] (assuming  $\alpha_y \ll \beta_y$ ) as

$$\sin \theta_{\text{RAD}}(y) \approx \beta_y(y)/k_0. \quad (5.4)$$

As it is observed in (5.4), the angle  $\theta_{\text{RAD}}$  takes positive values as long as  $\beta_y > 0$ . However, in the case of periodic structures, the phase constant  $\beta_{yn}$  of each space harmonic (SH) comprising the Floquet expansion of the fields is given by

$$\beta_{yn}(y) = \beta_y(y) + \frac{2n\pi}{P} \quad (5.5)$$

where  $P$  is the period of the structure and thus each  $n$ -th SH could radiate with a different angle given by

$$\sin \theta_{\text{RAD}_n}(y) \approx \frac{\beta_{yn}(y)}{k_0} = \frac{\beta_y(y)}{k_0} + \frac{2n\pi}{k_0 P}. \quad (5.6)$$

Therefore, by choosing a suitable value for  $P$ , some of the  $n = -1, -2, \dots$  space

harmonics can radiate backward ( $|\beta_{yn}/k_0| < 1$ ) with the angle defined by (5.6), while the rest of harmonics lie in the slow-wave regime ( $|\beta_{yn}/k_0| > 1$ ) and do not contribute to leaky radiation. Typically, only the  $n = -1$  harmonic is desired for radiation, and this single-harmonic radiation condition can be satisfied by a proper choice of the period  $P$  ( $\lambda_0/2 < P < \lambda_0$  for single  $n = -1$  backward leaky-wave radiation [113]).

According to the previous discussion, the conventional HMLWA (see Fig. 5.13a) can be modulated with a periodic function of period  $P$  in order to make it radiate only with the  $n = -1$  space harmonic. To this aim, the strip width  $W$  is locally modulated along the antenna length by the following sinusoidal function:

$$W(y) = W_m(y) \left[ 1 + M(y) \sin\left(\frac{2\pi}{P}y\right) \right] \quad (5.7)$$

where  $W_m(y)$  is the average value of the strip width  $W(y)$  at the longitudinal position  $y$ , and  $M(y)$  is the modulation index of the sine function. The resulting sinusoidally modulated HMLWA is shown in Fig. 5.13b, where it can be seen the sinusoidal variation that has been performed along the PEC wall side.

It is important to note that in order to design a tapered illumination function along the HMLWA length, the radiated fields must be properly controlled both in phase and amplitude [141]. Thus, the sinusoidal modulation of the HMLWA width cannot be uniform anymore, but it must be further modulated leading to a non-uniform SM structure. Specifically, the average strip width  $W_m$  is varied to control the phase constant of the fundamental mode  $\beta_y$  and to avoid that it falls within the fast-wave region ( $\beta_y/k_0 < 1$ ), while the uniform period  $P \approx \lambda_0/2$  provides backward radiation from the  $n = -1$  SH ( $|\beta_{y-1}/k_0| < 1$ ). To this aim, the minimum average width of the strip has been fixed to  $W_m = 5$  mm and a modulated sine function with period  $P = 11.5$  mm has been used. For fixed values of  $W_m(y)$  and  $M(y)$ , the corresponding value of the complex wavenumber is now determined by applying the Bloch-Floquet theorem to extract the  $ABCD$

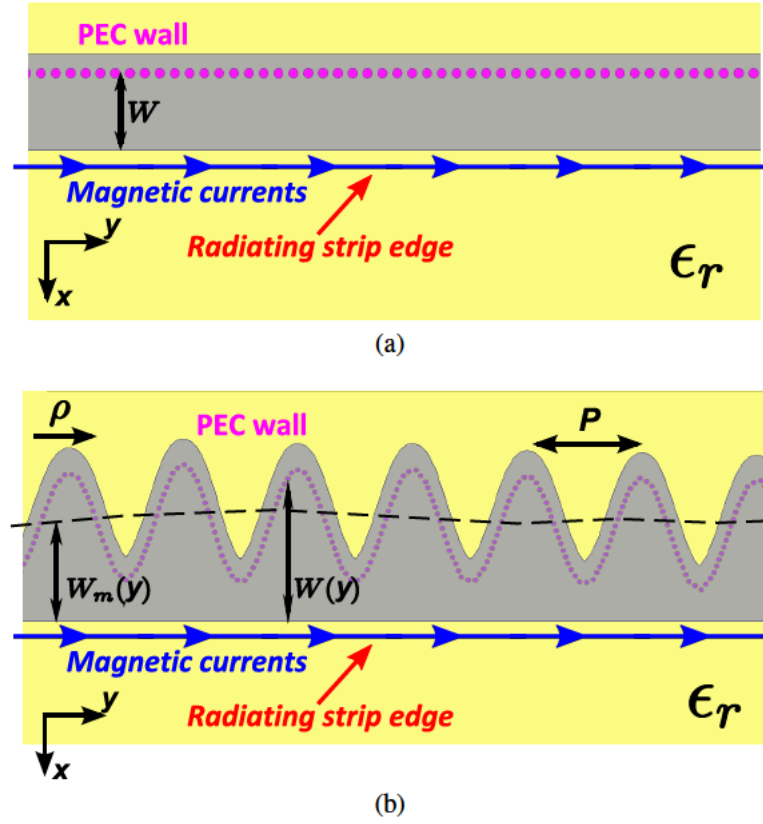


Figure 5.13: Top view for two different variations of the HMLWA with their main geometrical parameters: a) conventional HMLWA, and b) sinusoidally modulated HMLWA.

parameters from a full-wave analysis of the HMLWA [221]. Varying  $W_m(y)$  and  $M(y)$  allows then for a control of the radiation angle and the leakage rate as illustrated in Fig. 5.14 with a two-dimensional dispersion chart for the  $n = -1$  SH. The values for  $\theta_{\text{RAD}}$  and  $\alpha$  plotted in this figure correspond to a range of useful values of  $W_m$  from 5 mm to 10 mm, and their corresponding variations in width,  $\Delta W_m = W_m M$ , from 0 mm to 7 mm [these variations in  $\Delta W_m = W_m M$  come determined by the oscillating part in (5.7)].

In particular, it is observed that the leakage rate  $\alpha$  increases with  $\Delta W_m$  for a constant value of  $W_m$ , which can be explained by a higher excitation of the  $n = -1$  SH due to a deeper modulation index  $M$ , as commonly occurs in SM

LWAs [113], [117], [133], [217]. On the other hand, increasing values of  $W_m$  provide decreasing radiation angles  $\theta_{\text{RAD}}$  tending to broadside  $\theta = 0^\circ$  (isocurves plotted with dashed blue line), eventually entering the open stop band zone for  $W_m > 9$  mm and  $\Delta W_m < 4$  mm.

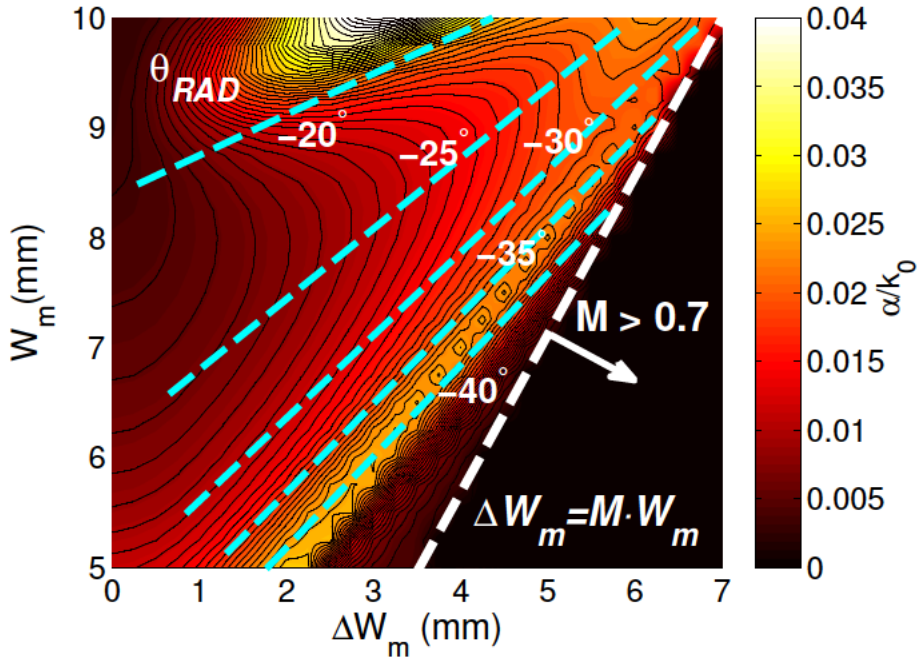


Figure 5.14: Two-dimensional dispersion chart at the design frequency of 15 GHz for the leakage rate  $\alpha$  and the radiation angle  $\theta_{\text{RAD}}$  of the  $n = -1$  space harmonic of the sinusoidally modulated HMLWA.

In order to show the capability to control both the amplitude and phase of the radiated fields for the  $n = -1$  space harmonic, a tapered illumination function has been synthesized to obtain a focused near-field pattern at the design frequency of 15 GHz (see Fig. 5.15). In this way, the focal height has been fixed at  $z_F = 5.5\lambda_0 = 110$  mm and the longitudinal position of the focal point is set to  $y_F = -0.65\lambda_0 = -13$  mm, which will allow that several 1-D LWAs can be arranged around a central point ( $y = 0$ ) to obtain a 3-D near-field focus, as it will be shown in the next sections. This prescribed focal position requests the variation

for  $\theta_{\text{RAD}}(y)$  and  $\alpha(y)/k_0$  shown in Fig. 5.15a, as described in [121]. The corresponding theoretical near-field pattern obtained with an in-house code developed in [124] is plotted in Fig. 5.15b, which shows that the fields have been suitably focused at the focal position  $(z_F, y_F)$ .

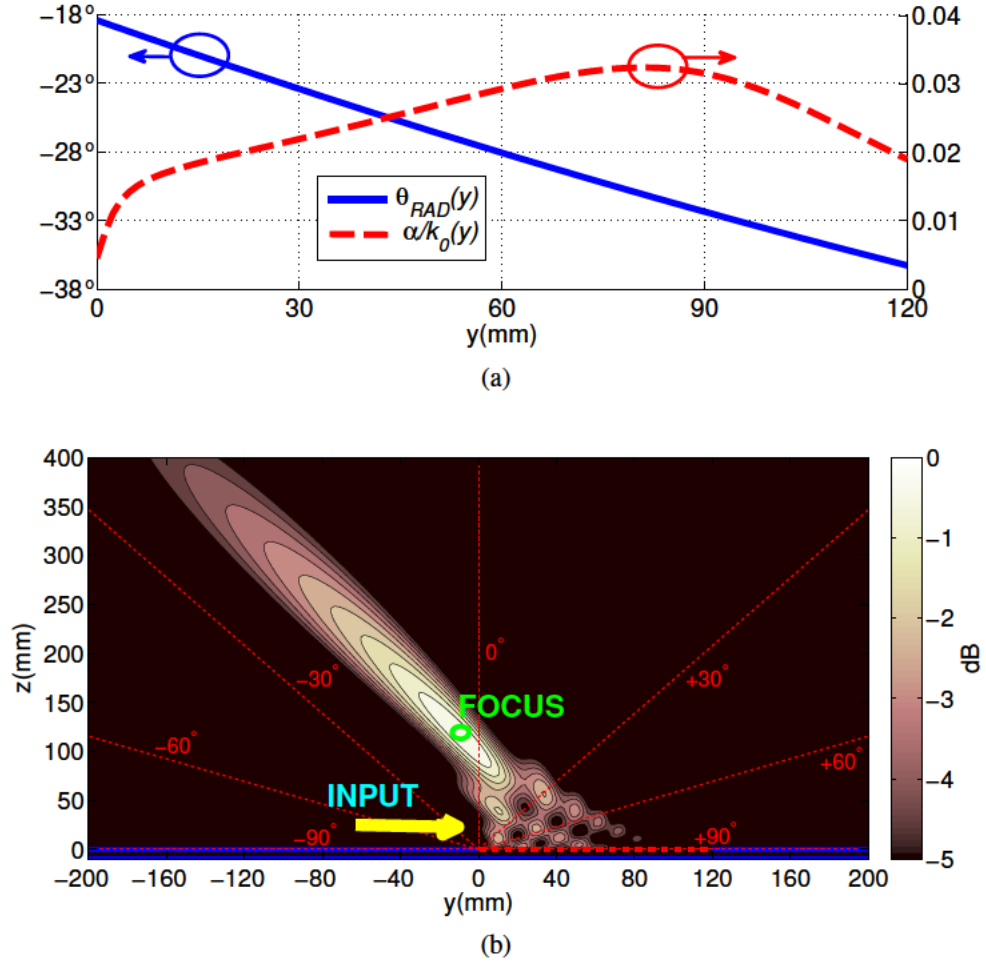


Figure 5.15: Synthesis of a near-field focusing pattern at a focal distance  $z_F = 5.5\lambda_0 = 110$  mm for a 1-D HMLWA with length  $L_A = 6\lambda_0 = 120$  mm at the design frequency of 15 GHz. a) Tapering along the antenna length of  $\theta_{\text{RAD}}$  and  $\alpha/k_0$ . b) Corresponding near-field pattern for the illustrated variation of the leaky mode.

The variations of the tapered illumination function shown in Fig. 5.15a needs to be translated into their corresponding geometrical non-uniform sinusoidal mod-

ulation for  $W(y)$ . Thus, the data obtained in the dispersion chart of Fig. 5.14 are used as a look-up table in order to determine the requested values for  $W_m(y)$  and  $\Delta W_m(y)$ , as shown in Fig. 5.16. The total value for the strip width  $W$  along the complete radiating length is also plotted in Fig. 5.16.

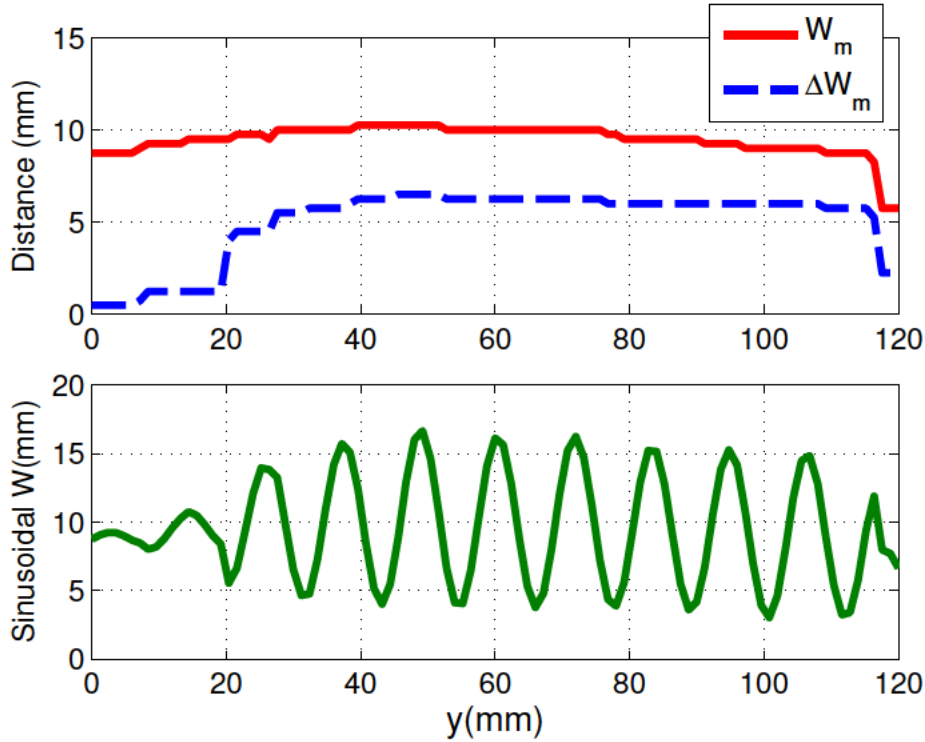


Figure 5.16: Tapering along the antenna length of the width of the HMLWA to synthesize a near-field focusing pattern at the design frequency of 15 GHz.

### 5.2.3 Design of the Radial Array Lens

From the design of the 1-D sinusoidally modulated HMLWA described in Section 5.2.2, which shows the capability to radiate backward and to provide 2-D near-field focusing, a radial array configuration has been conceived with the purpose of obtaining a 3-D near-field focus over the center of the array. Conventionally, microwave near-field focusing lenses have been based on the ability to focus the radiated electromagnetic fields within a prescribed region of the free space. To

this aim two main approaches are found: i) to conform the radiating element so that all sections point to the same focal region as proposed in [153], and ii) to taper the radiated fields by changing the electrical properties along the device and thus avoiding to curve it [121]. Based on this second approach, there have been proposed several technologies and topologies such as focusing plates that require of an external source [222], focusing systems inside parallel-plate waveguides [223], or more integrated devices as in [125], [126]. Other possible designs have been conceived from tapered far-field radiations patterns that make use of a quadratic phase taper to approximate the radiated near-field pattern [224], or by using Bessel beams [225], [226].

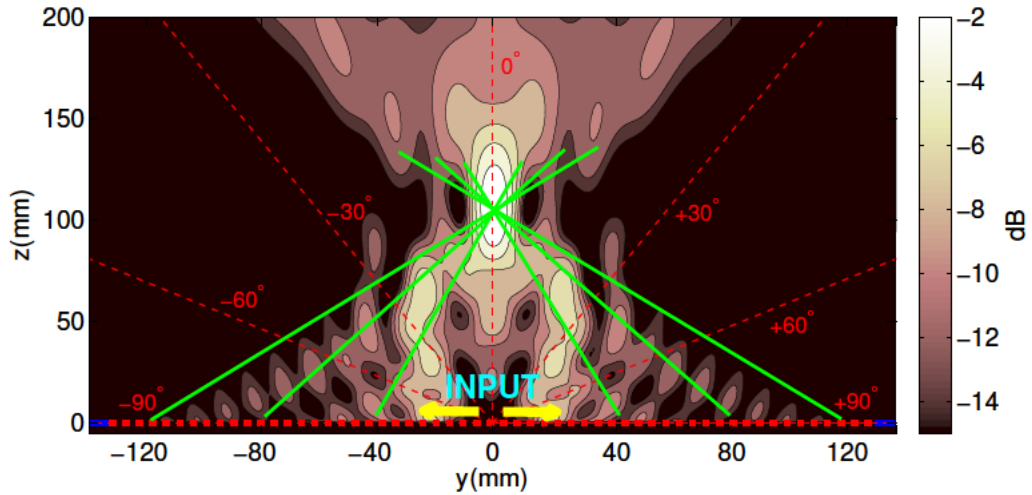


Figure 5.17: Simulated near fields for two symmetrically fed HMLWAs with a tapered illumination function at the design frequency of 15 GHz.

This work follows the second approach by making use of the structure proposed in Section 5.2.2 with capability to simultaneously and flexibly taper both the amplitude and phase of the radiated leaky-wave fields. Moreover, to keep a simple central feeding of the structure as in [125], [126], [224] and to obtain a single near-field focus over the central feeding point, the leaky wave must radiate backward. In order to validate the approach for the proposed focusing system, it is first considered a simpler design based on two symmetric 1-D HMLWAs.

Fig. 5.17 shows the simulated fields for two symmetrically fed 1-D HMLWAs that have been tapered along their lengths to produce the leaky-wave near fields shown in Fig. 5.15. It can be seen that the focusing pattern is obtained at the center position ( $y = 0$ ) and at the prescribed focal height  $z_F = 5.5\lambda_0 = 110$  mm. The variation of the local pointing angle along the antenna length has been marked with green lines to highlight the tapering of the local effective radiation angle  $\theta_{\text{RAD}}(y)$  of the two corresponding leaky waves propagating at opposite directions.

The symmetric configuration with two HMLWAs can only provide 2-D near-field focusing [223] in the  $zy$ -plane, in the form of a fan-focused beam in the  $xz$ -plane (as usually happens with 1-D line source LWAs). In order to obtain a 3-D focus, it is proposed an innovative configuration formed by  $N = 8$  1-D HMLWAs radially arranged around a central fed. The proposed design is shown in Fig. 5.18 together with an illustrative view of the desired focal region and the different contributions of all sections of the antennas.

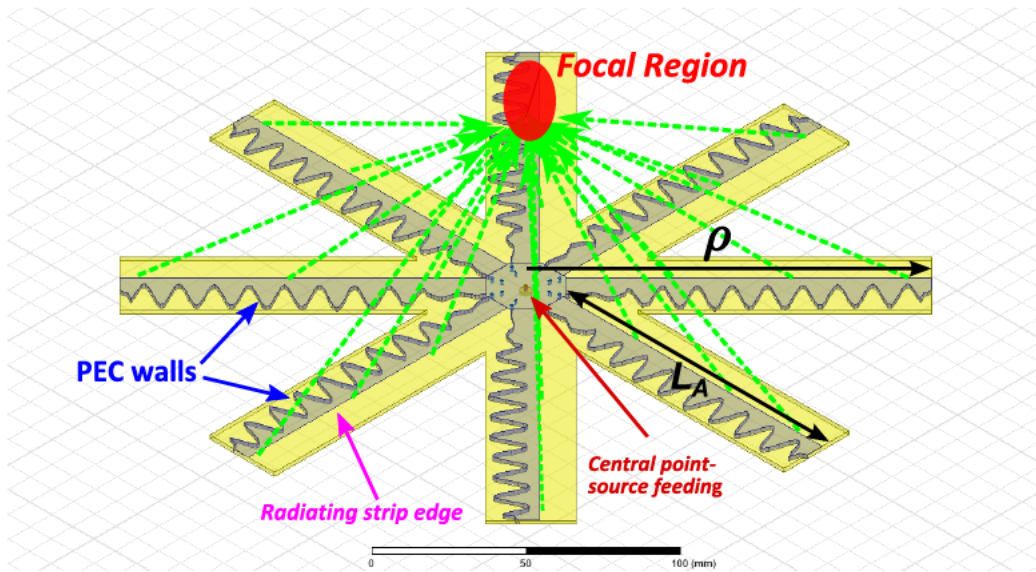


Figure 5.18: Scheme of the 3-D near-field focusing system consisting of a radial array with 8 sinusoidally modulated HMLWAs.

As each HMLWA is polarized linearly with its radiated  $E$ -field contained within the  $xy$ -plane [72], the polarization of the complete array is defined as the

result of combining all the individual polarizations of each 1-D HMLWA. This resulting polarization is illustrated in Fig. 5.19, where the radiated  $E$ -field for each HMLWA is represented with a red arrow and the resulting array polarization at the focal point is represented with a black arrow.

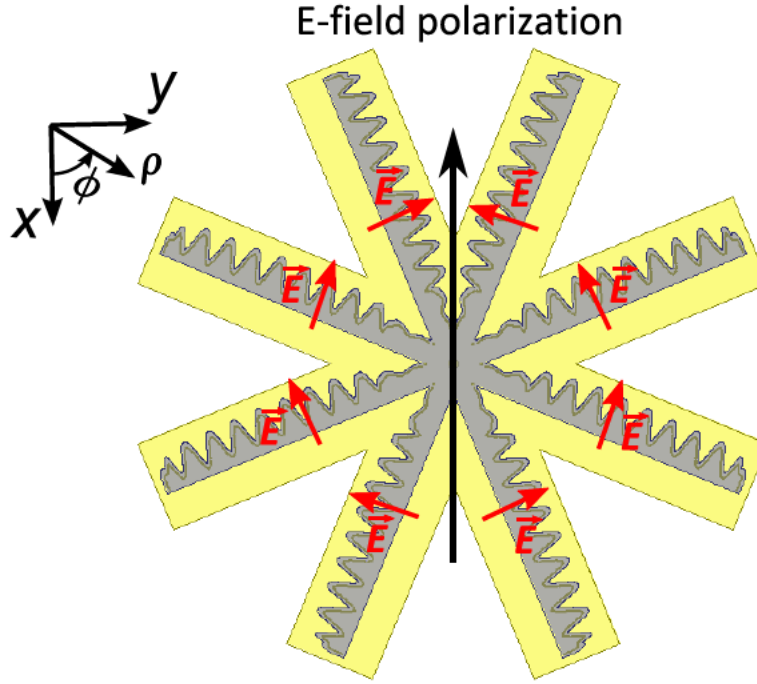


Figure 5.19:  $E$ -field polarization arrangement for each element of the array (red arrows), and resulting array polarization (black arrow).

To confirm the desired near-field focusing behavior of the designed radial array, a full-wave simulation (HFSS [90]) of the near fields in linear scale is plotted in Fig. 5.20 at the design frequency of 15 GHz for the plane  $\phi = 45^\circ$ . This simulation shows that the desired near-field focusing pattern can actually be obtained by the arrangement of the  $N = 8$  HMLWAs.

An important characteristic of the proposed radial array is that it can simply be fed by a single coaxial probe. A detailed view of the employed feeding is shown in Fig. 5.21. Specifically, the inner conductor of the coaxial (highlighted in pink color) passes through the substrate and then is soldered to the metal top

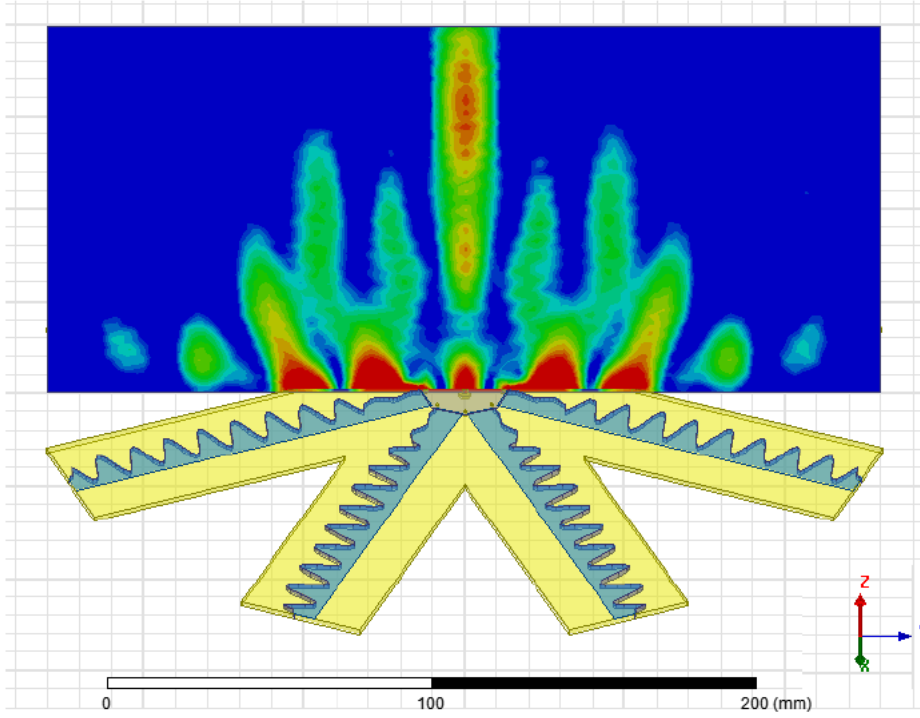


Figure 5.20: Simulated near-fields for the designed radial array of 8 sinusoidally modulated HMLWAs at the design frequency of 15 GHz.

layer (as can also be seen in Fig. 5.22). Moreover, it can be observed that the 1-D HMLWAs are radially arranged around a radius  $R_0$  from the coaxial probe. As seen in Fig. 5.21, the PEC wall of the HMLWAs is formed by a row of metallic via holes that are separated a distance  $s = 1$  mm and have a diameter  $d = 0.5$  mm for the modulated HMLWA part and  $d_0 = 1$  mm for the matching vias at the beginning of each antenna.

#### 5.2.4 Measured Results

In this section measured results of the near-field focusing lens are shown for the design frequency of 15 GHz. Moreover, several figures of merit such as focal depth, focal width, and input matching have been obtained. The designed radial array has been manufactured using the commercial substrate Taconic TLY-5 with

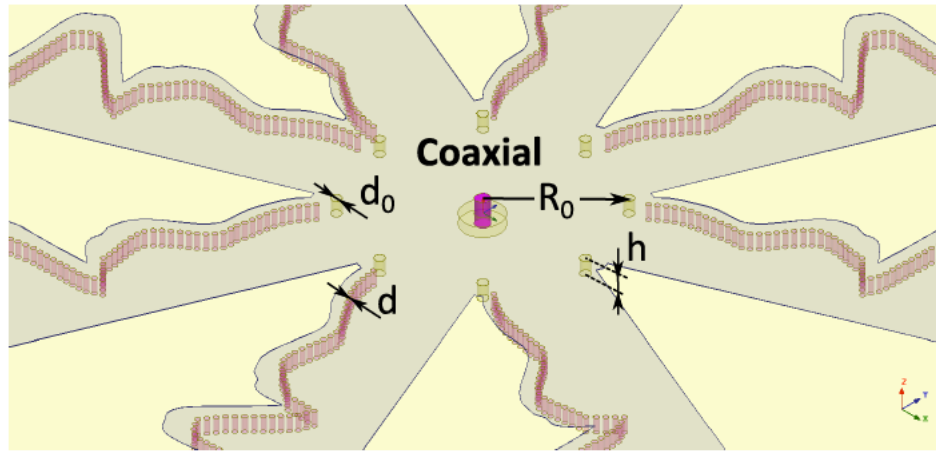


Figure 5.21: Detailed view of the employed coaxial feeding with some of its main geometrical parameters:  $R_0 = 13$  mm,  $d = 0.5$  mm,  $d_0 = 1$  mm and  $h = 1.57$  mm.

thickness  $h = 1.57$  mm, relative permittivity  $\epsilon_r = 2.2$ , and loss tangent  $\tan \delta = 0.0009$ . A photograph of the prototype is shown in Fig. 5.22, where it can be observed the eight HMLWAs radially arranged around a central feeding.

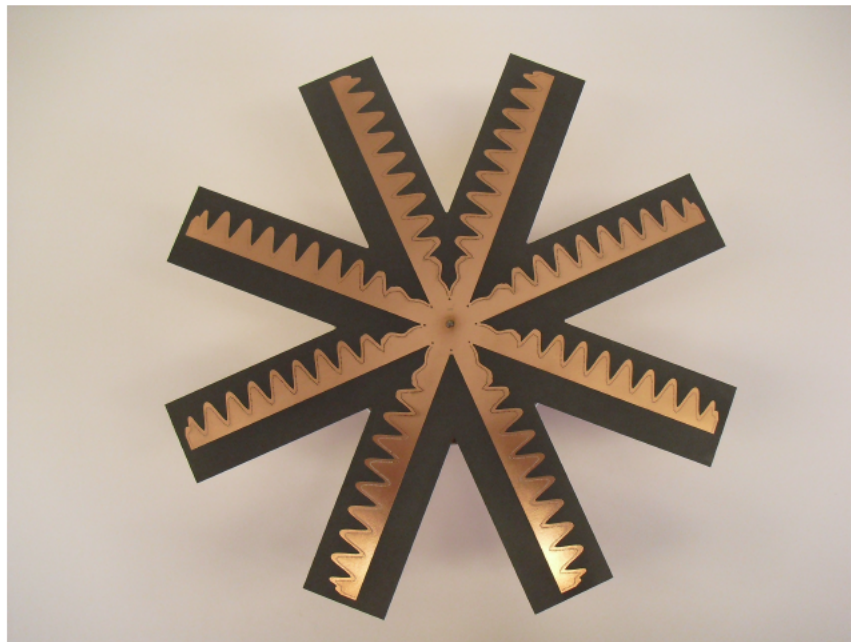


Figure 5.22: Top photographic view of the manufactured prototype of the radial array with  $N = 8$  sinusoidally modulated HMLWAs.

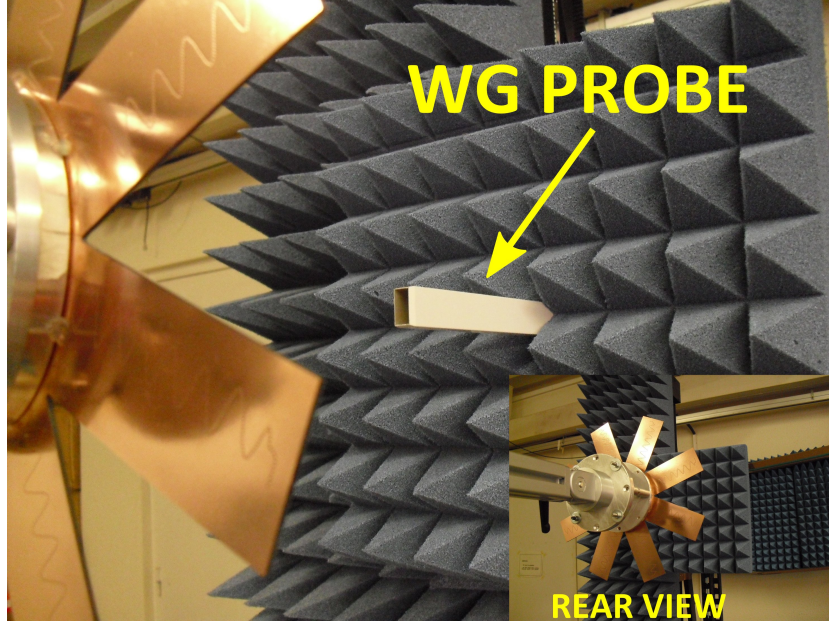


Figure 5.23: Photographs of the near-field measurement setup used for the radial array.

As explained in previous sections, the proposed radial array configuration possesses the capability to focus the radiated near fields into a prescribed 3-D focal region above the center of the array, acting as a microwave lens as schemed in Fig. 5.18. To experimentally validate this concept, the radial array has been measured by means of a near-field measurement system equipped with a standard rectangular waveguide WR62 as measurement probe. Fig. 5.23 shows a photograph of the setup employed to measure the radiated fields along a  $xy$ -plane for an arbitrary distance  $z$ .

In order to obtain the real performance of the proposed structure and thus its focusing capability, several cuts at the focal height  $z = 5.5\lambda_0 = 110$  mm for different azimuthal angles  $\phi$  have been measured. Fig. 5.24 shows the normalized radiated  $E$ -field along a transverse plane at  $\phi = 0^\circ$  and a focal height  $z = 5.5\lambda_0 = 110$  mm. Measured results (continuous blue line) are compared with HFSS simulations (red line) obtaining good agreement. Particularly, the focal width  $\Delta\rho$  is correctly estimated, which at  $-3$  dB is  $\Delta\rho = 20$  mm. However, it

is observed a slight increment of the side-lobe levels around the focus, which can be explained by the perturbation introduced by the measurement probe.

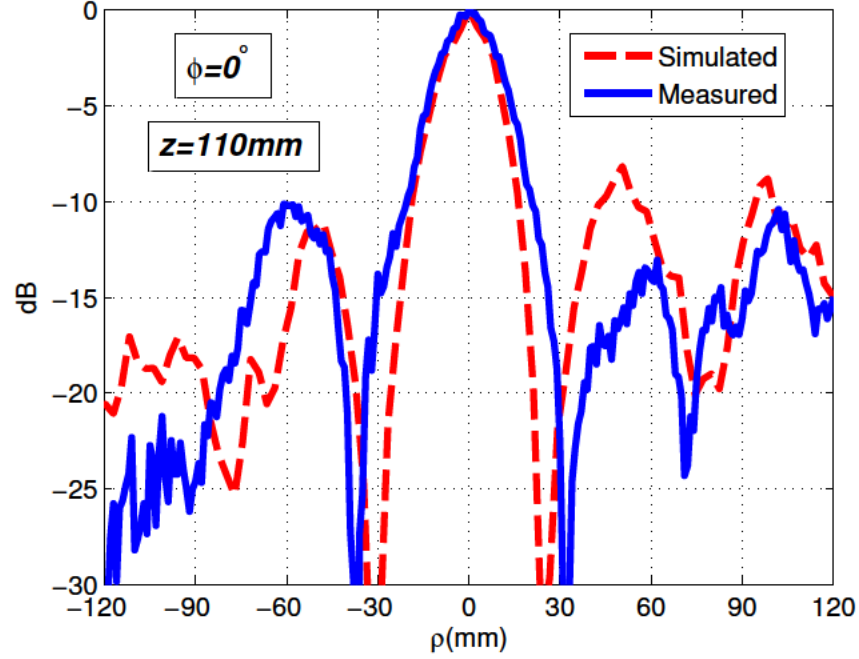


Figure 5.24: Measured and simulated transverse cuts along  $\rho$  for the focal height  $z_F = 110$  mm at the plane  $\phi = 0^\circ$ .

The transverse cut for the  $E$ -field along  $\phi = 45^\circ$  at the prescribed focal height of  $z = 5.5\lambda_0 = 110$  mm is shown in Fig. 5.25. Measured results are compared with simulations and the agreement for this cut is also good, showing a focal width at  $-3$  dB of  $\Delta\rho = 18$  mm, similar to the one obtained at  $\phi = 0^\circ$  (the small difference can be attributed to the lack of symmetry along  $\phi$  as a result of the necessary flip of the SM HMLWA to obtain linear polarization as explained with Fig. 5.19).

A transverse cut along  $\phi = 90^\circ$  is represented in Fig. 5.26 at the focal height  $z = 5.5\lambda_0 = 110$  mm. As in the previous cuts, the correspondence between simulations and measurements is good. For this cut the focal width at  $-3$  dB is  $\Delta\rho = 15$  mm, comparable to the values obtained for other angles, which confirms

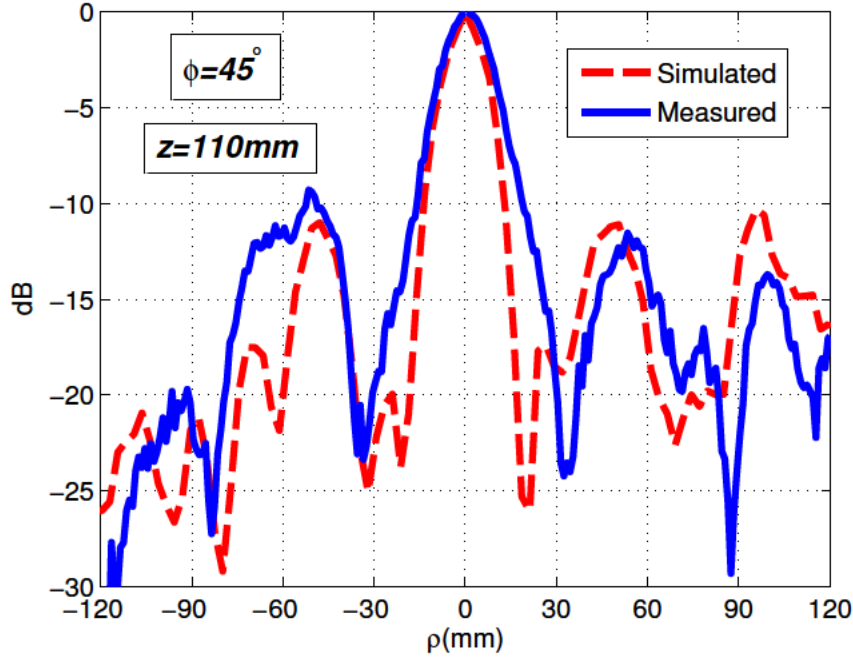


Figure 5.25: Measured and simulated transverse cuts along  $\rho$  for the focal height  $z_F = 110$  mm at the plane  $\phi = 45^\circ$ .

the fairly good electromagnetic symmetry of the focal region along  $\phi$ , despite the above mentioned geometrical asymmetry of the HMLWA branches.

Another important parameter to evaluate the performance of the proposed device as a microwave lens is the focal depth  $\Delta z$ ; i.e., the half-power width of the focus along the  $z$ -axis. Fig. 5.27 shows an axial cut for the normalized  $E$ -field along the  $z$ -axis at the central position of  $\rho = 0$ . The comparison of measured results with simulations shows good correspondence between them. A focal depth of  $\Delta z = 60$  mm is obtained, approximately three times larger than the focal width. This ellipsoidal shape of the focal region (prolate spheroid) is common to all planar near-field focused lenses [125], [126], [220]–[224] as a result of their 2-D (planar) aperture topology. The capability to focus the energy also along the axial direction demonstrates that a 3-D focus is actually obtained at the prescribed focal region of  $\rho = 0$  and  $z = 5.5\lambda_0 = 110$  mm for the design frequency of 15 GHz.

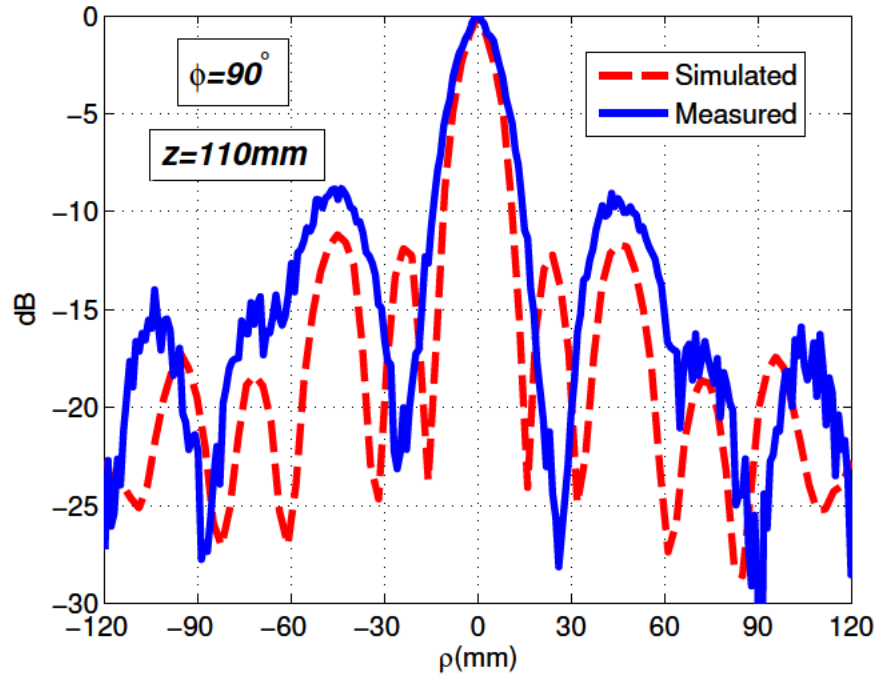


Figure 5.26: Measured and simulated transverse cuts along  $\rho$  for the focal height  $z_F = 110$  mm at the plane  $\phi = 90^\circ$ .

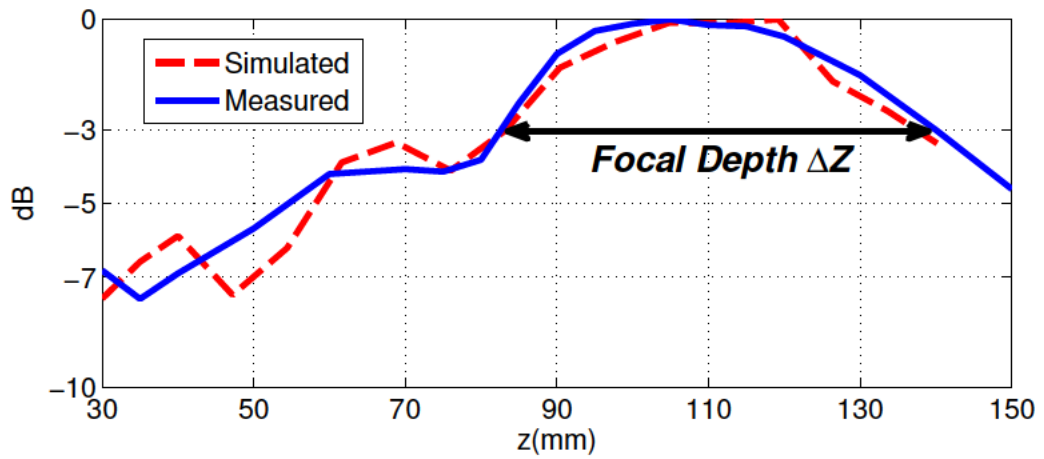


Figure 5.27: Measured and simulated axial cuts along  $z$ -axis at the center position  $\rho = 0$ .

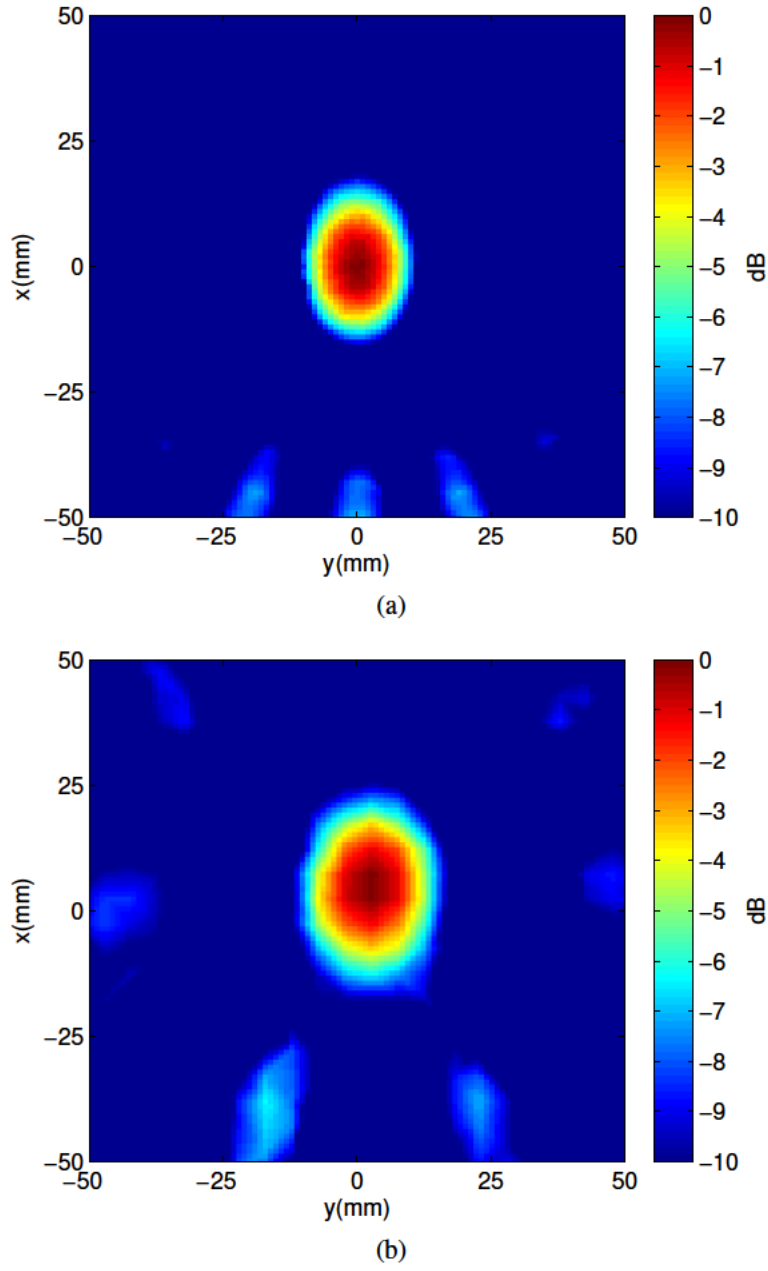


Figure 5.28: Near-field plane at the focal height  $z_F = 110$  mm for the design frequency of 15 GHz: a) simulated and b) measured.

Transverse cuts in the  $xy$ -plane for the focal distance  $z = z_F = 110$  mm are represented in Fig. 5.28, where measured near fields for the  $xy$ -plane at the focal height  $z = 5.5\lambda_0 = 110$  mm are compared with simulated ones. A clearly

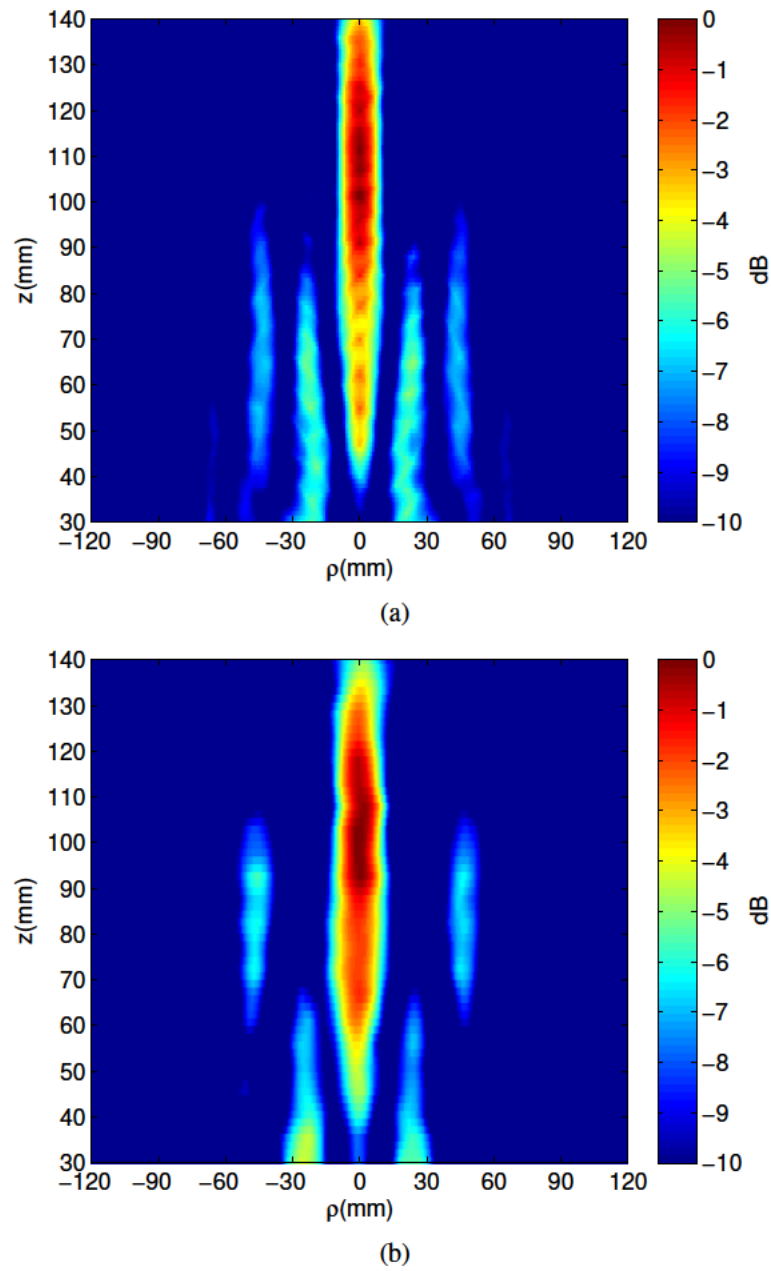


Figure 5.29: Near-field plane at  $\phi = 0^\circ$  along the  $z$ -axis for the design frequency of 15 GHz: a) simulated and b) measured.

symmetric (circular) focused spot in the  $xy$ -plane is obtained in coherence with the represented values of the different transverse and axial cuts. Moreover, it can be seen that the measured focusing pattern shown in Fig. 5.28b is slightly wider

compared with the simulated one shown in Fig. 5.28a. These differences can be attributed to small discrepancies between the structure simulated in HFSS and the measured prototype as well as by the perturbation introduced by the measurement probe.

Fig. 5.29 shows the simulated and measured near-fields for the  $\rho z$ -plane at  $\phi = 0^\circ$ . It can be observed that the highest intensity (plotted in red color) is obtained at the focal height  $z_F = 110$  mm. Both results show a similar focusing pattern, demonstrating a good agreement and that a 3-D near-field focus above the center of the array has been obtained.

Finally, the measured  $S_{11}$  parameter is compared with simulations in Fig. 5.30. Although some discrepancies are observed between both results, the key point is that a good input matching ( $S_{11} < -15$  dB) is obtained at the design frequency of 15 GHz and over a wide band ( $\sim 0.5$  GHz). It should be highlighted that this type of leaky-wave lenses are strongly dispersive with frequency, so the near-field focused beam can be scanned to higher focal distances as frequency is increased, until it eventually breaks into a conical shaped focused spot (or several spots), as shown in [126].

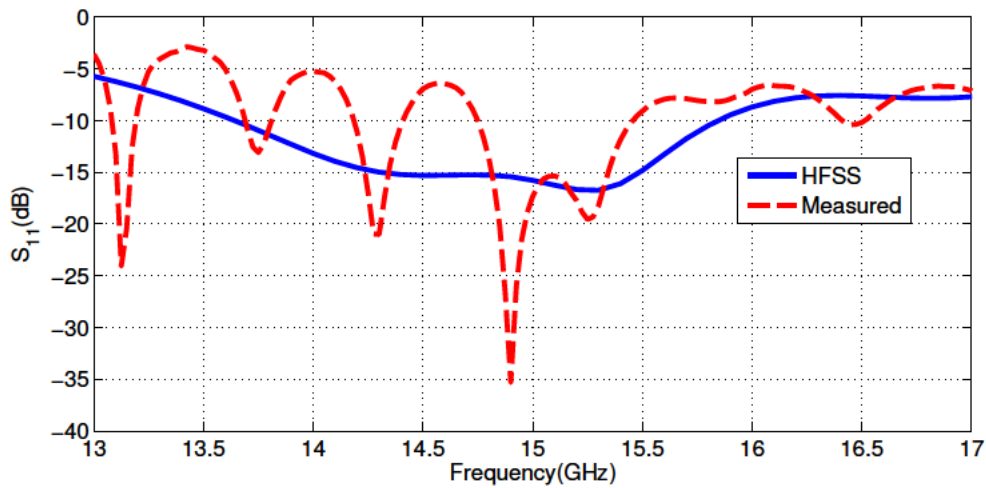


Figure 5.30: Measured and simulated input matching for the radial array of  $N = 8$  sinusoidally modulated HMLWAs.

### 5.2.5 Conclusion

An innovative type of microwave lens conceived from an array of sinusoidally modulated half-mode leaky-wave antennas (HMLWAs) has been presented in this section. The array consists of eight HMLWAs radially arranged around a single central feeding. The HMLWAs have been sinusoidally modulated in order to excite Floquet space harmonics that allow for backward radiation. Each HMLWA has been designed only to radiate with the  $n = -1$  space harmonic. In particular, by modifying the modulation index of the sinusoidal function and the width of the HMLWA, a simultaneous control of both the amplitude and phase of the radiated fields has been obtained, which has made possible the design of a shaped near-field focusing pattern. This fact in combination with the radial arrangement of the HMLWAs has allowed us to obtain a 3-D focus above the center of the array. The proposed design of the microwave lens has been validated with near-field measurements for the design frequency of 15 GHz. The present novel design demonstrates the utility of non-uniform sinusoidally modulated leaky-wave antennas in order to freely synthesize complex aperture distributions (in both amplitude and phase).

# Chapter 6

## Conclusions

Finally, the main conclusions of this thesis have been summarized in this last chapter. As stated along the Introduction of this thesis, the leaky-wave theory has been thoroughly investigated over the last decades. As a result of it, a wide variety of antennas and devices have been developed based on this radiation principle. Moreover, the constant emergence of new technologies has favoured that novel kind of devices could be envisioned and implemented. An example of this has happened with the technology of substrate integrated waveguide, which is characterized by a low-profile, low-losses and easiness of manufacture. These advantageous properties have attracted an increasing interest in it, which has been accompanied with the development of a large variety of SIW devices that were previously restricted to other technologies, such as conventional rectangular waveguide.

In order to contribute to the development of new leaky-wave devices, several designs have been conceived and implemented in SIW technology. Besides, the most relevant aspects related to their design have been dealt along the different chapters of this thesis. In particular, they can be summarized in the following form:

Chapter 1 has covered the main bases of SIW technology, which has been used to develop the different designs of this thesis. Concretely, the SIW equivalent width compared to conventional rectangular waveguides and the computation

of its material losses, have been described. The main methods used to analyze the SIW devices have also been addressed, moreover, some of the most used transitions between SIW and planar transmission lines, such as microstrip and coplanar, have been outlined. Finally, some of the main applications and devices that have already been reported in SIW technology have been discussed.

In Chapter 2 it has been described a new type of leaky-wave antenna (LWA) implemented in SIW technology. Concretely, this antenna is based on a conventional SIW structure with one of its rows of metallic posts sparse enough to allow the leakage of energy through them. In this manner, the  $TE_{10}$  mode propagating along the SIW becomes a leaky mode, whose phase constant and leakage rate can be independently controlled by varying the separation between posts and the SIW width. With the purpose of showing this capability to flexibly control the leaky mode, several prototypes have been designed and measured.

In Chapter 3 a modal tool based on the transverse resonance analysis of the SIW LWA cross section has been developed. To this aim, the rows of metallic posts that delimit the width of the SIW have been characterized by an equivalent impedance obtained from an analysis of TE plane wave incidence. On the other hand, the radiation impedance has been considered from an electrically thin substrate approximation of a dielectric filled parallel-plate waveguide with truncated upper plate. By combining all these elements that constitute the SIW LWA cross section, a transverse equivalent network has been used, and as a result, a modal analysis has been performed to compute the leaky mode as function of the main geometrical parameters of the antenna.

In Chapter 4 it has been performed the analysis and synthesis of several designs of tapered leaky-wave devices radiating both in the free space and inside the substrate. The modal tool developed in Chapter 3 has been used, which has allowed an efficient calculation of the leaky mode as function of the main geometrical parameters of the SIW. The design of conformal antennas has been presented in Section 4.2, moreover, several applications such as an angular bandpass filter in

Section 4.3, near-field focusing inside a parallel-plate waveguide in Section 4.4, and a quasi-optical multiplexer in Section 4.5 have been developed, including the manufacture and measure of the prototypes.

In Chapter 5 two designs of 1-D LWAs radially arranged around a central feeding have been presented. The first radial array has been designed to provide a pencil beam radiation pattern in the far-field region from an array of eight 1-D SIW LWAs, which has been demonstrated with experimental results in Section 5.1. A similar radial arrangement has been used in Section 5.2, but each arm of the array has been formed by sinusoidally modulated half-mode LWAs instead of 1-D SIW LWAs. In this manner, each arm of array can radiate backward thanks to the excitation of space harmonics which has allowed the synthesis of 3-D near-field focusing over the center of the array.

Finally, the main conclusions of this thesis have been summarized in this chapter, and a list with the most relevant publications that have been generated during this thesis has been added in the last section.



# Appendix A

## Radiated Fields by 1D LWAs

One dimensional leaky-wave antennas can be considered in terms of radiation as a magnetic line source whose electric field at the aperture can be expressed as a complex function

$$E_{\text{RAD}}^{\text{APERT}}(z) = M(z) \cdot e^{j\phi(z)} \quad (\text{A.1})$$

and its amplitude  $M(z)$  and phase  $\phi(z)$  terms can be respectively obtained as function of the complex wavenumber  $k_z$  along the line source:

$$k_z(z) = k_0 \sin \theta_{\text{RAD}}(z) - j\alpha(z) \quad (\text{A.2})$$

by

$$\alpha(z) = \frac{1}{2} \frac{|M(z)|^2}{\frac{1}{\eta} \int_0^L |M(\tau)|^2 d\tau - \int_0^z |M(\tau)|^2 d\tau} \quad (\text{A.3})$$

$$\beta(z) = k_0 \sin \theta_{\text{RAD}}(z) = -\frac{\partial \phi(z)}{\partial z} \quad (\text{A.4})$$

where  $k_0$  is the free-space wavenumber,  $\eta$  the radiation efficiency,  $\alpha(z)$  the leaky-wave leakage rate, and  $\theta_{\text{RAD}}$  the pointing angle of the leaky wave [82].

Next, by taking the Fourier transform of the fields  $E_{\text{RAD}}^{\text{APERT}}(z)$  radiated at the

aperture, the radiation pattern can be obtained for  $z > 0$  [82]:

$$E(y, z) = \frac{1}{2\pi} \int_{-\infty}^{\infty} \tilde{E}_{\text{RAD}}^{\text{APERT}}(k_z) e^{-jk_y y} e^{-jk_z z} dk_z \quad (\text{A.5})$$

Alternatively, for the case of line source antennas the radiated field can be computed as the superposition of discrete point sources separated a distance  $dz \rightarrow 0$  [227]. In this manner, from the radiated field of an infinitesimal dipole, whose electrical field components can be defined as [228]:

$$E_r = \eta \frac{I_0 l \cos \theta}{2\pi r^2} \left[ 1 + \frac{1}{jk_0 r} \right] e^{-jk_0 r} \quad (\text{A.6})$$

$$E_\theta = j\eta \frac{k_0 I_0 l \sin \theta}{4\pi r} \left[ 1 + \frac{1}{jk_0 r} - \frac{1}{(k_0 r)^2} \right] e^{-jk_0 r} \quad (\text{A.7})$$

$$E_\phi = 0 \quad (\text{A.8})$$

and in the far-field region ( $k_0 r \gg 1$ ) can be simplified by

$$E_\theta \approx j\eta \frac{k_0 I_0 l e^{-jk_0 r}}{4\pi r} \sin \theta \quad (\text{A.9})$$

$$E_r \approx E_\phi = 0 \quad (\text{A.10})$$

The total field radiated by a line source of length  $L_A$  can be obtained as the sum of  $N$  point sources (with  $N > 10L_A/\lambda_0$ ):

$$E_\theta = j\eta \frac{k_0 l}{4\pi r} \sin \theta \sum_{n=0}^{N-1} I_n e^{j(k_0 n d \sin \theta + \phi_n)} \quad (\text{A.11})$$

From the previous equation, it can be extracted the array factor  $AF(\theta)$ , which is defined as:

$$AF(\theta) = \sum_{n=0}^{N-1} I_n e^{j(k_0 n d \sin \theta + \phi_n)} \quad (\text{A.12})$$

and it can be used to determine the radiation pattern of the line source [228].

# Bibliography

- [1] K. Wu, D. Deslandes, and Y. Cassivi, "The substrate integrated circuits - a new concept for high-frequency electronics and optoelectronics", in *6th Int. Conf. on Telecommunications in Modern Satellite, Cable and Broadcasting Service. TELSIS 2003.*, vol. 1, Nis, Serbia and Montenegro, Oct. 2003, pp. 3 –10.
- [2] M. Bozzi, A. Georgiadis, and K. Wu, "Review of substrate-integrated waveguide circuits and antennas", *IET Microw. Antennas Propag.*, vol. 5, no. 8, pp. 909–920, Jun. 2011.
- [3] D. Deslandes and K. Wu, "Integrated microstrip and rectangular waveguide in planar form", *IEEE Microw. Wireless Compon. Lett.*, vol. 11, no. 2, pp. 68 –70, Feb. 2001.
- [4] J. Hirokawa and M. Ando, "Single-layer feed waveguide consisting of posts for plane TEM wave excitation in parallel plates", *IEEE Trans. Antennas Propag.*, vol. 46, no. 5, pp. 625–630, May 1998.
- [5] H. Uchimura, T. Takenoshita, and M. Fujii, "Development of a "laminated waveguide"", *IEEE Trans. Microw. Theory Tech.*, vol. 46, no. 12, pp. 2438–2443, Dec. 1998.
- [6] F. Xu and K. Wu, "Guided-wave and leakage characteristics of substrate integrated waveguide", *IEEE Trans. Microw. Theory Tech.*, vol. 53, no. 1, pp. 66–73, Jan. 2005.

- [7] D. Deslandes and K. Wu, "Design consideration and performance analysis of substrate integrated waveguide components", in *32nd European Microwave Conf.*, Milan, Italy, Sep. 2002, pp. 1–4.
- [8] Y. Cassivi, L. Perregrini, P. Arcioni, M. Bressan, K. Wu, and G. Conciauro, "Dispersion characteristics of substrate integrated rectangular waveguide", *IEEE Microw. Wireless Compon. Lett.*, vol. 12, no. 9, pp. 333–335, Sep. 2002.
- [9] W. Che, K. Deng, D. Wang, and Y. Chow, "Analytical equivalence between substrate-integrated waveguide and rectangular waveguide", *IET Microw. Antennas Propag.*, vol. 2, no. 1, pp. 35–41, Feb. 2008.
- [10] F. Ladani, S. Jam, and R. Safian, "Comment on 'analytical equivalence between substrate-integrated waveguide and rectangular waveguide'", *IET Microw. Antennas Propag.*, vol. 7, no. 1, pp. 24–25, Jan. 2013.
- [11] F. Xu, Y. Zhang, W. Hong, K. Wu, and T. J. Cui, "Finite-difference frequency-domain algorithm for modeling guided-wave properties of substrate integrated waveguide", *IEEE Trans. Microw. Theory Tech.*, vol. 51, no. 11, pp. 2221–2227, Nov. 2003.
- [12] M. Bozzi, L. Perregrini, and K. Wu, "Modeling of conductor, dielectric, and radiation losses in substrate integrated waveguide by the boundary integral-resonant mode expansion method", *IEEE Trans. Microw. Theory Tech.*, vol. 56, no. 12, pp. 3153–3161, Dec. 2008.
- [13] L. Yan, W. Hong, K. Wu, and T. Cui, "Investigations on the propagation characteristics of the substrate integrated waveguide based on the method of lines", *Proc. IEE Microw., Antennas and Propag.*, vol. 152, no. 1, pp. 35–42, Feb. 2005.
- [14] D. Deslandes and K. Wu, "Accurate modeling, wave mechanisms, and design considerations of a substrate integrated waveguide", *IEEE Trans. Microw. Theory Tech.*, vol. 54, no. 6, pp. 2516–2526, Jun. 2006.

- [15] J. Varela and J. Esteban, "Analysis of laterally open periodic waveguides by means of a generalized transverse resonance approach", *IEEE Trans. Microw. Theory Tech.*, vol. 59, no. 4, pp. 816–826, Apr. 2011.
- [16] R. E. Collin, *Field theory of guided waves*. IEEE press New York, 1991, vol. 2.
- [17] M. Bozzi, M. Pasian, L. Perregrini, and K. Wu, "On the losses in substrate-integrated waveguides and cavities", *International Journal of Microwave and Wireless Technologies*, vol. 1, pp. 395–401, 05 Oct. 2009.
- [18] M. Bozzi, L. Perregrini, and K. Wu, "Modeling of losses in substrate integrated waveguide by boundary integral-resonant mode expansion method", in *IEEE MTT-S Int. Microwave Symp. Dig.*, Atlanta, USA, Jun. 2008, pp. 515–518.
- [19] D. Deslandes and K. Wu, "Analysis and design of current probe transition from grounded coplanar to substrate integrated rectangular waveguides", *IEEE Trans. Microw. Theory Tech.*, vol. 53, no. 8, pp. 2487–2494, Aug. 2005.
- [20] D. Deslandes, "Design equations for tapered microstrip-to-substrate integrated waveguide transitions", in *IEEE MTT-S Int. Microwave Symp. Dig.*, Anaheim, USA, May 2010, pp. 704 –707.
- [21] D. Deslandes and K. Wu, "Single-substrate integration technique of planar circuits and waveguide filters", *IEEE Trans. Microw. Theory Tech.*, vol. 51, no. 2, pp. 593–596, Feb. 2003.
- [22] S. T. Choi, K. S. Yang, K. Tokuda, and Y.-H. Kim, "A V-band planar narrow bandpass filter using a new type integrated waveguide transition", *IEEE Microw. Wireless Compon. Lett.*, vol. 14, no. 12, pp. 545–547, Dec. 2004.

- [23] X.-P. Chen and K. Wu, "Substrate integrated waveguide cross-coupled filter with negative coupling structure", *IEEE Trans. Microw. Theory Tech.*, vol. 56, no. 1, pp. 142–149, Jan. 2008.
- [24] H. J Tang, W. Hong, Z. C Hao, J. X Chen, and K. Wu, "Optimal design of compact millimetre-wave SIW circular cavity filters", *Electron. Lett.*, vol. 41, no. 19, pp. 1068–1069, Sep. 2005.
- [25] Z.-C. Hao, W. Hong, X.-P. Chen, J. X. Chen, K. Wu, and T.-J. Cui, "Multilayered substrate integrated waveguide (MSIW) elliptic filter", *IEEE Microw. Wireless Compon. Lett.*, vol. 15, no. 2, pp. 95–97, Feb. 2005.
- [26] Z.-C. Hao, W. Hong, J.-X. Chen, X.-P. Chen, and K. Wu, "Compact super-wide bandpass substrate integrated waveguide (SIW) filters", *IEEE Trans. Microw. Theory Tech.*, vol. 53, no. 9, pp. 2968–2977, Sep. 2005.
- [27] Z. Hao, W. Hong, J. Chen, H. Zhou, and K. Wu, "Single-layer substrate integrated waveguide directional couplers", *Proc. IEE Microw., Antennas and Propag.*, vol. 153, no. 5, pp. 426–431, Oct. 2006.
- [28] T. Djerafi and K. Wu, "Super-compact substrate integrated waveguide cruciform directional coupler", *IEEE Microw. Wireless Compon. Lett.*, vol. 17, no. 11, pp. 757–759, Nov. 2007.
- [29] Z. Hao, W. Hong, J. X Chen, X. Chen, and K. Wu, "Planar diplexer for microwave integrated circuits", *Proc. IEE Microw., Antennas and Propag.*, pp. 455–459, Dec. 2005.
- [30] H.-J. Tang, W. Hong, J.-X. Chen, G. Q. Luo, and K. Wu, "Development of millimeter-wave planar diplexers based on complementary characters of dual-mode substrate integrated waveguide filters with circular and elliptic cavities", *IEEE Trans. Microw. Theory Tech.*, vol. 55, no. 4, pp. 776–782, Apr. 2007.

- [31] F. F. He, K. Wu, W. Hong, H.-J. Tang, H.-B. Zhu, and J. X. Chen, "A planar magic-T using substrate integrated circuits concept", *IEEE Microw. Wireless Compon. Lett.*, vol. 18, no. 6, pp. 386–388, Jun. 2008.
- [32] X. Xu, R. Bosisio, and K. Wu, "A new six-port junction based on substrate integrated waveguide technology", *IEEE Trans. Microw. Theory Tech.*, vol. 53, no. 7, pp. 2267–2273, Jul. 2005.
- [33] E. Moldovan, R. Bosisio, and K. Wu, "W-band multiport substrate-integrated waveguide circuits", *IEEE Trans. Microw. Theory Tech.*, vol. 54, no. 2, pp. 625–632, Feb. 2006.
- [34] W. D'Orazio and K. Wu, "Substrate-integrated-waveguide circulators suitable for millimeter-wave integration", *IEEE Trans. Microw. Theory Tech.*, vol. 54, no. 10, pp. 3675–3680, Oct. 2006.
- [35] S. Germain, D. Deslandes, and K. Wu, "Development of substrate integrated waveguide power dividers", in *IEEE CCECE 2003. Canadian Conf. on Electrical and Computer Engineering*, vol. 3, Montreal, Canada, May 2003, pp. 1921–1924.
- [36] Y. Cassivi, L. Perreggini, K. Wu, and G. Conciauro, "Low-cost and high-Q millimeter-wave resonator using substrate integrated waveguide technique", in *32nd European Microwave Conf.*, Milan, Italy, Sep. 2002, pp. 1–4.
- [37] Y. Cassivi and K. Wu, "Low cost microwave oscillator using substrate integrated waveguide cavity", *IEEE Microw. Wireless Compon. Lett.*, vol. 13, no. 2, pp. 48–50, Feb. 2003.
- [38] A. Georgiadis, S. Via, A. Collado, and F. Mira, "Push-push oscillator design based on a substrate integrated waveguide (SIW) resonator", in *European Microwave Conf. (EuMC)*, Rome, Italy, Sep. 2009, pp. 1231–1234.

- [39] Z. Chen, W. Hong, J. Chen, and J. Zhou, "Design of high-Q tunable SIW resonator and its application to low phase noise VCO", *IEEE Microw. Wireless Compon. Lett.*, vol. 23, no. 1, pp. 43–45, Jan. 2013.
- [40] J.-X. Chen, W. Hong, Z.-C. Hao, H. Li, and K. Wu, "Development of a low cost microwave mixer using a broad-band substrate integrated waveguide (SIW) coupler", *IEEE Microw. Wireless Compon. Lett.*, vol. 16, no. 2, pp. 84–86, Feb. 2006.
- [41] Z. Li and K. Wu, "24-GHz frequency-modulation continuous-wave radar front-end system-on-substrate", *IEEE Trans. Microw. Theory Tech.*, vol. 56, no. 2, pp. 278–285, Feb. 2008.
- [42] M. Abdolhamidi and M. Shahabadi, "X-band substrate integrated waveguide amplifier", *IEEE Microw. Wireless Compon. Lett.*, vol. 18, no. 12, pp. 815–817, Dec. 2008.
- [43] H.-Y. Jin, G.-J. Wen, and Y.-B. Jin, "A novel spatial power combiner based on SIW and HMSIW", in *IEEE MTT-S Int. Microwave Workshop Series on Art of Miniaturizing RF and Microwave Passive Components. IMWS*, Chengdu, China, Dec. 2008, pp. 233–236.
- [44] L. Yan, W. Hong, G. Hua, J. Chen, K. Wu, and T. J. Cui, "Simulation and experiment on SIW slot array antennas", *IEEE Microw. Wireless Compon. Lett.*, vol. 14, no. 9, pp. 446–448, Sep. 2004.
- [45] D. Deslandes and K. Wu, "Substrate integrated waveguide leaky-wave antenna: concept and design considerations", in *APMC 2005. Asia-Pacific Microwave Conf. Proc.*, Suzhou, China, Dec. 2005, pp. 346–349.
- [46] F. Xu, K. Wu, and X. Zhang, "Periodic leaky-wave antenna for millimeter wave applications based on substrate integrated waveguide", *IEEE Trans. Antennas Propag.*, vol. 58, no. 2, pp. 340–347, Feb. 2010.

- [47] A. J. Martinez-Ros, J. L. Gomez-Tornero, and G. Goussetis, “Independent control of the leakage rate and pointing angle of a novel planar leaky-wave antenna”, in *Proc. of the 5th European Conf. on Antennas and Propagation (EuCAP)*, Rome, Italy, Apr. 2011, pp. 1919–1922.
- [48] Y. J. Cheng, W. Hong, and K. Wu, “Design of a monopulse antenna using a dual V-type linearly tapered slot antenna (DVL TSA)”, *IEEE Trans. Antennas Propag.*, vol. 56, no. 9, pp. 2903–2909, Sep. 2008.
- [49] G. Q. Luo, Z. F. Hu, L. X. Dong, and L.-L. Sun, “Planar slot antenna backed by substrate integrated waveguide cavity”, *IEEE Antennas Wireless Propag. Lett.*, vol. 7, pp. 236–239, 2008.
- [50] J. C. Bohorquez, H. A. F. Pedraza, I. C. H. Pinzon, J. A. Castiblanco, N. Pena, and H. F. Guarnizo, “Planar substrate integrated waveguide cavity-backed antenna”, *IEEE Antennas Wireless Propag. Lett.*, vol. 8, pp. 1139–1142, 2009.
- [51] M. Awida and A. Fathy, “Substrate-integrated waveguide Ku-band cavity-backed 2x2 microstrip patch array antenna”, *IEEE Antennas Wireless Propag. Lett.*, vol. 8, pp. 1054–1056, 2009.
- [52] W. Yang and J. Zhou, “Wideband low-profile substrate integrated waveguide cavity-backed E-shaped patch antenna”, *IEEE Antennas Wireless Propag. Lett.*, vol. 12, pp. 143–146, 2013.
- [53] H. Wang, D.-G. Fang, B. Zhang, and W.-Q. Che, “Dielectric loaded substrate integrated waveguide (SIW) H-plane horn antennas”, *IEEE Trans. Antennas Propag.*, vol. 58, no. 3, pp. 640–647, Mar. 2010.
- [54] Y. J. Cheng, W. Hong, and K. Wu, “Millimeter-wave substrate integrated waveguide multibeam antenna based on the parabolic reflector principle”, *IEEE Trans. Antennas Propag.*, vol. 56, no. 9, pp. 3055–3058, Sep. 2008.

- [55] Y. J. Cheng, W. Hong, K. Wu, Z.-Q. Kuai, C. Yu, J. X. Chen, J. Zhou, and H.-J. Tang, "Substrate integrated waveguide (SIW) Rotman lens and its Ka-band multibeam array antenna applications", *IEEE Trans. Antennas Propag.*, vol. 56, no. 8, pp. 2504–2513, 2008.
- [56] P. Chen, W. Hong, Z. Kuai, and J. Xu, "A double layer substrate integrated waveguide Blass matrix for beamforming applications", *IEEE Microw. Wireless Compon. Lett.*, vol. 19, no. 6, pp. 374–376, Jun. 2009.
- [57] M. Ettorre, A. Neto, G. Gerini, and S. Maci, "Leaky-wave slot array antenna fed by a dual reflector system", *IEEE Trans. Antennas Propag.*, vol. 56, no. 10, pp. 3143–3149, Oct. 2008.
- [58] Y. J. Cheng, X. Y. Bao, and Y. X. Guo, "60-GHz LTCC miniaturized substrate integrated multibeam array antenna with multiple polarizations", *IEEE Trans. Antennas Propag.*, vol. 61, no. 12, pp. 5958–5967, Dec. 2013.
- [59] H. Ermert, "Guiding and radiation characteristics of planar waveguides", *IEE Journal on Microwaves, Optics and Acoustics*, vol. 3, no. 2, pp. 59–62, Mar. 1979.
- [60] W. Menzel, "A new travelling wave antenna in microstrip", *Arch. Elektron. Uebertrag. Tech.*, vol. 33, no. 4, pp. 137–140, Apr. 1979.
- [61] A. Oliner and K. Lee, "Microstrip leaky wave strip antennas", in *Antennas and Propagation Soc. Int. Symp.*, vol. 24, Philadelphia, USA, Jun. 1986, pp. 443–446.
- [62] A. A. Oliner, "Leakage from higher modes on microstrip line with application to antennas", *Radio Sci.*, vol. 22, pp. 907–912, Nov. 1987.
- [63] K. S. Lee, "Microstrip line leaky wave antenna", PhD thesis, Polytechnic Inst., Brooklyn, New York, Jun. 1986.

- [64] Y.-D. Lin, J.-W. Sheen, and C.-K. Tzuang, "Analysis and design of feeding structures for microstrip leaky wave antenna", *IEEE Trans. Microw. Theory Tech.*, vol. 44, no. 9, pp. 1540–1547, Sep. 1996.
- [65] C.-J. Wang, H.-L. Guan, and C. Jou, "Two-dimensional scanning leaky-wave antenna by utilizing the phased array", *IEEE Microw. Wireless Compon. Lett.*, vol. 12, no. 8, pp. 311–313, Aug. 2002.
- [66] Y. Li, Q. Xue, E. K.-N. Yung, and Y. Long, "A fixed-frequency beam-scanning microstrip leaky wave antenna array", *IEEE Antennas Wireless Propag. Lett.*, vol. 6, pp. 616–618, Dec. 2007.
- [67] Y. Li and Y. Long, "Frequency-fixed beam-scanning microstrip leaky-wave antenna with multi-terminals", *Electron. Lett.*, vol. 42, no. 1, pp. 7–8, Jan. 2006.
- [68] G.-J. Chou and C.-K. Tzuang, "Oscillator-type active-integrated antenna: the leaky-mode approach", *IEEE Trans. Microw. Theory Tech.*, vol. 44, no. 12, pp. 2265–2272, Dec. 1996.
- [69] C. Hu, J. Wu, and C. Jou, "An active frequency-tuned beam-scanning leaky-wave antenna", *Microwave Opt. Technol. Lett.*, vol. 17, no. 1, pp. 43–45, 1998.
- [70] C.-J. Wang, C. Jou, and J.-J. Wu, "A novel two-beam scanning active leaky-wave antenna", *IEEE Trans. Antennas Propag.*, vol. 47, no. 8, pp. 1314–1317, Aug. 1999.
- [71] J. Radcliffe, G. Thiele, and G. Zelinski, "A microstrip leaky wave antenna and its properties", in *26th Antenna Measurement Techniques Association Meeting*, St. Mountain, USA, Oct. 2004.
- [72] G. Zelinski, G. Thiele, M. Hastriter, M. Havrilla, and A. Terzuoli, "Half width leaky wave antennas", *IET Microw. Antennas Propag.*, vol. 1, no. 2, pp. 341–348, Apr. 2007.

- [73] Y. Li, Q. Xue, E.-N. Yung, and Y. Long, “Quasi microstrip leaky-wave antenna with a two-dimensional beam-scanning capability”, *IEEE Trans. Antennas Propag.*, vol. 57, no. 2, pp. 347–354, Feb. 2009.
- [74] ———, “The periodic half-width microstrip leaky-wave antenna with a backward to forward scanning capability”, *IEEE Trans. Antennas Propag.*, vol. 58, no. 3, pp. 963–966, Mar. 2010.
- [75] Y. J. Cheng, W. Hong, and K. Wu, “Millimeter-wave half mode substrate integrated waveguide frequency scanning antenna with quadri-polarization”, *IEEE Trans. Antennas Propag.*, vol. 58, no. 6, pp. 1848–1855, Jun. 2010.
- [76] L. Liu, C. Caloz, and T. Itoh, “Dominant mode leaky-wave antenna with backfire-to-endfire scanning capability”, *Electron. Lett.*, vol. 38, no. 23, pp. 1414–1416, Nov. 2002.
- [77] A. Grbic and G. Eleftheriades, “Periodic analysis of a 2-D negative refractive index transmission line structure”, *IEEE Trans. Antennas Propag.*, vol. 51, no. 10, pp. 2604–2611, Oct. 2003.
- [78] C. Caloz, T. Itoh, and A. Rennings, “CRLH metamaterial leaky-wave and resonant antennas”, *IEEE Antennas Propag. Mag.*, vol. 50, no. 5, pp. 25–39, Oct. 2008.
- [79] C. Wang, H. Guan, and C. Jou, “A novel method for short leaky-wave antennas to suppress the reflected wave”, *Microwave Opt. Technol. Lett.*, vol. 36, no. 2, pp. 129–131, 2003.
- [80] I.-Y. Chen, C.-J. Wang, H.-L. Guan, and C. Jou, “Studies of suppression of the reflected wave and beam-scanning features of the antenna arrays”, *IEEE Trans. Antennas Propag.*, vol. 53, no. 7, pp. 2220–2225, Jul. 2005.
- [81] Y.-L. Chiou, J.-W. Wu, J.-H. Huang, and C. Jou, “Design of short microstrip leaky-wave antenna with suppressed back lobe and increased fre-

- quency scanning region”, *IEEE Trans. Antennas Propag.*, vol. 57, no. 10, pp. 3329 –3333, Oct. 2009.
- [82] A. A. Oliner and D. R. Jackson, “Leaky-wave antennas”, in *Antenna Engineering Handbook*, J. L. Volakis, Ed., 4th, New York: McGraw-Hill, Jun. 2007, ch. 11.
- [83] G.-J. Chou and C.-K. C. Tzuang, “An integrated quasi-planar leaky-wave antenna”, *IEEE Trans. Antennas Propag.*, vol. 44, no. 8, pp. 1078 –1085, Aug. 1996.
- [84] J. L. Gómez-Tornero, D. Canete-Rebenaque, and A. Alvarez-Melcon, “Printed-circuit leaky-wave antenna with pointing and illumination flexibility”, *IEEE Microw. Wireless Compon. Lett.*, vol. 15, no. 8, pp. 536 –538, Aug. 2005.
- [85] J. L. Gomez-Tornero, G. Goussetis, A. Feresidis, and A. Melcon, “Control of leaky-mode propagation and radiation properties in hybrid dielectric-waveguide printed-circuit technology: experimental results”, *IEEE Trans. Antennas Propag.*, vol. 54, no. 11, pp. 3383 –3390, Nov. 2006.
- [86] J. L. Gomez-Tornero, D. Caete-Rebenaque, and A. Alvarez-Melcon, “Microstrip leaky-wave antenna with control of leakage rate and only one main beam in the azimuthal plane”, *IEEE Trans. Antennas Propag.*, vol. 56, no. 2, pp. 335 –344, Feb. 2008.
- [87] W. Hong, B. Liu, G. Luo, Q. Lai, J. Xu, Z. Hao, F. He, and X. Yin, “Integrated microwave and millimeter wave antennas based on SIW and HM-SIW technology”, in *Int. Workshop on Antenna Technology: Small and Smart Antennas Metamaterials and Applications, IWAT '07.*, Cambridge, UK, Mar. 2007, pp. 69 –72.
- [88] S. Yang, S. Suleiman, and A. Fathy, “Low profile multi-layer slotted substrate integrated waveguide (SIW) array antenna with folded feed network for mobile DBS applications”, in *IEEE Antennas and Propagation Soc. Int. Symp.*, Honolulu, USA, Jun. 2007, pp. 473 –476.

- [89] N. Marcuvitz, *Waveguide handbook*. P. Peregrinus on behalf of the Institution of Electrical Engineers, 1986.
- [90] *Ansoft HFSS v11*, <http://www.ansoft.com/products/hf/hfss/>, 2007.
- [91] A. J. Martinez-Ros, J. L. Gomez-Tornero, and G. Goussetis, “Planar leaky-wave antenna with flexible control of the complex propagation constant”, *IEEE Trans. Antennas Propag.*, vol. 60, no. 3, pp. 1625 –1630, Mar. 2012.
- [92] P. Lampariello, F. Frezza, H. Shigesawa, M. Tsuji, and A. Oliner, “A versatile leaky-wave antenna based on stub-loaded rectangular waveguide .I. Theory”, *IEEE Trans. Antennas Propag.*, vol. 46, no. 7, pp. 1032 –1041, Jul. 1998.
- [93] T. Zhao, D. Jackson, J. Williams, H.-Y. Yang, and A. Oliner, “2-D periodic leaky-wave antennas-part I: metal patch design”, *IEEE Trans. Antennas Propag.*, vol. 53, no. 11, pp. 3505 –3514, Nov. 2005.
- [94] J. L. Gomez-Tornero, F. Quesada-Pereira, and A. Alvarez-Melcon, “Novel microwave network for the leaky-wave analysis of evanescent fields in stub-loaded structures”, *IEEE Trans. Microw. Theory Tech.*, vol. 56, no. 6, pp. 1405 –1412, Jun. 2008.
- [95] A. J. Martinez-Ros, J. L. Gomez-Tornero, F. Quesada-Pereira, and A. Alvarez-Melcon, “Transverse resonance analysis of a planar leaky wave antenna with flexible control of the complex propagation constant”, in *IEEE Int. Symp. on Antennas and Propagation (APSURSI)*, Spokane, USA, Jul. 2011, pp. 1289 –1292.
- [96] E. Kuester, R. Johnk, and D. Chang, “The thin-substrate approximation for reflection from the end of a slab-loaded parallel-plate waveguide with application to microstrip patch antennas”, *IEEE Trans. Antennas Propag.*, vol. 30, no. 5, pp. 910 –917, Sep. 1982.

- [97] Y. Leviatan, P. G. Li, A. T. Adams, and J. Perini, "Single post inductive obstacle in rectangular waveguide", *IEEE Trans. Microw. Theory Tech.*, vol. 31, no. 10, pp. 806–812, Oct. 1983.
- [98] F. Capolino, D. R. Wilton, and W. A. Johnson, "Efficient computation of the 2-D Green's function for 1-D periodic structures using the Ewald method", *IEEE Trans. Antennas Propag.*, vol. 53, no. 9, pp. 2977–2984, Sep. 2005.
- [99] F. D. Quesada Pereira, V. E. Boria Esbert, J. Pascual García, A. Vidal Pantaleoni, A. Álvarez Melcón, J. Gómez Tornero, and B. Gimeno Martínez, "Efficient analysis of arbitrarily shaped inductive obstacles in rectangular waveguides using a surface integral equation formulation", *IEEE Trans. Microw. Theory Tech.*, vol. 55, no. 4, pp. 715–721, Apr. 2007.
- [100] *CST Microwave Studio 2009*, <http://www.cst.com>, Wellesley Hills, MA, USA, 2009.
- [101] J. L. Gomez-Tornero and A. Alvarez-Melcon, "Radiation analysis in the space domain of laterally shielded planar transmission lines: 2. applications", *Radio Sci.*, vol. 39, no. 3, RS3006–, May 2004.
- [102] H. Shigesawa, M. Tsuji, P. Lampariello, F. Frezza, and A. Oliner, "Coupling between different leaky-mode types in stub-loaded leaky waveguides", *IEEE Trans. Microw. Theory Tech.*, vol. 42, no. 8, pp. 1548–1560, Aug. 1994.
- [103] J. L. Gomez-Tornero, A. delaTorreMartinez, D. Rebenaque, M. Gugliemi, and A. Alvarez-Melcon, "Design of tapered leaky-wave antennas in hybrid waveguide-planar technology for millimeter waveband applications", *IEEE Trans. Antennas Propag.*, vol. 53, no. 8, pp. 2563–2577, Aug. 2005.
- [104] J. Pendry, D. Schurig, and D. Smith, "Controlling electromagnetic fields", *Science*, vol. 312, no. 5781, pp. 1780–1782, 2006.

- [105] P. Checcacci, V. Russo, and A. Scheggi, “Holographic antennas”, *IEEE Trans. Antennas Propag.*, vol. 18, no. 6, pp. 811 –813, Nov. 1970.
- [106] M. ElSherbiny, A. Fathy, A. Rosen, G. Ayers, and S. Perlow, “Holographic antenna concept, analysis, and parameters”, *IEEE Trans. Antennas Propag.*, vol. 52, no. 3, pp. 830 –839, Mar. 2004.
- [107] M. Nannetti, F. Caminita, and S. Maci, “Leaky-wave based interpretation of the radiation from holographic surfaces”, in *IEEE Antennas and Propagation Soc. Int. Symp.*, Honolulu, USA, Jun. 2007, pp. 5813 –5816.
- [108] S. Maci, G. Minatti, M. Casaletti, and M. Bosiljevac, “Metasurfing: addressing waves on impenetrable metasurfaces”, *IEEE Antennas Wireless Propag. Lett.*, vol. 10, pp. 1499 –1502, 2011.
- [109] S. Podilchak, A. Freundorfer, and Y. Antar, “Broadside radiation from a planar 2-D leaky-wave antenna by practical surface-wave launching”, *IEEE Antennas Wireless Propag. Lett.*, vol. 7, pp. 517 –520, 2008.
- [110] A. Sutinjo, M. Okoniewski, and R. Johnston, “A holographic antenna approach for surface wave control in microstrip antenna applications”, *IEEE Trans. Antennas Propag.*, vol. 58, no. 3, pp. 675 –682, Mar. 2010.
- [111] B. Fong, J. Colburn, J. Ottusch, J. Visser, and D. Sievenpiper, “Scalar and tensor holographic artificial impedance surfaces”, *IEEE Trans. Antennas Propag.*, vol. 58, no. 10, pp. 3212 –3221, Oct. 2010.
- [112] G. Minatti, F. Caminita, M. Casaletti, and S. Maci, “Spiral leaky-wave antennas based on modulated surface impedance”, *IEEE Trans. Antennas Propag.*, vol. 59, no. 12, pp. 4436 –4444, Dec. 2011.
- [113] A. Oliner and A. Hessel, “Guided waves on sinusoidally-modulated reactance surfaces”, *IRE Trans. on Antennas and Propagation*, vol. 7, no. 5, pp. 201 –208, Dec. 1959.

- [114] L. Matekovits, G. C. Vietti Colomé, and M. Orefice, “Controlling the bandlimits of TE-surface wave propagation along a modulated microstrip-line-based high impedance surface”, *IEEE Trans. Antennas Propag.*, vol. 56, no. 8, pp. 2555 –2562, Aug. 2008.
- [115] S. Podilchak, L. Matekovits, A. Freundorfer, K. Esselle, and Y. Antar, “Modulated strip-line leaky-wave antenna using a printed grating lens and a surface-wave source”, in *14th Int. Symp. on Antenna Technology and Appl. Electromagnetics the Amer. Electromagnetics Conf. (ANTEM-AMEREM)*, Ottawa, Canada, Jul. 2010, pp. 1 –3.
- [116] L. Matekovits, “Analytically expressed dispersion diagram of unit cells for a novel type of holographic surface”, *IEEE Antennas Wireless Propag. Lett.*, vol. 9, pp. 1251 –1254, 2010.
- [117] A. Patel and A. Grbic, “A printed leaky-wave antenna based on a sinusoidally-modulated reactance surface”, *IEEE Trans. Antennas Propag.*, vol. 59, no. 6, pp. 2087 –2096, Jun. 2011.
- [118] A. J. Martinez-Ros, J. L. Gomez-Tornero, and F. Quesada-Pereira, “Efficient analysis and design of novel SIW leaky-wave antenna”, *IEEE Antennas Wireless Propag. Lett.*, vol. 12, pp. 496–499, 2013.
- [119] Y. J. Cheng, W. Hong, K. Wu, and Y. Fan, “Millimeter-wave substrate integrated waveguide long slot leaky-wave antennas and two-dimensional multibeam applications”, *IEEE Trans. Antennas Propag.*, vol. 59, no. 1, pp. 40 –47, Jan. 2011.
- [120] J.-L. Gomez-Tornero, “Unusual tapering of leaky-wave radiators and their applications”, in *Proc. of the 5th European Conf. on Antennas and Propagation (EuCAP)*, Rome, Italy, Apr. 2011, pp. 821 –824.
- [121] P. Burghignoli, F. Frezza, A. Galli, and G. Schettini, “Synthesis of broad-beam patterns through leaky-wave antennas with rectilinear geometry”, *IEEE Antennas Wireless Propag. Lett.*, vol. 2, no. 1, pp. 136 –139, 2003.

- [122] J. L. Gomez-Tornero, A. Weily, and Y. Guo, “Rectilinear leaky-wave antennas with broad beam patterns using hybrid printed-circuit waveguides”, *IEEE Trans. Antennas Propag.*, vol. 59, no. 11, pp. 3999 –4007, Nov. 2011.
- [123] J. L. Gomez-Tornero, A. J. Martinez-Ros, and R. Verdu-Monedero, “FFT synthesis of radiation patterns with wide nulls using tapered leaky-wave antennas”, *IEEE Antennas Wireless Propag. Lett.*, vol. 9, pp. 518 –521, 2010.
- [124] J. L. Gomez-Tornero, F. Quesada-Pereira, A. Alvarez-Melcon, G. Goussetis, A. Weily, and Y. Guo, “Frequency steerable two dimensional focusing using rectilinear leaky-wave lenses”, *IEEE Trans. Antennas Propag.*, vol. 59, no. 2, pp. 407 –415, Feb. 2011.
- [125] J. L. Gomez-Tornero, D. Blanco, E. Rajo-Iglesias, and N. Llombart, “Holographic surface leaky-wave lenses with circularly-polarized focused near-fields. Part I: concept, design and analysis theory”, *IEEE Trans. Antennas Propag.*, vol. 61, no. 7, pp. 3475–3485, Jul. 2013.
- [126] D. Blanco, J. L. Gomez-Tornero, E. Rajo-Iglesias, and N. Llombart, “Holographic surface leaky-wave lenses with circularly-polarized focused near-fields. Part II: experiments and description of frequency steering of focal length”, *IEEE Trans. Antennas Propag.*, vol. 61, no. 7, pp. 3486–3494, Jul. 2013.
- [127] M. Takahashi, J.-I. Takada, M. Ando, and N. Goto, “A slot design for uniform aperture field distribution in single-layered radial line slot antennas”, *IEEE Trans. Antennas Propag.*, vol. 39, no. 7, pp. 954 –959, Jul. 1991.
- [128] L. Josefsson and P. Persson, *Conformal array antenna theory and design*, ser. IEEE Press Series on Electromagnetic Wave Theory. Piscataway, NJ: John Wiley & Sons, 2006.

- [129] W. Hong, T.-L. Chen, C.-Y. Chang, J.-W. Sheen, and Y.-D. Lin, "Broad-band tapered microstrip leaky-wave antenna", *IEEE Trans. Antennas Propag.*, vol. 51, no. 8, pp. 1922–1928, Aug. 2003.
- [130] J.-W. Wu, C.-J. Wang, and C. Jou, "Method of suppressing the side lobe of a tapered short leaky wave antenna", *IEEE Antennas Wireless Propag. Lett.*, vol. 8, pp. 1146–1149, 2009.
- [131] R. Siragusa, E. Perret, P. Lemaitre-Auger, H. Van Nguyen, S. Tedjini, and C. Caloz, "A tapered CRLH interdigital/stub leaky-wave antenna with minimized sidelobe levels", *IEEE Antennas Wireless Propag. Lett.*, vol. 11, pp. 1214–1217, 2012.
- [132] N. Nguyen-Trong, T. Kaufmann, and C. Fumeaux, "A wideband omnidirectional horizontally polarized traveling-wave antenna based on half-mode substrate integrated waveguide", *IEEE Antennas Wireless Propag. Lett.*, vol. 12, pp. 682–685, 2013.
- [133] S. Podilchak, L. Matekovits, A. Freundorfer, Y. Antar, and M. Orefice, "Controlled leaky-wave radiation from a planar configuration of width-modulated microstrip lines", *IEEE Trans. Antennas Propag.*, vol. 61, no. 10, pp. 4957–4972, Oct. 2013.
- [134] L. Matekovits and Y. Ranga, "Controlling the phase of the scattered and/or radiated field from a high impedance surface of quasi-periodic sequences", *IEEE Antennas Wireless Propag. Lett.*, vol. 12, pp. 321–324, 2013.
- [135] J. Radcliffe, G. Thiele, R. Penno, S. Schneider, and L. Kempel, "Microstrip leaky wave antenna performance on a curved surface", in *IEEE Antennas and Propagation Soc. Int. Symp.*, Albuquerque, USA, Jul. 2006, pp. 4247–4250.
- [136] O. Losito, "Design of conformal tapered leaky wave antenna", in *Progress in Electromagnetics Research Symp.*, Prague, Czech Republic, Aug. 2007, pp. 177–181.

- [137] A. J. Martinez-Ros, J. L. Gomez-Tornero, and G. Goussetis, “Conformal tapered microstrip leaky-wave antennas”, in *6th European Conf. on Antennas and Propagation (EuCAP)*, Prague, Czech Republic, Mar. 2012, pp. 154–158.
- [138] M. Hashemi and T. Itoh, “Dispersion engineered metamaterial-based transmission line for conformal surface application”, in *IEEE MTT-S Int. Microwave Symp. Dig.*, Atlanta, USA, Jun. 2008, pp. 331–334.
- [139] K. Hosseini and Z. Atlasbaf, “Design of a cylindrical CRLH leaky-wave antenna using conformal mapping”, in *2012 Sixth Int. Symp. on Telecommunications (IST)*, Tehran, Iran, Nov. 2012, pp. 33–36.
- [140] Y. J. Cheng, H. Xu, D. Ma, J. Wu, L. Wang, and Y. Fan, “Millimeter-wave shaped-beam substrate integrated conformal array antenna”, *IEEE Trans. Antennas Propag.*, vol. 61, no. 9, pp. 4558–4566, 2013.
- [141] A. J. Martinez-Ros, J. L. Gomez-Tornero, and G. Goussetis, “Holographic pattern synthesis with modulated substrate integrated waveguide line-source leaky-wave antennas”, *IEEE Trans. Antennas Propag.*, vol. 61, no. 7, pp. 3466–3474, 2013.
- [142] J. L. Gomez-Tornero, “Analysis and design of conformal tapered leaky-wave antennas”, *IEEE Antennas Wireless Propag. Lett.*, vol. 10, pp. 1068–1071, 2011.
- [143] A. J. Martinez-Ros, J. L. Gomez-Tornero, and G. Goussetis, “Frequency scanning leaky-wave antenna for positioning and identification of RFID tags”, in *2011 IEEE Int. Conf. on RFID-Technologies and Applications (RFID-TA)*, Sitges, Spain, Sep. 2011, pp. 451–456.
- [144] R. Mailloux, “Synthesis of spatial filters with Chebyshev characteristics”, *IEEE Trans. Antennas Propag.*, vol. 24, no. 2, pp. 174–181, Mar. 1976.

- [145] A. Abbaspour-Tamijani, K. Sarabandi, and G. Rebeiz, “Antenna-filter-antenna arrays as a class of bandpass frequency-selective surfaces”, *IEEE Trans. Microw. Theory Tech.*, vol. 52, no. 8, pp. 1781–1789, 8.
- [146] G. Q. Luo, W. Hong, H.-J. Tang, and K. Wu, “High performance frequency selective surface using cascading substrate integrated waveguide cavities”, *IEEE Microw. Wireless Compon. Lett.*, vol. 16, no. 12, pp. 648–650, Dec. 2006.
- [147] G. Q. Luo, W. Hong, Q.-H. Lai, K. Wu, and L.-L. Sun, “Design and experimental verification of compact frequency-selective surface with quasi-elliptic bandpass response”, *IEEE Trans. Microw. Theory Tech.*, vol. 55, no. 12, pp. 2481–2487, Dec. 2007.
- [148] D. Kinowski, M. Guglielmi, and A. Roederer, “Angular bandpass filters: an alternative viewpoint gives improved design flexibility”, *IEEE Trans. Antennas Propag.*, vol. 43, no. 4, pp. 390–395, Apr. 1995.
- [149] F. Bayatpur and K. Sarabandi, “Miniaturized FSS and patch antenna array coupling for angle-independent, high-order spatial filtering”, *IEEE Microw. Wireless Compon. Lett.*, vol. 20, no. 2, pp. 79–81, Feb. 2010.
- [150] P. Franchi and R. Mailloux, “Theoretical and experimental study of metal grid angular filters for sidelobe suppression”, *IEEE Trans. Antennas Propag.*, vol. 31, no. 3, pp. 445–450, May 1983.
- [151] J. Ortiz, J. Baena, V. Losada, F. Medina, and J. Araque, “Spatial angular filtering by FSSs made of chains of interconnected SRRs and CSRRs”, *IEEE Microw. Wireless Compon. Lett.*, vol. 23, no. 9, pp. 477–479, 2013.
- [152] Y. J. Lee, J. Yeo, R. Mittra, and W. S. Park, “Application of electromagnetic bandgap (EBG) superstrates with controllable defects for a class of patch antennas as spatial angular filters”, *IEEE Trans. Antennas Propag.*, vol. 53, no. 1, pp. 224–235, Jan. 2005.

- [153] I. Ohtera, “Diverging/focusing of electromagnetic waves by utilizing the curved leakywave structure: application to broad-beam antenna for radiating within specified wide-angle”, *IEEE Trans. Antennas Propag.*, vol. 47, no. 9, pp. 1470–1475, Sep. 1999.
- [154] A. J. Martinez-Ros, J. L. Gomez-Tornero, and G. Goussetis, “Flexible pattern synthesis with SIW LWAs”, in *6th European Conf. on Antennas and Propagation (EuCAP)*, Prague, Czech Republic, Mar. 2012, pp. 229–233.
- [155] ———, “Microstrip half-mode leaky-wave antenna operating at 94 GHz”, in *2011 IEEE MTT-S Int. Microwave Workshop Series on Millimeter Wave Integration Technologies (IMWS)*, Sitges, Spain, Sep. 2011, pp. 45–48.
- [156] A. J. Martinez-Ros, J. L. Gomez-Torneo, D. Zelenchuk, G. Goussetis, and V. Fusco, “Substrate integrated waveguide leaky wave antenna designed for millimeter wave bands”, in *IET Seminar Millimeter Wave Technologies for Gigabit per Second Wireless Commun.*, Belfast, UK, Sep. 2012, pp. 79–82.
- [157] D. Zelenchuk, A. J. Martinez-Ros, T. Zvolensky, J. L. Gomez-Tornero, G. Goussetis, N. Buchanan, D. Linton, and V. Fusco, “W-band planar wide-angle scanning antenna architecture”, *Journal of Infrared, Millimeter, and Terahertz Waves*, vol. 34, pp. 127–139, 2 2013.
- [158] P. Henry and J. Ruscio, “A low-loss diffraction grating frequency multiplexer”, *IEEE Trans. Microw. Theory Tech.*, vol. 26, no. 6, pp. 428–433, Jun. 1978.
- [159] M. Iyer, R. Seager, and J. Vardaxoglou, “Wireless chip to chip interconnection for multichip modules using leaky wave antennas”, *Electron. Lett.*, vol. 29, no. 23, pp. 2030–2031, 1993.
- [160] T. Akiyama, K. Inagaki, T. Ohira, and M. Hikita, “Two-dimensional optical signal-processing beamformer using multilayer polymeric optical wave-

- guide arrays”, *IEEE Trans. Microw. Theory Tech.*, vol. 49, no. 10, pp. 2055–2061, 2001.
- [161] G. Eleftheriades and O. Siddiqui, “Negative refraction and focusing in hyperbolic transmission-line periodic grids”, *IEEE Trans. Microw. Theory Tech.*, vol. 53, no. 1, pp. 396–403, Jan. 2005.
- [162] E. Afshari, H. Bhat, and A. Hajimiri, “Ultrafast analog Fourier transform using 2-D LC lattice”, *IEEE Trans. Circuits Syst. I*, vol. 55, no. 8, pp. 2332–2343, Sep. 2008.
- [163] S. Gupta, S. Abielmona, and C. Caloz, “Microwave analog real-time spectrum analyzer (RTSA) based on the spectral–spatial decomposition property of leaky-wave structures”, *IEEE Trans. Microw. Theory Tech.*, vol. 57, no. 12, pp. 2989–2999, Dec. 2009.
- [164] T. Kodera and C. Caloz, “Integrated leaky-wave antenna–duplexer/diplexer using CRLH uniform ferrite-loaded open waveguide”, *IEEE Trans. Antennas Propag.*, vol. 58, no. 8, pp. 2508–2514, 2010.
- [165] C. Wu and T. Itoh, “Wideband/image-rejection distributed mixer integrated with a CRLH leaky wave antenna”, in *2010 Asia-Pacific Microwave Conf. Proc. (APMC)*, Yokohama, Japan, Dec. 2010, pp. 634–637.
- [166] J. Goodman, *Introduction To Fourier Optics*, ser. McGraw-Hill physical and quantum electronics series. Roberts & Company Publishers, 2005.
- [167] O. Losito, “The diverging-focusing properties of a tapered leaky wave antennas”, in *3rd European Conf. on Antennas and Propagation (EuCAP)*, Berlin, Germany, Mar. 2009, pp. 1304–1307.
- [168] M. Garcia-Vigueras, J. L. Gomez-Tornero, G. Goussetis, A. Weily, and Y. Guo, “Enhancing frequency-scanning response of leaky-wave antennas using high-impedance surfaces”, *IEEE Antennas Wireless Propag. Lett.*, vol. 10, pp. 7–10, 2011.

- [169] M. Antoniadou and G. Eleftheriades, “A CPS leaky-wave antenna with reduced beam squinting using NRI-TL metamaterials”, *IEEE Trans. Antennas Propag.*, vol. 56, no. 3, pp. 708–721, 2008.
- [170] C. Caloz, S. Abielmona, H. Van Nguyen, and A. Rennings, “Dual composite right/left-handed (D-CRLH) leaky-wave antenna with low beam squinting and tunable group velocity”, *Phys. Status Solidi B*, vol. 244, no. 4, pp. 1219–1226, 2007.
- [171] J. L. Gomez-Tornero, A. J. Martinez-Ros, A. Alvarez-Melcon, F. Mesa, and F. Medina, “Substrate integrated waveguide leaky-wave antenna with reduced beam squint”, in *European Microwave Conf. (EuMC)*, Nuremberg, Germany, Oct. 2013, pp. 491–494.
- [172] D. Sievenpiper, “Superluminal waveguides based on non-Foster circuits for broadband leaky-wave antennas”, *IEEE Antennas Wireless Propag. Lett.*, vol. 10, pp. 231–234, 2011.
- [173] I. Ohtera, “Focusing properties of a microwave radiator utilizing a slotted rectangular waveguide”, *IEEE Trans. Antennas Propag.*, vol. 38, no. 1, pp. 121–124, Jan. 1990.
- [174] G. Andrasic, J. James, and J. Hand, “Investigation of quasi-leaky-wave applicator using FD-TD computations”, in *Proc. 7th IEE Int. Conf. on Antennas and Propag. ICAP 91.*, vol. 2, York, UK, Apr. 1991, pp. 584–587.
- [175] I.-H. Lin, C. Caloz, and T. Itoh, “Near-field focusing by a nonuniform leaky-wave interface”, *Microw. Opt. Technol. Lett.*, vol. 44, no. 5, pp. 416–418, 2005.
- [176] M. Bogosonovic and A. Williamson, “Antenna array with beam focused in near-field zone”, *Electron. Lett.*, vol. 39, no. 9, pp. 704–705, May 2003.

- [177] K. Stephan, J. B. Mead, D. Pozar, L. Wang, and J. Pearce, “A near field focused microstrip array for a radiometric temperature sensor”, *IEEE Trans. Antennas Propag.*, vol. 55, no. 4, pp. 1199–1203, Apr. 2007.
- [178] S. Karimkashi and A. Kishk, “Focused microstrip array antenna using a Dolph-Chebyshev near-field design”, *IEEE Trans. Antennas Propag.*, vol. 57, no. 12, pp. 3813–3820, Dec. 2009.
- [179] Y. Monnai and H. Shinoda, “Focus-scanning leaky-wave antenna with electronically pattern-tunable scatterers”, *IEEE Trans. Antennas Propag.*, vol. 59, no. 6, pp. 2070–2077, Jun. 2011.
- [180] R. Siragusa, P. Lemaitre-Auger, and S. Tedjini, “Tunable near-field focused circular phase-array antenna for 5.8-GHz RFID applications”, *IEEE Antennas Wireless Propag. Lett.*, vol. 10, pp. 33–36, 2011.
- [181] A. Buffi, P. Nepa, and G. Manara, “Design criteria for near-field-focused planar arrays”, *IEEE Antennas Propag. Mag.*, vol. 54, no. 1, pp. 40–50, Feb. 2012.
- [182] J. Liu, D. Jackson, and Y. Long, “Propagation wavenumbers for half- and full-width microstrip lines in the  $EH_1$  mode”, *IEEE Trans. Microw. Theory Tech.*, vol. 59, no. 12, pp. 3005–3012, Dec. 2011.
- [183] O. Losito, “A new broadband microstrip leaky-wave antenna”, *ACES J.*, vol. 23, no. 3, pp. 243–248, 2008.
- [184] C. H. Durney and M. F. Iskander, “Antennas for medical applications”, English, in *Antenna Handbook*, Y. Lo and S. Lee, Eds., Springer US, 1988, pp. 1729–1788.
- [185] E. Nyfors and P. Vainikainen, *Industrial microwave sensors*, ser. Artech House microwave library. Artech House, 1989.

- [186] J. L. Gomez-Tornero, D. Rebenaque, F. Quesada-Pereira, J. Martinez, and A. Alvarez-Melcon, "PAMELA: a useful tool for the study of leaky-wave modes in strip-loaded open dielectric waveguides", *IEEE Antennas Propag. Mag.*, vol. 48, no. 4, pp. 54–72, Aug. 2006.
- [187] R. Collin, *Foundations for Microwave Engineering*, 2nd. Wiley India Pvt. Limited, 2007.
- [188] G. Lovat, P. Burghignoli, and D. Jackson, "Fundamental properties and optimization of broadside radiation from uniform leaky-wave antennas", *IEEE Trans. Antennas Propag.*, vol. 54, no. 5, pp. 1442–1452, May 2006.
- [189] J. W. Sherman III, "Properties of focused apertures in the Fresnel region", *IRE Trans. on Antennas and Propagation*, vol. 10, no. 4, pp. 399–408, Jul. 1962.
- [190] W. C. Brown, "The history of power transmission by radio waves", *IEEE Trans. Microw. Theory Tech.*, vol. 32, no. 9, pp. 1230–1242, Sep. 1984.
- [191] O. Momeni and E. Afshari, "Electrical prism: a high quality factor filter for millimeter-wave and terahertz frequencies", *IEEE Trans. Microw. Theory Tech.*, vol. 57, no. 11, pp. 2790–2799, Nov. 2009.
- [192] J. Wong, K. Balmain, and G. Eleftheriades, "A diplexer based on the spatial filtering property of planar anisotropic transmission-line metamaterials", in *IEEE Int. Workshop on Antenna Technology Small Antennas and Novel Metamaterials*, New York, USA, Mar. 2006, pp. 241–244.
- [193] A. J. Martinez-Ros and J. L. Gomez-Tornero, "Quasi-optical multiplexing using leaky-wave near-field focusing techniques in substrate integrated waveguide technology", in *2013 IEEE MTT-S Int. Microwave Symp. Dig. (IMS)*, Seattle, USA, Jun. 2013, pp. 1–3.
- [194] J. J. Stamnes, "Focusing of two-dimensional waves", *J. Opt. Soc. Am.*, vol. 71, no. 1, pp. 15–31, Jan. 1981.

- [195] T.-L. Chen and Y.-D. Lin, “Aperture-coupled microstrip line leaky wave antenna with broadside mainbeam”, *Electron. Lett.*, vol. 34, no. 14, pp. 1366–1367, Jul. 1998.
- [196] Y. Li, Q. Xue, E. Yung, and Y. Long, “Circularly-polarised microstrip leaky-wave antenna”, *Electron. Lett.*, vol. 43, no. 14, pp. 739–740, Jul. 2007.
- [197] K. Solbach and B. Adelseck, “Dielectric image line leaky wave antenna for broadside radiation”, *Electron. Lett.*, vol. 19, no. 16, pp. 640–641, 1983.
- [198] M. Guglielmi and D. Jackson, “Broadside radiation from periodic leaky-wave antennas”, *IEEE Trans. Antennas Propag.*, vol. 41, no. 1, pp. 31–37, 1993.
- [199] P. Burghignoli, G. Lovat, and D. Jackson, “Analysis and optimization of leaky-wave radiation at broadside from a class of 1-D periodic structures”, *IEEE Trans. Antennas Propag.*, vol. 54, no. 9, pp. 2593–2604, 2006.
- [200] J. Hirokawa and M. Ando, “Post-wall waveguide slot array antennas”, in *Proc. of the First European Conf. on Antennas and Propagation (EuCAP)*, Nice, France, Nov. 2006, pp. 1–5.
- [201] A. Sutinjo and M. Okoniewski, “A surface wave holographic antenna for broadside radiation excited by a traveling wave patch array”, *IEEE Trans. Antennas Propag.*, vol. 59, no. 1, pp. 297–300, 2011.
- [202] S. Lim, C. Caloz, and T. Itoh, “Metamaterial-based electronically controlled transmission-line structure as a novel leaky-wave antenna with tunable radiation angle and beamwidth”, *IEEE Trans. Microw. Theory Tech.*, vol. 53, no. 1, pp. 161–173, Jan. 2005.

- [203] S. Paulotto, P. Baccarelli, F. Frezza, and D. Jackson, “Full-wave modal dispersion analysis and broadside optimization for a class of microstrip CRLH leaky-wave antennas”, *IEEE Trans. Microw. Theory Tech.*, vol. 56, no. 12, pp. 2826–2837, 2008.
- [204] K.-C. Chen, Y. Qian, C.-K. Tzuang, and T. Itoh, “A periodic microstrip radial antenna array with a conical beam”, *IEEE Trans. Antennas Propag.*, vol. 51, no. 4, pp. 756–765, Apr. 2003.
- [205] A. J. Martinez-Ros, J. L. Gomez-Tornero, and G. Goussetis, “Broadside radiation from radial arrays of substrate integrated leaky-wave antennas”, in *6th European Conf. on Antennas and Propagation (EuCAP)*, Prague, Czech Republic, Mar. 2012, pp. 252–254.
- [206] T. Tamir, H. C. Wang, and A. Oliner, “Wave propagation in sinusoidally stratified dielectric media”, *IEEE Trans. Microw. Theory Tech.*, vol. 12, no. 3, pp. 323–335, May 1964.
- [207] A. H. Nayfeh and O. Asfar, “Parallel-plate waveguide with sinusoidally perturbed boundaries”, *J. Appl. Phys.*, vol. 45, no. 11, pp. 4797–4800, Nov. 1974.
- [208] A. K. Mallick and G. Sanyal, “Electromagnetic wave propagation in a rectangular waveguide with sinusoidally varying width”, *IEEE Trans. Microw. Theory Tech.*, vol. 26, no. 4, pp. 243–249, Apr. 1978.
- [209] A. W. Snyder and R. A. Sammut, “Radiation from optical waveguides: leaky-mode interpretation”, *Electron. Lett.*, vol. 15, no. 2, pp. 58–60, Jan. 1979.
- [210] G. Kowalski, “Microstrip meanderlines”, *AEU - International Journal of Electronics and Communications*, vol. 29, no. 6, pp. 248–250, 1975.

- [211] N. V. Nair and K. Mallick, "An analysis of a width-modulated microstrip periodic structure", *IEEE Trans. Microw. Theory Tech.*, vol. 32, no. 2, pp. 200–204, Feb. 1984.
- [212] C. Caloz, "Metamaterial dispersion engineering concepts and applications", *Proc. IEEE*, vol. 99, no. 10, pp. 1711–1719, Oct. 2011.
- [213] C. Holloway, E. F. Kuester, J. Gordon, J. O'Hara, J. Booth, and D. Smith, "An overview of the theory and applications of metasurfaces: the two-dimensional equivalents of metamaterials", *IEEE Antennas Propag. Mag.*, vol. 54, no. 2, pp. 10–35, Apr. 2012.
- [214] T. Lopetegi, M. A. G. Laso, J. Hernandez, M. Bacaicoa, D. Benito, M. Garde, M. Sorolla, and M. Guglielmi, "New microstrip "Wiggly-Line" filters with spurious passband suppression", *IEEE Trans. Microw. Theory Tech.*, vol. 49, no. 9, pp. 1593–1598, Sep. 2001.
- [215] M. A. G. Laso, T. Lopetegi, M. J. Erro, D. Benito, M. Garde, M. Muriel, M. Sorolla, and M. Guglielmi, "Real-time spectrum analysis in microstrip technology", *IEEE Trans. Microw. Theory Tech.*, vol. 51, no. 3, pp. 705–717, Mar. 2003.
- [216] S. Podilchak, A. Freundorfer, and Y. Antar, "Planar leaky-wave antenna designs offering conical-sector beam scanning and broadside radiation using surface-wave launchers", *IEEE Antennas Wireless Propag. Lett.*, vol. 7, pp. 155–158, 2008.
- [217] Z. Mekkioui, "Determination of non uniform sinusoidal microstrip leaky-wave antenna radiating performances in millimeter band", *Int. Journal of Electric and Electronic Engineering. Proceeding of World Academy of Science, Engineering and Technology*, vol. 75, pp. 1290–1294, 2011.
- [218] Q.-H. Lai, W. Hong, Z.-Q. Kuai, Y. S. Zhang, and K. Wu, "Half-mode substrate integrated waveguide transverse slot array antennas", *IEEE Trans. Antennas Propag.*, vol. 57, no. 4, pp. 1064–1072, Apr. 2009.

- [219] Q. Lai, C. Fumeaux, and W. Hong, “Periodic leaky-wave antennas fed by a modified half-mode substrate integrated waveguide”, *IET Microw. Antennas Propag.*, vol. 6, no. 5, pp. 594–601, Apr. 2012.
- [220] A. J. Martinez-Ros and J. L. Gomez-Tornero, “Free space near field focusing from an array of sinusoidally modulated half-mode LWAs”, in *IEEE Antennas and Propagation Soc. Int. Symp. (APSURSI)*, Orlando, USA, Jul. 2013, pp. 1568–1569.
- [221] D. M. Pozar, *Microwave Engineering*, 2nd. John Wiley & Sons, Inc, 1998.
- [222] A. Grbic and R. Merlin, “Near-field focusing plates and their design”, *IEEE Trans. Antennas Propag.*, vol. 56, no. 10, pp. 3159–3165, Oct. 2008.
- [223] A. J. Martinez-Ros, J. L. Gomez-Tornero, F. J. Clemente-Fernandez, and J. Monzo-Cabrera, “Microwave near-field focusing properties of width-tapered microstrip leaky-wave antenna”, *IEEE Trans. Antennas Propag.*, vol. 61, no. 6, pp. 2981–2990, Jun. 2013.
- [224] M. Ettorre, M. Casaletti, G. Valerio, R. Sauleau, L. Le Coq, S. Pavone, and M. Albani, “On the near-field shaping and focusing capability of a radial line slot array”, *IEEE Trans. Antennas Propag.*, vol. 62, no. 4, pp. 1991–1999, Apr. 2014.
- [225] M. Ettorre and A Grbic, “Generation of propagating Bessel beams using leaky-wave modes”, *IEEE Trans. Antennas Propag.*, vol. 60, no. 8, pp. 3605–3613, Aug. 2012.
- [226] P. Lemaitre-Augier, S. Abielmona, and C. Caloz, “Generation of Bessel beams by two-dimensional antenna arrays using sub-sampled distributions”, *IEEE Trans. Antennas Propag.*, vol. 61, no. 4, pp. 1838–1849, Apr. 2013.

- 
- [227] C. Caloz and T. Itoh, “Array factor approach of leaky-wave antennas and application to 1-D/2-D composite right/left-handed (CRLH) structures”, *IEEE Microw. Wireless Compon. Lett.*, vol. 14, no. 6, pp. 274 –276, Jun. 2004.
- [228] C. A. Balanis, *Antenna theory: analysis and design*, 3rd. John Wiley & Sons, 2012.



# Publications

## International Journals

- [J1] A. J. Martinez-Ros, J. L. Gomez-Tornero, and G. Goussetis, “Planar leaky-wave antenna with flexible control of the complex propagation constant”, *IEEE Trans. Antennas Propag.*, vol. 60, no. 3, pp. 1625 –1630, Mar. 2012
- [J2] A. J. Martinez-Ros, J. L. Gomez-Tornero, and F. Quesada-Pereira, “Efficient analysis and design of novel SIW leaky-wave antenna”, *IEEE Antennas Wireless Propag. Lett.*, vol. 12, pp. 496–499, 2013
- [J3] A. J. Martinez-Ros, J. L. Gomez-Tornero, and G. Goussetis, “Holographic pattern synthesis with modulated substrate integrated waveguide line-source leaky-wave antennas”, *IEEE Trans. Antennas Propag.*, vol. 61, no. 7, pp. 3466–3474, 2013
- [J4] D. Zelenchuk, A. J. Martinez-Ros, T. Zvolensky, J. L. Gomez-Tornero, G. Goussetis, N. Buchanan, D. Linton, and V. Fusco, “W-band planar wide-angle scanning antenna architecture”, *Journal of Infrared, Millimeter, and Terahertz Waves*, vol. 34, pp. 127–139, 2 2013
- [J5] A. J. Martinez-Ros, J. L. Gomez-Tornero, F. J. Clemente-Fernandez, and J. Monzo-Cabrera, “Microwave near-field focusing properties of width-tapered microstrip leaky-wave antenna”, *IEEE Trans. Antennas Propag.*, vol. 61, no. 6, pp. 2981–2990, Jun. 2013

- [J6] A. J. Martinez-Ros, J. L. Gomez-Tornero, and G. Goussetis, “Pencil beam radiation pattern from a single layer SIW LWA with simple feeding”, *IET Microw. Antennas Propag.*, to be published
- [J7] A. J. Martinez-Ros, J. L. Gomez-Tornero, and G. Goussetis, “Conformal tapered substrate integrated waveguide leaky-wave antenna”, *IEEE Trans. Antennas Propag.*, to be published
- [J8] J. L. Gomez-Tornero, A. J. Martinez-Ros, and J. Monzo-Cabrera, “Simple electronic near-field beamforming using multi-tone microwave signals with a leaky-wave focused applicator”, *IEEE Antennas Wireless Propag. Lett.*, to be published
- [J9] J. L. Gomez-Tornero, A. J. Martinez-Ros, S. Mercader-Pellicer, and G. Goussetis, “Simple broadband quasi-optical spatial multiplexer in substrate integrated technology”, *IEEE Trans. Microw. Theory Tech.*, submitted for publication
- [J10] A. J. Martinez-Ros, J. L. Gomez-Tornero, V. Losada, F. Mesa, and F. Medina, “Non-uniform sinusoidally modulated half-mode leaky-wave lines for near-field focusing pattern synthesis”, *IEEE Trans. Antennas Propag.*, submitted for publication
- [J11] A. J. Martinez-Ros, J. L. Gomez-Tornero, and G. Goussetis, “Quasi-elliptic angular bandpass filter using a single-layer modulated SIW travelling-wave line”, *IEEE Trans. Microw. Theory Tech.*, submitted for publication

### International Conferences

- [IC1] A. J. Martinez-Ros, J. L. Gomez-Tornero, and G. Goussetis, “Independent control of the leakage rate and pointing angle of a novel planar leaky-wave antenna”, in *Proc. of the 5th European Conf. on Antennas and Propagation (EuCAP)*, Rome, Italy, Apr. 2011, pp. 1919 –1922

- 
- [IC2] A. J. Martinez-Ros, J. L. Gomez-Tornero, F. Quesada-Pereira, and A. Alvarez-Melcon, "Transverse resonance analysis of a planar leaky wave antenna with flexible control of the complex propagation constant", in *IEEE Int. Symp. on Antennas and Propagation (APSURSI)*, Spokane, USA, Jul. 2011, pp. 1289–1292
- [IC3] P. Vera, F. Quesada, A. Alvarez Melcon, A. Martinez Ros, J. Tornero, B. Gimeno, and V. Boria Esbert, "Novel integral equation formulation for the analysis of capacitive waveguide filters containing dielectric objects", in *IEEE Int. Symp. on Antennas and Propagation (APSURSI)*, Spokane, USA, Jul. 2011, pp. 197–200
- [IC4] A. J. Martinez-Ros, J. L. Gomez-Tornero, and G. Goussetis, "Microstrip half-mode leaky-wave antenna operating at 94 GHz", in *2011 IEEE MTT-S Int. Microwave Workshop Series on Millimeter Wave Integration Technologies (IMWS)*, Sitges, Spain, Sep. 2011, pp. 45–48
- [IC5] A. J. Martinez-Ros, J. L. Gomez-Tornero, and G. Goussetis, "Frequency scanning leaky-wave antenna for positioning and identification of RFID tags", in *2011 IEEE Int. Conf. on RFID-Technologies and Applications (RFID-TA)*, Sitges, Spain, Sep. 2011, pp. 451–456
- [IC6] A. J. Martinez-Ros, J. L. Gomez-Tornero, and G. Goussetis, "Broadside radiation from radial arrays of substrate integrated leaky-wave antennas", in *6th European Conf. on Antennas and Propagation (EuCAP)*, Prague, Czech Republic, Mar. 2012, pp. 252–254
- [IC7] A. J. Martinez-Ros, J. L. Gomez-Tornero, and G. Goussetis, "Conformal tapered microstrip leaky-wave antennas", in *6th European Conf. on Antennas and Propagation (EuCAP)*, Prague, Czech Republic, Mar. 2012, pp. 154–158

- [IC8] A. J. Martinez-Ros, J. L. Gomez-Tornero, and G. Goussetis, “Flexible pattern synthesis with SIW LWAs”, in *6th European Conf. on Antennas and Propagation (EuCAP)*, Prague, Czech Republic, Mar. 2012, pp. 229–233
- [IC9] A. J. Martinez-Ros, J. L. Gomez-Torneo, D. Zelenchuk, G. Goussetis, and V. Fusco, “Substrate integrated waveguide leaky wave antenna designed for millimeter wave bands”, in *IET Seminar Millimeter Wave Technologies for Gigabit per Second Wireless Commun.*, Belfast, UK, Sep. 2012, pp. 79–82
- [IC10] A. J. Martinez-Ros and J. L. Gomez-Tornero, “Quasi-optical multiplexing using leaky-wave near-field focusing techniques in substrate integrated waveguide technology”, in *2013 IEEE MTT-S Int. Microwave Symp. Dig. (IMS)*, Seattle, USA, Jun. 2013, pp. 1–3
- [IC11] A. J. Martinez-Ros, J. L. Gomez-Tornero, and G. Goussetis, “Modulated leaky waves to mold the radiation from substrate integrated waveguide antennas”, in *IEEE Antennas and Propagation Soc. Int. Symp. (APSURSI)*, Orlando, USA, Jul. 2013, pp. 1566–1567
- [IC12] A. J. Martinez-Ros and J. L. Gomez-Tornero, “Free space near field focusing from an array of sinusoidally modulated half-mode LWAs”, in *IEEE Antennas and Propagation Soc. Int. Symp. (APSURSI)*, Orlando, USA, Jul. 2013, pp. 1568–1569
- [IC13] J. L. Gomez-Tornero, A. J. Martinez-Ros, A. Alvarez-Melcon, F. Mesa, and F. Medina, “Substrate integrated waveguide leaky-wave antenna with reduced beam squint”, in *European Microwave Conf. (EuMC)*, Nuremberg, Germany, Oct. 2013, pp. 491–494
- [IC14] A. J. Martinez-Ros, R. Guzman-Quiros, and J. L. Gomez-Tornero, “Static and electronic shaping of the radiated electromagnetic fields in radial arrays

of substrate integrated leaky-wave antennas”, in *European Microwave Conf. (EuMC)*, Nuremberg, Germany, Oct. 2013, pp. 1667–1670

### National Journals

- [NJ1] A. J. Martinez-Ros, M. García-Vigueras, R. Gúzman-Quiros, and J. L. Gomez-Tornero, “Control del mecanismo de radiación de una antena leaky-wave en tecnología planar”, *IV Jornadas de Introducción a la Investigación de la UPCT*, vol. 4, pp. 91–93, May 2011
- [NJ2] R. Gúzman-Quiros, M. García-Vigueras, A. J. Martinez-Ros, and Gomez-Tornero, “Control electrónico del haz radiado en antenas leaky wave activas”, *IV Jornadas de Introducción a la Investigación de la UPCT*, vol. 4, pp. 94–96, May 2011
- [NJ3] M. García-Vigueras, A. J. Martinez-Ros, R. Gúzman-Quiros, and Gomez-Tornero, “Control de la directividad en broadside en antena leaky-wave 1D”, *IV Jornadas de Introducción a la Investigación de la UPCT*, vol. 4, pp. 97–99, May 2011
- [NJ4] A. J. Martinez-Ros, J. A. Lorente Acosta, and J. L. Gomez-Tornero, “Síntesis de diagramas de radiación de una antena leaky-wave en tecnología de guía de onda integrada en sustrato”, *V Jornadas de Introducción a la Investigación de la UPCT*, vol. 5, pp. 87–89, Apr. 2012
- [NJ5] J. A. Lorente Acosta, A. J. Martinez-Ros, and A. Alvarez Melcon, “Obtención del circuito equivalente de filtros guía-onda de banda estrecha”, *V Jornadas de Introducción a la Investigación de la UPCT*, vol. 5, pp. 93–95, Apr. 2012
- [NJ6] R. Gúzman-Quiros, A. J. Martinez-Ros, and J. L. Gomez-Tornero, “Escaneo electrónico del haz de radiación en antenas leaky-wave 2D empleando

superficies de alta impedancia activas”, *VI Jornadas de Introducción a la Investigación de la UPCT*, vol. 6, pp. 127–130, May 2013

- [NJ7] A. J. Martinez-Ros, R. Gúzman-Quiros, and J. L. Gomez-Tornero, “Aplicación de diseño holográfico para reducir el nivel de lóbulo secundario en antenas leaky-wave en tecnología SIW”, *VI Jornadas de Introducción a la Investigación de la UPCT*, vol. 6, pp. 130–133, May 2013

### National Conferences

- [NC1] A. Martínez Ros, M. Montesinos Illán, J. Galindo Rosique, J. Gómez Tornero, and A. Álvarez Melcón, “Control del mecanismo de radiación de una LWA en tecnología HMSIW”, in *XXIV Simposium Nacional de la Unión Científica Internacional de Radio (URSI 2009)*, Santander, Spain, Sep. 2009
- [NC2] J. Galindo Rosique, J. Gómez-Díaz, A. Martínez Ros, J. Gómez Tornero, and A. Álvarez Melcón, “Fenómeno de pared magnética en antenas ranuradas utilizando tecnología SIW”, in *XXIV Simposium Nacional de la Unión Científica Internacional de Radio (URSI 2009)*, Santander, Spain, Sep. 2009
- [NC3] M. García-Vigueras, R. Gúzman-Quiros, A. J. Martinez-Ros, J. Gómez-Díaz, and J. L. Gómez-Tornero, “Síntesis de la radiación en broadside en antena leaky-wave 1D”, in *XXVI Simposium Nacional de la Unión Científica Internacional de Radio (URSI 2011)*, Leganés, Spain, Sep. 2011
- [NC4] R. Gúzman-Quiros, M. García-Vigueras, A. J. Martinez-Ros, and J. L. Gómez-Tornero, “Reconfiguración electrónica del haz radiado en antenas leaky wave basadas en HIS activas”, in *XXVI Simposium Nacional de la Unión Científica Internacional de Radio (URSI 2011)*, Leganés, Spain, Sep. 2011
- [NC5] A. J. Martinez-Ros, J. L. Gómez-Tornero, and F. Quesada-Pereira, “Diseño de una antena leaky-wave en tecnología de guía de onda integrada en sub-

- strato para una frecuencia de 94 GHz”, in *XXVI Symposium Nacional de la Unión Científica Internacional de Radio (URSI 2011)*, Leganés, Spain, Sep. 2011
- [NC6] A. J. Martinez-Ros, J. L. Gómez-Tornero, F. Quesada-Pereira, and A. Alvarez-Melcon, “Análisis eficiente y control de la constante de propagación compleja de una antena leaky-wave en tecnología planar”, in *XXVI Symposium Nacional de la Unión Científica Internacional de Radio (URSI 2011)*, Leganés, Spain, Sep. 2011
- [NC7] A. J. Martinez-Ros, M. García-Vigueras, R. Gúzman-Quiros, and J. L. Gómez-Tornero, “Determinación del ángulo de apuntamiento y de la anchura de haz en una antena leaky-wave en tecnología planar”, in *XXVI Symposium Nacional de la Unión Científica Internacional de Radio (URSI 2011)*, Leganés, Spain, Sep. 2011
- [NC8] A. J. Martinez-Ros, J. L. Gómez-Tornero, R. Gúzman-Quiros, and M. García-Vigueras, “Holographic pattern synthesis with one-dimensional substrate integrated waveguide leaky-wave antennas”, in *XXVII Symposium Nacional de la Unión Científica Internacional de Radio (URSI 2012)*, Elche, Spain, Sep. 2012
- [NC9] R. Gúzman-Quiros, J. L. Gómez-Tornero, M. García-Vigueras, and A. J. Martinez-Ros, “Backward-to-forward electronic scanning in symmetrically excited 1D Fabry-Pérot leaky-wave antennas”, in *XXVII Symposium Nacional de la Unión Científica Internacional de Radio (URSI 2012)*, Elche, Spain, Sep. 2012
- [NC10] M. García-Vigueras, J. L. Gómez-Tornero, R. Gúzman-Quiros, and A. J. Martinez-Ros, “Optimización de la directividad en antenas leaky-wave 1D y 2D basadas en cavidades Fabry-Pérot”, in *XXVII Symposium Nacional de*

*la Unión Científica Internacional de Radio (URSI 2012)*, Elche, Spain, Sep. 2012

- [NC11] R. Gúzman-Quiros, J. L. Gómez-Tornero, A. J. Martínez-Ros, A. Weily, and Y. Guo, “Novel and simple electronically reconfigurable Fabry-Pérot antennas”, in *XXVIII Simposium Nacional de la Unión Científica Internacional de Radio (URSI 2013)*, Santiago de Compostela, Spain, Sep. 2013
- [NC12] A. J. Martínez-Ros, J. L. Gómez-Tornero, and R. Gúzman-Quiros, “Nuevo tipo de circuito multiplexador en tecnología SIW usando técnicas cuasi-ópticas y ondas de fuga”, in *XXVIII Simposium Nacional de la Unión Científica Internacional de Radio (URSI 2013)*, Santiago de Compostela, Spain, Sep. 2013

# Acknowledgments

El camino que ha llevado a la realización de esta tesis, ha supuesto para mí una etapa de gran enriquecimiento personal y profesional. Además, me ha aportado una gran cantidad de vivencias, la cuales ya han pasado a formar parte de mi vida. Por todo ello, aunque se me hace difícil el poder nombrar a todas las personas que me han ayudado a lo largo de este trayecto, por lo menos quisiera intentar devolver parte de ese apoyo en esta última sección.

En primer lugar, quisiera dar las gracias a mis amigos el haber estado siempre ahí, en concreto a Ángel A., Ángel, Antonio, Ana M., Ana, David, Fran, Joaquín, Katja, Leo, María José, Muriel, Pedro, Raquel Z., Raquel y Samuel.

También quiero acordarme de mis amigos con los que he pasado muchas tardes de sol y playa en el Portús, entre ellos de Armando, Diego, José, Miguel, Pedro, Toni...

Gracias también a Alberto, Fernando, Gregorio, Iván, José Luis, Juanma y Pedro, con los que he disfrutado de muchos momentos únicos en Cartagena.

No me olvido de mis amigos futboleros Amos, Borja, Joaquín y Juanma, con los que he compartido tantas risas y buenos momentos.

A mi amiga Marta con la que he disfrutado de un montón de conciertos de La Mar de Músicas.

También a mi compañero de vela Manolo, con el que he pasado muy buenos momentos navegando.

A todos mis compañeros del laboratorio con los que he compartido el día a día de esta tesis, además de compartir experiencias en viajes, congresos y demás... Entre

todos ellos, Attieh, Conchi, María, Jorge G., Jorge, José Antonio, Maite, Manuel, Mónica, Raúl y Sebas.

También agradecer a mi director José Luis que ha contribuido en la realización de esta tesis, la cual seguro sin él nunca hubiera podido ser la misma.

A Mercedes, Héctor, Salva y Miguel Ángel, por haber decidido realizar sus proyectos fin de carrera conmigo.

Al resto de compañeros de la universidad con los que también he compartido vivencias y me han ayudado con sus experiencias: David, Fernando, Juan Pascual, Juan Morales, José María, José Víctor... y en especial a Alejandro Álvarez por haberme escuchado en momentos de dudas.

A todas las personas que han formado parte de mi vida, y que por unos motivos o por otros ya no están.

A toda la gente que estuvo conmigo durante mi estancia en Belfast y que me ayudaron a que la experiencia fuera lo mejor posible, en concreto, Dmitry, Chris, Efstratios, George, Gwendal, Keissy, Manuel, Michael, Óscar, Pak, Peter, Rob...

Para finalizar, quiero también agradecer a mi familia, tíos, primos... y en especial a mis padres y a mi hermano, el apoyo y el cariño recibido durante esta tesis, así como a lo largo de toda mi vida, de ellos también es parte de esta tesis.

Cartagena, a 23 de julio de 2014